Steel Truss Retrofits to Provide Alternate Load Paths for Cut, Damaged, or Destroyed Members

PUBLICATION NO. FHWA-HRT-20-055

NOVEMBER 2020

U.S. Department of Transportation
Federal Highway Administration

Research, Development, and Technology
Turner-Fairbank Highway Research Center
6300 Georgetown Pike
McLean, VA 22101-2296

FOREWORD

This study was part of the Federal Highway Administration Hazard Mitigation Research Program addressing bridge vulnerabilities to single or multiple hazards, developing countermeasures for mitigation and adaptation, and developing analysis and design tools and methodologies. This report presents the results of a study on load-path redundancy and its importance in redistributing loads and maintaining stability, which may become necessary to prevent collapse at the onset of critical member failure. It focuses on long-span steel truss bridges of interest to the bridge engineering community and design and practicing engineers.

This research extensively investigated load-path redundancy, including quantification of alternate load path (ALP), which is defined as the spectra of the surrounding members undergoing load redistribution after sudden damage to bridge members. Bridge members were compared before and after potential retrofit to judge the effectiveness of retrofit schemes in improving the ALP. An integrated framework to quantify the ALP of long-span truss bridges in terms of demand-to-capacity ratio (*DCR*) for the linear elastic analysis and strain ratio (*SR*) for the nonlinear dynamic analysis was developed. Different performance levels in terms of *DCR* and *SR* are also presented for practicing engineers to use for the retrofit of long-span bridges to protect against progressive collapse.

Cheryl Allen Richter, P.E., Ph.D.
Director, Office of Infrastructure
Research and Development

TECHNICAL REPORT DOCUMENTATION PAGE

1. Report No. FHWA-HRT-20-055	2. Government Accession No.	3. Recipient's Catalog No.
4. Title and Subtitle Steel Truss Retrofits to Provide Alternate Load Paths for Cut, Damaged, or Destroyed Members		5. Report Date November 2020 6. Performing Organization Code
7. Author(s) A.K. Agrawal (ORCID: 0000-0001-6660-2299), M. Ettouney, X. Chen, H. Li (ORCID: 000-0002-0858-2258), and H. Wang		8. Performing Organization Report No.
9. Performing Organization Name and Address The City College of New York 160 Convent Avenue New York, NY 10031		10. Work Unit No. 11. Contract or Grant No. DTFH61-14-D-00010/0004
12. Sponsoring Agency Name and Address Office of Infrastructure Research and Development Federal Highway Administration 6300 Georgetown Pike McLean, VA 22101		13. Type of Report and Period Covered Final Report; August 2014–June 2018 14. Sponsoring Agency Code HRDI-20

15. Supplementary Notes
The Federal Highway Administration (FHWA) Study Managers were Eric Munley (FHWA, retired) and Sheila Rimal Duwadi, P.E. (HRDI-20).

16. Abstract
Continued stability and performance of long-span truss bridges after loss of a critical member is broadly attributed to "redundancy" because of alternate load paths (ALPs). This report presents an extensive investigation on the load-path redundancy of long-span truss bridges, including quantification of ALP, defined as the spectra of surrounding members undergoing load redistribution to prevent bridge collapse after sudden damage to a member or members. This research developed an integrated framework to quantify ALP of long-span truss bridges in terms of demand-to-capacity ratio (*DCR*) for linear elastic analysis and strain ratio for nonlinear dynamic (NLD) analysis. ALP of long-span truss bridges was investigated through finite-element simulations of two example long-span truss bridges. Results of the member removal analysis showed that the three-dimensionality of truss bridges, stemming from upper and lower braces, side trusses, floor beam trusses, and the deck, plays a primary role in protecting the bridge from collapse after removal of a member or members. Simulation results showed that the stress contribution to *DCR* changes from primarily axial to predominantly moment (both in-plane and out-of-plane) for truss members affected by sudden removal of another truss member. This change occurs because the superstructure tends to undergo torsional motion about its longitudinal axis due to the asymmetrical geometry created after removal of a member. Upper and lower braces and floor truss systems resist this torsional motion, thereby redistributing the load among truss members. Various retrofit approaches were investigated to improve ALP of two example bridges. The typical member strengthening approach used during seismic retrofit had limited effectiveness in improving ALP of long-span truss bridges; however, retrofits that involved member strengthening as well as adding new members as braces or parts of floor trusses (i.e., members that enhance the three-dimensionality of the bridge) were the most effective and added the least amount of additional weight. NLD analysis using LS-DYNA software (Hallquist 2014) resulted in more cost-effective retrofit than linear dynamic analysis using SAP2000 software (Computers and Structures, Inc.). Performance levels are presented for practicing engineers to use for the retrofit of long-span bridges to protect against progressive collapse. Experimental and theoretical needs for investigating ALP of long-span truss bridges are also discussed.

17. Key Words	18. Distribution Statement
Alternate load path, redundancy, long-span truss bridges, progressive collapse	No restrictions. This document is available to the public through the National Technical Information Service, Springfield, VA 22161. http://www.ntis.gov

19. Security Classif. (of this report)	20. Security Classif. (of this page)	21. No. of Pages	22. Price
Unclassified	Unclassified	216	N/A

SI* (MODERN METRIC) CONVERSION FACTORS

APPROXIMATE CONVERSIONS TO SI UNITS

Symbol	When You Know	Multiply By	To Find	Symbol
		LENGTH		
in	inches	25.4	millimeters	mm
ft	feet	0.305	meters	m
yd	yards	0.914	meters	m
mi	miles	1.61	kilometers	km
		AREA		
in^2	square inches	645.2	square millimeters	mm^2
ft^2	square feet	0.093	square meters	m^2
yd^2	square yard	0.836	square meters	m^2
ac	acres	0.405	hectares	ha
mi^2	square miles	2.59	square kilometers	km^2
		VOLUME		
fl oz	fluid ounces	29.57	milliliters	mL
gal	gallons	3.785	liters	L
ft^3	cubic feet	0.028	cubic meters	m^3
yd^3	cubic yards	0.765	cubic meters	m^3
	NOTE: volumes greater than 1,000 L shall be shown in m^3			
		MASS		
oz	ounces	28.35	grams	g
lb	pounds	0.454	kilograms	kg
T	short tons (2,000 lb)	0.907	megagrams (or "metric ton")	Mg (or "t")
		TEMPERATURE (exact degrees)		
°F	Fahrenheit	5 (F-32)/9 or (F-32)/1.8	Celsius	°C
		ILLUMINATION		
fc	foot-candles	10.76	lux	lx
fl	foot-Lamberts	3.426	candela/m^2	cd/m^2
		FORCE and PRESSURE or STRESS		
lbf	poundforce	4.45	newtons	N
lbf/in^2	poundforce per square inch	6.89	kilopascals	kPa

APPROXIMATE CONVERSIONS FROM SI UNITS

Symbol	When You Know	Multiply By	To Find	Symbol
		LENGTH		
mm	millimeters	0.039	inches	in
m	meters	3.28	feet	ft
m	meters	1.09	yards	yd
km	kilometers	0.621	miles	mi
		AREA		
mm^2	square millimeters	0.0016	square inches	in^2
m^2	square meters	10.764	square feet	ft^2
m^2	square meters	1.195	square yards	yd^2
ha	hectares	2.47	acres	ac
km^2	square kilometers	0.386	square miles	mi^2
		VOLUME		
mL	milliliters	0.034	fluid ounces	fl oz
L	liters	0.264	gallons	gal
m^3	cubic meters	35.314	cubic feet	ft^3
m^3	cubic meters	1.307	cubic yards	yd^3
		MASS		
g	grams	0.035	ounces	oz
kg	kilograms	2.202	pounds	lb
Mg (or "t")	megagrams (or "metric ton")	1.103	short tons (2,000 lb)	T
		TEMPERATURE (exact degrees)		
°C	Celsius	1.8C+32	Fahrenheit	°F
		ILLUMINATION		
lx	lux	0.0929	foot-candles	fc
cd/m^2	candela/m2	0.2919	foot-Lamberts	fl
		FORCE and PRESSURE or STRESS		
N	newtons	2.225	poundforce	lbf
kPa	kilopascals	0.145	poundforce per square inch	lbf/in^2

*SI is the symbol for International System of Units. Appropriate rounding should be made to comply with Section 4 of ASTM E380. (Revised March 2003)

TABLE OF CONTENTS

LIST OF FIGURES

LIST OF TABLES

LIST OF ABBREVIATIONS AND SYMBOLS

Abbreviations

2D	two-dimensional
3D	three-dimensional
AASHTO	American Association of State Highway and Transportation Officials
AISC	American Institute of Steel Construction
ALP	alternate load path
APM	alternate path method
ASCE	American Society of Civil Engineers
ASD	allowable strength design
B-S	Belytschko–Schwer
BRB	buckling-restrained brace
CSA	Canadian Standards Association
DispR	displacement ratio
DLA	dynamic load amplification
DM	diagonal member
DMR	dual member removal
DOF	degree of freedom
DR	dynamic relaxation
FEM	finite-element model
FHWA	Federal Highway Administration
FRP	fiberglass reinforced plastic
FS	floor truss system
GSA	General Services Administration
H-L	Hughes–Liu
LRFD	load and resistance factor design
MR	member removal
NLD	nonlinear dynamic
NLS	nonlinear static
PBD	performance-based design

Symbols

DCR	demand-to-capacity ratio
SR	strain ratio
DL	dead load
LL	live load
BL	blast
S	structural system
r_m	number of components
M	components
W	set of individual components (members)
i	subscript denoting *i*th component
D	demand
αDL	dead load factor
αLL	live load factor

DM	design metric
$LIM(DM)$	limit state of design metric
σ_y	yield stress
ε	strain
ε_y	yield strain
$_0$	subscript denoting base system/condition/set/metric
$_1$	subscript denoting new system/condition/set/metric
$_j$	subscript denoting jth limit state
P_r	axial force demand
P_c	axial force capacity
M_{rx}	bending moment demand with respect to the x-axis
M_{cx}	bending moment capacity with respect to the x-axis
M_{ry}	bending moment demand with respect to the y-axis
M_{cy}	bending moment capacity with respect to the y-axis
A_c	member cross-sectional area
S_{xx}	section modulus with respect to the x-axis
S_{yy}	section modulus with respect to the y-axis
σ_{rp}	axial stress
σ_{Mx}	stress due to moments with respect to the x-axis
σ_{My}	stress due to moments with respect to the y-axis
Ω	safety factor
σ_{allow}	allowable stress obtained from σ_y divided by Ω based on the allowable strength design approach
α	design coefficient for load and resistance factor design or allowable strength design method
P_e	elastic critical buckling strength of member
C_m	reduction coefficient
M_1	smaller moment
M_2	larger moment
EQ	seismic load
$_R$	subscript denoting response
I	node
J	node
$\hat{}$	quantity defined in local element coordinate system
$\hat{X}$	local x-axis
$\hat{Y}$	local y-axis
$\hat{Z}$	local z-axis
e_1, e_2, e_3	unit vectors associated with $\hat{X}$, $\hat{Y}$, and $\hat{Z}$
$\bar{}$	quantity defined in global element coordinate system
$\bar{X}$	global x-axis
$\bar{Y}$	global y-axis
$\overrightarrow{b_1}$	unit vector along global axis $\bar{X}$
$\overrightarrow{b_2}$	unit vector along global axis $\bar{Y}$
$\overrightarrow{e_1^0}$	unit vector along local axis $\hat{X}$ in initial configuration
$\overrightarrow{e_2^0}$	unit vector along local axis $\hat{Y}$ in initial configuration

$\overrightarrow{e_1}$	unit vector along local axis $\hat{X}$
$\overrightarrow{e_2}$	unit vector along local axis $\hat{Y}$
$\hat{d}^T$	displacement matrix
δ_{IJ}	change in length (from nodes *I* to *J*)
$\hat{\theta}_{xIJ}$	torsional deformation
$\hat{\theta}_{yI}, \hat{\theta}_{yJ}, \hat{\theta}_{zI}, \hat{\theta}_{zJ}$	bending rotational deformations (first subscript is direction; second subscript is node)
A, B, C, n	input constants
ε^p	effective plastic strain
ε^*	normalized effective strain rate
E	Young's modulus
G	shear modulus
I_{xx}	moment of inertia (*xx* component)
I_{yy}	moment of inertia (*yy* component)
ρ	density
F_x	concentrated force along *x* direction
F_y	concentrated force along *y* direction
F_z	concentrated force along *z* direction
M_x	concentrated moment along *x* direction
M_y	concentrated moment along *y* direction
M_z	concentrated moment along *z* direction
u_x	displacement in *x* direction
u_y	displacement in *y* direction
u_z	displacement in *z* direction
F	force
h	height
L	length
σ_u	ultimate stress
K	effective length factor
Δ	difference
D_s	global damping factor
δ_e	logarithmic decrement
q	number of cycles
u_1	peak amplitude of the first peak
u_{q+1}	peak amplitude of the (q+1)th peak
ζ	damping ratio
M_{in}	in-plane moment
M_{out}	out-of-plane moment
S_s	short period
S_1	1-second period
$\{U\}_i$	3D beam global displacements and rotations vector of the *i*th beam
$\{U\}_{i1}$	vector of the six global displacement and rational measures of the first node of the beam
$\{U\}_{i2}$	vector of the six global displacement and rational measures of the second node of the beam

u_{1X}	displacement in the global X direction for node 1
u_{1Y}	displacement in the global Y direction for node 1
u_{1Z}	displacement in the global Z direction for node 1
u_{2X}	displacement in the global X direction for node 2
u_{2Y}	displacement in the global Y direction for node 2
u_{2Z}	displacement in the global Z direction for node 2
θ_{1X}	rotation along the global X direction for node 1
θ_{1Y}	rotation along the global Y direction for node 1
θ_{1Z}	rotation along the global Z direction for node 1
θ_{2X}	rotation along the global X direction for node 2
θ_{2Y}	rotation along the global Y direction for node 2
θ_{2Z}	rotation along the global Z direction for node 2
u_{jk}	displacement in the global axis for the jth node and kth global degree of freedom
θ_{jk}	rotation in the global axis for the jth node and kth global degree of freedom
$\boldsymbol{r}$	member 3 × 3 rotation matrix
$\boldsymbol{p}$	position vector
$\boldsymbol{I_X}$	unit vector in the global X direction
$\boldsymbol{I_Y}$	unit vector in the global Y direction
$\boldsymbol{I_Z}$	unit vector in the global Z direction
$\boldsymbol{i_r}$	unit vector in the local $x(r)$ direction
$\boldsymbol{i_s}$	unit vector in the local $y(s)$ direction
$\boldsymbol{i_t}$	unit vector in the local $z(t)$ direction
$[T]_i$	transformation matrix
$\boldsymbol{o}$	a 3 × 3 null matrix
$\{U_L\}_i$	3D beam local displacements and rotations vector of the ith beam
$\{U_L\}_{i1}$	vector of the six local displacement and rational measures of the first node of the beam
$\{U_L\}_{i2}$	vector of the six local displacement and rational measures of the second node of the beam
u_{1r}	displacement in the local $x(r)$ direction for node 1
u_{1s}	displacement in the local $y(s)$ direction for node 1
u_{1t}	displacement in the local $z(t)$ direction for node 1
u_{2r}	displacement in the local $x(r)$ direction for node 2
u_{2s}	displacement in the local $y(s)$ direction for node 2
u_{2t}	displacement in the local $z(t)$ direction for node 2
θ_{1r}	rotation along the local $x(r)$ direction for node 1
θ_{1s}	rotation along the local $y(s)$ direction for node 1
θ_{1t}	rotation along the local $z(t)$ direction for node 1
θ_{2r}	rotation along the local $x(r)$ direction for node 2
θ_{2s}	rotation along the local $y(s)$ direction for node 2
θ_{2t}	rotation along the local $z(t)$ direction for node 2
u_s	displacement in the local $y(s)$ direction
u_t	displacement in the local $z(t)$ direction
$\varepsilon_t(r, s)$	strain due to bending about the local t axis
$\varepsilon_s(r, t)$	strain due to bending about the local s axis
$\varepsilon_{ts}(r, t, s)$	total bending strain along the beam

ε_r	axial strain due to the axial deformation
$\varepsilon(r, t, s)$	total strain due to bending and axial along the beam
$[\alpha]$	constant matrix
$[\beta]$	constant matrix
F_{1r}	internal axial force
δ	axial elongation
K^a	axial stiffness
M_{1s}	bending moment in the local *r*-*t* plane at node 1 of the beam
M_{2s}	bending moment in the local *r*-*t* plane at node 2 of the beam
M_{1t}	bending moment in the local *r*-*s* plane at node 1 of the beam
M_{2t}	bending moment in the local *r*-*s* plane at node 2 of the beam
K_s^b	flexural stiffness in the *s* direction
K_t^b	flexural stiffness in the *t* direction
φ_s	shear factor in the *s* direction
φ_t	shear factor in the *t* direction
A_s	effective area in shear in the *s* direction
A_t	effective area in shear in the *t* direction
I_s	moment of inertia about the *s*-axis
I_t	moment of inertia about the *t*-axis
M_{1r}	torsional moment
K^t	torsional stiffness
J_t	torsion constant
F_e	Euler stress
r_g	radius of gyration
F_{cr}	critical stress
P_n	nominal axial force using allowable strength design

CHAPTER 1. INTRODUCTION

BACKGROUND

Bridges are considered crucial links in the transportation network of highways and railways in the country and are expected to perform as designed throughout their functional life. Based on analysis of the National Bridge Inventory database, 752 (0.12 percent) of 614,387 highway bridges in the United States have a maximum span longer than 122 m (400 ft) (FHWA n.d.). Approximately 300 (~40 percent) of these bridges are either deck-truss or through-truss types. Figure 1 shows a histogram of these long-span truss bridges by decade built. As the figure demonstrates, most long-span truss bridges in the United States were built from the 1920s to the 1970s.

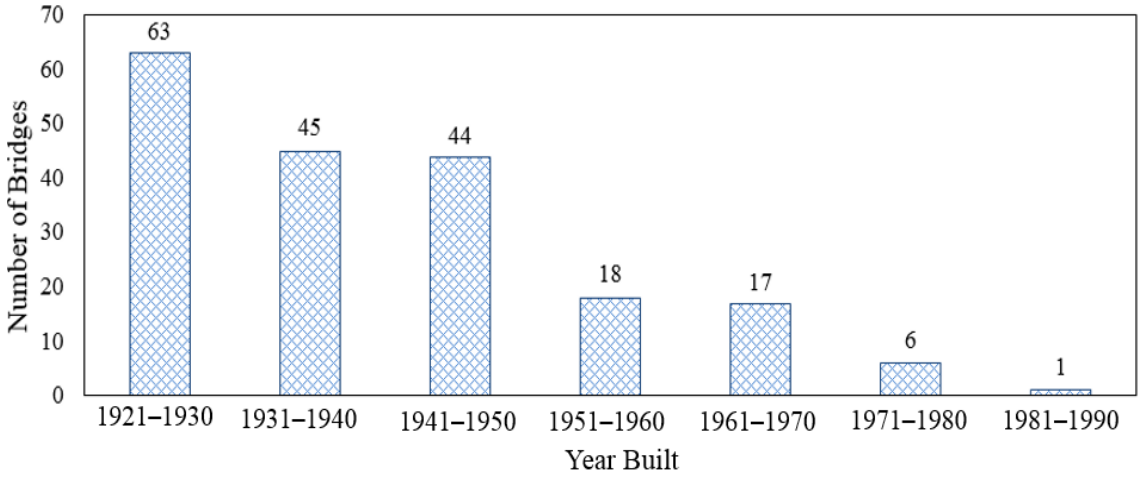

Source: FHWA.

Figure 1. Chart. Long-span truss bridges in the United States by decade built.

A truss bridge system consists of simple members that can support a large amount of weight, and these bridges can be considerably long. Theoretically, the members in a simple truss system are subjected only to axial force (tension or compression) rather than bending. However, the actual behavior of truss bridges could be significantly more complex and may involve axial forces and moments (both in-plane and out-of-plane).

Many truss bridges built between the 1920s and 1970s are aging and may have critical members with significant deterioration. Lee et al. (2013) analyzed bridge failures in the United States from 1980 to 2012 and observed that, although girder bridges are the most common structural type of failed bridges, truss bridges are much more vulnerable to failure than girder bridges. Even though truss bridges account for only 29 percent of the failures, they make up less than 4 percent of the total number of bridges.

In the event of loss of critical members of a truss bridge because of corrosion or terrorist events, such as intentional member cutting or blast loading, continued stability and performance of the bridge can be broadly attributed to "redundancy." Unfortunately, the redundancy of long-span truss bridges, which is quantified based on the behavior of these bridges after failure of a

member or members, is not well understood and was generally not considered in the design of existing long-span truss bridges. Many bridges with failed members have survived without collapse, whereas many bridges with local damage to a critical member have collapsed. The next sections discuss various examples of survival as well as collapse of truss bridges after failure of a critical member or members to highlight the challenges associated with understanding the complex behavior of truss bridges.

Bridges That Survived Local Member Damage

On May 7, 1975, the main girder of the Lafayette Street Bridge over the Mississippi River in St. Paul, MN, was found to have a crack that originated at the lateral bracing gusset to the transverse stiffener weld area due to the lack of fusion (Fisher et al. 1977). Brittle failure of the girder in the central span occurred after the crack's penetration through the web thickness of the girder. However, collapse of one girder did not lead to the collapse of the entire bridge.

The Yukon River Bridge, located approximately 32 km (20 mi) south of the city of Whitehorse in Canada and carrying the Alaska Highway, is a two-span Warren through-truss bridge. It was damaged because of an impact by an overheight vehicle in 1982. The impact damaged many tension members, including a bottom chord member near the midspan, which opened by approximately 50 mm (2 inches) after the accident (Beauchamp et al. 1984). Significant vertical deflection and horizontal displacement at the roller support were also observed. However, the bridge survived without collapse. The bridge was restored to fully functional condition by replacing all damaged members. Interestingly, Beauchamp et al. (1984) observed that the bridge did not collapse because the floor system, acting as an equivalent bottom chord, took over most of the broken truss's dead load (*DL*). Similarly, one of the web verticals near the midspan of the East Brough's Bridge, a Pratt through-truss bridge in London, Ontario, Canada, was severed because of an impact by a bus in 2000 (Jelinek and Bartlett 2002). Although the bridge was heavily damaged, it escaped complete collapse.

On January 20, 2017, a resident engineer on an active painting job noticed a fractured truss member (U19-19′) in the north truss of the Delaware River Bridge, as shown in figure 2. The bridge continued to perform under full live load (*LL*) during the period between when the failure occurred and when it was discovered. This is another example that shows that certain truss systems can carry a full traffic load even after the loss of a member.

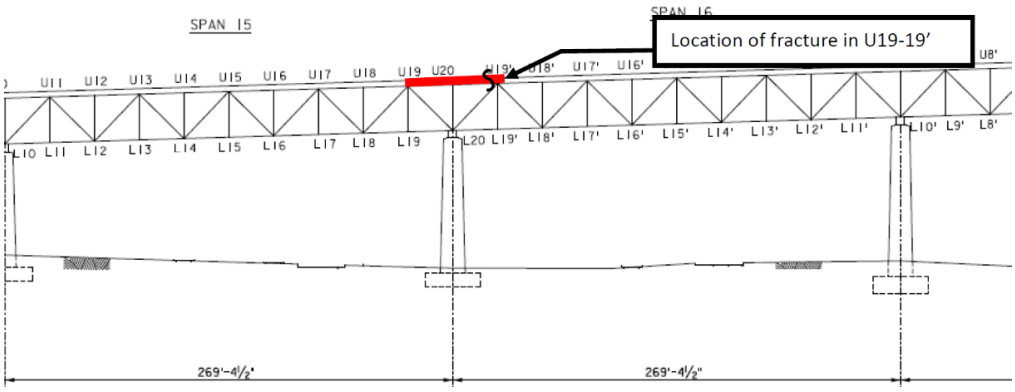

Source: FHWA.

A. Elevation view of the fractured truss member.

Source: FHWA.

B. Close-up photo of the fractured member.

Figure 2. Photos. Fractured upper chord member of the Delaware River Bridge (FHWA 2017).

The Federal Highway Administration (FHWA) (2013) investigated the after-fracture performance of a two-line simple-span truss bridge that was part of the Milton–Madison Bridge and was slated for explosive demolition. During the testing, a built-up bottom chord member at the midspan of the bridge was completely severed during a controlled blast test. Figure 3 shows half of the lower chord severely damaged. It was observed that the total removal of the bottom chord member did not cause collapse of the bridge. In fact, the analyses presented in FHWA (2013), Diggelmann et al. (2013), and Cha et al. (2014) show that the bridge likely could have remained functional under normal service loads even after complete loss of the bottom chord member.

Source: FHWA.

Figure 3. Photo. Blast-induced fracture of the bottom chord member in the Milton–Madison Bridge (FHWA 2013).

Bridges That Collapsed After Local Member Damage

Silver Bridge, which collapsed in 1967, is considered the earliest case of collapse of an entire bridge structure because of local damage to a member. In the evening hours of December 15, 1967, the Silver Bridge across the Ohio River collapsed because of a single eyebar corrosion cracking and stress concentration, resulting in the deaths of 46 people (Lichtenstein 1993). Figure 4 shows a photograph of the collapsed bridge. The collapse of this bridge led to the establishment of the current National Bridge Inspection Standards (Lichtenstein 1993). Follow-up study on this bridge collapse led to further understanding of redundancy and fracture-critical bridges.

Source: NTSB.

Figure 4. Photo. Silver Bridge collapse in 1967 (NTSB 1968).

The suspended span of the Sung Soo Grand Bridge, a Gerber-type truss bridge across the Han River in Seoul, Korea, collapsed on October 21, 1994, killing 32 and injuring 17 people (Cho et al. 2001). The suspended trusses were connected to anchor trusses by vertical hangers acting as pins or hinges between piers. The structural failure was caused by improper welding of the steel trusses of the suspension structure beneath the concrete slab roadway. Figure 5 shows a photograph of the bridge after the collapse of the suspended span.

Figure 5. Photo. Collapse of suspended span of the Sung Soo Grand Bridge.

Collapse of the I-35W Bridge in Minneapolis, MN, in 2007 is the most recent example of collapse of a steel deck-truss bridge because of local damage (Hao 2010). Collapse of this bridge, shown in figure 6, resulted in the loss of 13 lives and injuries to 145 people. Per investigation by the National Transportation Safety Board (NTSB), the bridge collapsed because of undersized gusset plates U10 and U11, which were half as thick (12.5 mm (0.5 inches)) as a gusset plate in the U12 joint (NTSB 2008a–d). Investigation into the causes of this bridge failure led to a greater emphasis on not only the design of gusset plates in truss bridges but also the insufficiency of conventional one-dimensional influence line models compared to detailed three-dimensional (3D) models for design. In this bridge, gusset plates were the pivots responsible for transferring loads from the deck and truss members to the supporting piers. This load path resulted in force flow with high amplitude in the diagonal members (DMs) attached to these gusset plates. However, a conventional one-dimensional influence line model probably gave zero or very low amplitude of the bending moment in this area because of the model's transition from a positive to a negative sign. This model result could have led to the undersized design of the gusset plates in this bridge. The investigation also highlighted the significant role played by redundancy and alternate load paths (ALPs) in preventing such failures (Hao 2010).

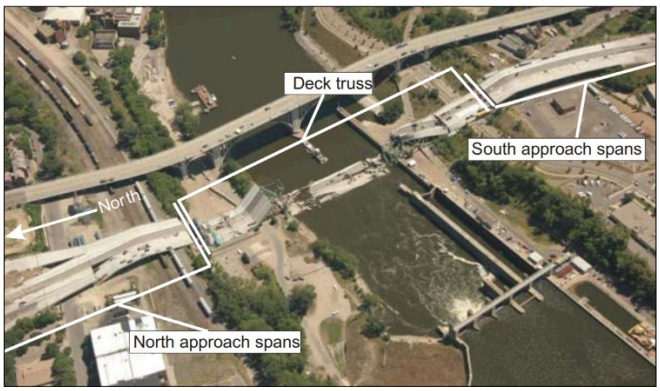

Source: NTSB.

Figure 6. Photo. I-35W Bridge collapse (NTSB 2008d).

From the study of bridges that survived local member damage, Liu et al. (2013) noted that both the East Brough's Bridge and the Lewes Bridge would have collapsed if the load path in these bridges was from the floor system to the panel point of the main trusses, and joints were pin connections that structurally isolated the main trusses from each other and from the floor system, assumptions that are made in typical truss bridge design. In reality, structural features in these two bridges facilitated ALPs to enhance their redundancy. Some of these prominent features were as follows: (1) truss connections that were designed as pinned were actually rigid joints consisting of the gusset plates with many fasteners to transfer moments; (2) trusses that were designed to carry loads independently were interconnected by lateral and diagonal bracings, floor trusses, and sway frame members; and (3) the floor system that was assumed not to contribute to stiffness, strength, or load sharing between the trusses was rigidly connected to the trusses at the floor beams. Isolated studies have also documented the effects of these structural features on the behavior of trusses. For example, Nagavi and Aktan (2003) showed that 3D finite-element models (FEMs) with rigid joints more accurately simulated the behavior of steel through-truss bridges with riveted gusset plates, especially the inelastic response, than conventional two-dimensional (2D) and 3D truss models. DelGrego et al. (2008) observed floor system–truss interaction during the monitoring of a railroad through-truss bridge.

Redundancy is defined as "the quality of a bridge that enables it to perform its design function in the damaged state" (AASHTO 2014, sec 6.2: 6–7). In general, redundancy in truss bridges can be classified as internal (member) redundancy, structural redundancy, and load-path redundancy (FHWA 2013). A structural system can have internal redundancy because of multiple parallel elements within a member, such as a built-up member made from many different plates and other structural shapes that are bolted or riveted together. Fracture in one part of such members may be arrested by other parts of the member. Structural redundancy is directly related to the static indeterminacy of the structure. For example, continuous-span structures would have structural redundancy. Load-path redundancy is based on available paths for load redistribution in the event of failure of a critical member. All three forms of redundancy may play a role in preventing the collapse of a bridge after the failure of a critical member. However, the contribution of load-path redundancy to the overall redundancy of a long-span truss bridge is not very well understood.

Barth et al. (2014) mentioned that a sound explanation of load-path redundancy could lead to a more efficient manner of designing and rating highway bridges, thereby avoiding structure collapse and potential disasters. More recently, the American Association of State Highway and Transportation Officials (AASHTO) *Guide Specifications for Analysis and Identification of Fracture Critical Members and System Redundant Members* was published to address the issue of load-path redundancy in different types of bridges, including truss bridges (AASHTO 2018a). These guide specifications provide prescriptive recommendations on the selection of members to be removed during redundancy analysis. They also provide load factors for the Redundancy-I case, when loads are applied before the failure (so that the effect of dynamic amplification can be captured), and the Redundancy-II case (for normal use of the bridge without wind after a member failure). Both the linear method with dynamic amplification factor and the dynamic method (where member removal (MR) can be simulated) are recommended in these guide specifications. However, they do not provide an approach to quantify redundancy. Rather, they provide guidance on the design and evaluation of a bridge after the damage of a fracture-critical member. The AASHTO *Guide Specifications for Internal Redundancy of Mechanically-Fastened*

Built-up Steel Members provides guidance on evaluating internal redundancy in built-up members traditionally designed as fracture-critical members (AASHTO 2018b). These guide specifications also provide guidance on special inspection intervals for fracture-critical members.

Past Studies on Progressive Collapse of Buildings

In general, bridge collapse originating from the failure of a critical member, section, or connection is quite similar to progressive collapse in building structures. Blandford (1997) noted that progressive failure of a structure involves analyzing the structure's response to the failure or damage of one or more of its members. The loss or failure of a member or members causes force redistribution to the remaining structural members. Based on building collapses, the definition of progressive collapse that has been widely accepted in the engineering profession was given by Ellingwood (2006): "A progressive collapse initiates as a result of local structural damage and develops, in a chain reaction mechanism, into a failure that is disproportionate to the initiating local damage." Local structural damage can be initiated by causes, such as blast, impact, and others.

Past research on progressive collapse advanced in the aftermath of high-profile building failures. For example, the Ronan Point building collapse in England in 1968 triggered the development and improvement of building codes and specifications in many countries, such as Canada, Denmark, France, the Netherlands, Sweden, the United Kingdom, and West Germany. Based on general lessons learned from the progressive collapse events and other numerous failures, Prendergast (1995) presented several prescriptive guidelines to increase resistance against progressive collapse, such as the following: (1) local resistance should be increased in key regions to inhibit initiation of the collapse process, (2) structural redundancy in the building structural system must be provided so that the system can seek ALPs when needed, and (3) all structural and nonstructural components should be interconnected to minimize debris projectiles. Terrorist attacks on the Alfred P. Murrah Federal Building in 1995 and the World Trade Center towers in 2001 led to standardized design approaches for buildings to protect against progressive collapse in the United States (GSA 2003; DOD 2009). Improvements in building practices to address low-probability high-consequence events and to lessen building vulnerability to progressive collapse currently are based on the fundamental considerations and assessment of general structural integrity, ALP method, prescriptive design provisions, critical member design, and MR methods.

Past Studies on Progressive Collapse of Bridges

Unlike buildings, bridges are much more vulnerable to collapse in the event of localized failure because they have less or no redundancy and unidentified ALPs. Woodward and Zoli (2005) noted that long-span bridges are generally not designed to be resistant to progressive collapse. The development and adoption of comprehensive AASHTO load and resistance factor design (LRFD) provisions in 2012 and 2014 represent explicit consideration of redundancy, ductility, and operational importance in the form of load-factor modifiers (AASHTO 2012, 2014). However, consideration of these three factors may have a negligible effect on the design, particularly for bridges with single-point vulnerabilities and the potential for abrupt member loss. In the current code, nonredundant elements must be designed to resist an added 5 percent of the factored design loads used to design all other members. However, no instructions are given about

how to perform a proper analysis or the level of *LL* that the bridge should be able to carry in its damaged condition. A nonredundant bridge may be vulnerable to collapse because of sudden loss of a critical member even though the member may have been designed to resist a higher factored design load. Load factors that can be applied to the analysis of the damaged structure are also currently lacking (Grubb et al. 2015). The current AASHTO approach also does not provide discussion on the dynamic aspects of member loss that have been reported in FHWA (2013). Hence, unlike the progressive collapse of buildings, there has been no advancement in the development of design guidelines or provisions to protect against progressive collapse of bridges in the United States even though a number of high-profile progressive bridge failures have been observed during the last several decades. Although two recent AASHTO guide specifications do provide prescriptive guidance for the analysis of progressive collapse vulnerabilities of bridges, they do not address the role of ALP in long-span truss bridges (AASHTO 2018a, b).

RESEARCH MOTIVATION AND NEEDS

The main objective of this study was to investigate the load-path redundancy of long-span truss bridges in the event of loss or failure of one or more of their critical members. Although the load-path redundancy of truss bridges has been discussed in case studies, such as that by Beauchamp et al. (1984), no studies have investigated factors contributing to the load-path redundancy of truss bridges. In current practice, a bridge system is designed by ensuring that the capacity of each of the structural members and components stays below the load effects caused by a set of pertinent design load combinations. However, such a design approach does not guarantee sufficient levels of redundancy to withstand an accidental single point of failure or regional damage resulting from intentional threats or other hazards. Because of their operational importance for economic, social, and security requirements and their high replacement costs, major truss bridges should have sufficient load-path redundancy and the capability to survive extraordinary events beyond the scope of conventional design criteria. These extraordinary events are generally loss of a member or members because of intentional member cutting, blast loads, vehicular impacts, strong wind loads, and so forth.

RESEARCH OBJECTIVES AND OUTCOME

A wide variety of factors that affect the stability and load-carrying capacity of long-span truss bridges need to be studied. The overall objective of this research was to develop an understanding of the behavior of long-span steel truss bridges in the event of sudden loss of a member or members. Specific objectives of this study included the following:

- Development of an integrated framework to quantify the redundancy or existing ALP before and after a postulated event involving long-span steel truss bridges.

- Development of an evaluation procedure to understand the relationship between the ALPs, system performance, and overall bridge stability, ensuring sufficient reserve capacity.

- Investigation of retrofit approaches that can improve the ALP of long-span truss bridges cost-effectively.

In summary, the main outcome of this research is to prescribe a process that can objectively identify ALPs in a steel truss bridge after an abnormal event. Using an objective identification of ALPs in producing an optimal retrofit strategy after such an event is demonstrated through detailed investigation of two example long-span truss bridges.

SUMMARY OF THE CHAPTERS OF THIS REPORT

The detailed work performed to achieve the research's objectives is described in the chapters of this report as follows.

Chapter 2 describes the conventional definition of ALP and redundancy and proposes a novel approach to quantify ALP. The definition and properties of ALP are outlined, and the ALP methodology is introduced through demand-to-capacity ratio (*DCR*) based on linear static analysis and strain ratio (*SR*) based on nonlinear dynamic (NLD) analysis.

Chapter 3 describes the finite-element modeling process. This chapter describes in detail both the linear static and the NLD analysis approaches. For the linear static method, conventional beam elements of the popular SAP2000 computer code were used for modeling truss members (Computers and Structures, Inc. 2014). Because NLD analysis for MR may require significant computational resources, an efficient element type that is built in computer-coded LS-DYNA for the NLD analysis method was explored (Hallquist 2014). The accuracy of using such an element type was validated through several examples with varying degrees of complexity.

Chapter 4 presents detailed modeling of the I-35W Bridge in as-built condition to understand its behavior before collapse. FEMs of the bridge for both the linear static and the NLD analysis were validated through comparison with existing models and research on this bridge. Then, the resulting ALPs were identified objectively for dynamic MR events. ALPs were identified for two distinct approaches: the linear static approach using *DCR* as a metric and the NLD approach using *SR* as a metric.

Chapter 5 investigates various retrofit approaches for improving ALP of the I-35W truss bridge. For this purpose, the bridge was first seismically retrofitted to resist a hypothetical earthquake of the magnitude that may be experienced in a high seismic zone, such as San Diego, CA. Typical seismic retrofit primarily involves strengthening truss members by changing the I-shaped sections to box sections and increasing the cross-sectional area. Results showed that the seismic retrofit of strengthening a member led to limited improvement in ALP of the bridge. Therefore, other retrofit strategies were investigated based on the information gained from the identified ALPs. This information was used to choose the retrofit procedure or strategy that resulted in addition of members at vulnerable locations so that these members contributed to the three-dimensionality of the bridge. While retrofitting, a performance-based design (PBD) paradigm was followed by introducing several performance criteria in terms of limit states. It was shown that (1) following an ALP-based retrofit strategy produces more efficient (in terms of added retrofit weight) designs, (2) using a limit state based on the NLD approach produces more efficient retrofits than using a limit state based on the linear static analysis, and (3) allowing for a more relaxed performance criteria or limit state (in terms of accepting more ductile behavior) results in lesser increase in retrofit weight. Thus, bridge engineers can make decisions between

various retrofit strategies by balancing the acceptance of higher risk and lower performance versus savings on extra retrofit weights or costs.

Chapter 6 repeats the analyses in chapter 5 for the Ikitsuki Bridge in Japan, which is a through-truss bridge. It is shown that the observations and conclusions of chapter 5 are still applicable for this different type of bridge.

Chapter 7 presents some suggestions for future work, both experimental and analytical, to address some of the knowledge gaps identified in this research.

Chapter 8 presents a summary, conclusions, and recommendations.

CHAPTER 2. ALP AND REDUNDANCY

INTRODUCTION

Conventionally, ALPs are defined as changes in the load paths and load distribution experienced by other members in the event of loss of a critical member. The concept of ALP is more advanced for buildings than for bridges. For buildings, the General Services Administration (GSA) (2003) criteria use the alternate path method (APM) to prevent progressive building collapse and allow the use of both linear static and NLD analysis to identify structural members in the alternate path structure. Redundancy of a structure tends to promote an overall more robust structure and helps to ensure that ALPs are available in the case of local failure of a critical member. Additionally, redundancy of a structure generally provides multiple locations for yielding to occur, which increases the probability that the damage will be constrained. In 2016, GSA upgraded their 2003 progressive collapse requirements of explicit design for loss of vertical load-bearing elements by adopting a threat-based approach and APM in Unified Facilities Criteria 04-023-03 (GSA 2003; DOD 2009; GSA 2016). This method requires the building to be able to compensate for vertical load-bearing elements that are notionally removed one at a time at specific plan and elevation locations.

A detailed framework for addressing issues related to low-probability high-consequence events during progressive collapse of buildings can be found in Ellingwood (2006). This work also summarizes measures for progressive collapse risk mitigation and identifies challenges for implementing general provisions in national standards, such as American Society of Civil Engineers (ASCE) Standard 7: *Minimum Design Loads for Buildings and Other Structures* (ASCE/SEI 2010). To reduce the probability of progressive collapse, it may be necessary to design key elements in a structural system to withstand stipulated "abnormal" loads that are far in excess of what would be required under a normal design condition in order to facilitate the development of ALPs. Redundancy, as a key to preventing progressive collapse through ALPs, means that no critical element's failure should initiate a series reaction of successive loss of members that would take down the building. For each critical element, one or more redundant counterparts should take over the critical load scenario in case the critical member fails (Ellingwood and Dusenberry 2005). El-Tawil et al. (2007) investigated the progressive collapse of steel frame structures using a macromodel-based simulation approach and noted that the collapsing system continually seeks ALPs in order to survive in the dynamic process. Their work showed that a nonlinear APM is useful for judging the ability of a system to absorb the loss of a critical member. Compared to an elastic APM analysis, inelastic APM simulation provides more resolution, shows failure progression, and provides information on the likelihood of complete versus partial collapse. Izzuddin et al. (2008) investigated the APM for buildings and showed that ALPs are beneficial in improving redundancy and structural robustness in buildings.

For bridges, although load-path redundancy may currently be considered in the classification of fracture-critical members for design and fabrication (Lwin 2012), structural and internal redundancy considerations have not yet been codified in AASHTO LRFD specifications. However, two recent AASHTO guide specifications provide prescriptive guidance on selection of members to be removed, analysis methods, evaluation of bridges for different types of

analysis following a member loss, and internal redundancy evaluation of built-up members (AASHTO 2018a, b).

Codes, such as the Canadian Standards Association (CSA) CAN/CSA-S6-00, have been permitting engineers to consider redundancy through system behavior (CSA 2006). In a previous study on ALP, for example, Sanders et al. (1975) tested the load capacity of the single-lane truss Hubby Bridge over the Des Moines River (which was scheduled for removal) by cutting its vertical member at one cross section. The test results showed that cutting the member did not result in a significant decrease in the load-carrying capacity of the bridge. Sanders et al. (1975) attributed this capability of redistributing loads to the frame action inherent in trusses and the semicontinuous nature of the deck truss. Csagoly and Jaeger (1979) analyzed the failure of a number of bridges to support the existence of multiple load paths where load redistribution took place after damage to a critical member. They also noted that the construction of single-load-path bridges was prohibited by the 1979 Ontario Highway Bridge Design Code. Frangopol and Curley (1987) proposed various indices to quantify redundancy in terms of strengths of intact and damaged systems without identifying ALPs that contribute to redundancy. Sirisak (1996) investigated the structural integrity evaluation of truss bridges. They noted that the joints in these bridges may be more rigid than pinned joints and that a bridge truss that is assumed to be statically determinate may be highly indeterminate and show significant reserve strength when loaded beyond the classical limit load determined by the limit state of a single member. If the joints are treated as rigid, the failure of a member may not lead to an immediate collapse of the bridge; ALPs may be found. In such a situation, it may be more prudent to evaluate the system's strength without exclusively concentrating on component or member strength to identify ALPs. Williamson et al. (2010) investigated the safety of reinforced concrete bridges against blast loads and recommended increasing the redundancy of reinforced concrete bridges by proving multiple load paths. This includes, but is not limited to, decreasing the spacing of longitudinal girders and stringers and decreasing the deck beam spacing. Although local damage to the bridge deck, the supporting bridge girders, or both is undesirable, redundancy and ductility will often allow internal forces to redistribute when damage to these components occurs, thus allowing an ALP to be realized to maintain the global stability.

The detailed discussion in this section shows that although efforts have been made to quantify redundancy in bridges, which depends on multiple load paths in the event of damage to a critical member, ALP is generally defined qualitatively. One of the objectives of this research is to define ALP in terms of quantifiable load redistribution among members affected by the removal of a critical member. It is assumed that a truss bridge structure is load-path redundant if the structural system has sufficient ALPs after local damage. Otherwise, the truss bridge is nonredundant.

PROPOSED ALP DEFINITION AND REDUNDANCY

Based on the qualitative description of ALP described in the previous section, major shifts in the behavior of a structural system after a change (such as sudden local damage in a member) in an otherwise functionally acceptable structural system constitute an ALP within the system. However, an unacceptable structural performance or an unstable system after this dynamic process of local damage may not produce an ALP in the system. The change in the system can be attributed to the following two scenarios:

1. A hypothetical situation that is needed for design, such as an MR in a framed structure (including but not limited to trusses, frames, suspension systems, etc.).
2. An abnormal loading demand such as a blast, earthquake, tornado, shock or impact, and so forth.

The change is manifested in either complete loss of or degradation of the performance of one or more of the system components. However, this qualitative vision of ALPs is difficult for engineers to put into design practice.

One of the goals of this research is to objectively use ALP to attempt to find optimal design and retrofit measures for long-span truss bridges undergoing two specific abnormal hazards: MR and blast (*BL*) (which refers to blast demands, hazards, or threats). To achieve this goal, a concise and quantitative definition of ALP for these types of structural systems is introduced in the following.

For a structural system S with r_m components M, it is assumed that W is a set of individual components (members). The ith component M (M_i) is thus $M_i \in W$, $i = 1, 2, 3, \ldots r_m$. Conventional design practices for the system state that under a base (normal) loading condition or demand (D) (e.g., $D = (\alpha_{DL} DL + \alpha_{LL} LL)$, where α_{DL} and α_{LL} are DL and LL factors, respectively), the state of design metric in the ith component (DM_i), satisfies the system's acceptance criteria or design limit state ($LIM(DM)$), as shown in equation 1:

$$DM_i \leq LIM(DM) \tag{1}$$

In equation 1, DM_i could be the stress in the ith member, which should be less than or equal to the maximum allowable stress (which will be $LIM(DM)$). The performance of the system can be measured by any of the possible design metrics, such as the following:

- Internal forces, stresses.
- Reactions.
- Displacements, velocities, accelerations, deformations, strains.
- Other capacity or demand metrics.
- Combinations of any of the previous bulleted items.

Among these metrics, the following two were deemed reasonable for the work on ALPs in this research:

1. For linear elastic behavior, a popular design metric is the DCR, or DCR_i for the ith component based on linear elastic analysis. For this metric, the demand is calculated as the stress in the ith member, and the capacity is calculated as the maximum allowable stress ($0.6\sigma_y$) (where σ_y is the yield stress of the member), which is used for the design of steel truss members.
2. For nonlinear behavior, a reasonable design metric is the SR, or SR_i for the ith component, where SR_i is defined as shown in equation 2:

$$SR_i = \frac{Max(\varepsilon_i)}{\varepsilon_y} \quad (2)$$

In equation 2, $Max(\varepsilon_i)$ is the maximum strain in the ith component and ε_y is the pertinent yield strain. $Max(\varepsilon_i)$ needs to be obtained based on detailed NLD analysis simulating hazards causing the change, such as loss of a member.

For the purpose of this study, it is assumed, without any loss of generality, that the system is a *base* system. As such, the *base* system is renamed as S_0, the base loading condition as D_0, the base ith component as M_{0i}, the base structural set as W_0, and the base design metrics as DM_{0i}. Note that $M_{0i} \in W_0$.

It is assumed that the values of DM_{0i} have changed into a new set of values, DM_{1i}. Such a change can occur for numerous reasons, including the following:

1. A change in the topology of S from S_0 to a new topology S_1, which results in a change of the composition of W from W_0 to a new component set W_1. Such a change can occur if one or more members in W_0 are removed from the set (i.e., because of sudden member loss).
2. A change in D_0 to a new demand D_1 (e.g., $D_1 = (\alpha_{DL} DL + \alpha_{LL} LL + BL)$.

Many other reasons for such changes exist; however, they are beyond the scope of this report.

The new set of design metrics, DM_{1i}, is not equal to DM_{0i}, as shown in equation 3:

$$DM_{1i} \neq DM_{0i} \quad (3)$$

Note that, by their definitions, the states and distribution of DM_i identify the load path given S and its companion W. It can then be concluded that the *base* load path can be illustrated by the distribution of DM_{0i}. Similarly, it can be concluded that the *new* load path can be illustrated by the distribution of DM_{1i}. Hence, ALPs for the structural system can be quantified as the changes in the spectra of DM_{1i} (with respect to the spectra of DM_{0i}) due to the changes in the system, such as the loss of a member. This definition of an ALP needs to meet the following three important properties:

1. **Appropriateness.** For an ALP to be appropriate, it needs to accurately illustrate the flow of the loading throughout S: the applied loads all the way to the boundary conditions. Clearly, the choice of design metrics, DM_{1i} (such as stress or strain in the ith component of the changed system), meets this criterion.
2. **Generality.** For an ALP to be general, it needs to satisfy any steel truss structural system. The ALP as defined by DM_{1i} meets this criterion because no limit was placed on the applicable systems.
3. **Usefulness.** For an ALP to be useful, it needs the ability to be used in retrofit and initial design situations. The ALP, as defined by DM_{1i}, can be used in retrofit and initial design situations if equation 1 is developed further. Furthermore, identifying new load paths with limit state distributions that are beyond the $LIM(DM)$ is also of interest. A

reasonable set of jth and (j+1)th limit states can then be identified, as shown in equation 4:

$$LIM(DM)_j < DM_i \leq LIM(DM)_{j+1} \quad (4)$$

By identifying different desired limit states ($LIM(DM)_j$) appropriately, a useful ALP spectra of M_{1i}, as illustrated by DM_{1i}, will emerge. Using these ALP spectra for retrofit or initial designs can be helpful in attaining optimal retrofits. In equation 1, one could assume $LIM(DM)_j$, for example, as $0.6\sigma_y$ and $LIM(DM)_{j+1}$ as σ_y for truss members. Then, all members with stresses between these two limits can be identified to characterize the ALP for the particular member loss scenario.

DCR USING LINEAR STATIC ANALYSIS

The *DCR* of each truss member can be used to determine the potential for progressive collapse. This research uses SAP2000 to calculate *DCR*. In this software, a steel frame design/check module calculates axial, flexural, and shear forces or stresses at several locations along the length of a member and then compares those calculated values with acceptable limits. This comparison produces *DCR* for each of the members, which typically should not exceed a value of 1.0 if code requirements are to be satisfied. Table 1 and table 2 show the proposed limit states for *DCR* and *SR*, respectively, which can be used during the analysis of ALPs for long-span truss bridges.

Table 1. Proposed limit states for ALP analysis using *DCR* metric.

Limit State	Metric Range
Design limit	$DCR \leq 1.0$
Elastic limit	$1.0 < DCR \leq 1.67$
Beyond elastic limit	$DCR > 1.67$

Table 2. Proposed limit states for ALP analysis using *SR* metric.

Limit State	Metric Range
Elastic limit	$SR \leq 1.0$
Limited ductility	$1.0 < SR \leq 2.0$
Medium ductility	$1.0 < SR \leq 4.0$
High ductility	$SR > 4.0$

These limit states are based in general engineering practice. For linear elastic analysis, *DCR* is defined as the ratio of member stress to the maximum allowable stress in steel truss members ($0.6\sigma_y$). Hence, the limit state of $DCR \leq 1.0$ is commonly used to ensure that the stresses in steel members of a truss bridge are less than $0.6\sigma_y$. The limit state of $1.0 < DCR \leq 1.67$ may be used to evaluate whether the stresses in steel members are more than $0.6\sigma_y$ but less than σ_y. The value of *DCR* corresponding to σ_y in a truss member is $1 \div 0.6 = 1.67$. A limit state of $DCR > 1.67$ implies potential inelastic behavior in the member.

For NLD analysis, *SR* is defined for individual local members and has a similar meaning as the ductility ratio (which is a representation of global system behavior in terms of displacement).

Hence, values of $SR \leq 1.0$ imply completely elastic behavior at the element level, whereas values of $SR > 1.0$ imply nonlinear material member behavior responsible for the ductile behavior of the bridge system.

The *DCR* is obtained according to AASHTO (2010) and the American Institute of Steel Construction (AISC) (2010), which define the resistance by axial and flexure interaction equations. For doubly and singly symmetric members subject to axial force and flexure, *DCR* is calculated by equations 5 and 6:

$$DCR = \frac{P_r}{P_c} + \frac{8}{9}\left(\frac{M_{rx}}{M_{cx}} + \frac{M_{ry}}{M_{cy}}\right) \quad \text{where } \frac{P_r}{P_c} \geq 0.2 \tag{5}$$

$$DCR = \frac{P_r}{2P_c} + \left(\frac{M_{rx}}{M_{cx}} + \frac{M_{ry}}{M_{cy}}\right) \quad \text{where } \frac{P_r}{P_c} < 0.2 \tag{6}$$

Where:

P_r = axial force demand.
P_c = axial force capacity.
M_{rx} = bending moment demand with respect to the *x*-axis.
M_{cx} = bending moment capacity with respect to the *x*-axis.
M_{ry} = bending moment demand with respect to the *y*-axis.
M_{cy} = bending moment capacity with respect to the *y*-axis.

Equation 5 can be rewritten as equation 7 as follows:

$$\begin{aligned} DCR &= \frac{P_r}{P_c} + \frac{8}{9}\left(\frac{M_{rx}}{M_{cx}} + \frac{M_{ry}}{M_{cy}}\right) \\ &= \frac{\frac{P_r}{A_c}}{\frac{P_c}{A_c}} + \frac{8}{9}\left(\frac{\frac{M_{rx}}{S_{xx}}}{\frac{M_{cx}}{S_{xx}}} + \frac{\frac{M_{ry}}{S_{yy}}}{\frac{M_{cy}}{S_{yy}}}\right) \\ &= \frac{\sigma_{rp}}{\frac{P_c}{A_c}} + \frac{8}{9}\left(\frac{\sigma_{Mx}}{\frac{\sigma_y}{\Omega}} + \frac{\sigma_{My}}{\frac{\sigma_y}{\Omega}}\right) \\ &= \frac{\sigma_{rp} + \frac{8}{9}(\sigma_{Mx} + \sigma_{My})}{\sigma_{allow}} \end{aligned} \tag{7}$$

Where:

A_c = member cross-sectional area.
S_{xx} = section modulus with respect to the *x*-axis.
S_{yy} = section modulus with respect to the *y*-axis.
σ_{rp} = axial stress.
σ_{Mx} = stress due to moments with respect to the *x*-axis.
σ_{My} = stress due to moments with respect to the *y*-axis.

Ω = safety factor.
σ_{allow} = allowable stress obtained from σ_y divided by Ω based on the allowable strength design approach.

Safety factors for compression, flexure, and tensile yielding are 1.67. The tensile rupture case with a safety factor of 2.0 is not considered in this study. Examples of calculating *DCR* for compression and tension members are in appendix C.

Both allowable strength design (ASD) and LRFD designs consider a second-order analysis by adjusting the first-order analysis (AISC 2010), where the factor $(1 - \alpha P_r \div P_e)$ is recognized as an amplification factor accounting for the second-order moment caused by the P-δ effect (P_e is the elastic critical buckling strength of the member, and the design coefficient α is 1.0 for LRFD and 1.6 for ASD designs, respectively). For a steel truss bridge system, because the members are rigidly connected at truss joints that cause lateral moments, moments are not uniform along the length of a member and are largest at member ends. This nonuniform moment is accounted for by the reduction coefficient C_m (equation A-8-4 in AISC 2010). For a member subject to compression, M_1 and M_2 in the equation for C_m are the smaller and larger moments, respectively, calculated from a first-order analysis at the ends of an unbraced portion of the member in the plane of bending under consideration when no transverse loading is present between supports in this plane. The ratio of these moments, $M_1 \div M_2$, is positive when the member is bent in a reverse curvature and negative when the member is bent in a single curvature. However, this adjustment may not be needed when the second-order analysis is automatically included in the computer model. For *DCR* calculated in this research, the SAP2000 model is programmed to perform the second-order analysis during the calculation of *DCR*.

SR USING NLD ANALYSIS

SR is calculated from the results of NLD analysis in LS-DYNA and is obtained by dividing the total strain of the member section by the yield strain of the steel. As will be described in chapter 3, examples of long-span bridges in this study are modeled in LS-DYNA using Belytschko–Schwer (B-S) beam elements and a Mat 98 material model to represent material nonlinearities and strain hardening in steel. Strains are not explicitly exported from the analysis using LS-DYNA; rather, they are calculated from displacement, rotation, and strain relationship. The displacements can be obtained from the analysis directly. Detailed formulation on the calculation of the *SR* from the output of the beam element in LS-DYNA can be found in appendix A. Various limit states for using the *SR* metric are shown in table 2.

After characterizing the bridge members using *DCR* and *SR*, redundancy can be quantified by ALP using the following steps:

- Identify whether the structure needs retrofit after a triggering hazard such as MR.
- Identify components requiring retrofits.
- Determine the level of retrofit.
- Identify load redistribution among members through MR analysis.

LOADS AND LOAD COMBINATIONS

Models of example bridges may need to be analyzed for combinations of *DL, LL*, and seismic load (*EQ*). For design purposes, the load conditions in equations 8, 9, and 10 can be used:

$$1.0\ DL \tag{8}$$

$$1.0\ DL + 1.0\ LL \tag{9}$$

$$1.0\ DL + 0.75\ LL + 0.75(0.75\ EQ) \tag{10}$$

Based on literature review, load combinations for progressive collapse analysis are available only for buildings. For example, Ellingwood et al. (2007) presented load combinations for progressive collapse of buildings. This report noted that many standards, such as ASCE/SEI (2010), have recommended an *LL* factor of 0.5 because of a small probability of the accidental and design loads occurring jointly.

Superstructures of highway bridges are designed using load factors recommended in tables 3.4.1-1 and 3.4.1-2 of the AASHTO LRFD Specifications (2014). These AASHTO load factors were recommended based on extensive research and calibration. Some general principles for selecting load factors can be found in table 3.4.1-1 of AASHTO (2014). This report recommends using 0.5 as the load factor for the *LL* during extreme events because it is likely that a reduced *LL* will be present on the bridge during an extreme event when considering the likelihood of simultaneous load effects. Based on these observations, following the AASHTO LRFD (2017) load combination for extreme hazard events shown in equation 11 is recommended:

$$1.0\ DL + 0.5\ LL \tag{11}$$

ASD VERSUS LRFD

The *DCR* in this research was calculated based on an ASD approach where the demand is calculated using the load combination in equation 11 and the capacity is calculated as $0.6\sigma_y$. Table 3.4.1-2 in the current AASHTO LRFD bridge design specifications presents load combinations and load factors for Extreme Event II (AASHTO 2017). Following this table and table 3.10.1.1-2 in FHWA (2015), load combinations for MR in LRFD can be expressed as shown in equation 12:

$$1.5\ DL + 0.5\ LL \tag{12}$$

The resistance factor for the capacity in LRFD is 0.9 (i.e., the design stress is $0.9\sigma_y$). Hence, the *DCR* for the LRFD case will be as shown in equation 13:

$$\frac{1.5}{0.9}(DL)_{\mathrm{R}} + \frac{0.5}{0.9}(LL)_{\mathrm{R}} = 1.67(DL)_{\mathrm{R}} + 0.56(LL)_{\mathrm{R}} \tag{13}$$

The *DCR* for the ASD case (by using equation 11) will be as shown in equation 14:

$$\frac{1.0}{0.6}(DL)_{\mathrm{R}} + \frac{0.5}{0.6}(LL)_{\mathrm{R}} = 1.67(DL)_{\mathrm{R}} + 0.83(LL)_{\mathrm{R}} \quad (14)$$

In equations 13 and 14, $(DL)_{\mathrm{R}}$ and $(LL)_{\mathrm{R}}$ are the response of a member because of *DL* and *LL*, respectively, divided by σ_y. Generally, *LL* is significantly smaller than the total *DL* of bridges. For example, for the I-35W Bridge (table 15 in chapter 4), *LL* is 22 percent of the *DL*. Therefore, for this bridge, $(LL)_{\mathrm{R}} = 0.22(DL)_{\mathrm{R}}$. Using this, the *DCR* for ASD and LRFD can be approximated as $1.85(DL)_{\mathrm{R}}$ and $1.79(DL)_{\mathrm{R}}$, respectively. Hence, *DCR* calculated using ASD is slightly higher than *DCR* calculated using LRFD. The major difference between ASD and LRFD is in terms of limit states. For ASD, the primary limit states are *DCR* = 1 (allowable stress limit state) and *DCR* = 1.67 (yield stress limit state). For LRFD, these limit states are *DCR* = 1 for design and *DCR* = 1.11 for yield stress. However, because the main objective of the research is to investigate effective retrofit strategies, the proposed ALP approach can be applied to a specific bridge using the LRFD approach without any loss of generality.

SR in this research is calculated as the strain in a member for the load combination in equation 11 divided by ε_y. This *SR* can be interpreted similarly to ductility (i.e., *SR* = 1 represents the limit of elastic behavior). However, this value is based on the assumption that the total load on the bridge is represented by the load combination in equation 11. Hence, calculation of *SR* does not follow the ASD or the LRFD approach.

CHAPTER 3. FINITE-ELEMENT MODELING

INTRODUCTION

As discussed in chapters 1 and 2, few studies (e.g., Liu et al. 2013) have investigated the progressive collapse of truss bridges using an elastic FEM with a truss member modeled as a frame element to account for secondary moment effects. Fiorillo et al. (2015) investigated the redundancy of truss bridges by considering the model of the Aby truss bridge, a 33.5-meter (110-foot) simply supported bridge. This bridge, as a prototype, was tested to failure to study its remaining load-carrying capacity by Blanksvärd et al. (2014). Fiorillo et al. (2015) modeled this bridge in ABAQUS (Dassault 2013a, b) by four-node 2D shell elements to analyze the behavior of the superstructure and to determine the reserve capacity after a critical member failure. Although the bridge has only 175 elements and 98 nodes, it was modeled by 43,000 shell elements with 172,000 nodes so that behavior such as buckling and yielding after MR could be simulated. The computational time for each run of this model was estimated to be longer than 6 h. Modeling the long-span bridges in this study by shell elements in this way would have resulted in millions of elements and nodes. Simulation of such a large model would have required computational resources and time significantly beyond those available for this research.

In this research, a two-part modeling approach was adopted to investigate the ALP of truss bridges. To start, all truss bridges were modeled in SAP2000 and verified against available design, analysis, and modeling data to confirm the bridge's elastic behavior. This model was used to investigate the ALP of bridges using the *DCR* approach discussed in chapter 2. Detailed information on the modeling of example bridges in SAP2000 will be presented in later chapters. However, the elastic model of the bridge may not be sufficient for designing cost-effective retrofit measures to protect against progressive collapse. Software such as SAP2000 cannot simulate the removal of members dynamically for the redundancy analysis.

Therefore, the second modeling approach involved simulation of the NLD behavior of truss bridges due to loss of a critical member in LS-DYNA, which is a general-purpose multiphysics simulation software package used widely for simulations involving dynamical effects. LS-DYNA's explicit analysis capability provides options for modeling truss elements by beam element formulations that can be selected based on the geometry, loading, boundary conditions, and material properties of the structure being analyzed.

FINITE-ELEMENT MODELING IN LS-DYNA

Beam Element Formulation

Truss members in LS-DYNA are best modeled by beam or shell elements. As discussed in the previous section, using shell elements for long-span truss bridges is computationally cost-prohibitive. Two types of beam element formulations exist in LS-DYNA: Hughes–Liu (H-L) and B-S. Degenerated from the isoparametric eight-node solid element into the two-node beam geometry, the H-L beam element requires cross-section integrations to account for different shapes, and it generates a constant moment along the length. Using this element requires considerably fine element mesh to achieve desired accuracy. The B-S beam element, a resultant element in LS-DYNA, is formulated explicitly. This element produces a linearly

varying moment along a member. The bending effect in truss members may not be negligible after the sudden loss of a member. Thus, it is important to consider variations in the end moments of truss members. Moreover, considering the convergence issue related to sophisticated integration across the section, mesh accuracy, and iterations involved in multistage analysis, the B-S beam element seems to be more efficient in achieving this study's objectives.

Based on a classical resultant beam formulation, the B-S beam element with 6 degrees of freedom (DOFs) for each node was developed by Belytschko et al. (1977). This beam element is capable of treating large rotation using a co-rotation technique in the element formulation. This element is somewhat faster in computation because no numerical integration is performed over the cross section. However, it may be less accurate for elastoplastic analysis when partial section yielding is important. Because it is a resultant-based formulation, any type of cross section may be easily modeled by specifying its cross-sectional area and area moments of inertia. The B-S beam element differentiates between flexure about strong and weak axes by the assignment of a third node, n_3. Potential reductions in strength due to local buckling are not considered in this formulation.

The co-rotation technique, as shown in figure 7, uses two types of coordinate systems: one associated with each element to show the deformed shape, excluding the rigid body rotations, and the other embedded in the nodes to display the rigid body rotations. The element coordinate system is defined to have the local *x*-axis ($\hat{X}$) originating at node *I* and terminating at node *J*, and the local *y*-axis ($\hat{Y}$) and the local *z*-axis ($\hat{Z}$) are constructed normal to $\hat{X}$ and $\hat{Y}$. The element coordinate system ($\hat{X}$, $\hat{Y}$, $\hat{Z}$) and associated unit vector triad (e_1, e_2, e_3) are updated at every time step by the same technique used to construct the initial system. One advantage of the co-rotational formulation is the ease with which existing small displacement element formulations can be adapted to a larger displacement formulation having small deformations in the element system. In figure 7, $\bar{X}$ and $\bar{Y}$ are the *x*- and *y*-axes in the global coordinate system, respectively; $\hat{X}$ and $\hat{Y}$ are the *x*- and *y*-axes in the local coordinate system, respectively; $\overrightarrow{b_1}$ and $\overrightarrow{b_2}$ are the unit vectors along the global axes $\bar{X}$ and $\bar{Y}$, respectively; $\overrightarrow{e_1^0}$ and $\overrightarrow{e_2^0}$ are the unit vectors along the local axes $\hat{X}$ and $\hat{Y}$ in the initial configuration, respectively; and $\overrightarrow{e_1}$ and $\overrightarrow{e_2}$ are the unit vectors along the local axes $\hat{X}$ and $\hat{Y}$, respectively.

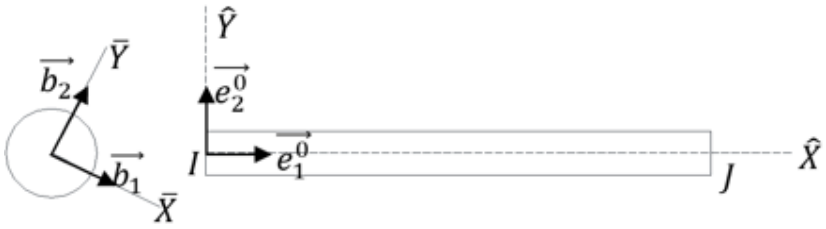

Source: FHWA.

A. Initial configuration.

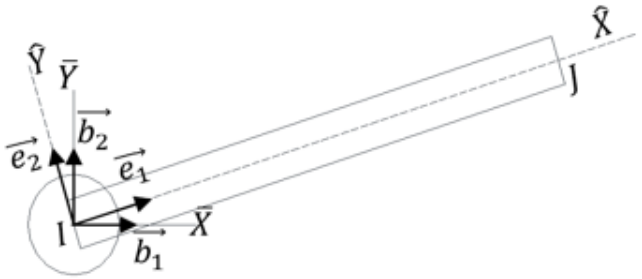

Source: FHWA.

B. Rigid rotational configuration.

Source: FHWA.

C. Deformed configuration.

Figure 7. Illustrations. Co-rotational coordinate system for the B-S beam element.

The displacements ($\hat{d}^T = \{\delta_{IJ}, \hat{\theta}_{xIJ}, \hat{\theta}_{yI}, \hat{\theta}_{yJ}, \hat{\theta}_{zI}, \hat{\theta}_{zJ}\}$) represent the deformation in the B-S beam element formulation, where δ_{IJ} is the change in the length, $\hat{\theta}_{xIJ}$ is the torsional deformation, and $\hat{\theta}_{yI}, \hat{\theta}_{yJ}, \hat{\theta}_{zI}, \hat{\theta}_{zJ}$ are the bending rotational deformations. Here, the superscript ˆ emphasizes that these quantities are defined in the local element coordinate system and *I* and *J* are the nodes at the ends of the beam. The internal forces and moments are then related to displacement and curvatures at the resultant element level. Using such a formulation, only forces and moments are calculated, not stresses (Hallquist 2014). This method of calculation is a major difference between this approach and approaches using shell or solid elements, where the calculation of internal forces and moments based on each single node is controlled by certain stress criteria. However, for truss bridges, the resultant force of each member is more crucial than the stress at a single point.

Simulation of Loads in LS-DYNA

The analysis for a long-span bridge involves two steps. In the first step, gravity loads should be applied to the structure. The application of gravity is important for the simulations during the second step where the added *LL* or extreme loading scenario, such as MR, is applied. Dynamic relaxation (DR) is needed during the first step, and the "restart" algorithm is used for the transition between the two steps. For the dynamic simulations using an explicit solver, all the loads, including the gravity loads, are considered dynamic, which is not the actual behavior of these loads. Because the structural response to these loads in LS-DYNA will experience dynamic magnification, the DR method is adopted to filter or remove undesirable dynamic effects. The second step is basically a "restart" from the first step and is a continuation of LS-DYNA run after the convergence of the DR phase.

Material Models

Material properties play an important role in controlling structural behavior under external loads. Accurate structural response requires a sound and effective stress–strain or constitutive relationship to describe the material behavior. Researchers have been trying to implement a proper material model that can successfully incorporate the typical response, such as elastic, post-yield (tension or compression), elastic and inelastic post-buckling, and stress reversal (in buckled or yielded members), of truss members (Schmidt and Gregg 1980; Papadrakakis 1983; Mueller and Wagner 1984; Hill et al. 1989; Murtha-Smith 1988; Blandford 1996).

The nonlinear behavior of the B-S element in LS-DYNA can be simulated by material models Mat 171 and Mat 98. Although the Mat 171 model was intended to represent both cyclic buckling and tensile yielding of steel concentric braces, which is similar to the behavior of truss members, it cannot be used for simulation of nonlinear behavior during MR. Hence, material model Mat 98 was used to investigate the behavior of bridges after the loss of a critical member. The Johnson–Cook material model (Mat 98) is expressed by the stress–strain relationship for beam members as shown in equation 15:

$$\sigma_y = \left(A + B\varepsilon^{p^n}\right)(1 + C \ln \varepsilon^*) \tag{15}$$

Where:

A, B, C, n = input constants.
ε^p = effective plastic strain.
ε^* = normalized effective strain rate.

As noted in equation 15, this material model considers the strain rate effect through the term ε^*, although this effect may not be significant during the removal of truss bridge members. This general-purpose material model considers material hardening nonlinearity by including the user-calibrated realistic material stress–strain curves. In addition, the model enables users to calibrate the constitutive model parameters via regression from laboratory data without using a sophisticated numerical algorithm. Users can verify the selected parameters to replicate the data used to obtain these parameters and reproduce the test results using simple numerical runs. A failure strain is defined for the material as well.

Mat 98 can be used during both DR and MR phases. However, it is not capable of simulating the reduction in the strength of a buckled member. When using this material model, buckling of a truss member due to sudden loss of a critical member can be identified through separate buckling analysis of the damaged bridge. If any member is likely to buckle, it will need to be retrofitted before performing dynamic MR analysis. Because the main objective of the research is to investigate cost-effective retrofitting of truss members to protect against progressive collapse, Mat 98 can be used to model inelastic tensile and compressive behavior while avoiding buckling behavior through retrofit as members prone to buckling are identified.

When compression buckling is not a concern during the MR analysis, it is sufficient to consider the typical stress–strain relationship in figure 8 during both compression and tension. In the elastic region, stress increases linearly with an increase in the strain, and it is quantified by the Young's modulus, $E = 2 \times 10^5$ MPa (29,000 ksi). Steel is a relatively ductile material and can undergo large strains before rupture. Low-carbon structural steel, such as A36 and A572, exhibits a well-defined yield point followed by a flat yield plateau. When high-strength steel is used, the yield plateau becomes less obvious. For a specific A992 steel in this research, parameters A, B, C, and n in equation 15 were calibrated based on the actual stress–true strain relationships obtained by Arasaratnam et al. (2011) from a standard uniaxial tensile test. The comparison between calibrated and experimental stress–strain results is shown in figure 9, and the calibrated parameters for the material model are presented in table 3.

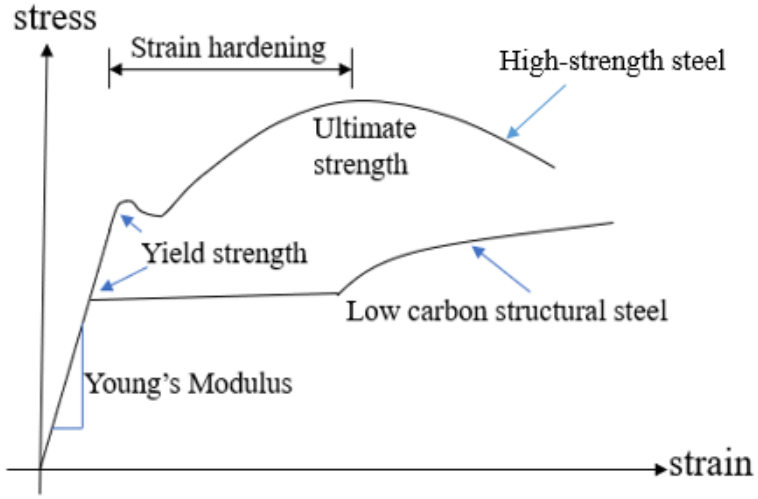

Source: FHWA.

Figure 8. Graph. Typical stress–strain curve for steel.

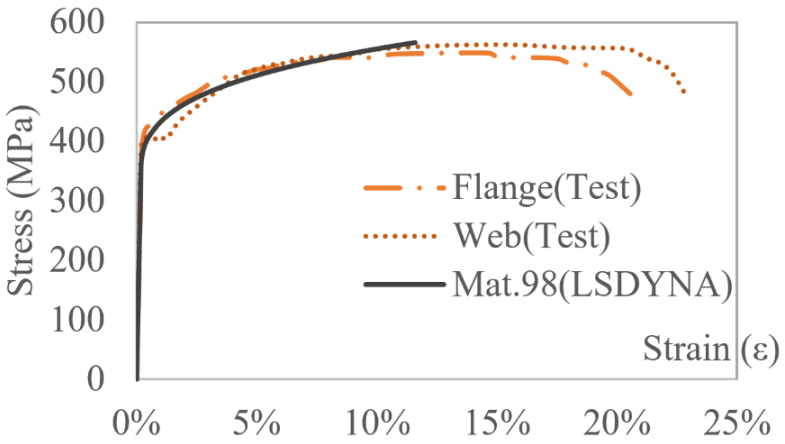

Source: FHWA.
1 MPa = 0.145 ksi.

Figure 9. Graph. Measured and calibrated stress–strain relationships for A992 steel and Mat 98 in LS-DYNA.

Table 3. Calibrated parameters for material model Mat 98.

Parameter	Unit (MPa)	Unit (ksi)
A	345	50
B	448	65
C	0.0162	0.0162
n	0.328	0.328
Failure strain	0.1	0.1

VERIFICATION OF BEHAVIOR OF THE B-S BEAM ELEMENT

To develop confidence in the capability of the B-S element with the Mat 98 material model, verification studies were performed for structures with single and multiple elements, as described in the following sections.

Example 1: Cantilever Beam

In this example, a beam that is cantilevered at one end was modeled by a single B-S beam element in LS-DYNA. Table 4 presents the sectional and material properties of this cantilever beam, which were obtained from real truss member U8-L8 (the vertical member at one of the piers, with a length of 18.288 m (60 ft)) of the I-35W Bridge that collapsed in 2007 (Hao 2010). This member had the largest area moment of inertia among truss members in the bridge. Figure 10 shows a section of the member, and figure 11 shows the six basic loading cases studied. Table 5 shows loading cases and results from analytical formulations and finite-element analysis using a single B-S element. Because LS-DYNA performs analysis by considering static loads as dynamic, damping is applied to achieve the stable (or steady-state) solution in the column "End B Translation From FEM" of table 5. This table demonstrates that the elastic behavior of a cantilever beam with concentrated force and displacement acting at the ends of the beam can be accurately represented by a single B-S element.

Table 4. Sectional and material properties for the example cantilevered beam.

Property	Parameter	Value
Sectional	Sectional dimensions	2 plates: 81.28 cm (32 inches) × 6.0325 cm (2.375 inches) 2 cover plates: 50.8 cm (20 inches) × 1.905 cm (0.75 inches) 1 web plate: 41.275 cm (16.25 inches) × 1.905 cm (0.75 inches)
Sectional	Cross-sectional area (A_c)	1.2528×10^{-1} m^2 (194.11 inches^2)
Sectional	Shear modulus (G)	1.2224×10^{-4} m^4 (293.7 inches^4)
Sectional	Moment of inertia (I_{xx})	8.7476×10^{-3} m^4 (21,016.9 inches^4)
Sectional	Moment of inertia (I_{yy})	6.0443×10^{-3} m^4 (14,521.5 inches^4)
Material	Density (ρ)	7,860 kg/m^3 (490.68 lb/ft^3)
Material	Young's modulus (E)	210 GPa (3.05×10^4 ksi)
Material	Poisson ratio	0.3
Material	Yield stress	345 MPa (50 ksi)
Material	Ultimate stress	448 MPa (65 ksi)

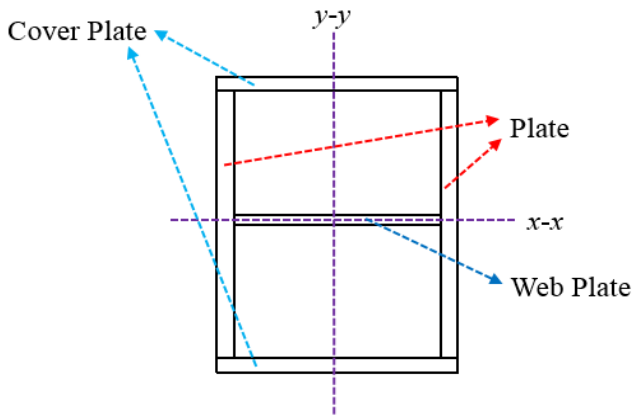

Source: FHWA.

Figure 10. Illustration. Section of the example cantilevered beam.

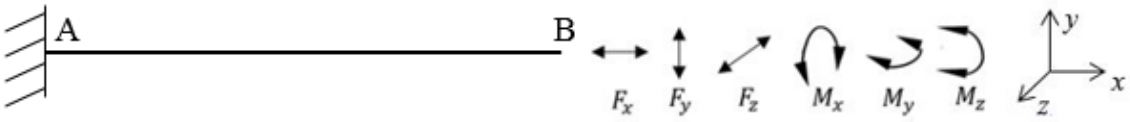

Source: FHWA.
Note: F_x, F_y, and F_z are concentrated forces along the x, y, and z directions, respectively, at the end of the beam, and M_x, M_y, and M_z are concentrated moments along the x, y, and z directions, respectively, at the end of the beam.

Figure 11. Illustration. Basic loading cases for the cantilevered beam.

Table 5. Comparison between analytical and FEM solutions for the cantilevered beam.

Load Case Number	Applied Force (N) or Moment (N·m) at End B	Analytical Solution (m)	End B Translation From FEM (m)
F_x	2.073×10^7	$u_x = 0.0144$	0.0144
F_y	2.312×10^5	$u_y = 0.372$	0.372
F_z	1.861×10^5	$u_z = 0.207$	0.207
M_x	1.080×10^4	$u_x = 0$	0
M_y	3.400×10^6	$u_z = 0.310$	0.310
M_z	4.229×10^6	$u_y = 0.557$	0.557

1 m = 3.281 ft; 1 N = 0.225 lb; 1 N·m = 0.738 lb·ft.
Note: u_x, u_y, and u_z are the displacements in the x, y, and z directions, respectively.

Example 2: Toggle Truss and Williams Toggle Frame

As typical examples of the snap-through phenomenon, the toggle truss and Williams toggle frame shown in figure 12 were modeled by the B-S element with the Mat 98 material model. The instability in these structures could be caused at both the elemental and the structural levels. The structure could collapse when it reaches structure-level instability. In the toggle truss, two members are connected by a pin, whereas in the Williams toggle frame, two beam members are connected by a rigid connection. Both of these shallow structures exhibit typical snap-through response when loaded by a force F at the apex.

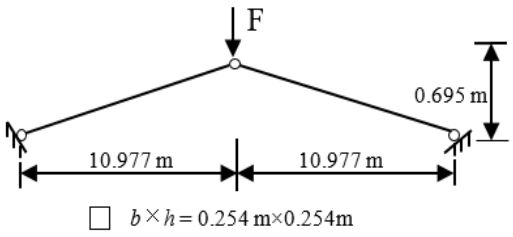

Source: FHWA.
1 m = 3.281 ft.

A. Toggle truss.

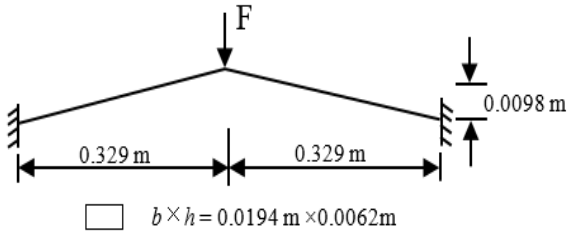

Source: FHWA.
1 m = 3.281 ft.

B. Williams toggle frame.

Figure 12. Illustrations. Typical truss systems.

For the toggle truss case, values of the Young's modulus and of yield stress were taken as 206 GPa (29,877.83 ksi) and 2.35×10^5 kPa (34.08 ksi), respectively. Figure 13 shows the constitutive stress–strain relationships for elastic and elastic-kinematic plastic materials. Figure 14 shows the comparison between LS-DYNA results and analytical solution results for both elastic and kinematic plastic systems based on Papadrakakis (1983). Finite-element and analytical results are in excellent agreement.

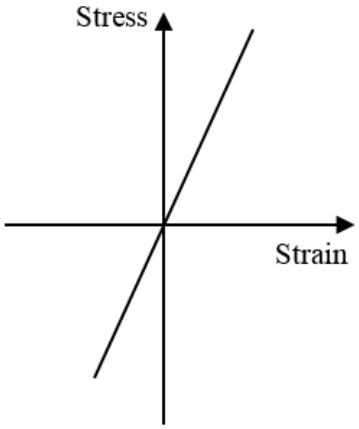

Source: FHWA.

A. Elastic material.

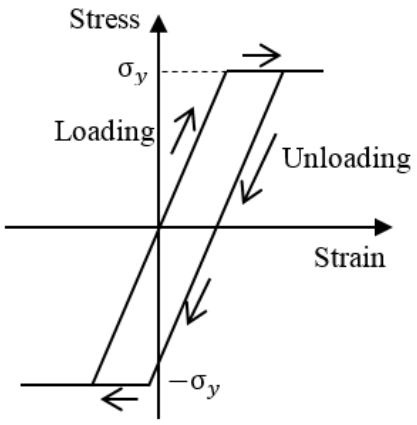

Source: FHWA.

B. Elastic-kinematic material.

Figure 13. Graphs. Constitutive stress–strain relationships for steel.

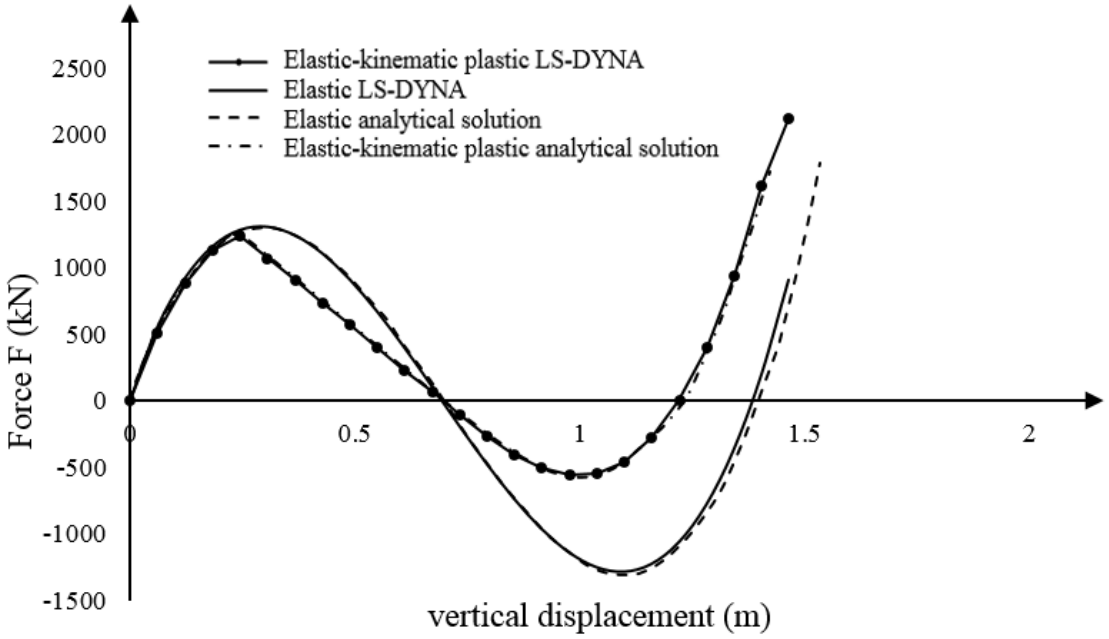

Source: FHWA.
1 m = 3.281 ft; 1 kN = 0.225 kips.

Figure 14. Graph. Load-displacement curves for the toggle truss system.

In the Williams toggle frame (Williams 1964), the frame is fully fixed against translation and rotation at both ends. The frame is loaded by force *F* at the apex. Table 6 shows material and sectional properties of members for this structure. Figure 15 shows force-deformation plots for the structure based on an analytical formulation by Williams (1964), finite-element formulations by Davalos (1989) and Warren (1998), and finite-element formulations with the B-S beam element in this research when frame elements are modeled by one and two elements. In the elastic region, good agreement is observed among force-deformation curves using different formulations. In the immediate inelastic region, the maximum difference between the force-deformation curve for the B-S element and the other curves is approximately 10 percent

when the frame element was modeled by one B-S beam element and is much smaller when two B-S beam elements were used to model the frame element. This example again shows the reliability of the modeling using the simplified B-S beam element.

Table 6. Material and sectional properties of Williams toggle truss element.

Description	Value
Young's modulus (E)	1.28×10^5 MPa (1,855 ksi)
Section area (A_c)	1.18×10^{-4} m^2 (0.183 inches^2)
Moment of inertia (I_{xx})	3.75×10^{-10} m^4 (9.0×10^{-4} inches^4)
Moment of inertia (I_{yy})	3.60×10^{-9} m^4 (8.65×10^{-3} inches^4)
Length (L)	0.329 m (12.936 inches)
Height (h)	9.80×10^{-3} m (0.386 inches)

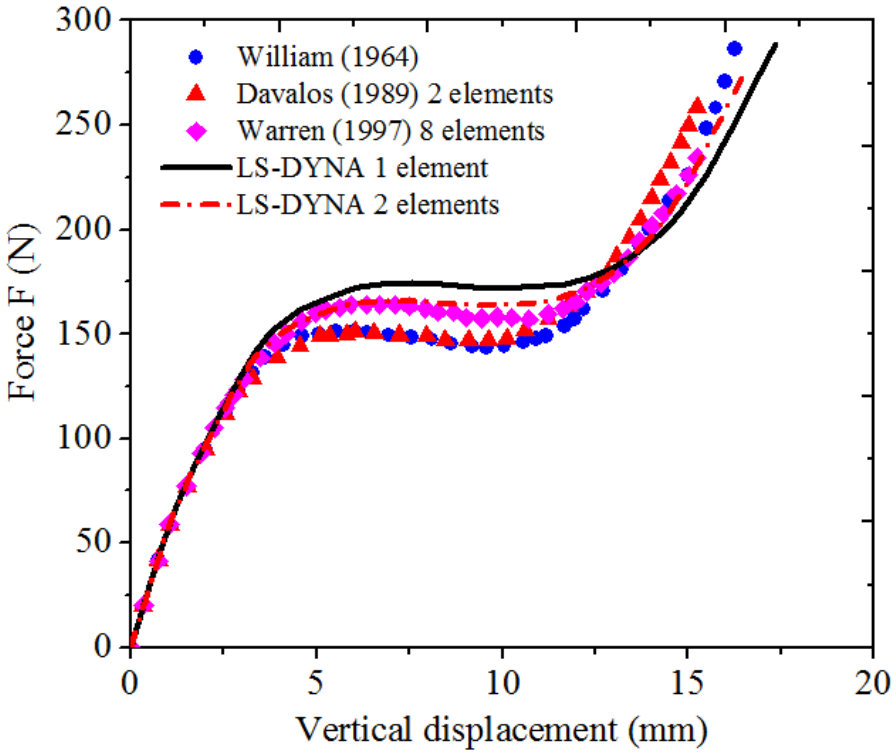

Source: FHWA.
1 N = 0.225 lb; 1 mm = 0.0394 inches.

Figure 15. Graph. Load-displacement curves for Williams toggle truss system.

Example 3: Aby Bridge

Aby Bridge, constructed in 1957, was a simply supported truss bridge superstructure carrying the Swedish northern mainline from Stockholm over the Aby River 80 km (49.7 mi) southwest of Luleå (Blanksvärd et al. 2014). In 2013, after its replacement by a new steel bridge, the old Aby Bridge was tested to failure to study its remaining load-carrying capacity. The bridge was 33.5 m (110 ft) long and 5.5 m (18 ft) wide. The truss's vertical members and the main transverse beams were spaced 4.125 m (13 ft) from each other. The truss height was 4.7 m (15 ft). The longitudinal

deck stringers were evenly spaced in the width. The southwest supports had four pins, whereas the northeast supports had four rollers. The steel truss members were built-up sections.

The loading on the bridge was applied by two hydraulic jacks that pulled the bridge downward, as shown in figure 16. The jacks were anchored to the underlying bedrock by two injected cables. Several test runs were made with different maximum loads to monitor strains and deflections under different conditions. Figure 17 shows the load-displacement plot of the bridge based on the test results. The bridge had substantial yielding deformations for a load of approximately 11,000 kN (2,472.9 kips).

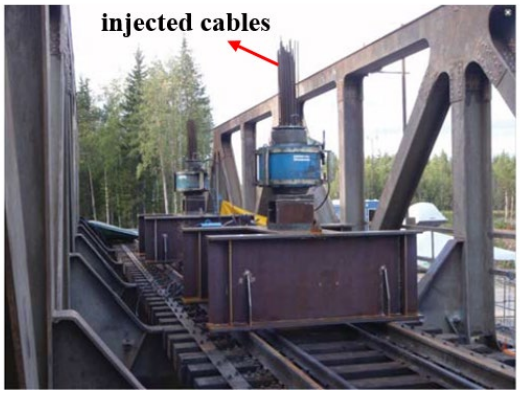

A. Loading arrangement in field test.

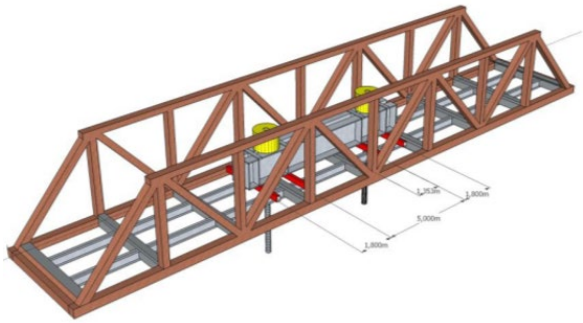

B. Loading arrangement in FEM analysis.

Figure 16. Photo and Illustration. Application of *LL* on the Aby Bridge.

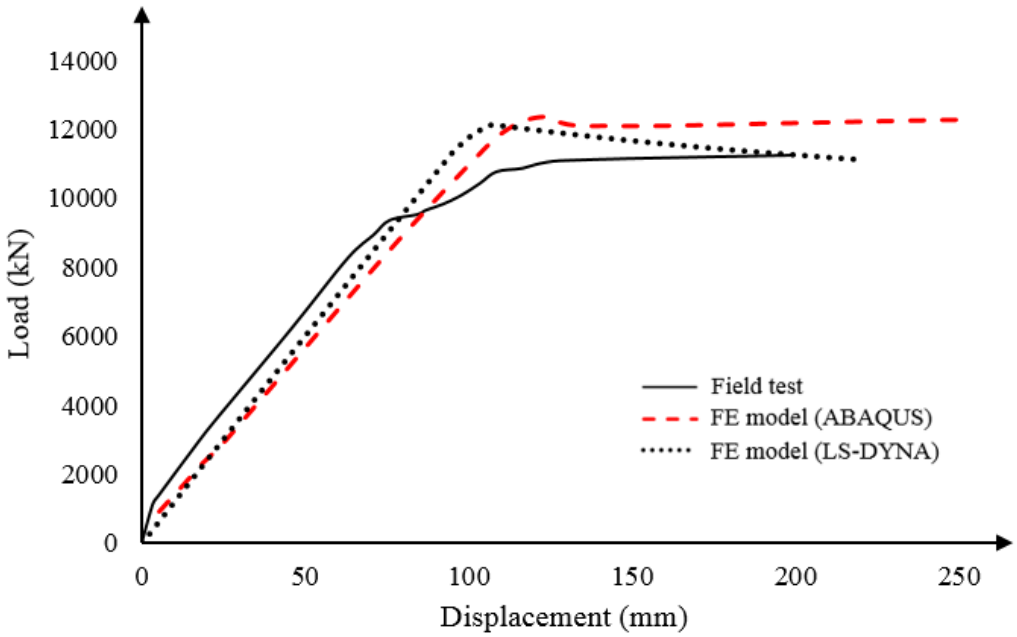

Source: FHWA.
1 kN = 0.225 kips; 1 mm = 0.0394 inches.

Figure 17. Graph. Load-displacement curves of the Aby Bridge.

Blanksvärd et al. (2014) performed finite-element modeling for a quarter of the bridge because of symmetry in two directions. Table 7 shows the material properties of the steel in the truss components. Figure 18 shows the model of Aby Bridge in LS-DYNA developed in this research using B-S beam elements. The loading from hydraulic jacks was applied through distributed beams in the FEM. Table 8 compares the computational effort required to model the truss by shell and B-S beam elements. Blanksvärd et al. (2014) used 43,000 four-node shell elements with 172,000 nodes, compared to 175 beam elements with 98 nodes in this research. The calculation time decreased from more than 6 h to 10 to 15 min.

Table 7. Material properties of steel in truss components.

Steel Member Type	Material	Yield Stress σ_y (MPa)	Ultimate Stress σ_u (MPa)
Main beams	SIS 1411	250–260	440
Verticals, diagonals, secondary systems	SIS 1311	200–220	370

1 MPa = 0.145 ksi.

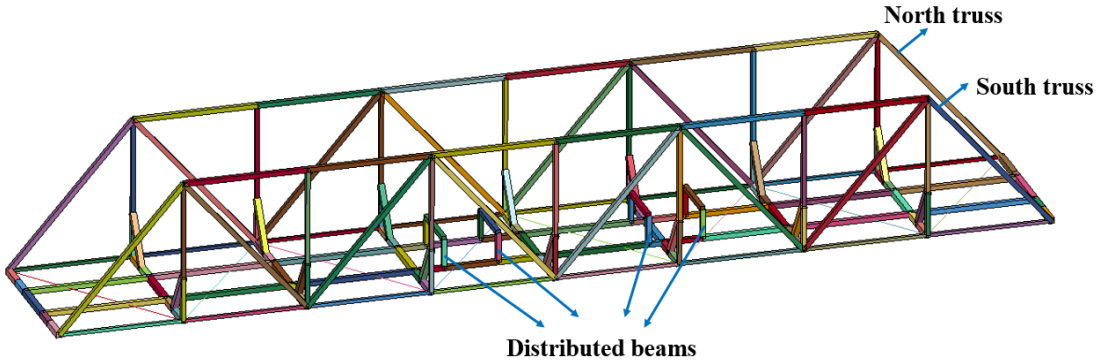

Source: FHWA.

Figure 18. Illustration. 3D FEM of Aby Bridge in LS-DYNA.

Table 8. Comparison between finite-element modeling approaches for the Aby Bridge.

Parameter	ABAQUS (Blanksvärd 2014)	LS-DYNA Simplified Model
Element type	Shell	Beam
Number of elements	43,000	175
Number of nodes	172,000	98
Computation time	Greater than 6 h	10–15 min

Because the test-to-failure results indicated the buckling of one top girder followed by yielding, material model Mat 171 was used to simulate both tensile and compressive behavior in the finite-element simulation. For this material model, the effective length factor *K* in the slenderness ratio was selected as 1.2 based on a parametric study. Figure 17 shows the load-displacement plots from the field test and the finite-element simulations by ABAQUS and LS-DYNA. The displacement was chosen from the maximum deformation point. Figure 17 shows that the load-displacement plots by ABAQUS and LS-DYNA agree well, although modeling and computation time using the B-S element was significantly shorter. Differences between these plots and that from the field test are probably because of loading facilities. The decreased slope in the load-displacement plot from LS-DYNA indicates buckling of the beam element.

Example 4: Simulation of MR

Although the study of redundancy of truss bridges has been a topic of research for quite some time, not many laboratory or field studies on the removal of members have been conducted to investigate redundancy. FHWA (2013) and Diggelmann et al. (2013) performed a full-scale testing of MR in a span of a bridge that was scheduled to be demolished. The tested single span was part of the US-421 Milton–Madison Bridge, a 19-span continuous truss bridge that connected Milton, KY, to Madison, IN. This bridge was constructed over the Ohio River in 1921 and was replaced in 2014. FHWA (2013) and Diggelmann et al. (2013) tested the northernmost approach span of this bridge for redundancy.

The tested bridge was a Pratt truss type 45.415 m (149 ft) in length with a center-to-center bearing. Figure 19 shows the bridge looking northwest. The Pratt truss was symmetric and

consisted of seven panels, each 6.4 m (21 ft) in length. The superstructure width was 7.32 m (24 ft), and the truss height was 6.70 m (22 ft). The deck system was located 1.45 m (4 ft and 9 inches) below the top chord of the truss. The deck system consisted of six lines of stringers spaced at 1.1176 m (3 ft and 8 inches). Floor transverse beams were attached to the verticals below the deck. Redundancy of this bridge was investigated through field testing by damaging a fracture-critical bottom chord member.

Source: FHWA.

Figure 19. Photo. Approach span of the Milton–Madison Bridge looking northwest (FHWA 2013).

In LS-DYNA, the deck system was modeled by shell elements with elastic material. Nodal rigid body constraints were applied for the nodal sets shared by the deck, transverse stringers, and floor system to account for the connection between these three systems. In addition, to highlight the sand-loaded zone in the field test, figure 20 indicates the location of the sand-loading zone in three bridge deck panels.

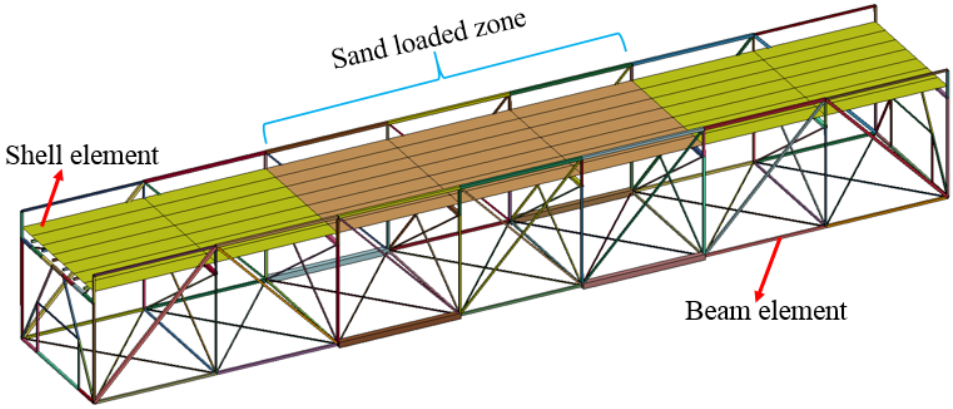

Source: FHWA.

Figure 20. Illustration. FEMs of the Milton–Madison Bridge in LS-DYNA with sand loading.

In modeling the bridge, Young's modulus for all steel members was assumed to be 200,000 MPa (29,000 ksi). Because of insufficient data on other material properties, they were assumed based

on the typical steels available during the period of construction of the bridge (design drawings simply implied that the steel was made of "carbon steel" with a minimum yield stress and ultimate tensile stress of 248.21 MPa (36 ksi) and 400 MPa (58 ksi), respectively). The original deck system was removed from the bridge in 1996 and replaced with an exodermic deck system with an overlay. The weight of the exodermic deck combined with the 38.1-millimeter (1.5-foot) concrete overlay was assumed to be 3.73 kPa (5.41 psi). A concrete deck of equivalent weight is 158.75 mm (6.25 inches) in thickness.

Information on overall bridge geometry and section properties in the LS-DYNA model (as shown in figure 20) was based on shop drawings and reports downloaded from the online database DataHub (DataHub n.d.). Before the controlled damage to selected bridge truss members, the bridge was loaded with 645 kN (2,870.25 kips) of sand spread across the three central panels of the deck width (figure 21). This loading magnitude represented approximately two-thirds of the original design *LL* (although it was distributed over only the three central panels rather than the full length of the bridge). This loading was maintained during controlled damage to selected bridge members. In the redundancy evaluation, the lower chord member L3US-L4US of the bridge was fractured in two steps using shape charges. One-half of the lower chord member cross section was fractured first. The structure was allowed to reach static equilibrium, and then a second blast caused complete fracture of the member.

Source: FHWA.

Figure 21. Photo. Sand loading on the Milton–Madison Bridge (FHWA 2013).

Because both *DL* and sand load are static loads, DR was used to bring the LS-DYNA model to the initial condition for the dynamic member fracture test. Although the actual field test consisted of two-step demolition of the member, as described in the previous paragraph, this process was simulated in LS-DYNA by complete fracture of the entire lower chord member L3US-L4US in one step because the B-S beam element is a resultant member where damage can be simulated only in the entire member.

The results from FEM analysis indicating the fundamental characteristics of the dynamic member loss process are shown in figure 22. The stress time history in the lower chord member

L4DS-L3DS, which is downstream of the removed upstream lower chord member L4US-L3US, included three stages. Total stress (including contributions of axial and bending) in this member was 41.69 MPa (6.05 ksi) after the application of gravity loading. This stress increased by 14.52 MPa (2.11 ksi) during the sand loading. Hence, total stress in the member was 56.21 MPa (8.16 ksi) before the MR, and the truss was in static condition. After the MR, the bridge vibrated for a few seconds while load redistribution occurred among truss members. Eventually, free vibration died down, and the bridge entered into another static equilibrium status without collapse. Increase in stress in the downstream member L4DS-L3DS because of the loss of its symmetric member L4US-L3US in the upstream truss was 15.77 MPa (2.28 ksi). The final axial stress in L4DS-L3DS after the removal of L4US-L3US was 71.98 MPa (10.44 ksi).

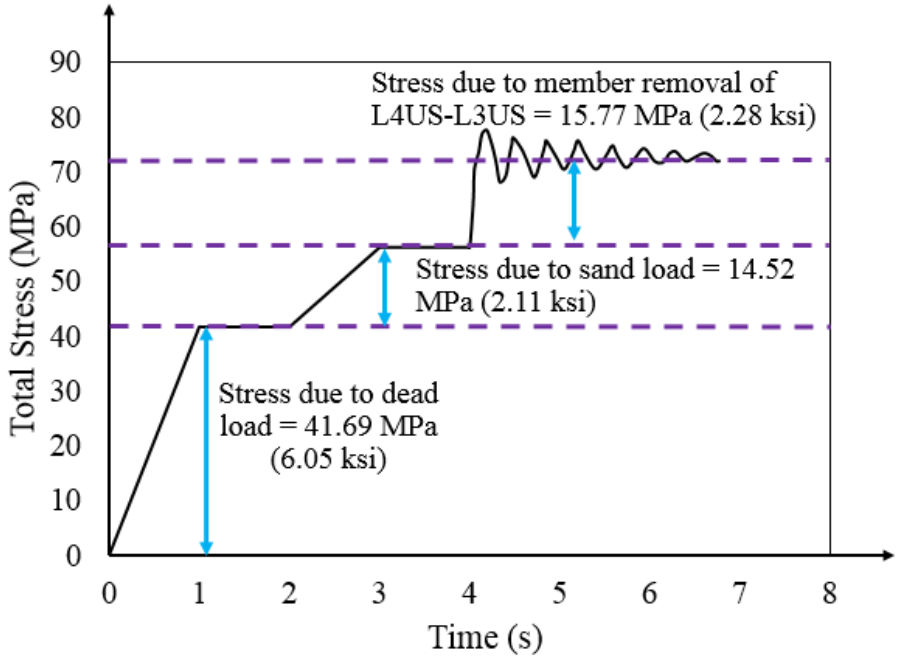

Source: FHWA.

Figure 22. Graph. Calculated total stress time history after sudden removal of a member of the Milton–Madison Bridge.

Figure 23 shows the time history plot of stresses measured during the field test. The increase in the steady-state stress in member L4DS-L3DS during the field test was approximately 16.55 MPa (2.4 ksi). This value was calculated as 15.77 MPa (2.28 ksi) from the LS-DYNA model. These values are reasonably close to each other. The minor difference could be due to the effect of the two successive blasts used to cut the member, which could not be simulated in LS-DYNA using the B-S beam element. Comparison of figure 22 and figure 23 shows dynamic amplification in stresses and vibration in truss members after the removal of a member both during the test and in the LS-DYNA simulation. These results also show that the B-S element with the Mat 98 material model in LS-DYNA can be used for realistic simulation of the dynamic effects of MR in a truss bridge.

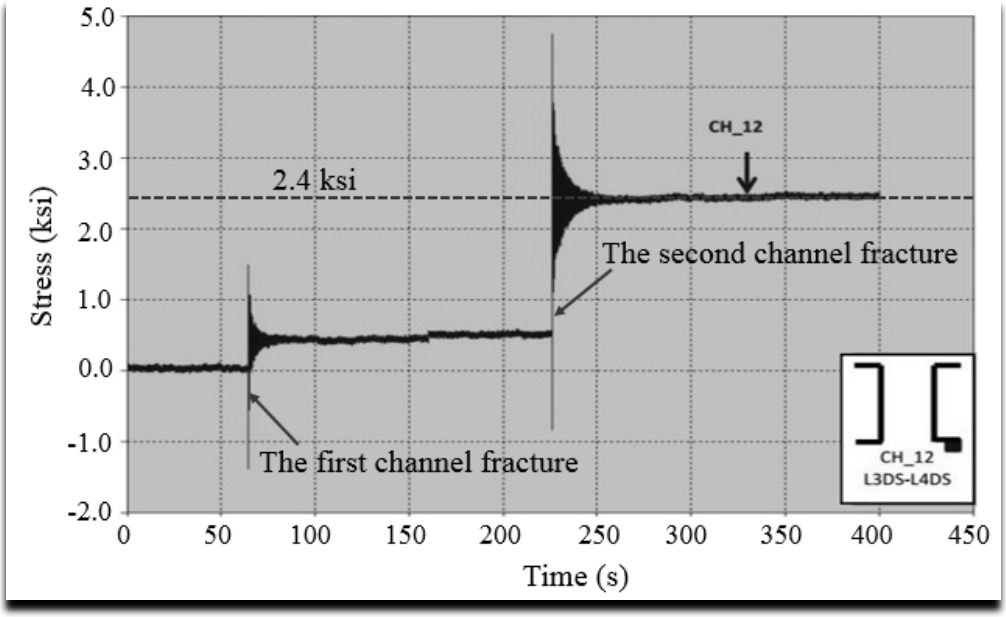

Source: FHWA.
1 ksi = 6.89 MPa.

Figure 23. Graph. Measured stress time history after fracture of a member of the Milton–Madison Bridge by blast (FHWA 2013).

CHAPTER 4. ALP ANALYSIS OF THE I-35W BRIDGE

INTRODUCTION

The I-35W Bridge, an eight-lane steel truss bridge carrying I-35W across Saint Anthony Falls of the Mississippi River in Minneapolis, MN, collapsed on August 1, 2007, killing 13 and injuring 145 people. The cause of this failure was determined to be an underdesigned gusset plate. Figure 24 shows the bridge before collapse. The collapse of this bridge heightened safety and redundancy concerns about truss bridges nationwide. This bridge is used for investigating ALPs and redundancy in long-span truss bridges because of the detailed information available on its design and inspection and the detailed investigation on its collapse by FHWA and NTSB.

Source: NTSB.

Figure 24. Photo. I-35W Bridge before collapse (NTSB 2008d).

Past studies on this bridge focused mainly on the inadequate capacity of undersized gusset plates at U10 and the connected vertical (Ocel and Wright 2008; Astaneh-Asl 2008; Hao 2010; Liao et al. 2011; Higgins et al. 2012). However, the failure of the gusset plate near one joint was only a localized phenomenon. Unlike the past research on the I-35W Bridge collapse, this research focuses on the global behavior of the bridge in the event of local damage, such as sudden loss of a member. In addition to axial forces, the effects of strong and weak axes moments were included in calculating total stress in truss members. The bridge was at significant risk of failure even with gusset plates of sufficient thickness because of increased deck loading from rehabilitations during the 1970s and the 1980s, insufficient capacity of major truss members, and lack of sufficient alternate load transfer paths.

Figure 25 shows a detailed framework for investigating ALP and retrofit strategies for this bridge. As noted in the figure, this research on the ALP was divided into three parts. In the first part, modeling and validation of FEMs of the bridge were performed based on the original design details of the bridge in 1965 and the as-built status of the bridge before collapse in 2007. The performance of the bridge under the service load was also checked. Collapse of the bridge based on *DCR* was investigated. Finite-element analysis results indicated that the *DCR* for many

members before the collapse was in excess of 1.0 (i.e., combined stresses due to *DL* and *LL* were greater than allowable stress). Hence, several members of a before-collapse model of the bridge were strengthened by increasing cross-sectional shape, areas, or both such that $DCR \leq 0.9$ under the $DL + LL$ load combination for all truss members. This model of the bridge was termed "Design Bridge" because the bridge has sufficient capacity to carry *DL*s and *LL*s. Behavior of this bridge after the removal of a member was investigated extensively to identify ALPs. *DCR* of truss members in this bridge was reduced to 0.9 or below so that the change in *DCR* after sudden removal of a member could be easily mapped to investigate the ALP (0.9 is an illustrative value; any value from 0.9 to 1.0 could have been considered).

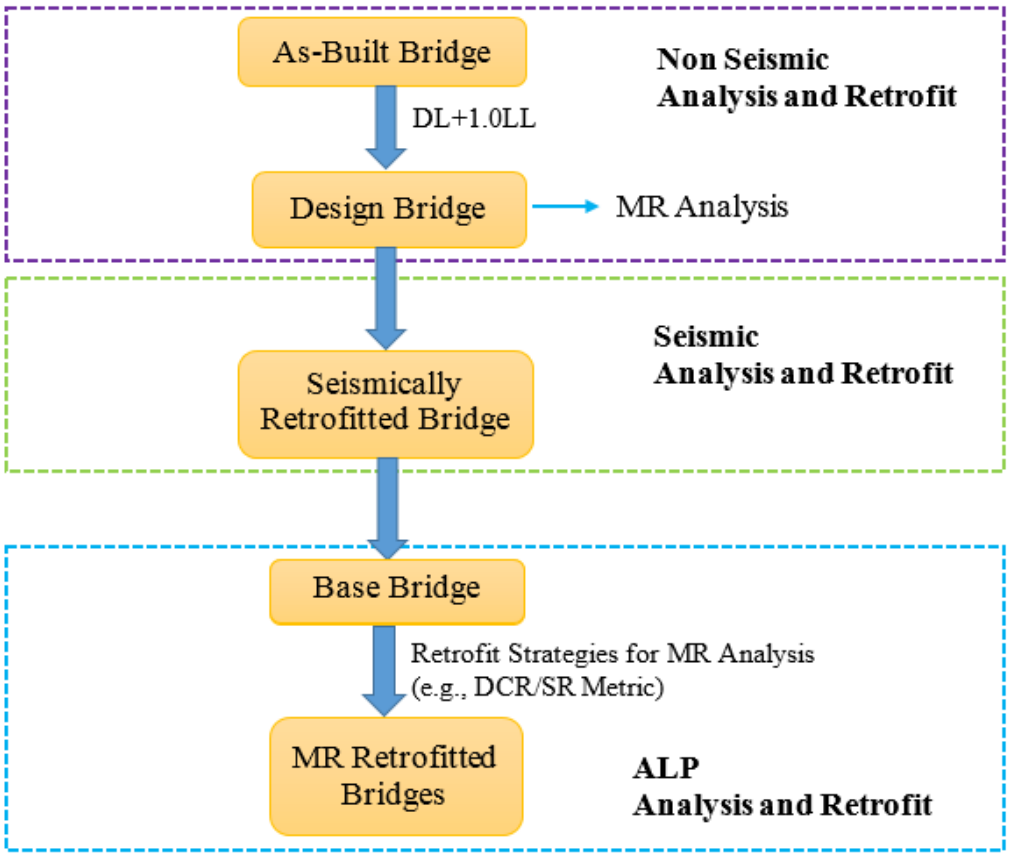

Source: FHWA.

Figure 25. Flowchart. Framework for the investigation of ALP in long-span truss bridges.

Unlike during extreme hazard events such as blast or member cutting, behavior of bridges during seismic loads is well understood by engineers, and bridges are retrofitted regularly to meet seismic demands. In the second part of this research framework, the Design Bridge was retrofitted to investigate the effects of seismic retrofits on ALP of a truss bridge. The seismic hazard considered was based on a 2,500-year earthquake in the San Diego area (termed the SD2500 hazard). It should be mentioned that the Design Bridge was in Minneapolis, MN, which is a low seismic region. It was found to have sufficient seismic resistance for a seismic hazard in Minnesota. The bridge retrofitted for the SD2500 hazard was termed "Base Bridge" and was considered for investigating retrofits for improving ALP of the bridge.

In the third part, the adaptability of various retrofit strategies on ALP and progressive collapse was examined extensively. Because of the differences between seismic events and sudden member loss, it is expected that seismic retrofits may not be sufficient to withstand member loss demands. Hence, effective retrofit strategies were investigated for mitigating sudden member loss demands on critical bridge components.

FINITE-ELEMENT MODELING OF THE BRIDGE

Basic Model Details

Detailed FEMs of the bridge were developed in SAP2000 and LS-DYNA. As shown in figure 26, the bridge had 29 nodes along the upper chord (denoted by "U") and 27 nodes along the bottom chord (denoted by "L"). Traffic on the bridge was in north and south directions, and two trusses were on the east and west sides. As shown in figure 26, nodes 1 (pier 5), 20 (pier 7), and 27 (pier 8) had roller supports, whereas node 8 (pier 6) had fixed constraint bearings.

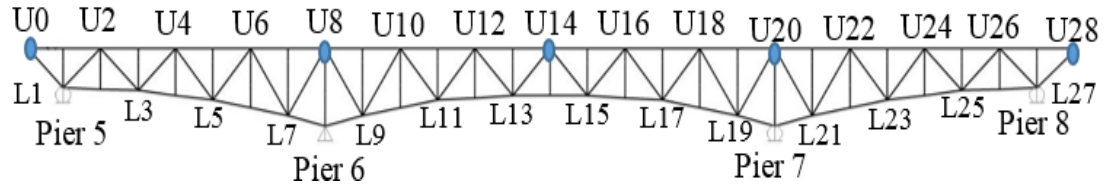

Source: FHWA.

A. 2D model (one side truss).

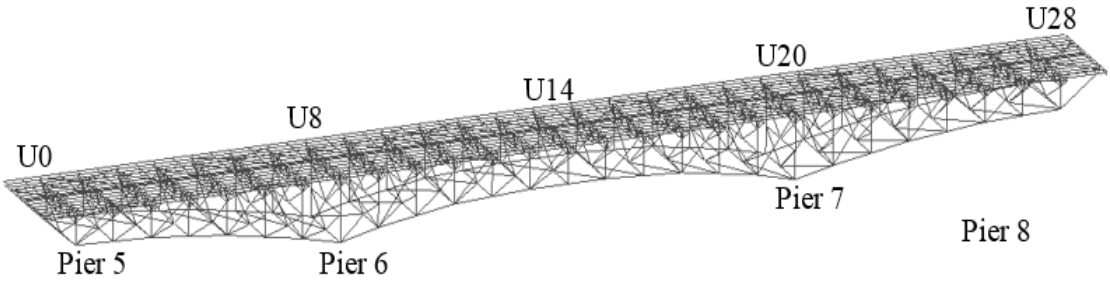

Source: FHWA.

B. 3D model.

Figure 26. Illustrations. 2D and 3D models of the I-35W Bridge in SAP2000.

The model of the bridge in LS-DYNA included main side trusses, floor trusses, floor stringers, diaphragms, and secondary bracing members. All truss members, bracings, and stringers were modeled by B-S beam elements with the Mat 98 material model to account for hardening in steel. Each element of the truss was modeled by a single beam element. Overall, the LS-DYNA model had 2,910 beam elements. The deck system in LS-DYNA was modeled by shell elements with elastic material for imposing the *DL* of the concrete deck on the truss system. The Young's modulus of the concrete in the deck was reduced such that the elasticity of the deck did not affect the truss behavior, and vertical deflection profiles of the bridge in LS-DYNA and SAP2000 agreed well. (The deck was not modeled in SAP2000. Rather, deck weights were applied at truss joints appropriately to include the effect of deck weight on the truss behavior). Nodal rigid body

constraints were applied for the nodal group shared by the deck, transverse stringers, and floor system to account for the connection between these three systems. All the joints in the SAP2000 and LS-DYNA models were treated as rigid.

The model in SAP2000 was similar to that in LS-DYNA except the equivalent nodal weight was assigned at deck stringers in SAP2000 and shell elements in LS-DYNA. All beam elements in SAP2000 were assigned elastic material properties. Geometrical, sectional, and material property data for the bridge models were obtained from shop drawings and bridge retrofit reports. Because of the complete symmetry of the bridge's west and east sides, cross-section areas for the main truss members in only the west side truss are listed in appendix B.

Dead Loads

After the bridge collapse, Ocel and Wright (2008) performed a detailed estimation of *DL*s on the bridge. They considered the bill of materials for both design drawings and shop drawings to estimate the steel weight and estimated the concrete deck weight based on original construction as well as rehabilitations. In addition, the *DL* consisted of vertical point loads from approach spans added at the ends of the main truss cantilevers. The original average thickness of the concrete deck was 165.1 mm (6.5 inches), and it increased by 50.8 mm (about 2 inches) after rehabilitations in 1977 and again substantially in 1998. Table 9 shows the *DL*s for the main span of the bridge based on calculations by Ocel and Wright (2008). *DL*1 represents the *DL* after construction of the bridge, and *DL*2 represents the *DL* in 2007 (before collapse of the bridge but not including construction load at the time of collapse). The *DL* on the truss span increased by approximately 24 percent from 1965 (time of construction) to 2007 (before collapse).

Table 9. *DL*s on the I-35W Bridge.

Component	*DL*1 (1965) (kN)	*DL*2 (2007) (kN)
Steel members	28,364	28,364
Concrete members	53,248	72,889
Approach span	5,585	6,989
Sum	87,197	108,239

1 kN = 0.225 kips.

Verification of the FEM of the Bridge Using DL

The accuracy of the FEM in SAP2000 was investigated by comparing vertical reactions for *DL* conditions (both *DL*1 and *DL*2) and axial forces in members for *DL*1. Table 10 shows vertical reactions for *DL*1 and *DL*2 from the FEM of the bridge in SAP2000. These results were also compared with those from the FHWA detailed as-built case available in Ocel and Wright (2008). The *DL* reactions from the SAP2000 model agreed very well with those in Ocel and Wright (2008); the maximum difference was less than 5 percent. The differences in reactions could be attributed to the modeling approach as well as points of application of loads.

Table 10. Main truss vertical reaction forces for *DL* condition.

DL Condition	Pier Location	Detailed As-Built Condition in 2007 per Ocel and Wright (2008) (D) (kN)	SAP2000 (S) (kN)	Difference: (S − D)/D (%)
*DL*1 (1965)	Pier 5 east	4,408	4,600	4.36
*DL*1 (1965)	Pier 6 east	16,605	16,595	−0.06
*DL*1 (1965)	Pier 7 east	16,298	16,354	0.34
*DL*1 (1965)	Pier 8 east	6,023	5,975	−0.79
*DL*1 (1965)	Pier 5 west	4,577	4,783	4.49
*DL*1 (1965)	Pier 6 west	16,632	16,572	−0.36
*DL*1 (1965)	Pier 7 west	16,338	16,352	0.08
*DL*1 (1965)	Pier 8 west	5,996	6,000	0.06
*DL*1 (1965)	Sum	86,878	87,230	0.41
*DL*2 (2007)	Pier 5 east	5,663	5,821	2.81
*DL*2 (2007)	Pier 6 east	20,360	20,349	−0.05
*DL*2 (2007)	Pier 7 east	19,901	20,056	0.78
*DL*2 (2007)	Pier 8 east	7,540	7,464	−1.00
*DL*2 (2007)	Pier 5 west	5,907	5,885	−0.38
*DL*2 (2007)	Pier 6 west	20,351	20,337	−0.07
*DL*2 (2007)	Pier 7 west	20,021	20,046	0.12
*DL*2 (2007)	Pier 8 west	7,393	7,554	2.18
*DL*2 (2007)	Sum	107,135	107,512	0.35

1 kN = 0.225 kips.

Table 11 through table 14 show comparisons between axial forces obtained from the SAP2000 model and those reported in Ocel and Wright (2008) for the FHWA detailed as-built *DL*1 case. The axial forces in the main truss members in the central span, the upper chords, the lower chords, and the diagonals agreed well with those from the design plans; the maximum difference was less than 10 percent. Because the loading assignment may vary when it is applied to the approach spans in different models, discrepancies exist in some members of the side spans. Members in the side spans have a lesser magnitude of axial force than those in the central span. Hence, even a small difference in the magnitude results in a larger percentage difference between results from Ocel and Wright (2008) and the SAP2000 model in table 11 and table 13. These percentage differences can be up to 61.40 and 46.80 percent in table 11 and table 13, respectively. All vertical members, except for those at the two end nodes, were modeled by adding two internal nodes for the connection of the vertical member to the floor truss members in the transverse direction. Therefore, verticals were subjected to biaxial forces due to the interaction with the floor truss system (FS), which may cause larger discrepancies in results because the design plan results may simply represent axial force for an entire member. However, the maximum discrepancy was still less than 23 percent for vertical members. Hence, the FEM of the bridge in SAP2000 can be considered to represent the I-35W Bridge reasonably well. It should be noted that a similar level of discrepancy was observed in models by FHWA and other consultants (Ocel and Wright 2008).

Table 11. Axial forces in upper chord members for *DL*1 case.

Upper Chord Member	Design Plans (1965) (D) (kN)	SAP2000 (S) (kN)	Difference: (S − D)/D (%)
U0-U1	1,953	1,708	−12.50
U1-U2	1,953	1,689	−13.50
U2-U3	−1,005	−1,087	8.10
U3-U4	−1,005	−1,087	8.10
U4-U5	2,295	2,121	−7.60
U5-U6	2,295	2,133	−7.10
U6-U7	7,838	8,071	3.00
U7-U8	7,838	8,091	3.20
U8-U9	6,899	7,097	2.90
U9-U10	6,899	7,086	2.70
U10-U11	−2,162	−2,060	−4.70
U11-U12	−2,162	−2,070	−4.20
U12-U13	−8,447	−8,514	0.80
U13-U14	−8,447	−8,116	−3.90
U14-U15	−8,447	−8,209	−2.80
U15-U16	−8,447	−8,608	1.90
U16-U17	−2,162	−2,323	7.50
U17-U18	−2,162	−2,314	7.00
U18-U19	6,899	6,758	−2.00
U19-U20	6,899	6,770	−1.90
U20-U21	7,838	7,911	0.90
U21-U22	7,838	7,894	0.70
U22-U23	2,295	2,440	6.30
U23-U24	2,295	2,431	5.90
U24-U25	−138	−55	−60.20
U25-U26	−138	−53	−61.40
U26-U27	3,541	3,484	−1.60
U27-U28	3,541	3,487	−1.50

1 kN = 0.225 kips.

Table 12. Axial forces in DMs for *DL*1 case.

DM	Design Plans (1965) (D) (kN)	SAP2000 (S) (kN)	Difference: (S − D)/D (%)
U0-L1	−2,491	−2,031	18.50
U2-L1	−2,945	−2,606	11.50
U2-L3	854	523	38.70
U4-L3	1,428	1,315	7.90
U4-L5	−2,847	−3,118	9.50
U6-L5	3,928	3,900	0.70
U6-L7	−5,222	−5,407	3.50
U8-L7	5,409	5,146	4.90
U8-L9	6,939	6,711	3.30
U10-L9	−7,473	−7,605	1.80
U10-L11	6,370	6,285	1.30
U12-L11	−5,405	−5,325	1.50
U12-L13	3,710	3,470	6.50
U14-L13	−952	−1,055	10.80
U14-L15	−952	−962	1.00
U16-L15	3,710	3,387	8.70
U16-L17	−5,405	−5,244	3.00
U18-L17	6,370	6,240	2.00
U18-L19	−7,473	−7,560	1.20
U20-L19	6,939	6,700	3.40
U20-L21	5,409	4,898	9.50
U22-L21	−5,222	−5,071	2.90
U22-L23	3,928	3,529	10.20
U24-L23	−2,847	−2,687	5.60
U24-L25	979	832	15.00
U26-L25	1,294	954	26.30
U26-L27	−3,430	−3,091	9.90
U28-L27	−4,510	−4,081	9.50

1 kN = 0.225 kips.

Table 13. Axial forces in lower chord members for *DL*1 case.

Lower Chord Member	Design Plans (1965) (D) (kN)	SAP2000 (S) (kN)	Difference: (S − D)/D (%)
L1-L2	356	516	45.10
L2-L3	356	522	46.80
L3-L4	−80	−79	1.50
L4-L5	−80	−83	3.80
L5-L6	−4,835	−5,004	3.50
L6-L7	−4,835	−5,005	3.50
L7-L8	−11,267	−11,460	1.70
L8-L9	−11,312	−11,528	1.90
L9-L10	−2,487	−2,691	8.20
L10-L11	−2,487	−2,693	8.30
L11-L12	5,832	5,371	7.90
L12-L13	5,832	5,374	7.90
L13-L14	9,057	8,312	8.20
L14-L15	9,057	8,312	8.20
L15-L16	5,832	5,505	5.60
L16-L17	5,832	5,503	5.60
L17-L18	−2,487	−2,467	0.80
L18-L19	−2,487	−2,466	0.80
L19-L20	−11,312	−11,246	0.60
L20-L21	−11,267	−11,232	0.30
L21-L22	−4,835	−5,117	5.80
L22-L23	−4,835	−5,117	5.80
L23-L24	−609	−749	22.90
L24-L25	−609	−745	22.30
L25-L26	−845	−836	1.10
L26-L27	−845	−839	0.80

1 kN = 0.225 kips.

Table 14. Axial forces in vertical members for *DL*1 case.

Vertical Member	Design Plans (1965) (D) (kN)	SAP2000 (S) (kN)	Difference: (S − D)/D (%)
U1-L1	−1,437	−1,524	6.10
U2-L2	1,183	955	19.30
U3-L3	−1,423	−1,123	21.10
U4-L4	1,041	1,046	0.50
U5-L5	−1,415	−1,192	15.70
U6-L6	1,223	1,147	6.20
U7-L7	−1,481	−1,190	19.60
U8-L8	−11,241	−11,420	1.60
U9-L9	−1,472	−1,225	16.80
U10-L10	1,205	1,138	5.60
U11-L11	−1,197	−1,155	3.40
U12-L12	1,201	1,049	12.70
U13-L13	−1,468	−1,202	18.10
U14-L14	1,085	1,013	6.60
U15-L15	−1,468	−1,202	18.10
U16-L16	1,201	1,048	12.80
U17-L17	−1,197	−1,155	3.50
U18-L18	1,205	1,136	5.70
U19-L19	−1,472	−1,226	16.70
U20-L20	−11,241	−11,206	0.30
U21-L21	−1,481	−1,191	19.60
U22-L22	1,223	1,145	6.40
U23-L23	−1,415	−1,189	16.00
U24-L24	1,041	1,049	0.70
U25-L25	−1,423	−1,109	22.10
U26-L26	1,183	969	18.10
U27-L27	−1,437	−1,573	9.50

1 kN = 0.225 kips.

Live Loads

According to AASHTO (2014), the *LL* is a combination of lane load with a magnitude of 0.87 kN/m (0.64 klf) and standard truckload. Because the I-35W Bridge is a long-span bridge where the truck effect may be negligible, only the lane load with multilane presence factor was applied on the bridge for the redundancy analysis. This was done to simplify the loading scenario on the bridge because of the large number of simulations required.

Material Properties

The behavior of the steel in the truss members was modeled by the stress–strain behavior in figure 8 in chapter 3, assuming a Young's modulus of 200 GPa (29,000 ksi).

Validation of FEMs in SAP2000 and LS-DYNA

A detailed validation of FEMs in SAP2000 and LS-DYNA was performed by comparing 2D and 3D models of the bridge. For example, figure 26 shows both 2D and 3D models of the bridge in SAP2000. The geometry and nodal details of the bridge are the same in LS-DYNA. One comparison is the *DL* of the two main trusses. Based on the layout and the cross-sectional areas provided in the drawings, the net weight of each of the two main trusses was calculated to be 5,622.95 kN (1,264.09 kips), which compares well with the value of 5,604.75 kN (1,260 kips) reported by Liao et al. (2009). Additional *DL*s, such as the concrete slab, floor trusses, sway frames, and so forth, were applied to each node according to Liao et al. (2009). Figure 27-A and figure 27-B show the deformation profile of 2D trusses in SAP2000 and LS-DYNA under self-weight. The self-weight of one side truss was 5,622.95 kN (1,264.09 kips) in SAP2000 and 5,610.16 kN (1,261.22 kips) in LS-DYNA (0.23-percent difference). Figure 27-C shows the plot of the deflection profile using the displacement extracted from the lower node of the truss. The difference in displacement between the two models was less than 5 percent, except for at nodes 2 and 3, where this difference was higher because of their proximity to boundary regions. Other comparisons, such as weight, total support reaction for *DL* + *LL*, maximum displacement at node 14 (the middle node) for *DL* + *LL* cases, and external force percentage for 2D models in SAP2000 and LS-DYNA, are shown in table 15.

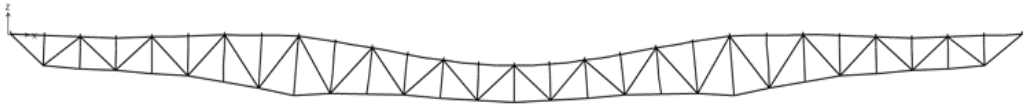

Source: FHWA.

A. 2D model in LS-DYNA.

Source: FHWA.

B. 2D model in SAP2000.

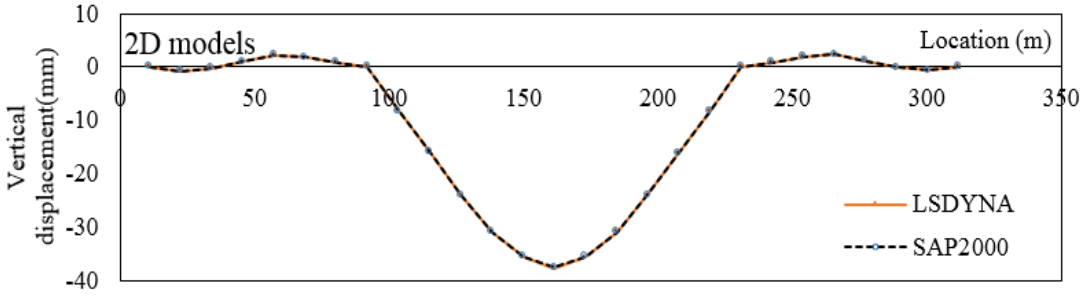

Source: FHWA.

C. Vertical displacement shape from FEM under steel self-weight of one side truss.

Figure 27. Illustrations and graph. Comparison between deformed shapes and vertical displacements from 2D models in SAP2000 and LS-DYNA.

Table 15. Comparisons between 2D models in SAP2000 and LS-DYNA.

Item	SAP2000	LS-DYNA	Difference Δ
Weight (one side truss) (kN)	5,623	5,610	0.2%
Total reaction force (kN) (*DL* + *LL*)	67,625	63,977	5.4%
Maximum displacement at node 14 (the middle node) for *DL* + *LL* case (mm)	371.53	374.68	0.85%
External force percentage (*DL* / (*DL* + *LL*))	82%	80%	2.3%

1 kN = 0.225 kips; 1 mm = 0.0394 inches.

Table 16 and table 17 show the comparison between displacements at nodes of 3D models of the bridge in SAP2000 and LS-DYNA under the loading cases of steel-truss self-weight and *DL*1, respectively. The maximum difference in vertical displacement between the two models was around 5 percent. Table 18 shows the contribution of steel and concrete to the total *DL*. The concrete deck contributed approximately 63 percent to the total bridge weight, almost three times as much as the steel members.

Table 16. Comparison between displacements from 3D models of the bridge under steel truss self-weight in SAP2000 and LS-DYNA.

Node Number	SAP2000 (S) (mm)	LS-DYNA (L) (mm)	Difference: (L − S)/S (%)
1	0	0	0
2	−6.32	−6.31	−0.14
3	−8.26	−8.22	−0.50
4	−5.96	−5.9	−1.03
5	−1.65	−1.62	−2.0
6	−0.35	−0.35	−0.32
7	−0.37	−0.37	−1.07
8	0	0	0
9	−19.70	−19.64	−0.29
10	−38.83	−38.76	−0.18
11	−58.24	−58.11	−0.23
12	−75.53	−75.48	−0.06
13	−87.11	−87.07	−0.05
14	−92.18	−93.26	1.17
15	−87.15	−87.28	0.15
16	−75.59	−75.68	0.12
17	−58.32	−58.32	−0.01
18	−38.90	−38.71	−0.50
19	−19.74	−19.72	−0.09
20	0	0	0
21	−0.29	−0.28	−4.72
22	−0.19	−0.18	−4.79
23	−1.40	−1.43	2.03
24	−5.65	−5.69	0.74
25	−7.92	−7.96	0.52
26	−6.02	−6.15	2.24
27	0	0	0

1 mm = 0.0394 inches.

Table 17. Comparison between displacements from 3D models of the bridge under *DL*1 (1965) in SAP2000 and LS-DYNA.

Node Number	SAP2000 (S) (mm)	LS-DYNA (L) (mm)	Difference: (L − S)/S (%)
1	0	0	0
2	−30.2	−28.7	−4.97
3	−44.8	−42.5	−5.13
4	−43.4	−41.1	−5.30
5	−30	−28.5	5
6	−17.8	−16.9	−5.06
7	−11.3	−10.8	−4.42
8	0	0	0
9	−44.1	−42	−4.76
10	−83.8	−79.8	−4.77
11	−127.5	−121.5	−4.71
12	−167.9	−159.7	−4.88
13	−195	−185.5	−4.87
14	−208.6	−198.3	−4.94
15	−195.4	−185.9	−4.86
16	−168.6	−160.4	−4.86
17	−128.4	−122.3	−4.75
18	−84.6	−80.6	−4.73
19	−44.5	−42.5	−4.49
20	0	0	0
21	−11.6	−11.1	−4.31
22	−18.2	−17.3	−4.95
23	−30.4	−28.9	−4.93
24	−43.5	−41.4	−4.83
25	−44.5	−42.3	−4.94
26	−30	−28.5	5
27	0	0	0

1 mm = 0.0394 inches.

Table 18. Weights of various portions of 3D full bridge models.

Item	Weight (kN)	Percentage
Steel members	25,391	22
Concrete members	72,886	63
DL additional	17,510	15
Sum	115,787	100

1 kN = 0.225 kips.

Damping Effect

In NLD analysis, the damping ratio affects the dynamic response of a structural system significantly. In general, long-span truss bridges likely have damping ratios of less than 2 percent. For example, Sarraf (1998) suggested a 2-percent damping ratio for an 80-meter (262.5-foot) span deck-truss bridge. Kanaji et al. (2003) suggested a damping ratio of 2 percent for the 980-meter (3,215.2-foot) Minato Bridge, a cantilever truss bridge with two 235-meter (771-foot) side spans and a 510-meter (1,673.2-foot) main span. Frangopol and Imai (2004) used a damping ratio of 5 percent for the Akashi Kaikyo Bridge, a suspension bridge with side spans of 960 m (3,149.61 ft) and a main span of 1,991 m (6,532.2 ft). Casciati et al. (2008) and Dyke et al. (2003) adopted a 3-percent critical damping ratio for the Bill Emerson Memorial Bridge, which is a fan-type medium-span cable-stayed bridge with a main span length of 350.6 m (1,150.3 ft). Mustafa et al. (2018) investigated damping in a Warren-type steel truss bridge consisting of five simply supported main spans, each having a length of 70.77 m (232.19 ft) and a width of 6.01 m (19.72 ft), through field monitoring and found that the damping in the first mode was approximately 0.93 percent.

Two approaches are available for dealing with damping in LS-DYNA. One is to control the global damping factor and the other is to control the material damping factor. Only limited types of material models have the option to input a selected damping factor. The elastic material model, for example, allows the use of damping ratios for axial and bending behaviors separately. Material model Mat 98 used to model the bridge in LS-DYNA does not allow the use of a material damping factor; rather, it allows the use of a global damping factor (D_s).

To select a reasonable value for the D_s to give a damping ratio between 1 and 2 percent for the first mode of the bridge, a parametric study was performed by varying the D_s in the Mat 98 material model. Normally, when a truss member is removed suddenly and the material model is not assigned a D_s, bridge members will continue to vibrate indefinitely because of the dynamical effect of the MR. When the bridge is assigned a certain value of D_s, the vibration of bridge members is damped out gradually. For long-span bridges, the damping ratio in the first mode is generally less than 2 percent and can be estimated by the logarithmic decrement method on the member vibration time history, as shown in equation 16:

$$\delta_e = \frac{1}{q}\ln\left(\frac{u_1}{u_{q+1}}\right) \approx 2\pi\zeta \qquad (16)$$

Where:

δ_e = logarithmic decrement.
q = number of cycles between 1st and (q+1)th peak amplitude.
u_1 = peak amplitude of the first peak.
u_{q+1} = peak amplitude of the (q+1)th peak.
ζ = damping ratio.

In the parametric study, vibration signatures for nodes of the truss due to dynamic effects of MR were generated by considering different values for D_s in the simulation. The displacement of randomly picked node 3 is plotted for different values of D_s in figure 28. When D_s is assigned values of 1.5 or 3.0, vibration decays more rapidly than when D_s is assigned values of 0.75 and

0.5. The converged value of displacement in all four cases is −0.0326 mm (−0.00128 inches), although the peak magnitude varies with damping. Table 19 shows damping values for four cases of D_s calculated from these vibration signatures by using equation 16. The damping ratio decreased from approximately 9 to 1 percent as D_s was reduced from 3 to 0.5. Based on the results in figure 28 and table 19, the value of D_s was selected to be 0.75 to achieve a damping value from 1.57 to 1.63 percent. Table 19 demonstrates that the difference in peak values of displacement for a damping ratio in the range of 3.90 to 1.14 percent was negligible. Hence, both peak dynamic and steady-state displacements due to MR can be obtained reliably by using the 0.75 value for D_s.

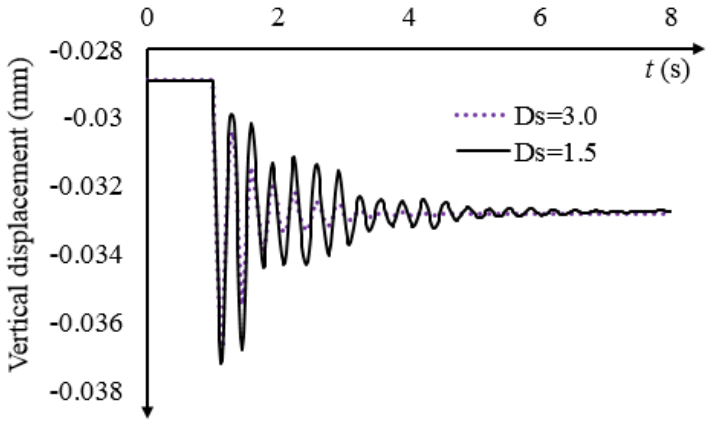

Source: FHWA.
1 mm = 0.0394 inches.

A. Displacement time history for D_s values of 3.0 and 1.5.

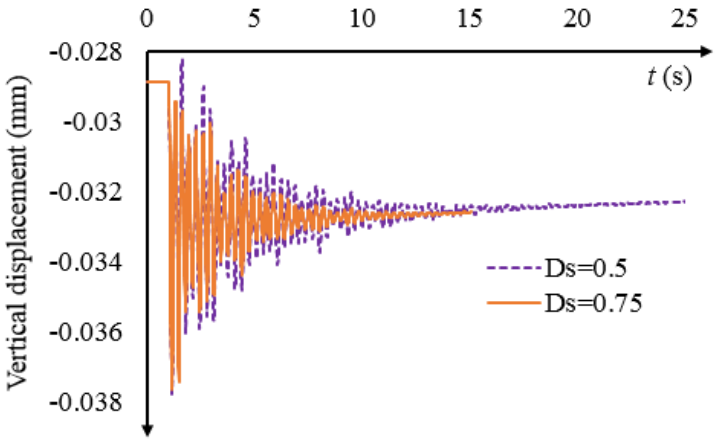

Source: FHWA.
1 mm = 0.0394 inches.

B. Displacement time history for D_s values of 0.5 and 0.75.

Figure 28. Graphs. Displacement time history of node 3 for various D_s values.

Table 19. Damping ratios for different values of D_s.

Global Damping Factor (D_s)	Damping Ratio Range (ζ)	Steady-State Value (mm)	Peak Value (mm)
3	9.26–7.74%	−0.0326	−0.0367
1.5	3.89–3.95%	−0.0326	−0.0373
0.75	1.57–1.63%	−0.0326	−0.0377
0.5	1.14–1.18%	−0.0326	−0.0378

1 mm = 0.0394 inches.

AS-BUILT BRIDGE AND NONSEISMIC RETROFITS

Figure 29 shows the *DCR* for the as-built bridge with loading conditions in 2007 (before collapse and without construction load) under the service load condition in equation 11. In this figure, bridge members with *DCR* less than 1.0 are shown in black solid lines and those with *DCR* greater than 1.0 are shown in red dotted lines. *DCR* of 1.0 implies that the stress in the member is at the allowable limit corresponding to $0.6\sigma_y$. *DCR* of 1.67 implies that the stress in the member is equal to σ_y. Figure 29 shows that diagonal and lower chord members near supports have *DCR*s larger than 1.0, which implies that the stress due to service loads (*DL* + *LL*) in these members was more than the allowable stress. This probably happened because the *DL* on the bridge increased by 24 percent from 1965 to 2007 because of rehabilitations. However, none of the members of the truss had *DCR* greater than 1.67 (i.e., all members of the truss were in elastic range under the combination of *DL*s and *LL*s).

For a bridge that has been designed for service loads, *DCR* for all members must be less than 1.0. Because the objective of this research was to study ALP in a well-designed bridge, retrofit of members with *DCR* greater than 1.0 was performed by strengthening the member (by changing I-shaped sections to box sections and increasing the cross-sectional area) so that *DCR* of all members became 0.9. This was done so that change in *DCR* of members after the removal of a critical member or members could be quantified easily (with respect to a uniform value of 0.9). This bridge model was designated the Design Bridge. Figure 30 shows the Design Bridge where retrofitted members are indicated by red dotted lines. This member strengthening resulted in a 2.65-percent increase in the weight of the steel in the bridge. Although target *DCR* for this bridge was 0.9, ALP analysis (i.e., after removal of a member) was performed by considering limit states of allowable (1.0) and yield (1.67) stresses.

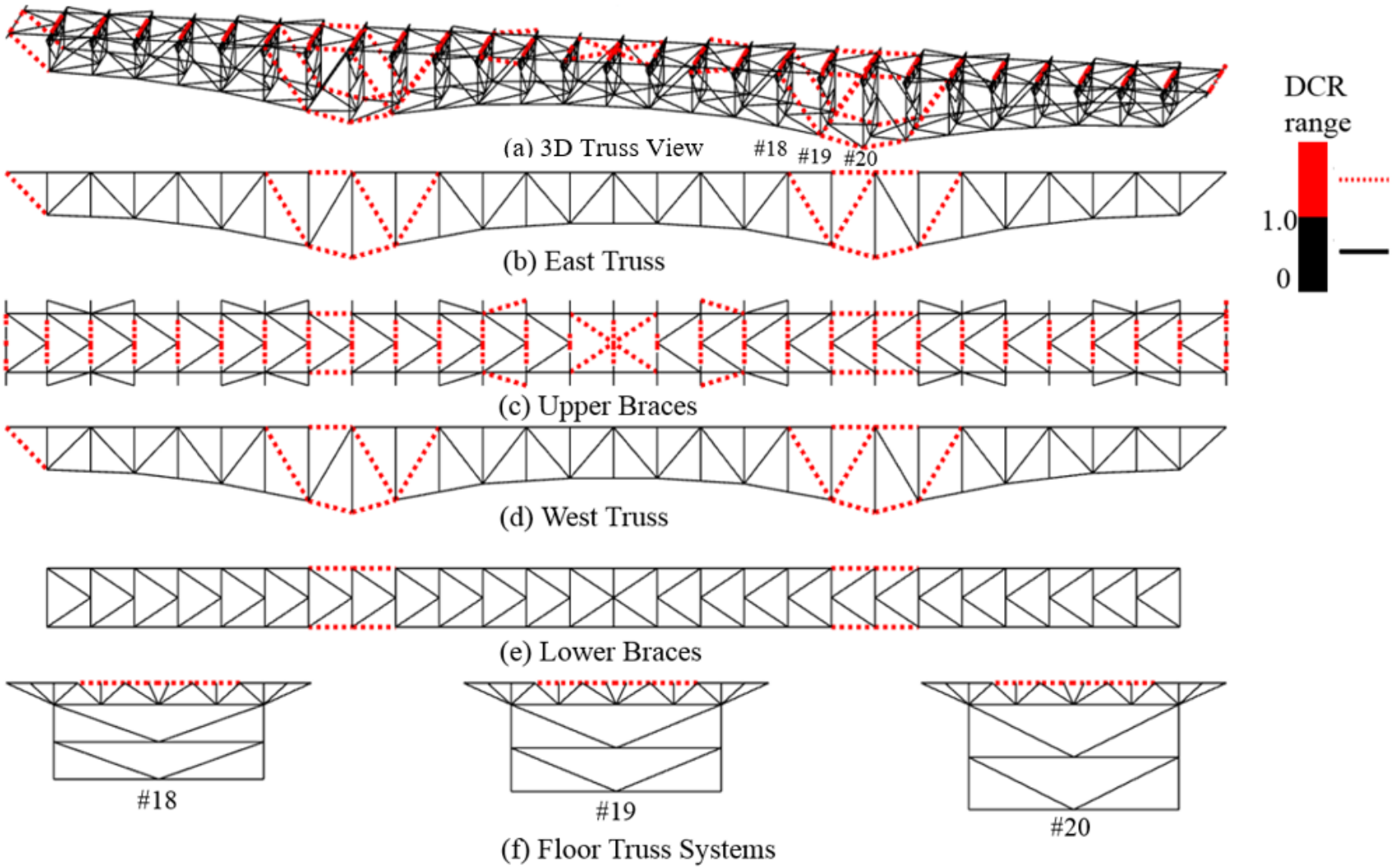

Source: FHWA.

Figure 29. Illustration. *DCR* spectra for the as-built bridge subjected to service loads.

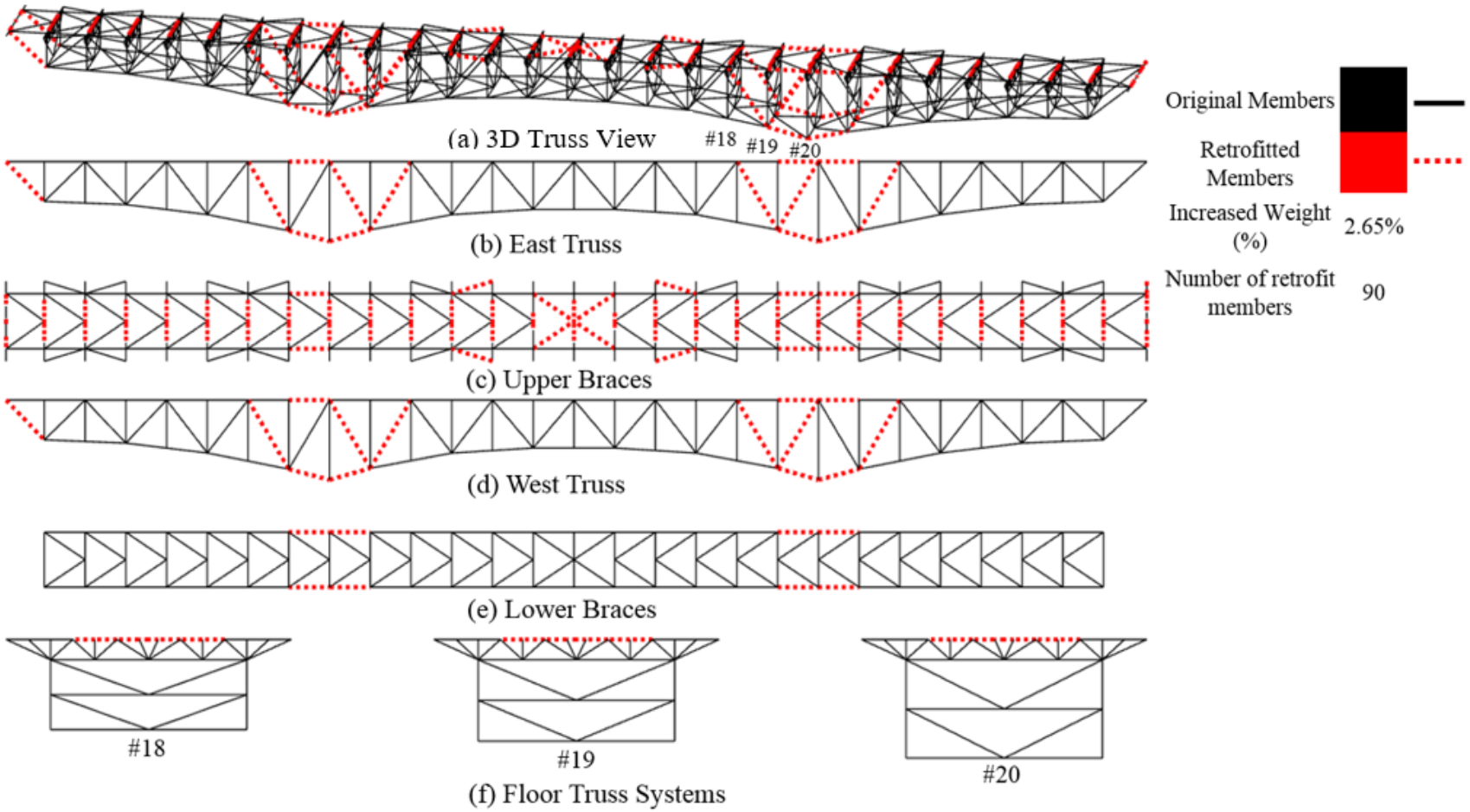

Source: FHWA.

Figure 30. Illustration. Members of the as-built bridge retrofitted by member strengthening to obtain the Design Bridge for the ALP analysis.

ALP ANALYSIS OF THE DESIGN BRIDGE

An exhaustive ALP analysis of the Design Bridge was performed by modeling the sudden loss of various members. The MR was investigated using the SAP2000 model for *DCR* and the LS-DYNA model for *SR*. Elastic static analysis was performed using SAP2000 after removing a target member from the model. *DCR* for all truss members was calculated from the results of the SAP2000 model. In LS-DYNA, MR was performed by assigning a specific part number and time interval in the card of *Load_remove_part. *SR* for all truss members was calculated from LS-DYNA results for different MR cases.

MR Event

MR analysis was performed by removing one critical member at a time. Members with the highest values of *DCR* under service load (*DL* + *LL*) were identified for removal. Analysis results indicated that vertical members were not critical in this specific bridge, so they were not considered for removal. On the other hand, diagonal, lower chord, and upper chord members were found to be critical. Considering the double symmetry of the bridge geometry, 10 members were chosen for removal from one-quarter of the bridge (the southern part of the west side truss), as shown in figure 31. Table 20 shows the 10 MR cases that were investigated. The MR scenario in SAP2000 was implemented by analyzing two separate states of the structure: before and after the loss of the member.

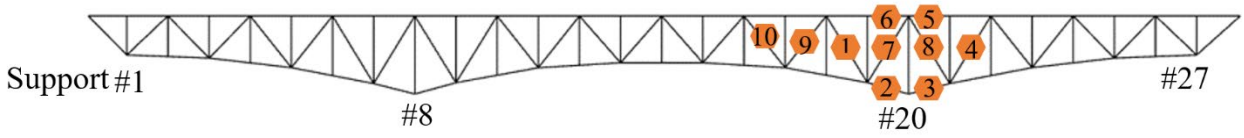

Source: FHWA.

Figure 31. Illustration. Location of critical members for removal in one-quarter of the bridge on the west side truss.

Table 20. MR cases.

MR Case Number	Location
1	DM
2	Lower chord
3	Lower chord
4	DM
5	Upper chord
6	Upper chord
7	DM
8	DM
9	DM
10	DM

ALP (MR) Analysis for Design Bridge: DCR Metric

The objective of the ALP analysis was to identify both the local and global effect of the specific local damage (MR) introduced. First, to investigate the stress variations due to loss of a member or members, *DCR* results before and after an MR event were compared in three panels in the east and west trusses when a member was removed in one of the panels in the west truss, as shown in figure 32. Because of the geometric and loading symmetry, the *DCR*s before MR were the same for symmetric members in the three panels of the east and west trusses. After DM U18-L19 in the west truss was removed, upper chord, lower chord, and vertical members near the removed member in the west truss experienced a significant increase in their internal forces compared to those in the east truss. The damage propagated to other members around the removed member. For vertical members, there were two internal nodes (in addition to two nodes at the ends of the member) in the FEM, whereas there was only one continuous physical member in the real bridge (which was connected to the FS through gusset plates). The internal nodes were connected to the floor truss members in the transverse direction. Because of the interaction with the FS, verticals were subjected to biaxial forces, which caused variation in *DCR* along the length of the vertical member.

In the intact bridge, overall torsional resistance of the bridge about its longitudinal axis is generally designed to keep the structure in equilibrium. Two major mechanisms contribute to the entire torsional resistance to sustain the balanced or unbalanced traffic loads:

- The two side trusses together with the deck, stringers, and upper braces as well as the lower braces could be treated as a hollow closed box section that provides torsional resistance.

- FSs in the transverse direction act as diaphragms to provide the hollow closed box section more rigidity.

The removal of a member undermines the structural integrity and symmetry of the bridge. By calculating the contributions of axial and flexural interactions to the *DCR* of a member, the impact of biaxial bending stress on the member and system can be investigated. For each member in the three panels, the contributions of axial force, in-plane moment (M_{in}), and out-of-plane moment (M_{out}) to its *DCR* were calculated and are expressed as percentages (i.e., contribution to *DCR* divided by the total *DCR*) in figure 33. For a typical truss member in figure 33, the numbers above and below a member show results for before and after the MR, respectively. For example, for member U17-U18, “56 42 2” above the member represents 56-, 42-, and 2-percent contributions of axial, M_{in}, and M_{out} to *DCR*, respectively, before the MR. Likewise, “3 90 7” below the member represents 3-, 90-, and 7-percent contributions of axial, M_{in}, and M_{out} to *DCR*, respectively, after the MR. For this member, the major contribution to *DCR* changed from 56-percent axial and 44-percent moment (total of M_{in} and M_{out}) before the MR to 3-percent axial and 97-percent moment after the MR.

Figure 33 also demonstrates that the contribution of axial forces to *DCR* is generally more than that of the total moment in all main truss members before the removal of a member, except for a few vertical members. Because of the unbalanced load introduced into the vertical members through the connections with the FS in the same panel, the moment component in verticals may

be more dominant than the axial force component even before the removal of a member. After the removal of a member, the major contributor to *DCR* in the upper and lower chords on the west truss changed from axial to total moment. In the east truss, lower chords in the nearby region experienced a similar change. However, the deck, stringers, and upper braces helped the upper chords maintain the shape without distortion. Hence, axial contribution to *DCR*s was dominant in upper chords. This discussion demonstrates that an analysis that treats truss members as primarily axial is not accurate and not reliable for evaluating the capacity of the truss members in the event of MR.

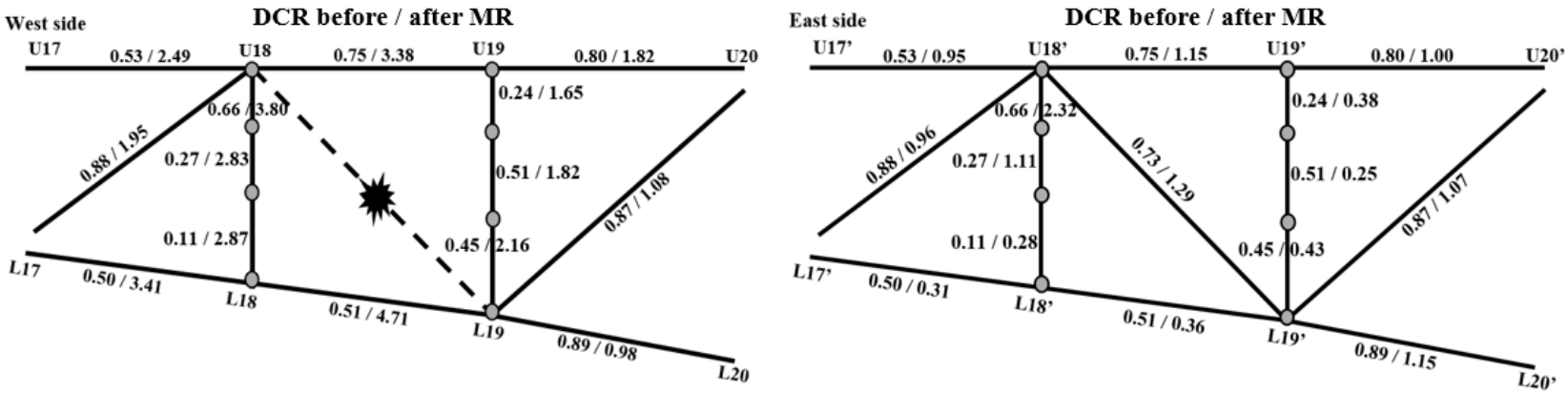

Source: FHWA.

Figure 32. Illustration. *DCR* before and after MR case 1 near the damaged location in west and east side trusses.

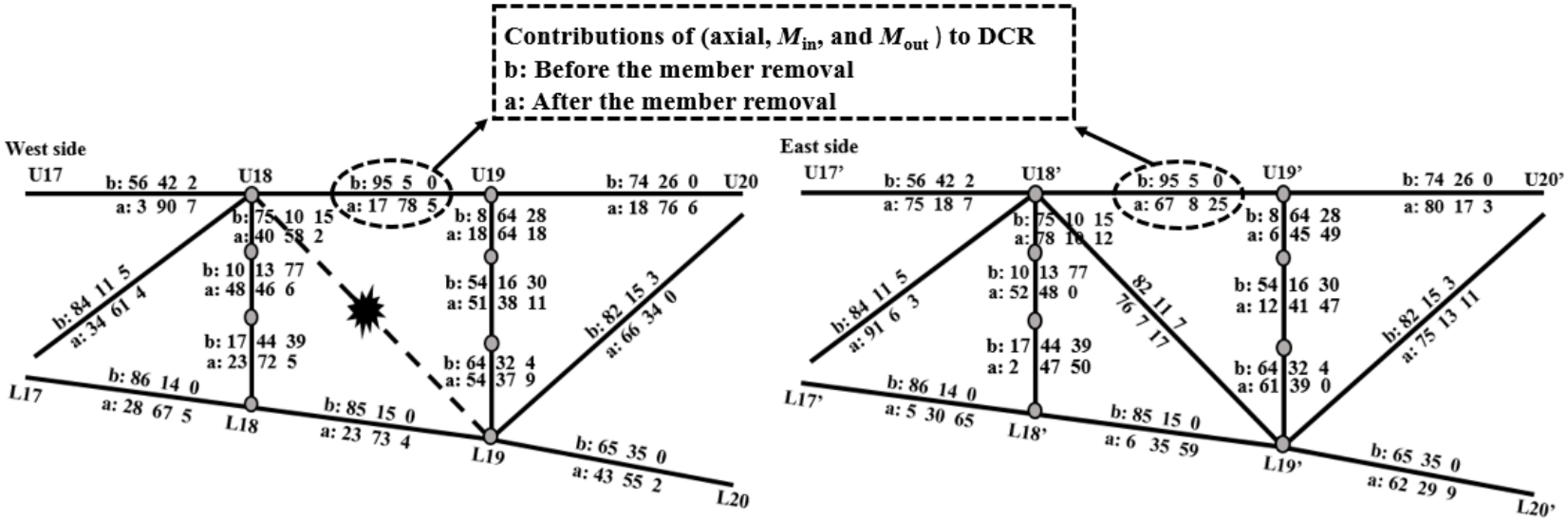

Source: FHWA.

Figure 33. Illustration. Contributions to *DCR* before and after MR case 1 near the damaged location in west and east side trusses.

The results presented in this section so far illustrate the localized view of the effect of damage to nearby members. To investigate the global view of the impact of damage to a member, distribution of *DCR* on 3D and 2D models of the bridge and its subcomponents (upper and lower braces and floor systems) is shown for 10 cases of MR (table 20) in figure 34 to figure 43. The six views (3D, east truss, upper braces, west truss, lower braces, and FS) of the bridge in each of these figures show the load path and can be defined as ALP spectra for *DCR* in order to quantify ALP. For MR case 1 in figure 34, the DM U18-L19 in the west side truss was removed. This led to load redistribution in the damaged system and an increase in the demand on the main truss members near the damaged zone on the same (west) side; the effect was less significant on members of the truss on the opposite (east) side. Because the member loss event is a localized phenomenon, damage to other members was concentrated around the damaged member. In this condition, the removed DM, as the web member, disrupted the normal load path. Compared with upper chord members, lower chord members were more dominant and effective in transferring the load to supports because the load always travels in the shortest path. If the load traveled to the upper chord, it needed to travel through vertical members before being transferred to the support, which is a longer path. Hence, the other three lower chords near support 8 were also affected even though they are far from the damaged zone. On the other hand, the increased demand in the #18 and #19 floor systems, as well as the upper brace and lower brace systems, indicated the 3D effect in load redistribution from west to east truss. This again shows the role these members play in resisting the bridge's tendency to undergo global torsional motion because of removal of a member from one side truss.

Figure 34 demonstrates that in addition to members near the damaged member, many members of the upper braces, lower braces, and FS have *DCR* greater 1.67 (i.e., these members probably yielded). MR case 2 in figure 35 shows the results for the removal of lower chord L18-L19. The loss of the lower chord member had less impact on both trusses than the removal of the DM in case 1. Members of the main truss remained in the elastic range, although a few members of the lower and upper braces and floor trusses probably yielded (i.e., they had a *DCR* larger than 1.67).

MR cases 3 and 4 simulated the loss of lower chord and diagonal members, respectively, in the side span. Results for these two cases are plotted in figure 36 and figure 37, respectively. Figure 36 shows that removal of the lower chord member L20-L21 in the side span led to redistribution of loads in both the side span and the central span. However, significant load redistribution occurred in the truss members on the other side (east side). There was no damage to members in the north side span. Figure 37 shows that removal of the DM L21-U22 in the south side span limited the damage to other members in the same span, although load redistribution occurred in the truss members on the other side (east side). In both cases 3 and 4, some members of the upper and lower braces probably yielded (i.e., their *DCR* was greater than 1.67).

Cases 5 and 6 simulated the loss of upper chord members on the right and left sides of support #20, respectively. Results for these two cases are presented in figure 38 and figure 39, respectively. These figures show that these two cases caused minor effects on other members of the truss, and there was significantly less load redistribution after the loss of these two members than in previous cases. This is because the deck, longitudinal stringers, transverse diaphragm between stringers, and upper braces effectively compensated for the loss of upper chord members. Hence, the loss of an upper chord member does not seem to create a potential threat to

the stability of the load-carrying system in this bridge. For both these cases, no members in the lower braces and floor trusses yielded, and fewer than three members in the upper braces yielded. In MR cases 7 to 10, the effect of the loss of a DM was similar to that in case 1. Results for these cases are shown in figure 40 to figure 43, respectively.

Results in figure 34 to figure 43 correspond to 10 MR cases in one-quarter of the bridge. Because of the symmetry of the west and east side trusses, an envelope can be drawn based on these 10 cases to show the ALP for the entire bridge. *DCR* values for truss members of the bridge for the 10 cases were tabulated, and the *DCR* value selected for a particular member was the largest *DCR* for that member among the 10 MR cases. This process was mirrored in both longitudinal and transverse directions to consider the MR events at the symmetric spot for the north end of the east side truss. The boundary conditions of roller and fixed support at joints 8 and 20, respectively, had a negligible effect on these results. Figure 44 shows the complete envelope for the entire bridge, which can be used to identify members to retrofit to provide effective ALP in case of loss of any member of the bridge. Some of the members illustrated by dash-dotted (red) lines in this figure are part of the ALP that are likely to yield after the removal of any member of the truss. After retrofit of members highlighted by dash-dotted (red) lines, all members of the truss will stay in the elastic zone after the removal of any member of the retrofitted bridge. Hence, the development of ALP spectra in figure 44 can be considered the quantification of ALP of the truss bridge from an effective retrofit point of view.

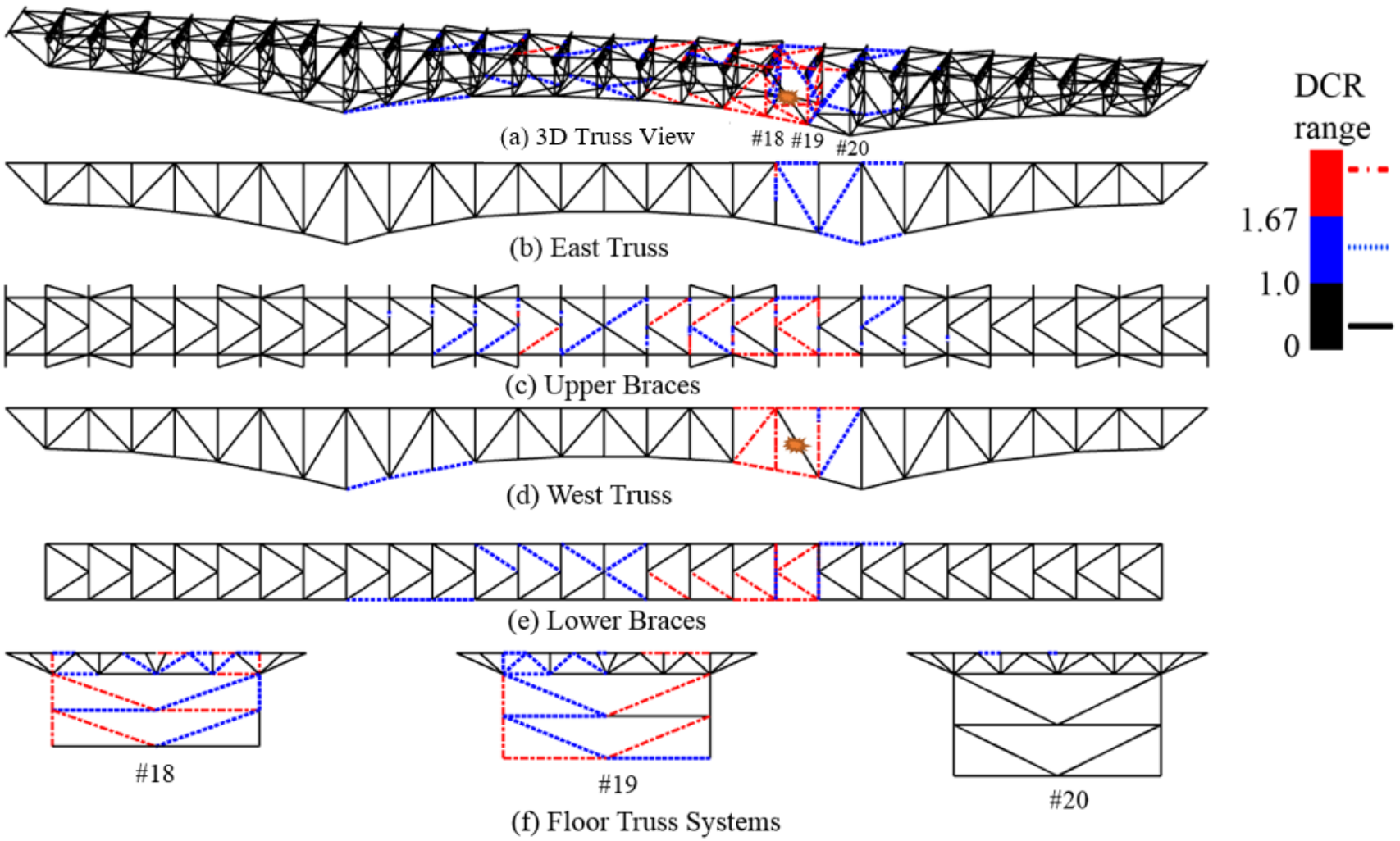

Source: FHWA.

Figure 34. Illustration. *DCR* spectra for the Design Bridge for diagonal member removal (MR case 1 in table 20).

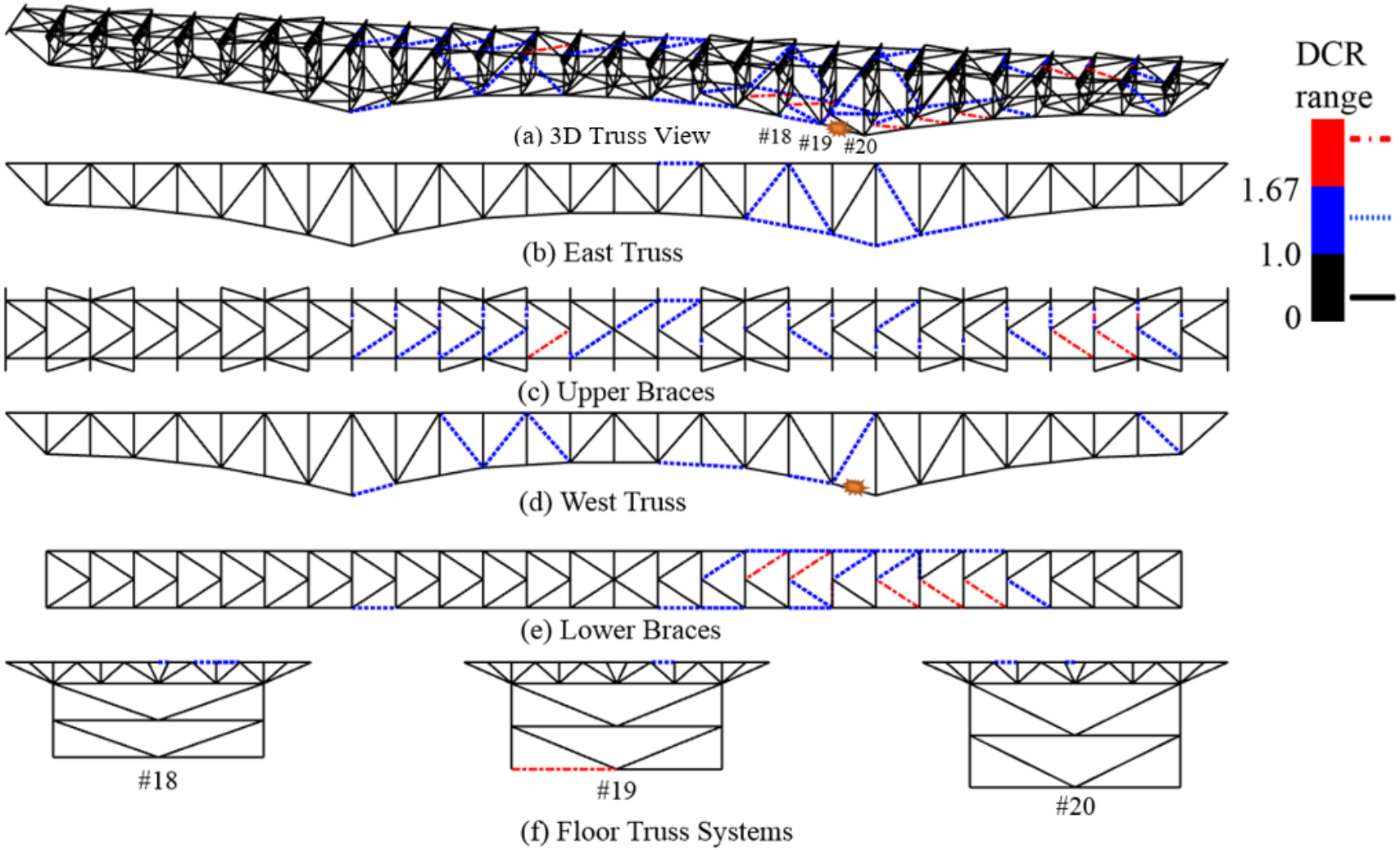

Source: FHWA.

Figure 35. Illustration. *DCR* spectra for the Design Bridge for lower chord MR (MR case 2 in table 20).

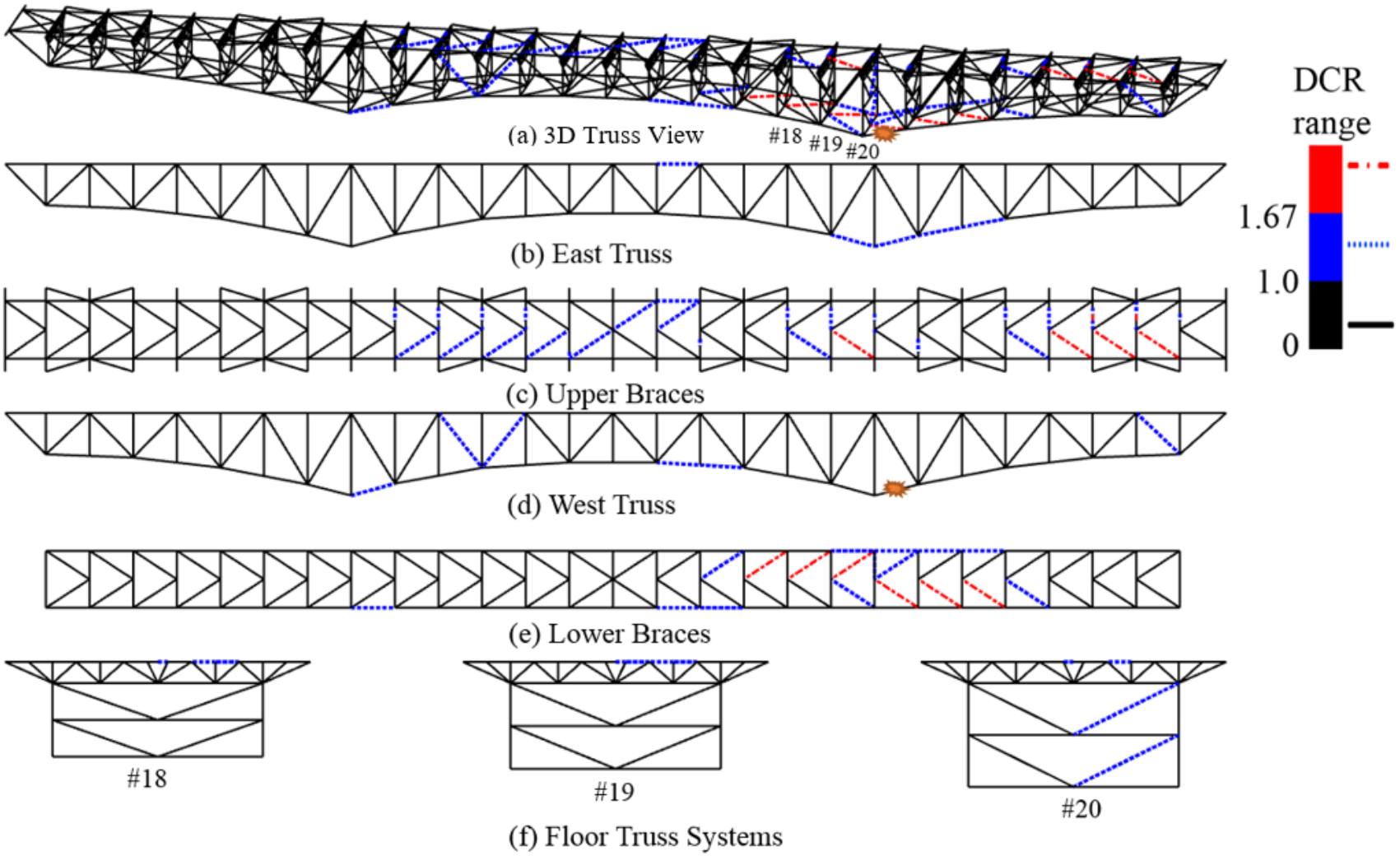

Source: FHWA.

Figure 36. Illustration. *DCR* spectra for the Design Bridge for lower chord MR (MR case 3 in table 20).

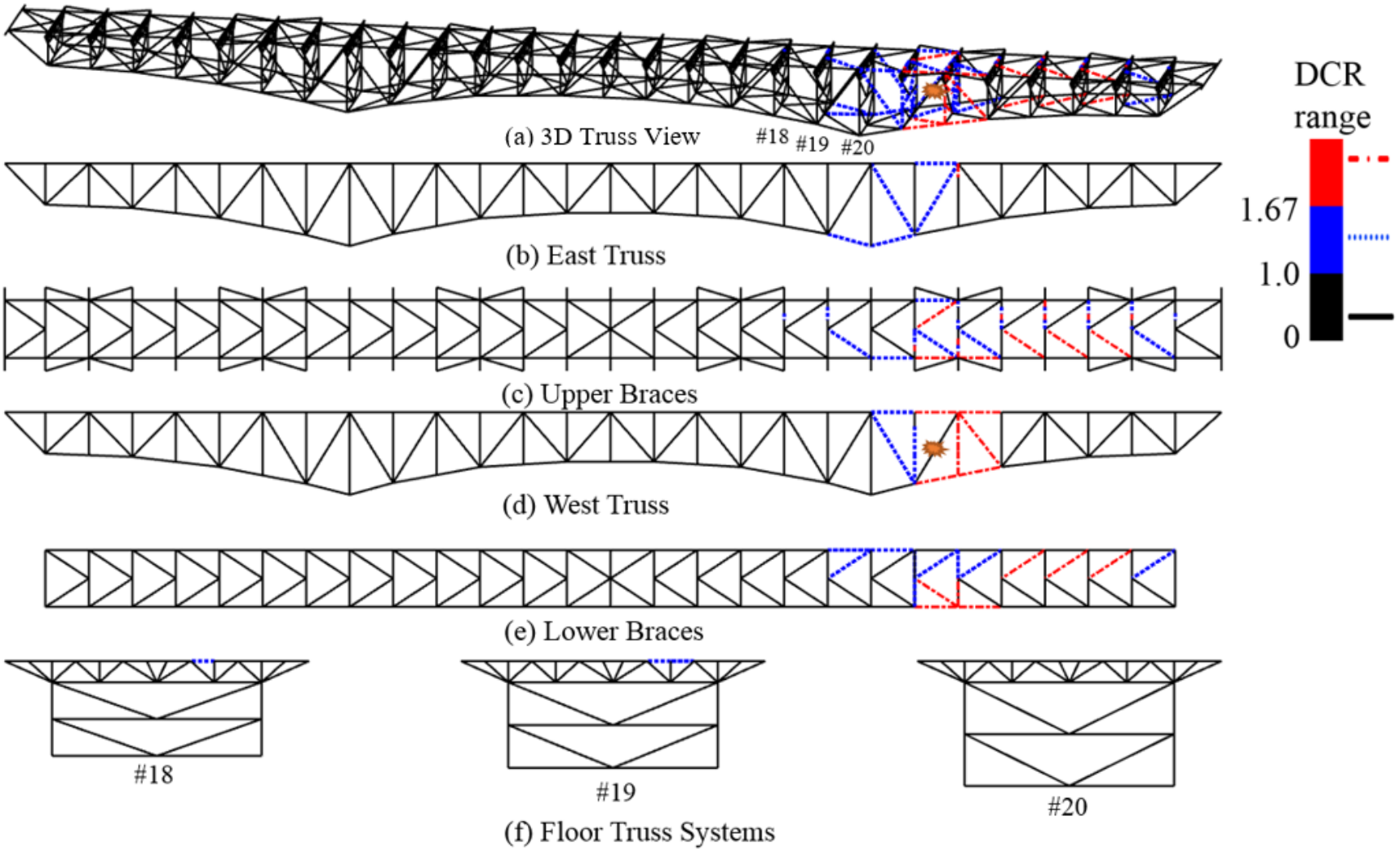

Source: FHWA.

Figure 37. Illustration. *DCR* spectra for the Design Bridge for diagonal member removal (MR case 4 in table 20).

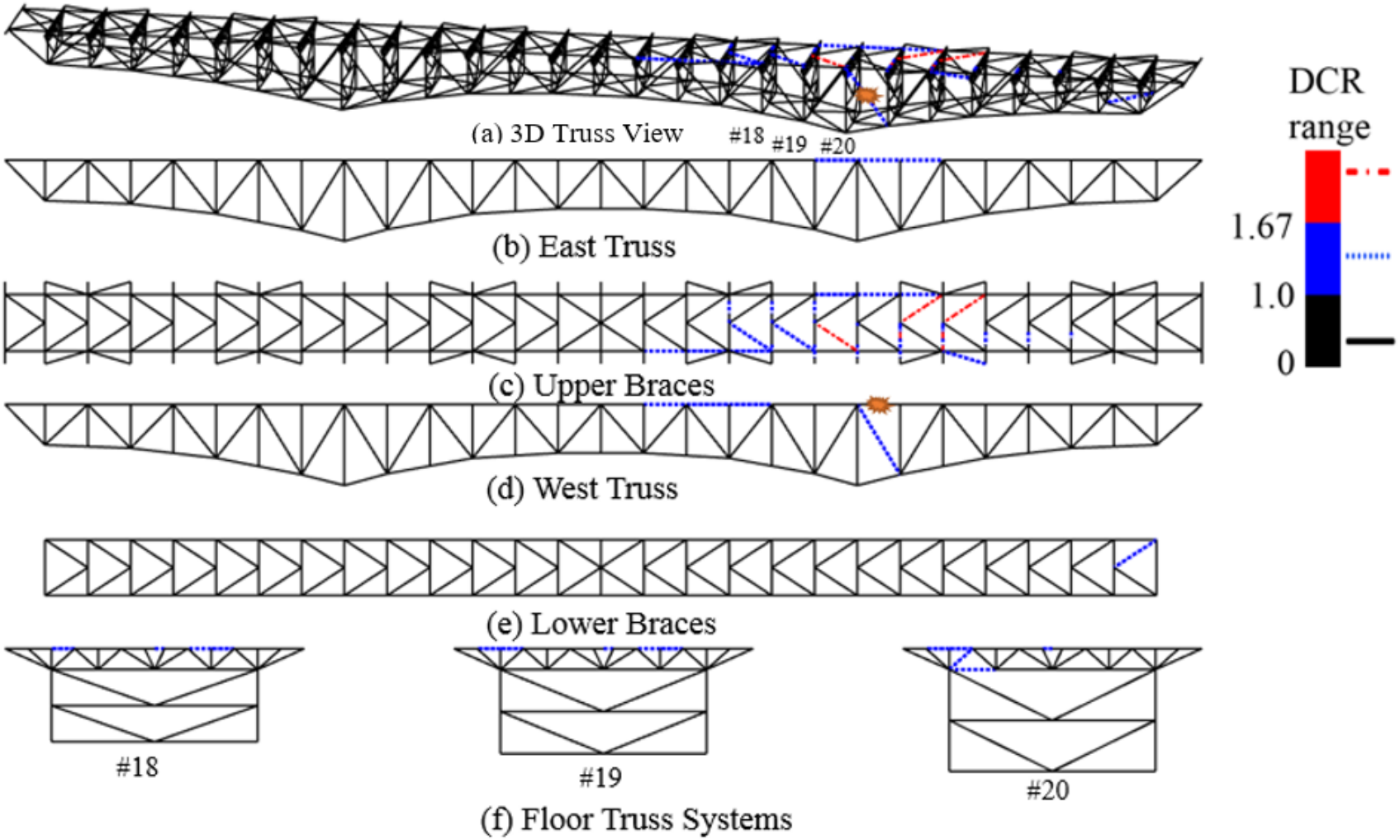

Source: FHWA.

Figure 38. Illustration. *DCR* spectra for the Design Bridge for upper chord MR (MR case 5 in table 20).

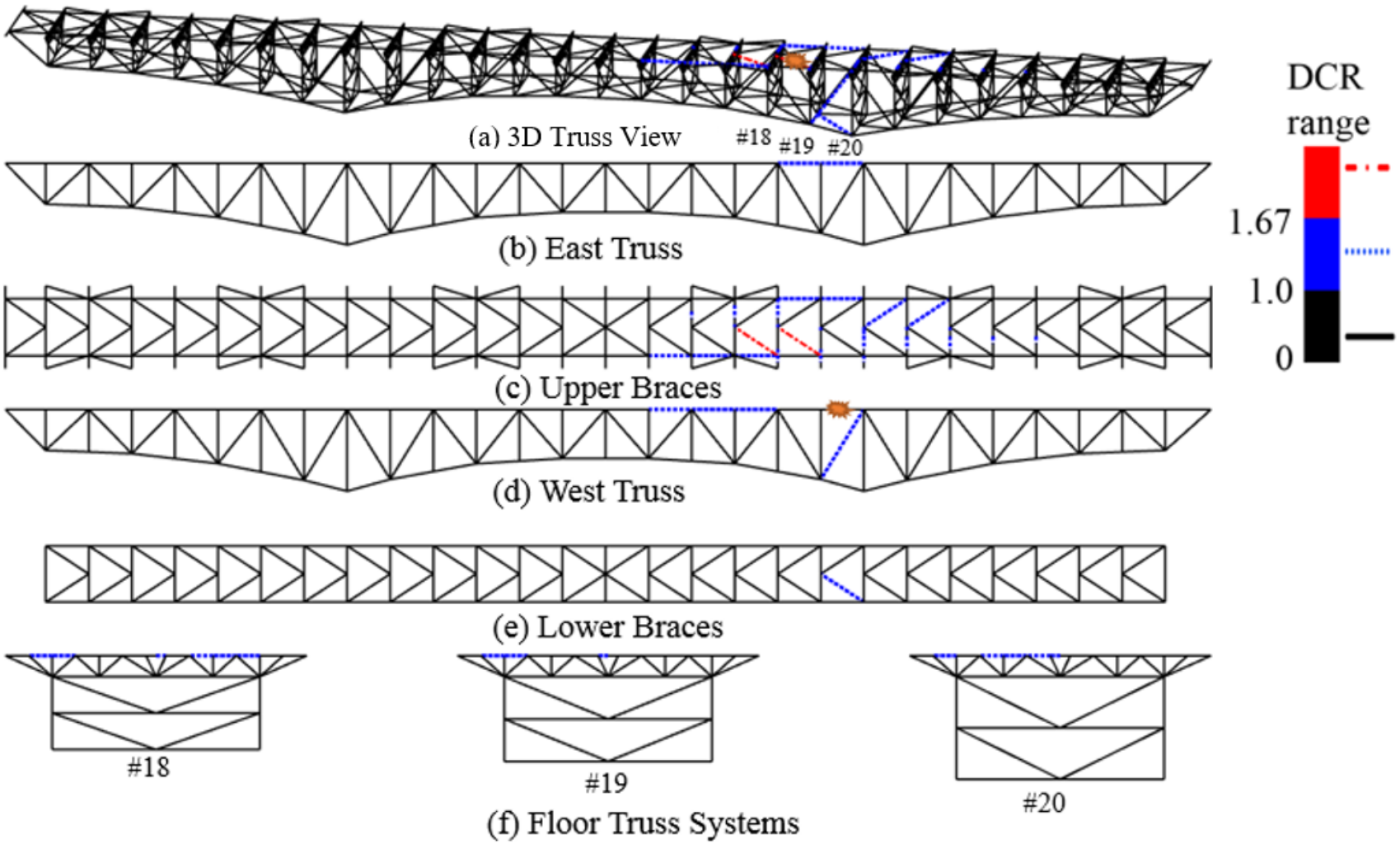

Source: FHWA.

Figure 39. Illustration. *DCR* spectra for the Design Bridge for upper chord MR (MR case 6 in table 20).

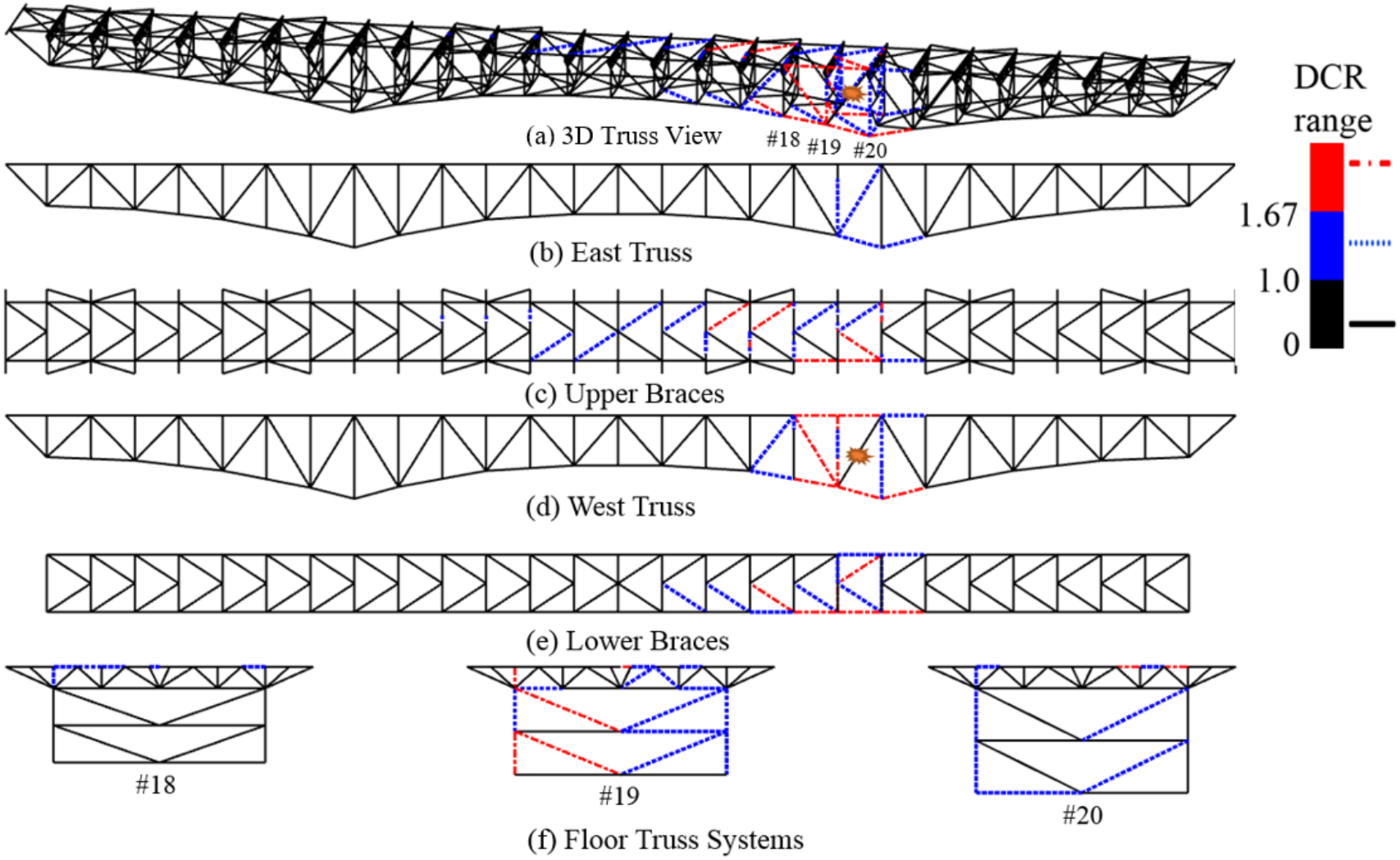

Source: FHWA.

Figure 40. Illustration. *DCR* spectra for the Design Bridge for diagonal member removal (MR case 7 in table 20).

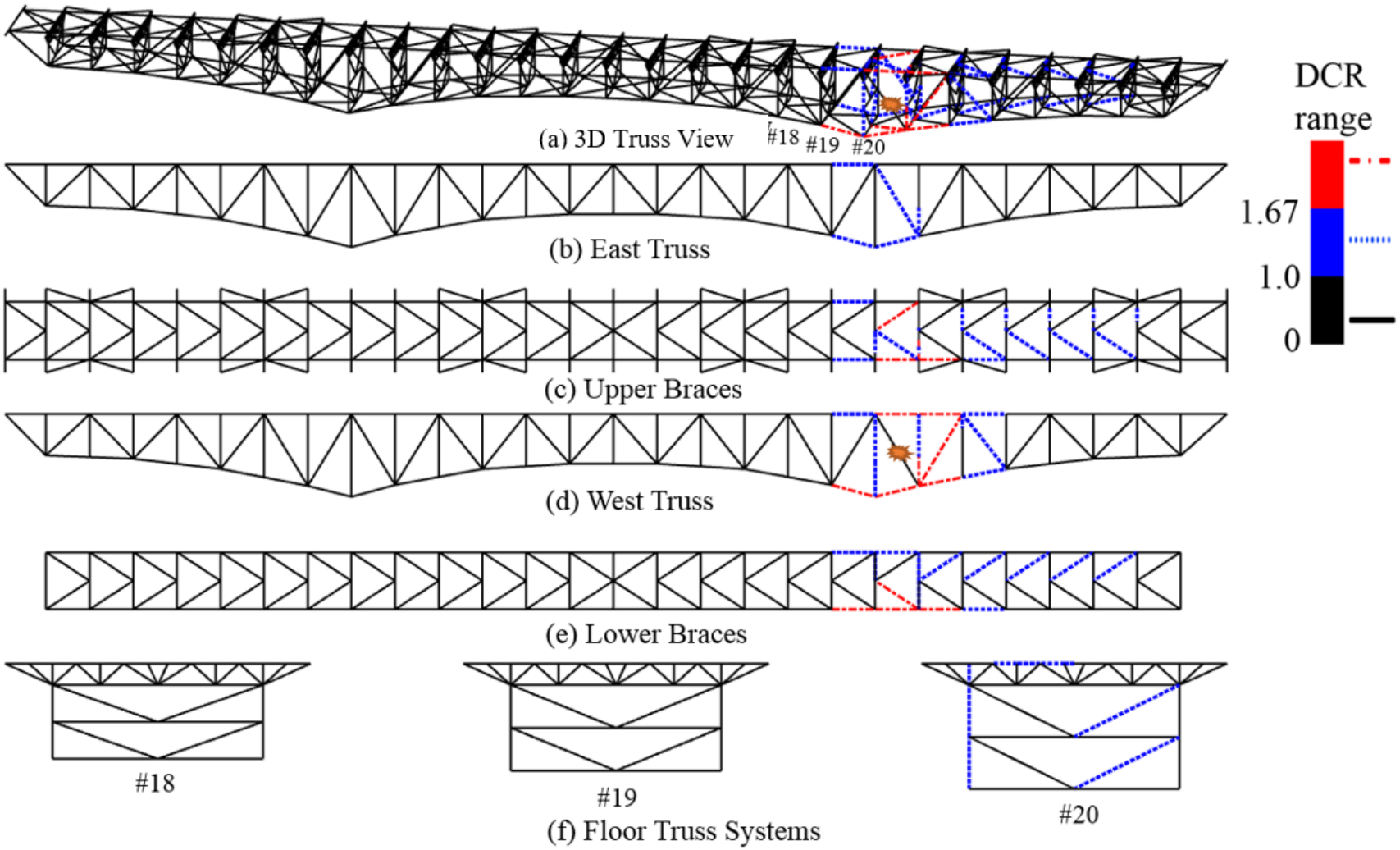

Source: FHWA.

Figure 41. Illustration. *DCR* spectra for the Design Bridge for diagonal member removal (MR case 8 in table 20).

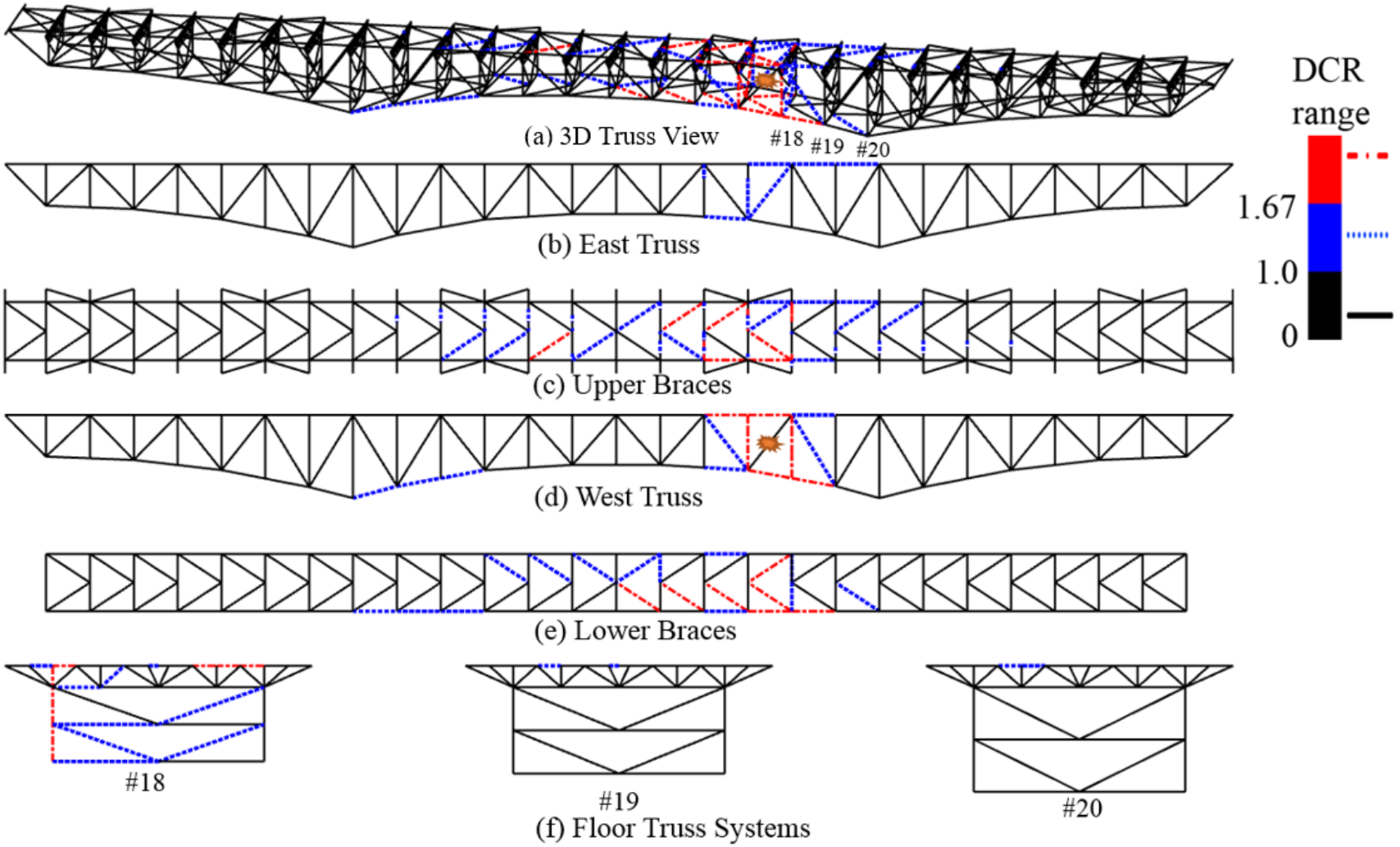

Source: FHWA.

Figure 42. Illustration. *DCR* spectra for the Design Bridge for diagonal member removal (MR case 9 in table 20).

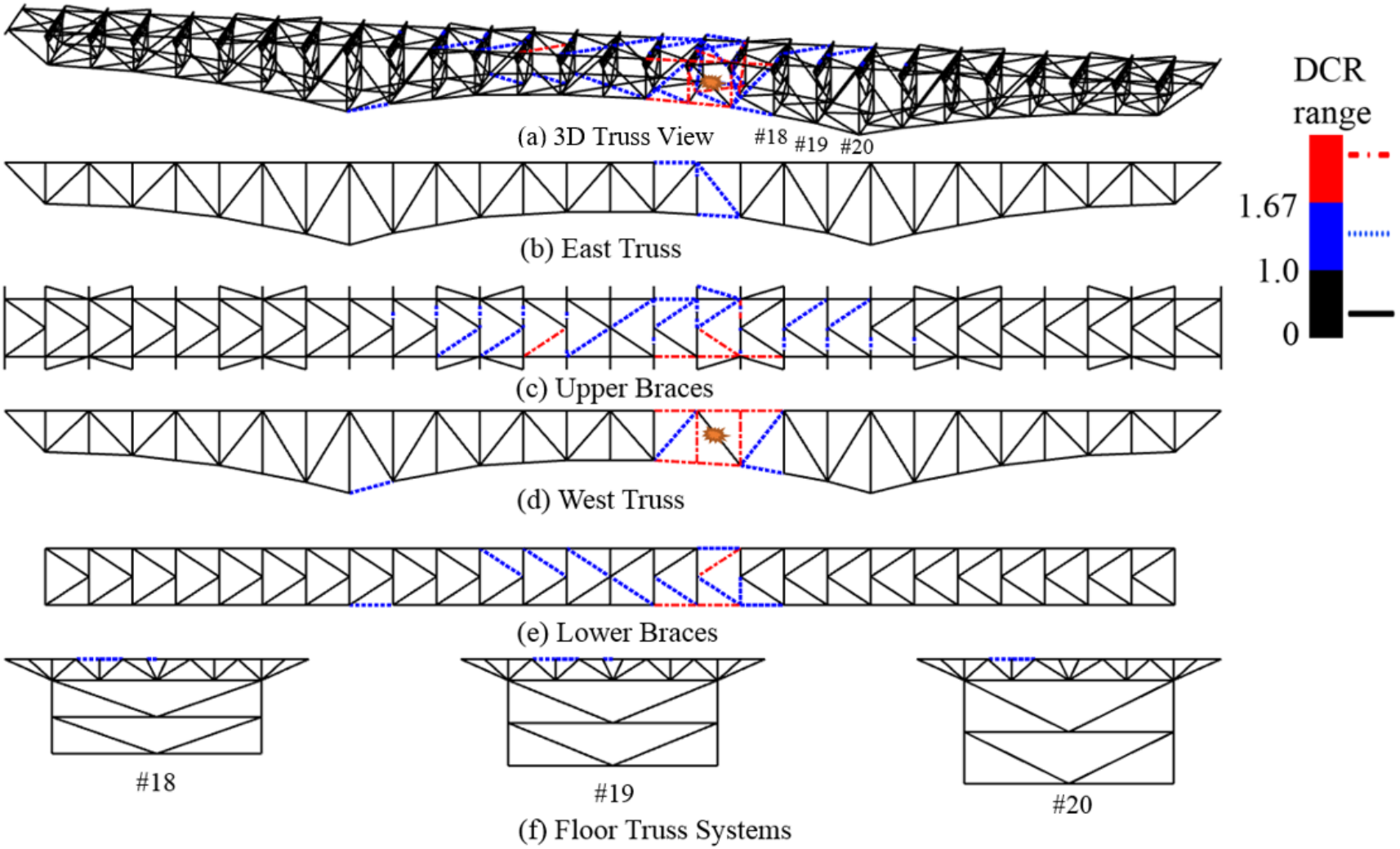

Source: FHWA.

Figure 43. Illustration. *DCR* spectra for the Design Bridge for diagonal member removal (MR case 10 in table 20).

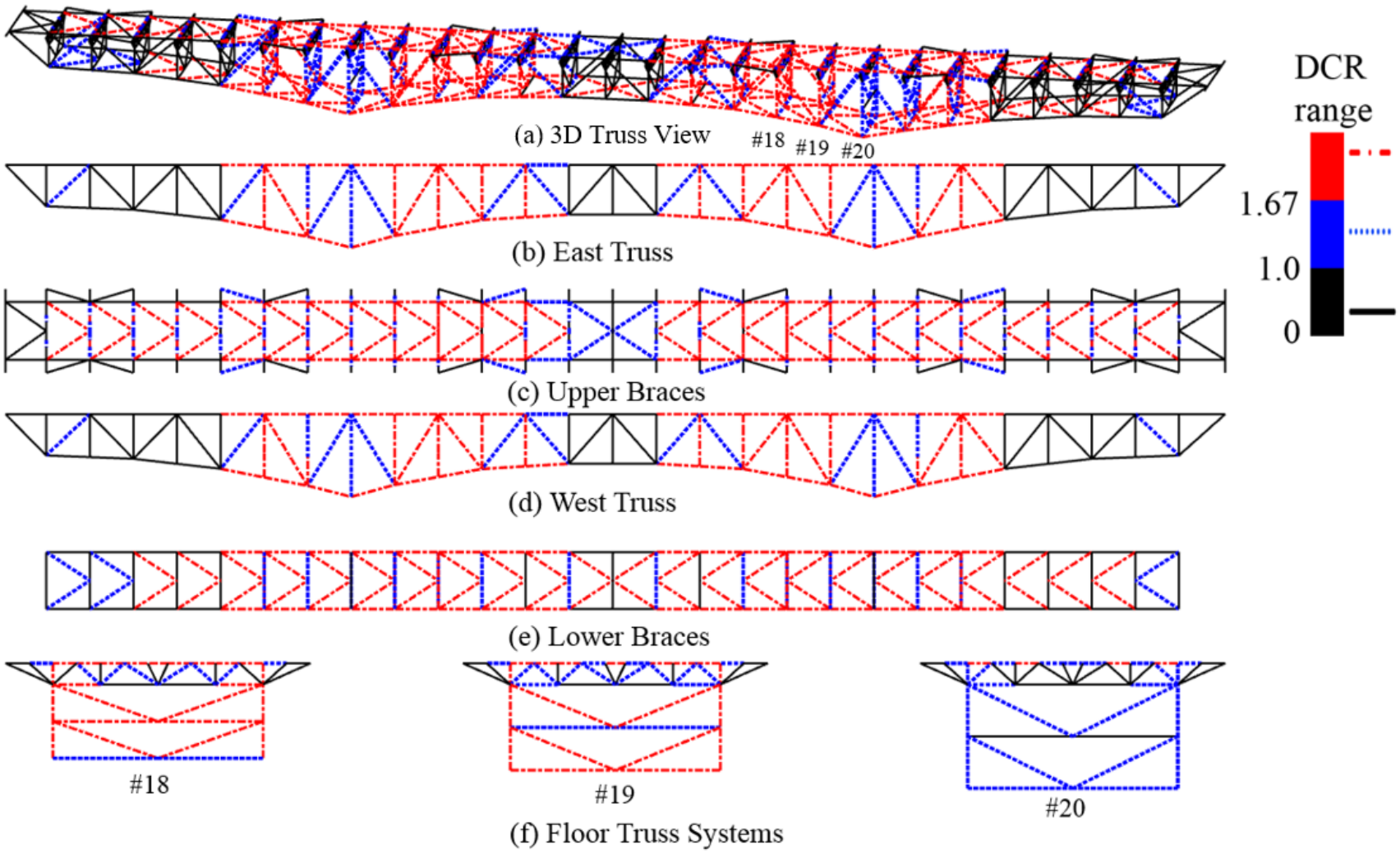

Source: FHWA.

Figure 44. Illustration. Complete envelope of *DCR* for the Design Bridge representing 40 MR cases (10 removal cases in each quarter of the bridge).

ALP (MR) Analysis for Design Bridge: SR Metric

The dynamic response of the structure at the instant of MR can be captured from the time history of forces and displacements in LS-DYNA. For example, figure 45 shows the vertical displacement of node 18 on the west side truss and node 18′ on the east side truss for MR case 1 in table 20. The load combination in this case was $DL + 0.5LL$, and the vertical displacement of nodes 18 and 18′ at the end of DR (about 6 s, when the response of the intact structure because of *DL*s and *LL*s reaches steady state) was 107 mm (4.21 inches). After the DM U18-L19 was removed at 6 s, the entire structure underwent dynamic vibration with a peak dynamic amplitude of 613 mm (24.13 inches) at node 18. However, this vibration was damped out after a few seconds, and the damaged structure (with member U18-L19 removed) gradually reached a new steady state with a steady-state vertical displacement of 504 mm (19.84 inches) at node 18. Although the east side truss also underwent dynamic vibration, the magnitude of vertical displacement was significantly lower, with steady-state displacement of 156 mm (6.14 inches) at node 18′ (compared to 107 mm (4.21 inches) before the MR). Larger permanent displacement on the damaged side (west side) implies that the dynamic effect was significantly larger in the truss with the damaged (removed) member. Larger peak and steady-state vertical displacement in the west side truss (compared to those in the east side truss) also show the bridge's tendency toward torsional rotation about its longitudinal axis.

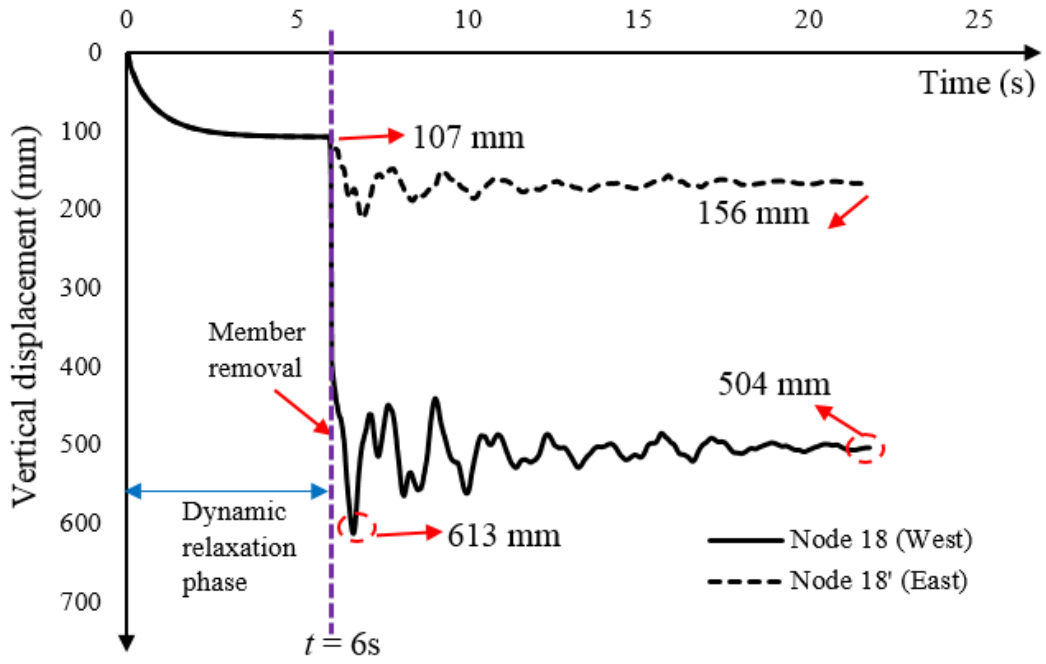

Source: FHWA.
1 mm = 0.0394 inches.

Figure 45. Graph. Nodal vertical displacement in MR case 1.

Figure 46-A and figure 46-B show axial force time histories for lower chord members L17-L18 and L18-L19 in the west side truss and corresponding members L17′-L18′ and L18′-L19′ in the east side truss, respectively. Similar to the displacement time histories in figure 45, the axial forces in members also had dynamic effects. For member L17-L18, the compressive force due to

DL + 0.5*LL* was 3,556 kN (799.1 kips) before the removal of DM U18-L19. After the removal, this force increased to a peak dynamic value of 10,312 kN (2,317.3 kips) before reaching a steady-state value of 6,601 kN (1,483.37 kips). Likewise, the axial force in member L18-L19 increased from 3,556 kN (799.1 kips) to a peak dynamic value of 10,744 kN (2,414.38 kips) before reaching a steady-state value of 7,516 kN (1,689.66 kips). However, axial forces in these members were below the yield limit, although total stress from combined axial and bending stresses was above the yield limit. Figure 46-B shows axial force time histories for lower chord members L17′-L18′ and L18′-L19′ on the east side truss. These two members had a compressive force of 3,664 kN (819.20 kips) before the removal of DM U18-L19 on the west side. Both of these members became unloaded because of the diagonal member removal on the west side. Because the removal of the DM caused a substantial amount of unsymmetrical deformation, in-plane and out-of-plane bending effects cannot be neglected. Figure 47-A and figure 47-B show time history plots of in-plane and out-of-plane moments for lower chord members on the west and east side trusses, respectively. This figure shows that the lower chord members of both trusses experienced a significant amount of moment, especially out-of-plane moment. The combined effect of axial forces and moments caused *SR* to increase beyond 1.0 (i.e., total strain became more than yield strain) around the damaged member, which is discussed further in figure 48.

Figure 48 to figure 57 present the *SR* metric for the 10 MR cases discussed in table 20. The detailed approach for calculating *SR* using the results from LS-DYNA can be found in appendix A. Truss members that had *DCR* values in the range of 1.0 to 1.67 in figure 34 have *SR*s less than 1 in figure 48. These members might have experienced overloading or unloading and may exhibit some hardening rather than linear elastic behavior. However, they are still in the elastic range. Members with *DCR* > 1.67 in figure 34 have *SR*s between 1 and 2 in figure 48, implying that these members underwent yielding. For MR case 2, figure 35 demonstrates that all members of the bridge stayed in elastic range. This is further confirmed from the *SR* metric plots in figure 49 (except for a few braces that show *DCR* > 1.67 in figure 35 but *SR* < 1.0 in figure 49). This observation for MR case 2 is also valid for MR cases 3, 5, and 6. For MR case 4 and cases 7 to 10, members around the damaged member and some of the upper braces, lower braces, and floor truss members have *SR* > 1.0, which implies yielding in these members. Figure 58 shows the complete envelope for the entire bridge based on the *SR* metric. Similar to figure 44, the complete envelope can be used to identify members to be retrofitted to improve ALP of the entire bridge in the event of loss of any member. Members with *SR* > 1.0 in this figure underwent yielding and may need to be retrofitted to ensure no damage in the event of failure of any member of the bridge.

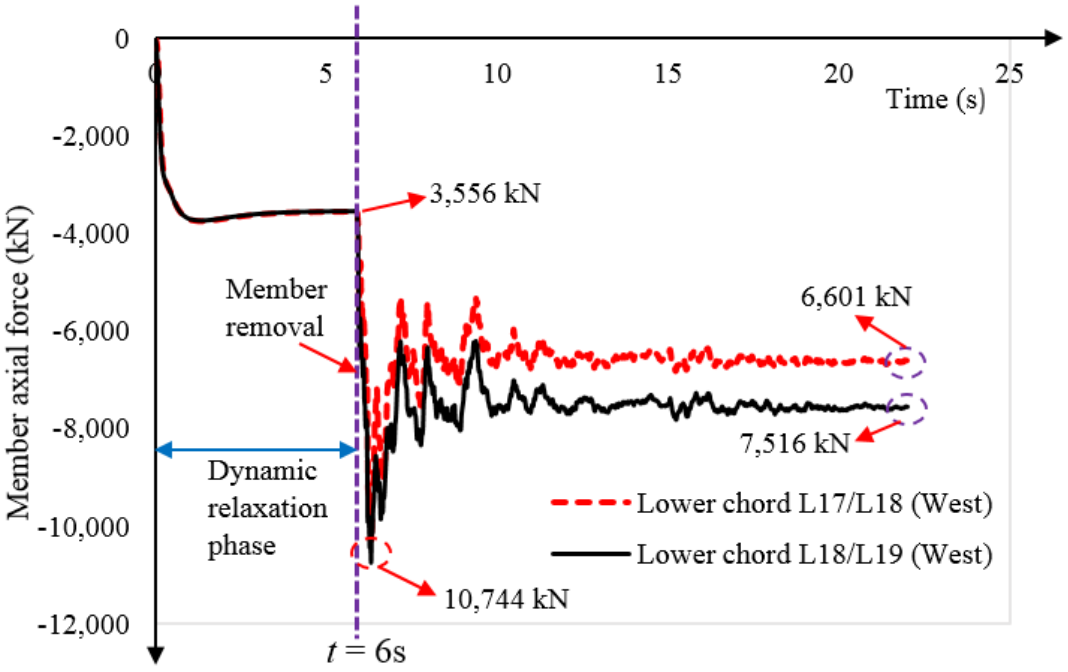

Source: FHWA.
1 kN = 0.225 kips.

A. Lower chord members in the west truss.

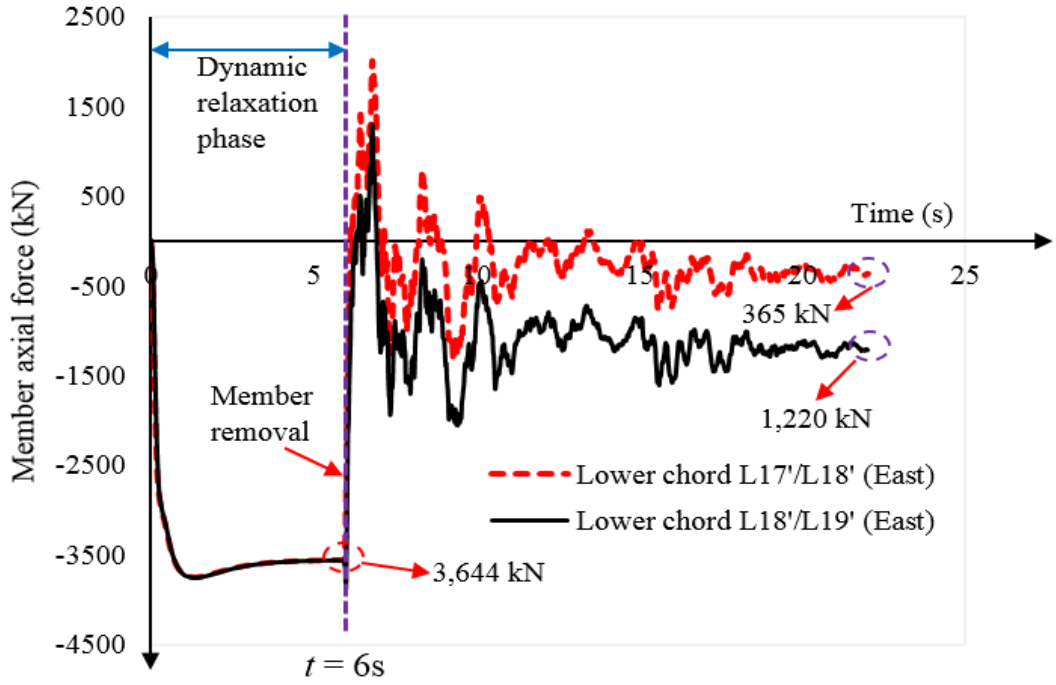

Source: FHWA.
1 kN = 0.225 kips.

B. Lower chord members in the east truss.

Figure 46. Graphs. Axial forces in lower chord members in west and east side trusses of the Design Bridge for MR case 1.

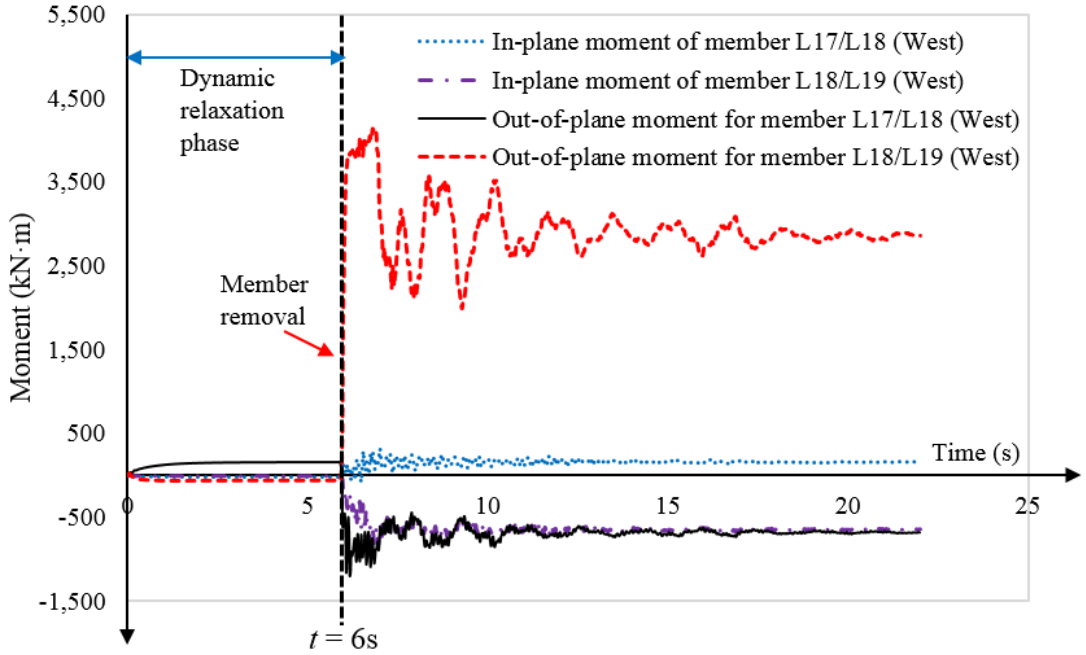

Source: FHWA.
1 kN·m = 23.73 kips·ft.

A. Lower chord members in the west truss.

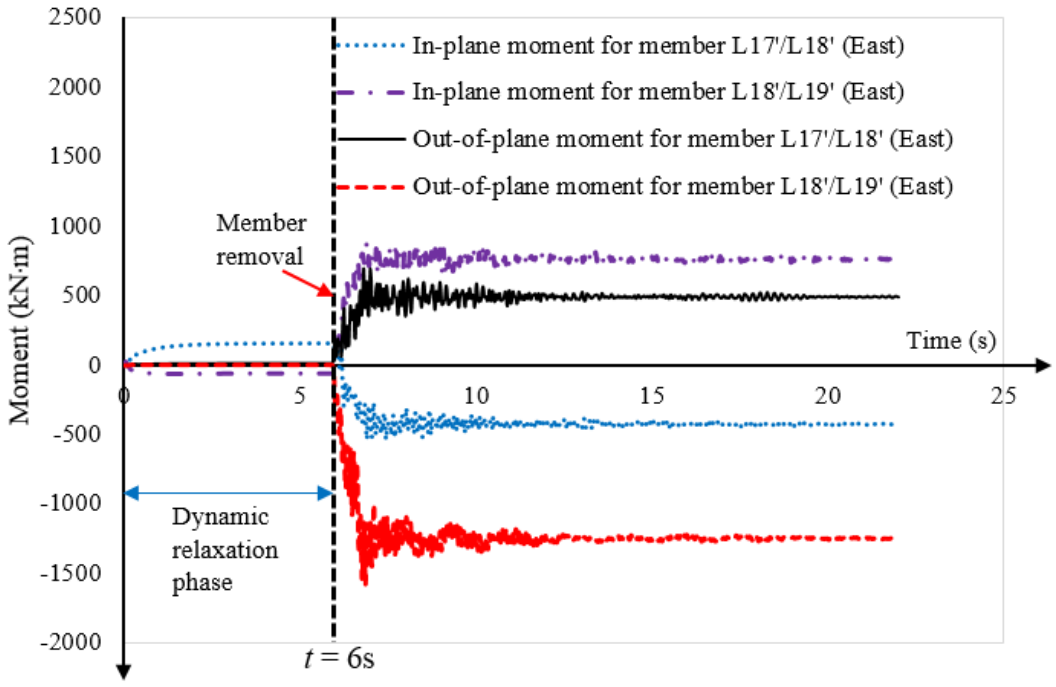

Source: FHWA.
1 kN·m = 23.73 kips·ft.

B. Lower chord members in the east truss.

Figure 47. Graphs. In-plane and out-of-plane moments in lower chord members in west and east side trusses of the Design Bridge for MR case 1.

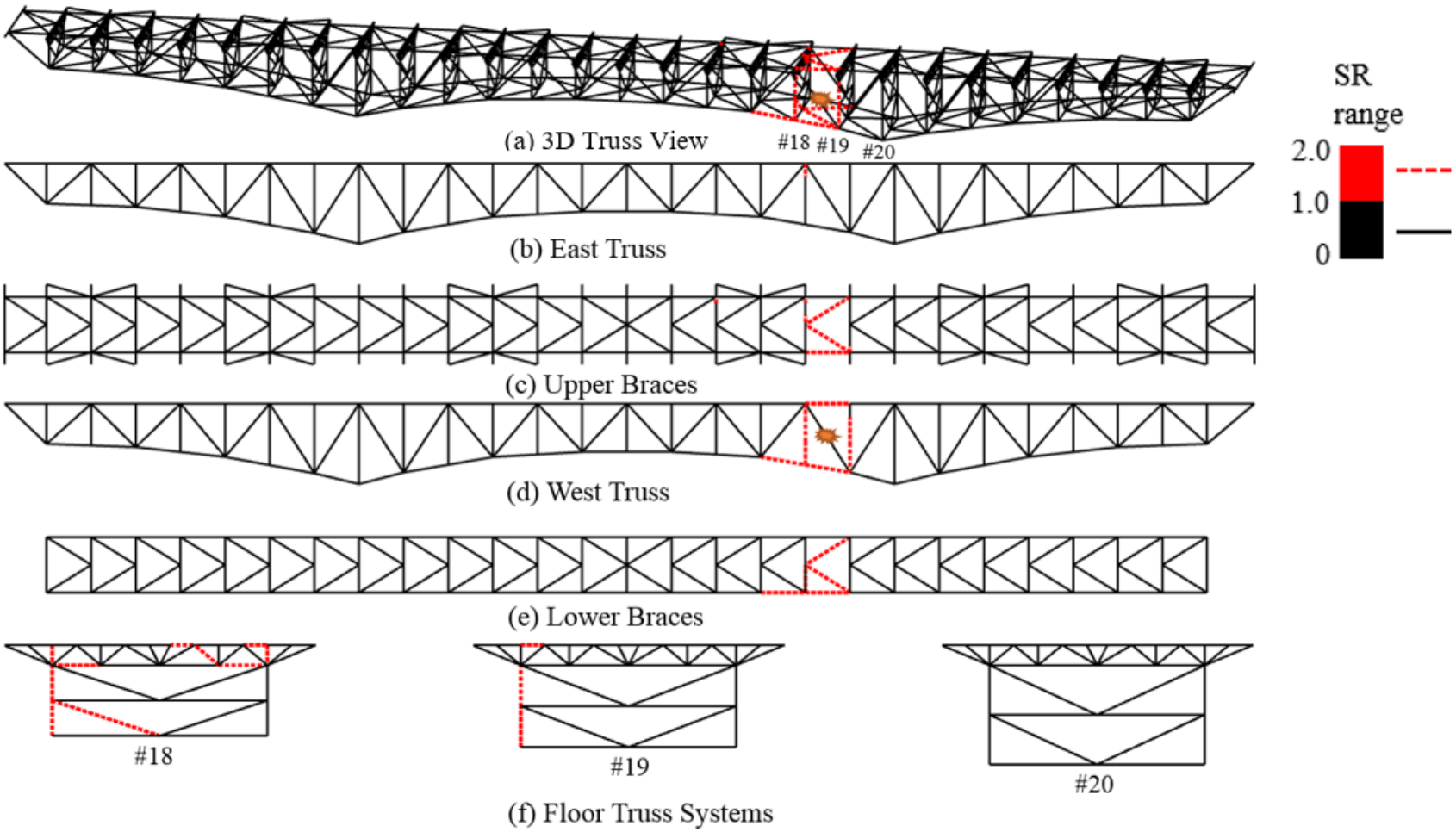

Source: FHWA.

Figure 48. Illustration. *SR* spectra for the Design Bridge for diagonal member removal (MR case 1 in table 20).

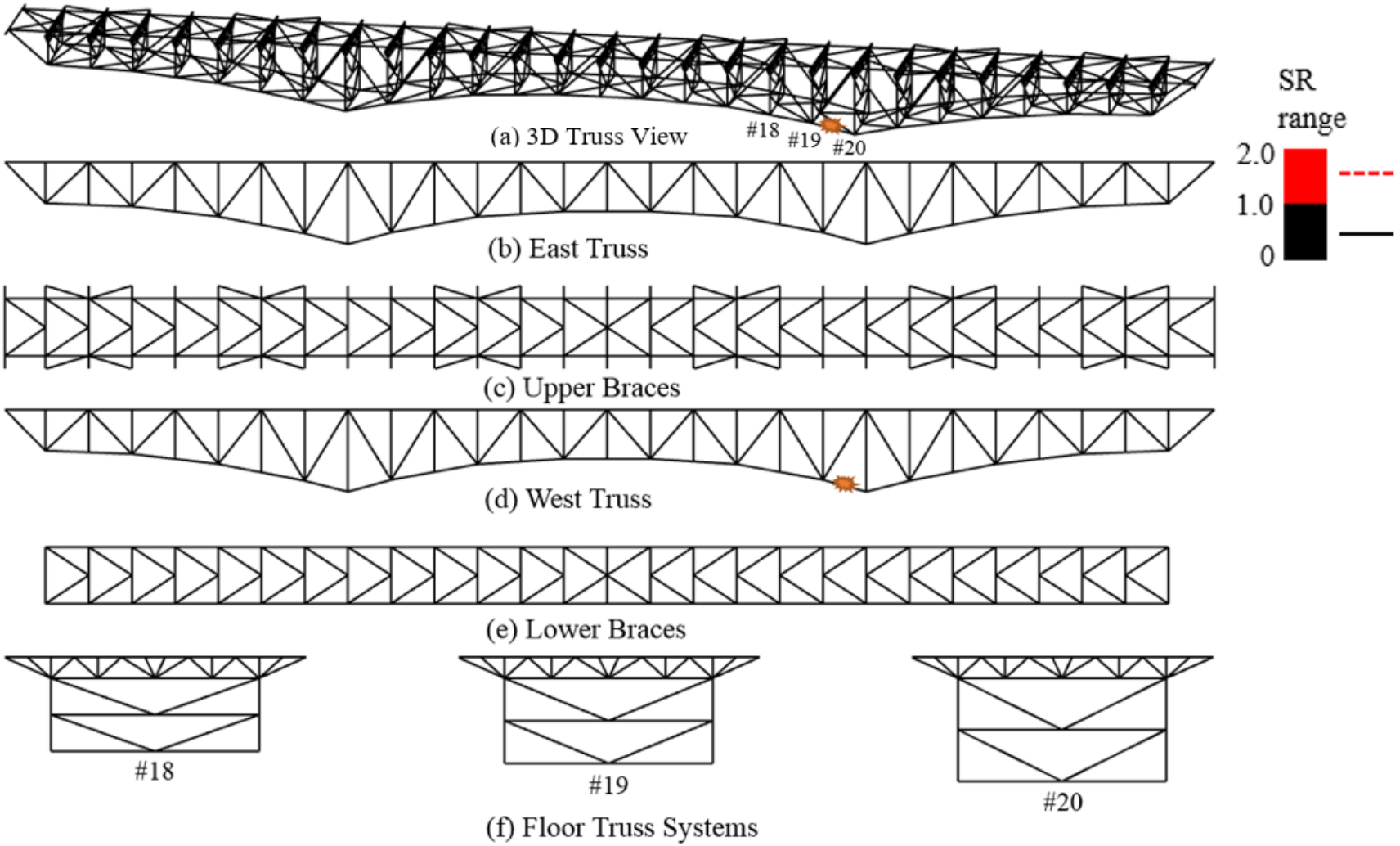

Source: FHWA.

Figure 49. Illustration. *SR* spectra for the Design Bridge for lower chord MR (MR case 2 in table 20).

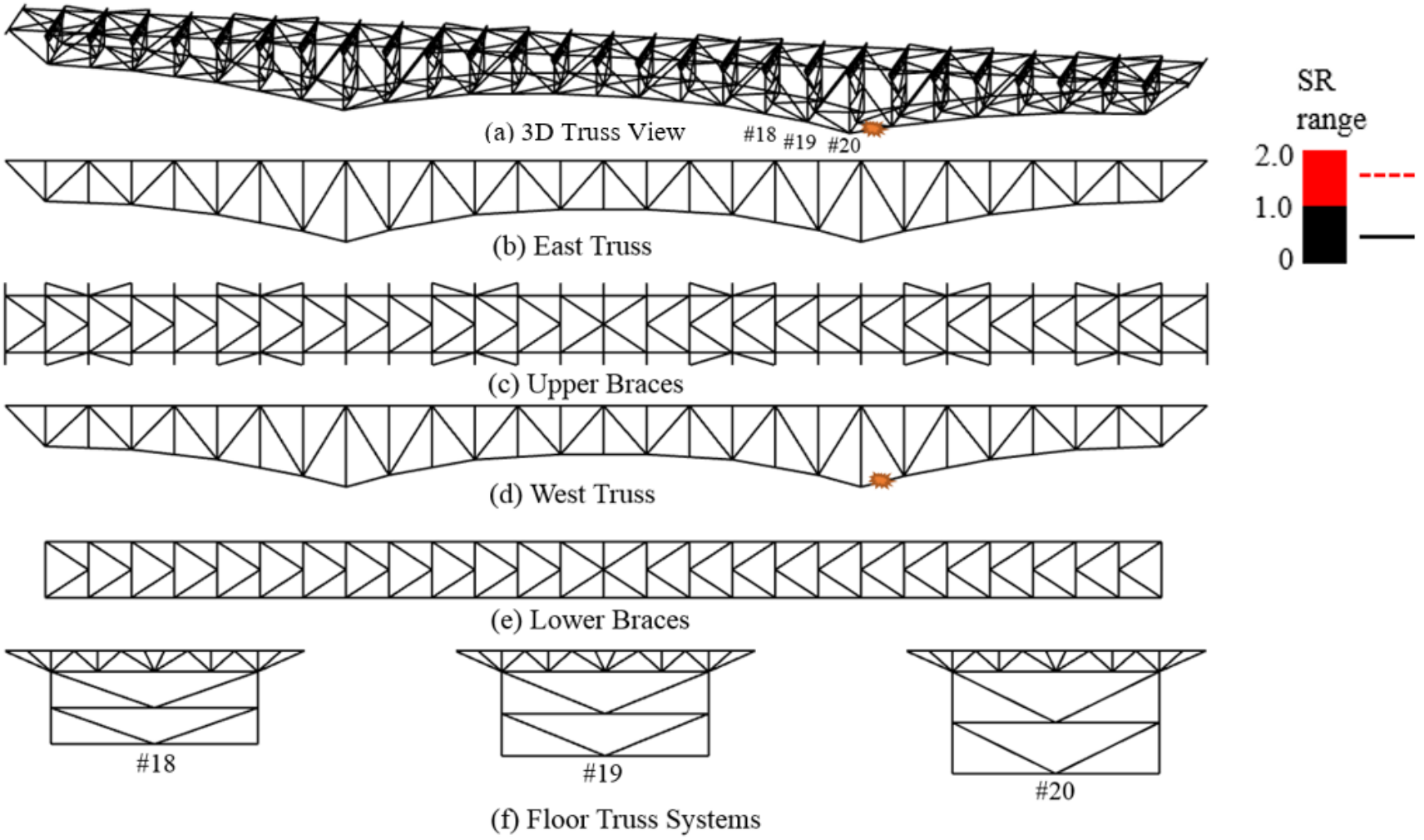

Source: FHWA.

Figure 50. Illustration. *SR* spectra for the Design Bridge for lower chord MR (MR case 3 in table 20).

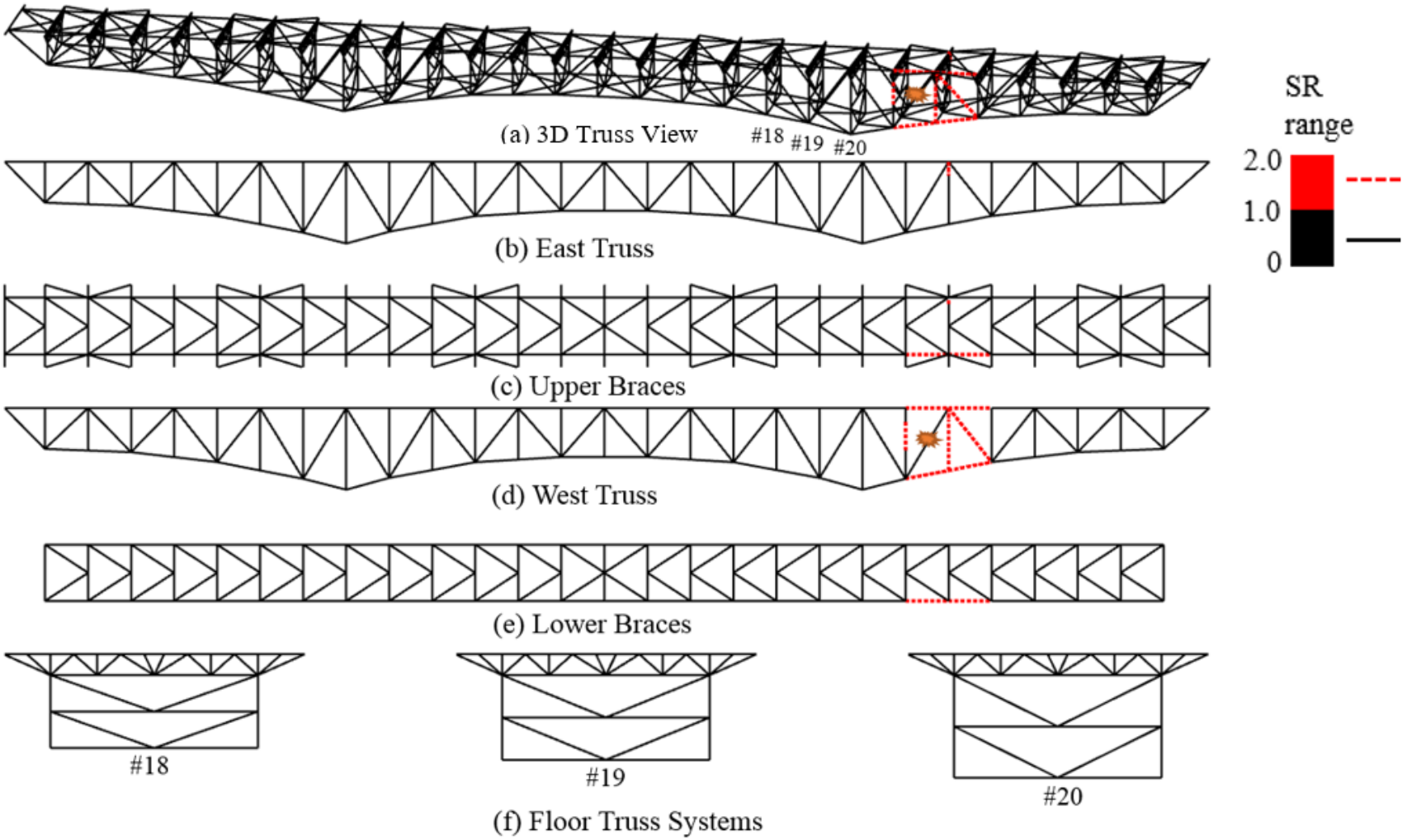

Source: FHWA.

Figure 51. Illustration. *SR* spectra for the Design Bridge for diagonal member removal (MR case 4 in table 20).

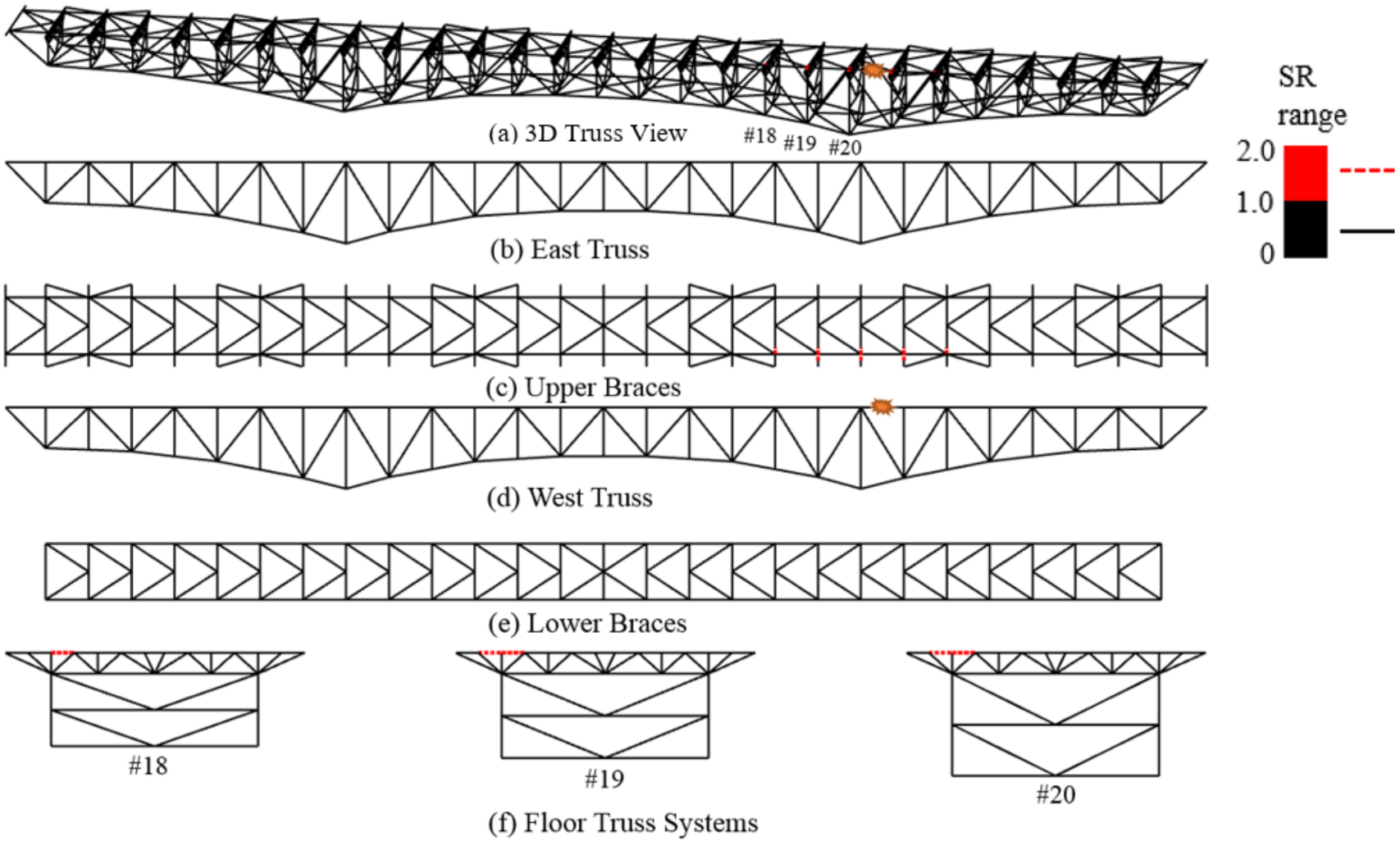

Source: FHWA.

Figure 52. Illustration. *SR* spectra for the Design Bridge for upper chord MR (MR case 5 in table 20).

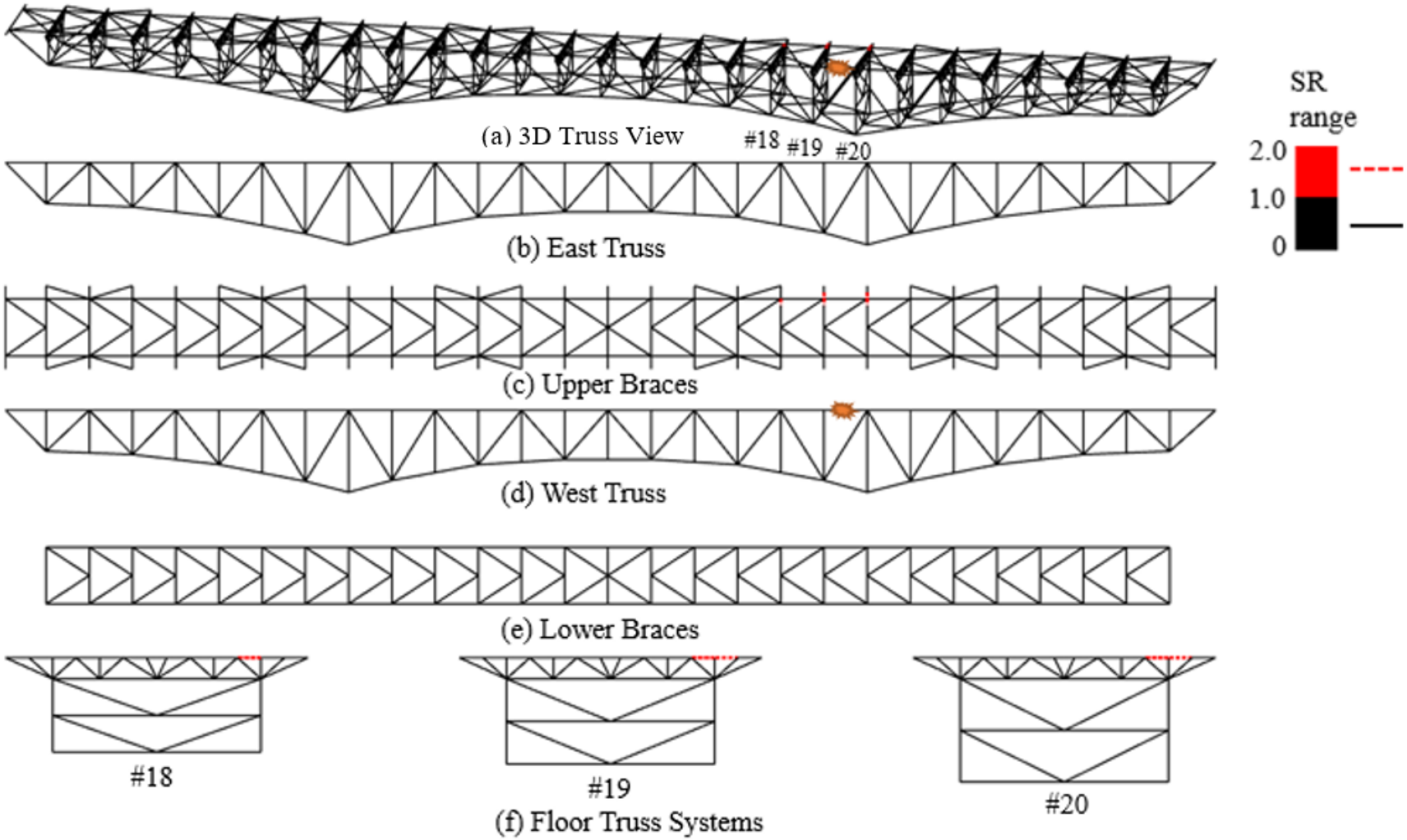

Source: FHWA.

Figure 53. Illustration. *SR* spectra for the Design Bridge for upper chord MR (MR case 6 in table 20).

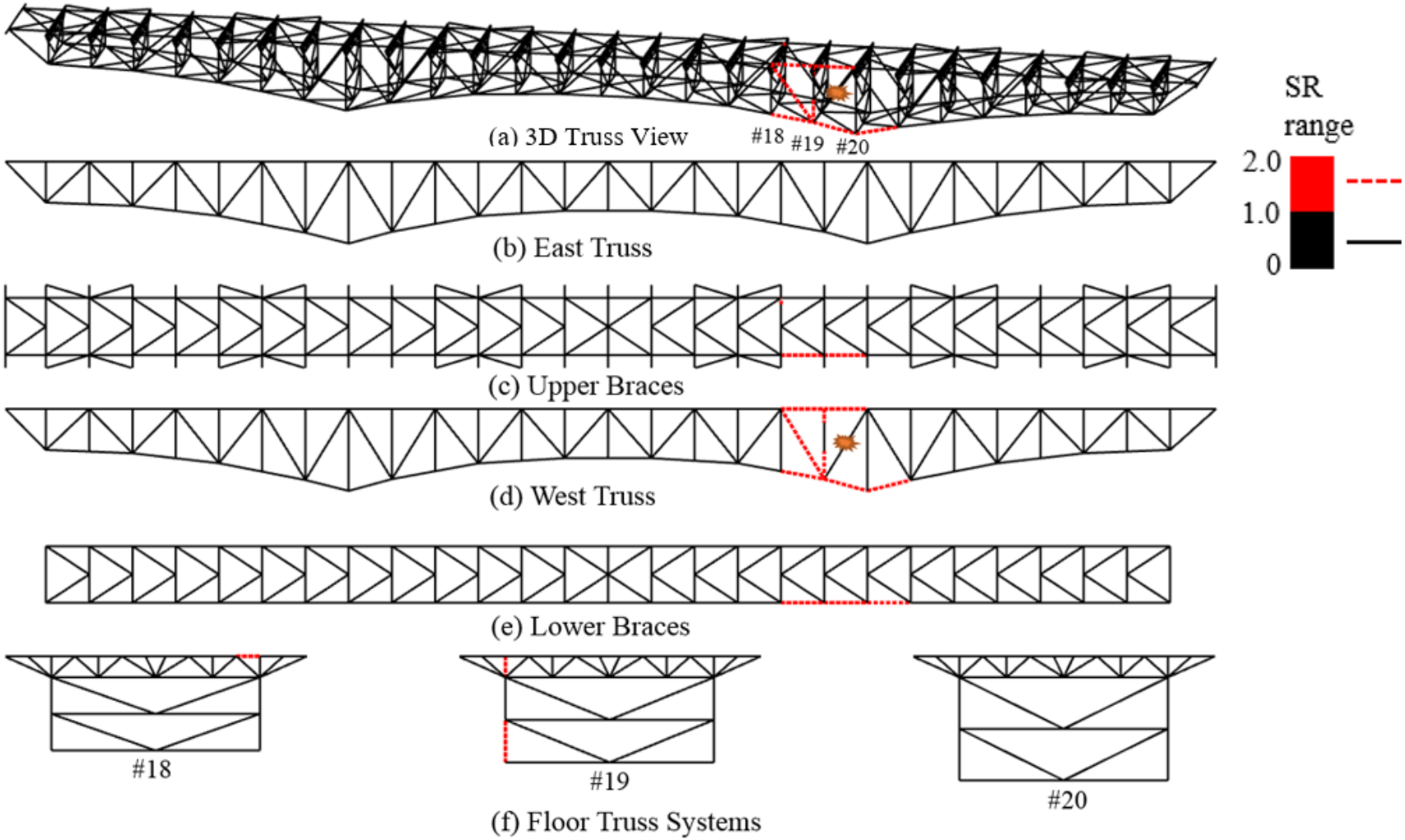

Source: FHWA.

Figure 54. Illustration. *SR* spectra for the Design Bridge for diagonal member removal (MR case 7 in table 20).

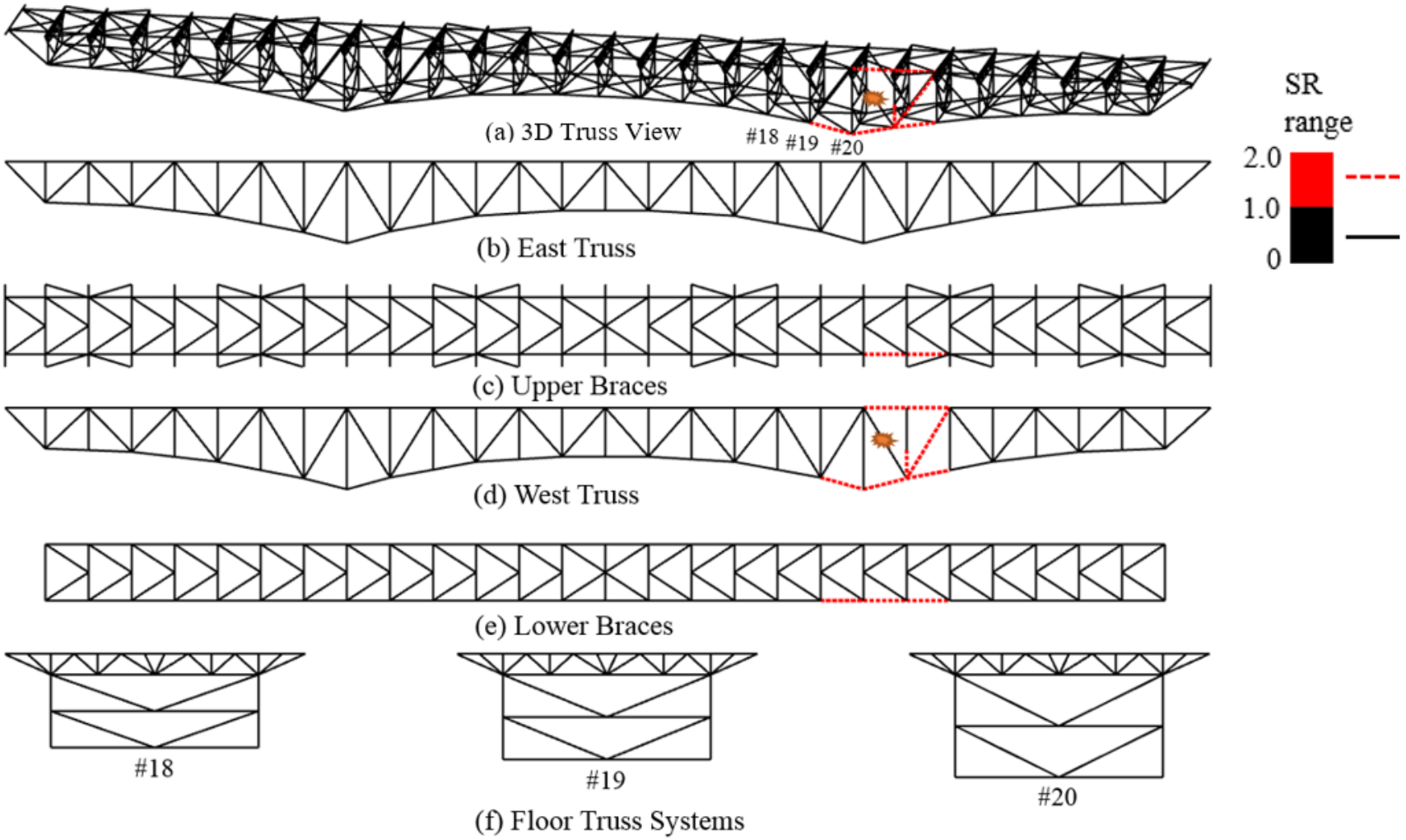

Source: FHWA.

Figure 55. Illustration. *SR* spectra for the Design Bridge for diagonal member removal (MR case 8 in table 20).

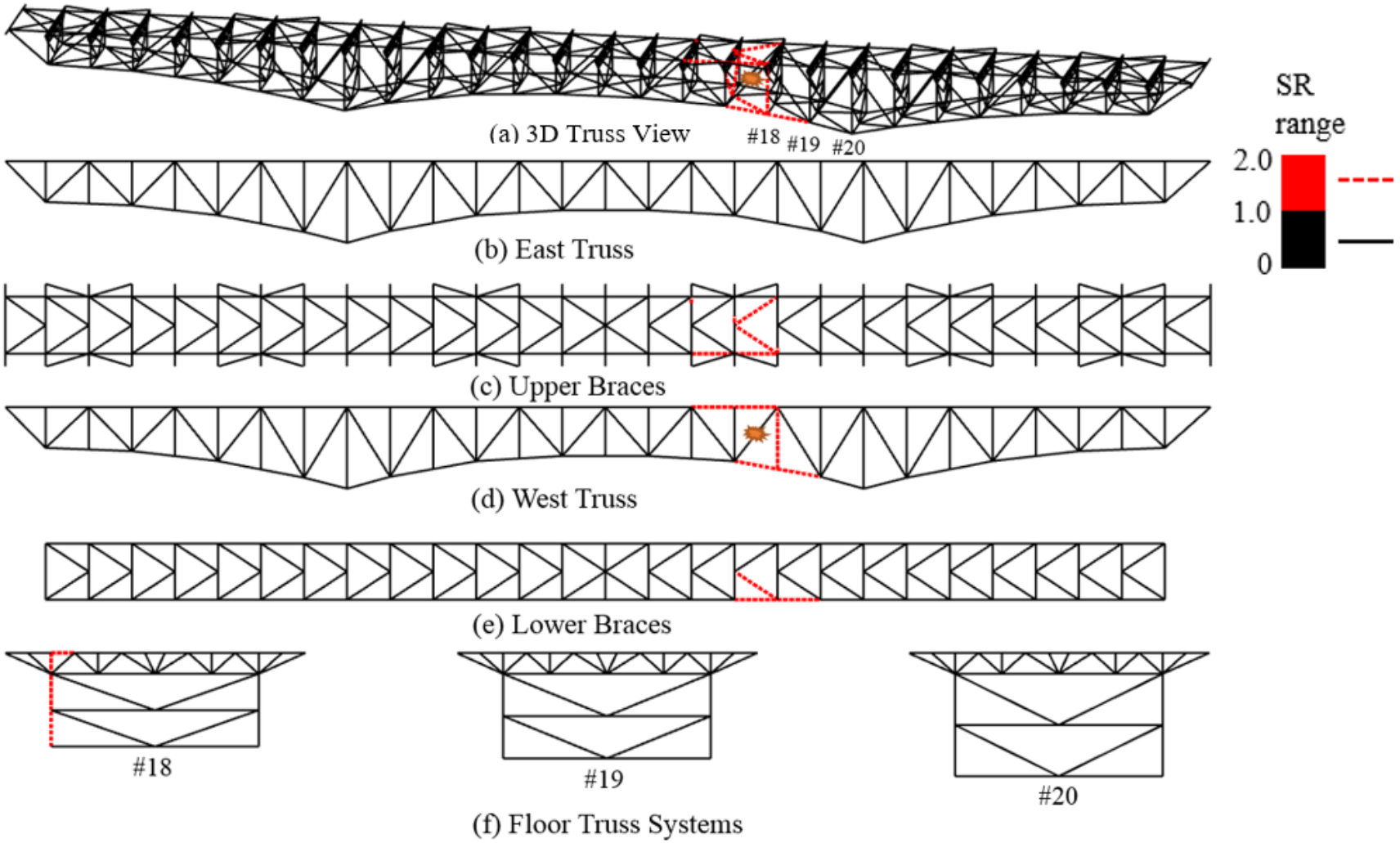

Source: FHWA.

Figure 56. Illustration. *SR* spectra for the Design Bridge for diagonal member removal (MR case 9 in table 20).

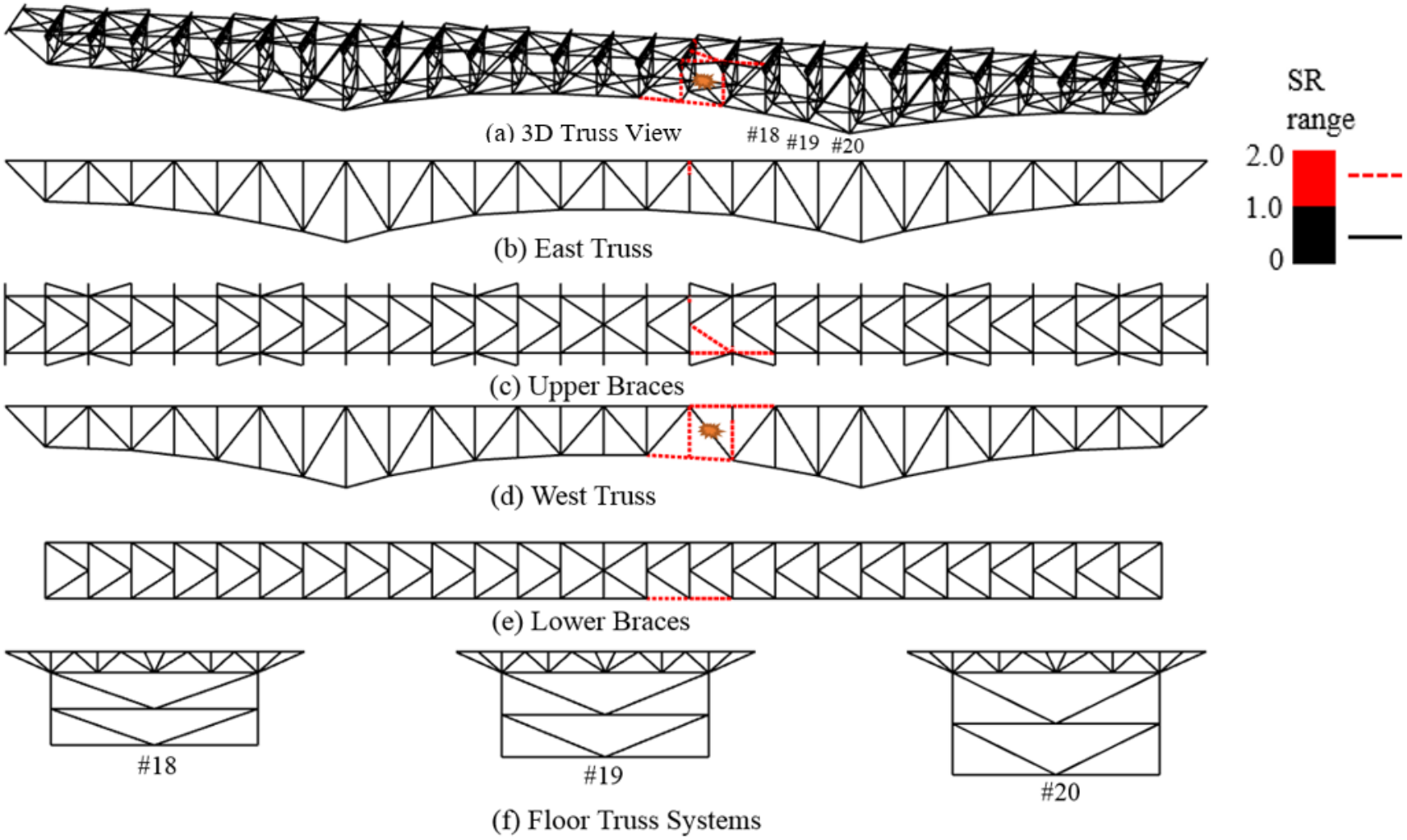

Source: FHWA.

Figure 57. Illustration. *SR* spectra for the Design Bridge for diagonal member removal (MR case 10 in table 20).

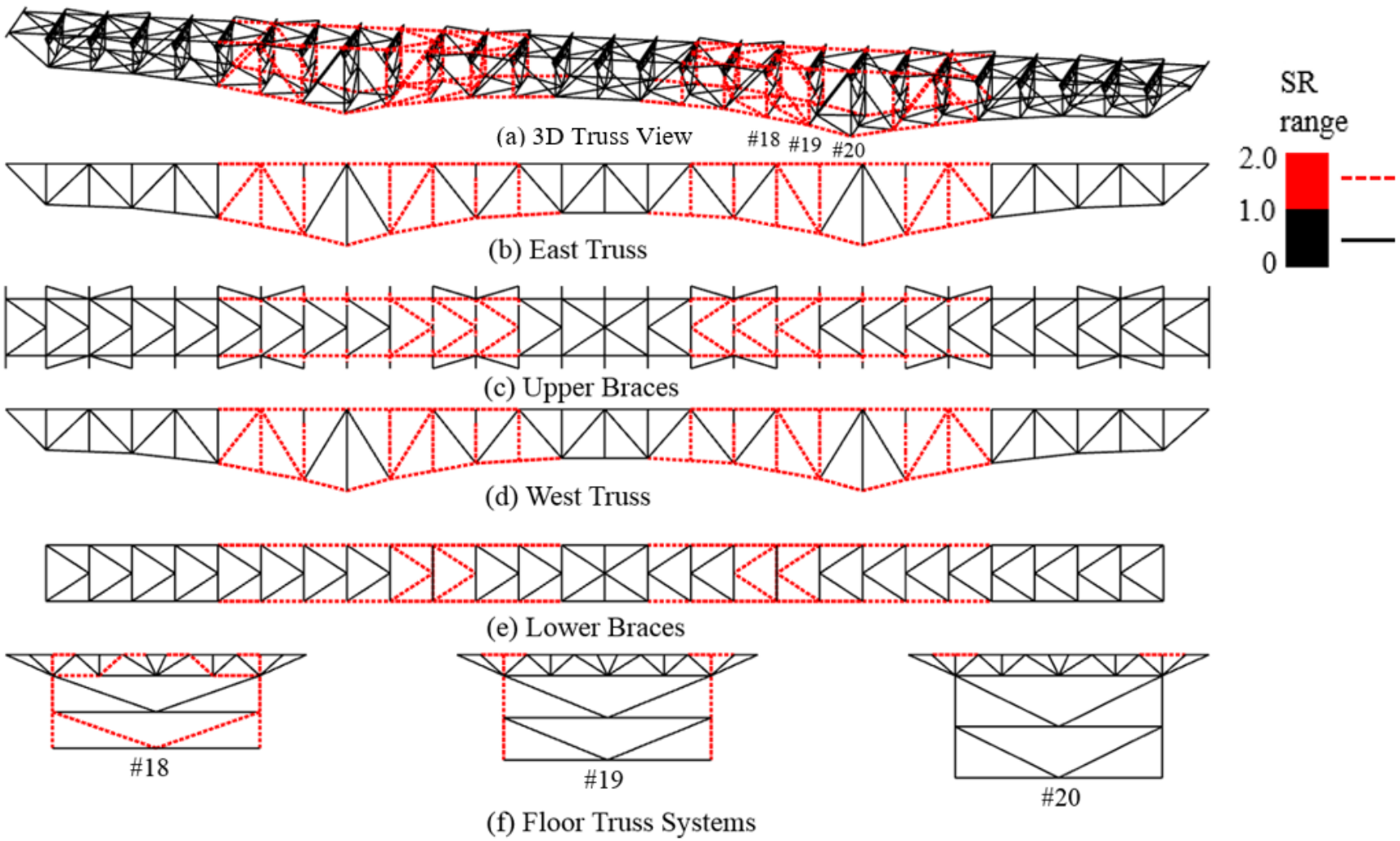

Source: FHWA.

Figure 58. Illustration. Complete envelope of *SR* for the Design Bridge representing 40 MR cases (10 removal cases in each quarter of the bridge).

Dual Member Removal Event

Actual simulation of blast loads requires finer mesh of the FEM and simulating blast loading using either *Mat-High-Explosive-Burn card in LS-DYNA or software such as ConWep (which is labeled distribution statement C) (Kingery and Bulmash 1984; Randers-Pehrson and Bannister 1997). Use of this software was beyond the scope of this project. Hence, an alternate approach was used to simulate the effect of the blast load.

Generally, a blast load results in the loss of several members of a truss within a certain zone, depending on the location of the blast and the amount of TNT used. In this research, blast load effect was represented by dual member removal (DMR), which is defined here as loss of one diagonal and one lower chord member because it has been observed that the loss of vertical and upper chord members has a lesser effect on the safety of the truss system. However, this approach is only a crude approximation to simulate the effect of blast loading. More research is needed to find the correlation between the blast load parameters (location, amount of TNT used), number of members lost, and impact on the number of bays in any truss.

Figure 59 shows the six cases for DMR. For the sake of comparison with MR cases, these six cases are numbered as 1, 2, 3, 4, 9, and 10, as illustrated in figure 59. In each case, one diagonal and one lower chord member was selected for removal in one-quarter of the bridge. Effects of these six cases on ALP of the bridge were investigated by both *DCR* and *SR* metrics. MR cases 5 and 8 in figure 31 were combined as case 3 of DMR because removal of upper chord members had negligible effect. Similarly, MR cases 6 and 7 in figure 31 were combined as case 2 of DMR. Hence, there were 6 unique cases of DMR in total for comparison to the 10 cases of MR investigated previously.

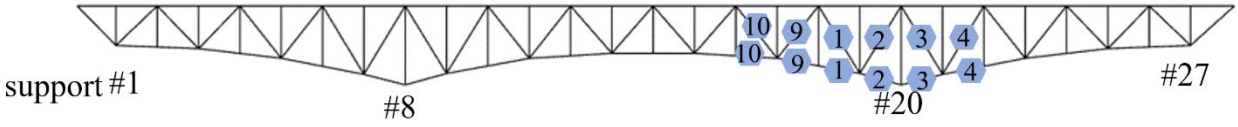

Source: FHWA.

Figure 59. Illustration. Cases of critical DMR in one-quarter of the bridge on the west side truss.

ALP (DMR) Analysis for Design Bridge: DCR Metric

Figure 60 shows the *DCR* before and after the removal of two members in DMR case 1. This figure demonstrates that the *DCR* after DMR increased significantly in west side truss members (where the dual members were removed). The increase in *DCR* was less in the east side truss members. Figure 60 also shows that the load path in the lower chord was completely disrupted because of DMR. Thus, loads designed to be transferred through the lower chord members to the support were detoured through the upper chord members to the FS via verticals.

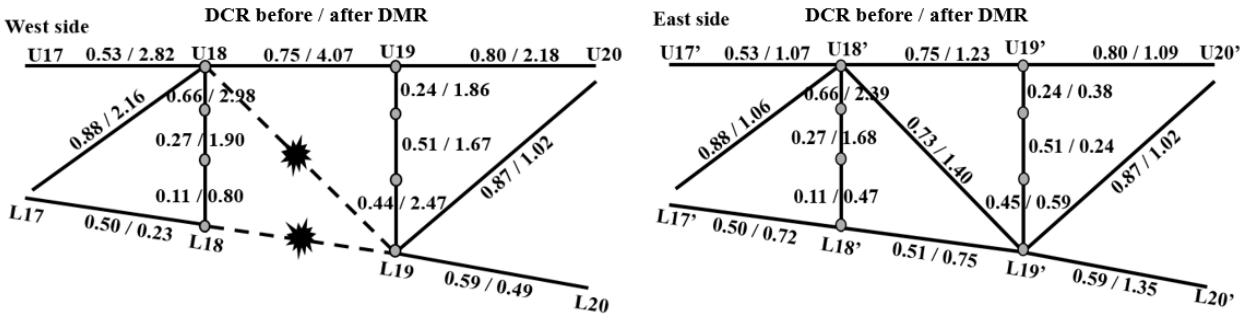

Source: FHWA.

Figure 60. Illustration. *DCR* before and after DMR case 1 near the damaged location in west and east side trusses.

Figure 61 shows the contributions of axial force and in-plane and out-of-plane moments to the *DCR* for DMR case 1. For example, for member L17-L18 in the west side truss, "1 83 16" implies 1-, 83-, and 16-percent contributions of axial force, M_{in}, and M_{out} to the *DCR*, respectively. Numbers above the member denote these contributions before DMR, and numbers below the member represent contributions after DMR. It is observed that the axial force contributed predominantly (86 percent) to the *DCR* of member L17-L18 before DMR. However, after DMR, M_{in} contributed predominantly (83 percent) to the *DCR*, and the contribution of axial force was reduced to 1 percent. This effect (change from axial to bending) was more prominent in lower chord members in the west side truss. Hence, lower chord members in the west side truss may be seriously distorted because of the DMR. Because the west side truss lost greater load-carrying capacity, members of the east side truss started carrying more load through axial force rather than bending. As a result, the increase in bending in the lower chord members of the east side truss after MR was less than that for the single MR case 1 in table 20. These results show that the load redistribution in the east side truss occurred over a broader range.

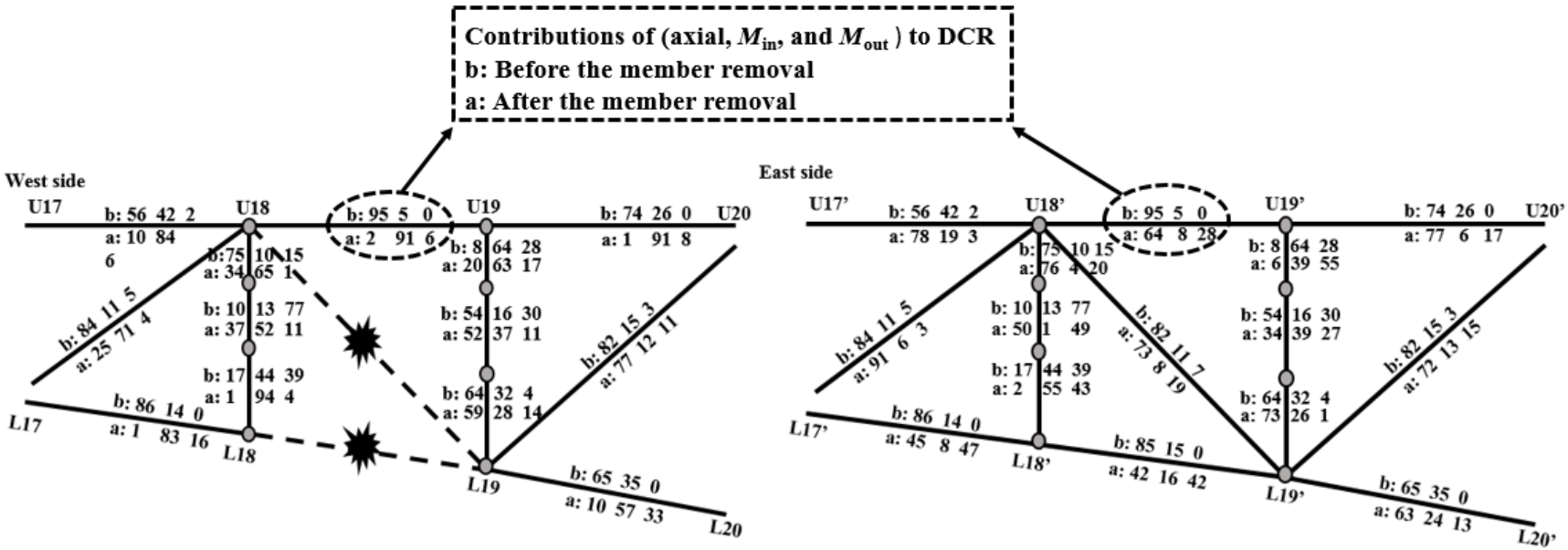

Source: FHWA.

Figure 61. Illustration. Contributions to *DCR* before and after DMR case 1 near the damaged location in west and east side trusses.

Figure 62 through figure 67 present *DCR* metric for six DMR cases. Although both single and dual member removals involve hypothetical damage imposed on the system, a global pattern of load redistribution can be identified by tracking the change in the reactions at each support. Table 21 and table 22 show the net change in the magnitude of the reaction force for MR and DMR cases, respectively. There are three key findings based on table 21 and table 22:

1. Because damage occurred in the west side truss near support #20, there was a net decrease in the reaction at support #20 in the west side truss and a net increase in the reaction at support #20 on the east side truss for all MR and DMR cases.
2. For the west side truss, the sum of the other three support reaction forces (i.e., at supports #1, #8, and #27) increased.
3. Support #1 (at the very far end of the damaged region on both the east and west side trusses) experienced the least change in the reaction. This could imply that the damage does not cause extra loading on support #1.

Because dual member damage hinders the original load path to transfer the load to its nearest support, the bridge seeks ALPs such that the load will be transferred to either the opposite side or the supports on the same side. However, additional load taken by the support will decrease as the support's distance from the damage zone increases. The load carried by the opposite side truss is transferred by the three-dimensionality of the bridge because of the upper and lower bracing systems, although these systems were designed to maintain the stability and geometrical shape of the bridge rather than to carry load. When damage is introduced into the bridge, loss of geometrical symmetry forces the bracing systems to carry redistributed loads. The impacted zone based on *DCR* plots for a DMR case is larger than that for an MR case.

Figure 68 shows the envelope of the *DCR* metric for the full bridge based on figure 62 through figure 67 for one-quarter of the bridge. The role of three-dimensionality is more prominent in DMR cases than the MR cases shown in figure 44 because most members of the lower braces, upper braces, and floor truss yielded during DMR case 1 (i.e., $DCR > 1.67$). Table 23 lists the number of truss members with $DCR \leq 1.0$, $1.0 < DCR \leq 1.67$, and $DCR > 1.67$ in envelopes for MR and DMR. The number of members with $DCR \leq 1.67$ decreased from 1,766 for MR to 1,689 for DMR, whereas the number of members with $DCR > 1.67$ increased from 118 for MR to 202 for DMR. These results show that DMR has significantly more impact than MR, as expected. It is conceivable that the effect of actual blast loading (instead of simplified representation by DMR) on the bridge may be even more significant.

Figure 62 through figure 67 also demonstrate that the west side truss between supports #8 and #20 started behaving like a cantilevered beam after two members near support #20 were damaged. This cantilevered portion of the truss had a tendency to rotate clockwise, which caused an increased net negative moment at support #8 to resist this tendency to rotate, as illustrated in figure 69. *DCR* of all west side truss members increased because of this net negative moment.

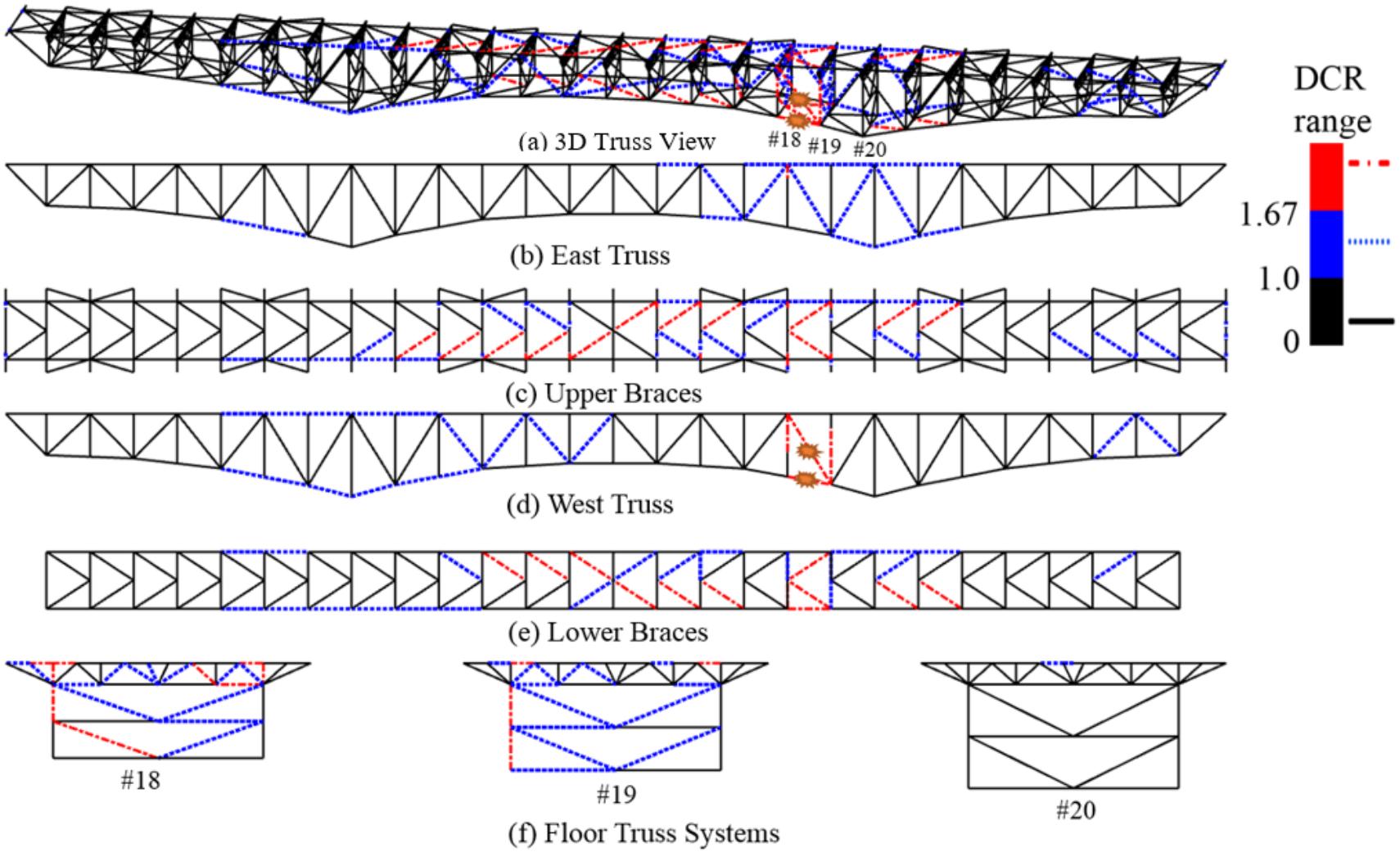

Source: FHWA.

Figure 62. Illustration. *DCR* spectra for the Design Bridge for DMR case 1.

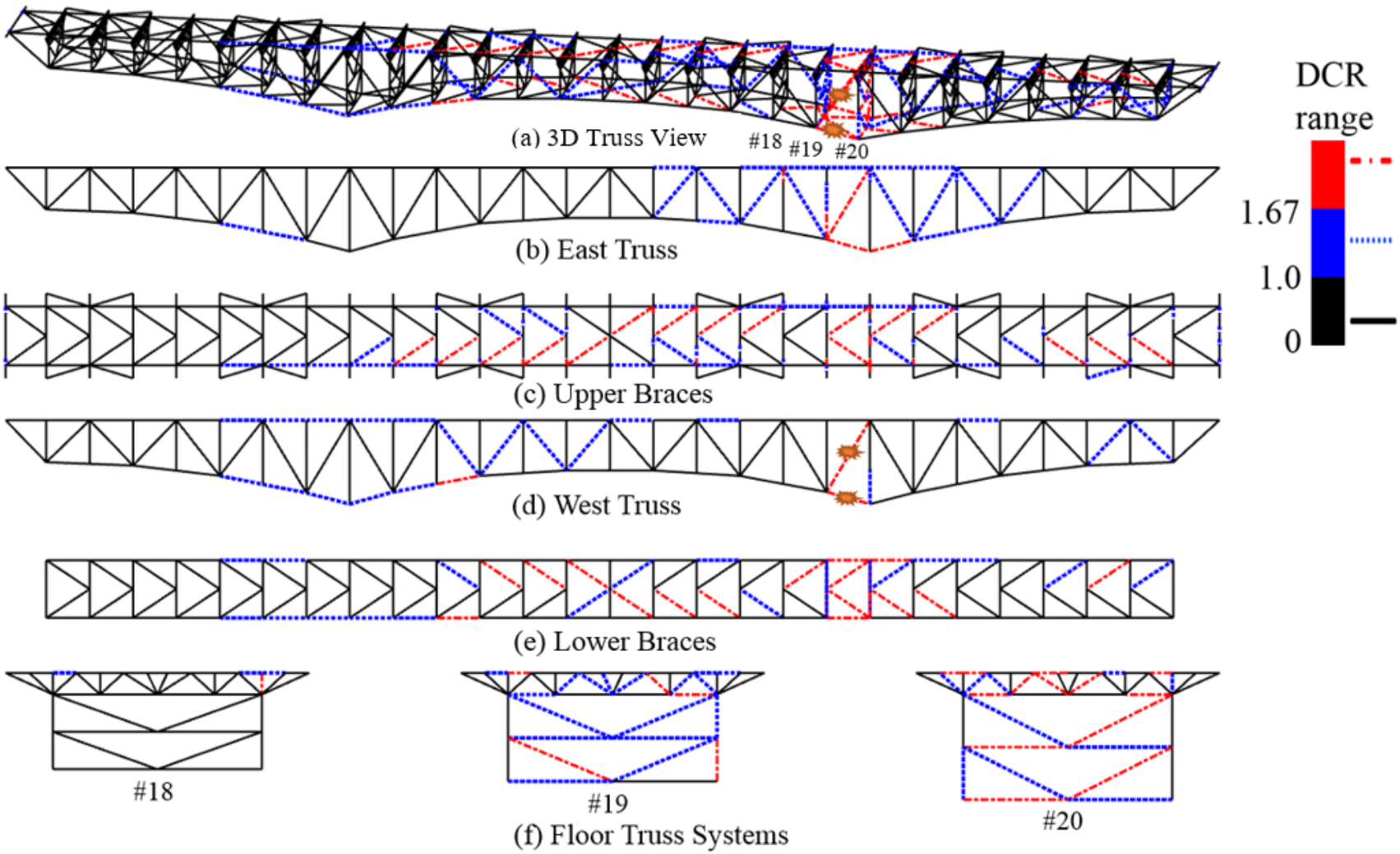

Source: FHWA.

Figure 63. Illustration. *DCR* spectra for the Design Bridge for DMR cases 2, 6, and 7.

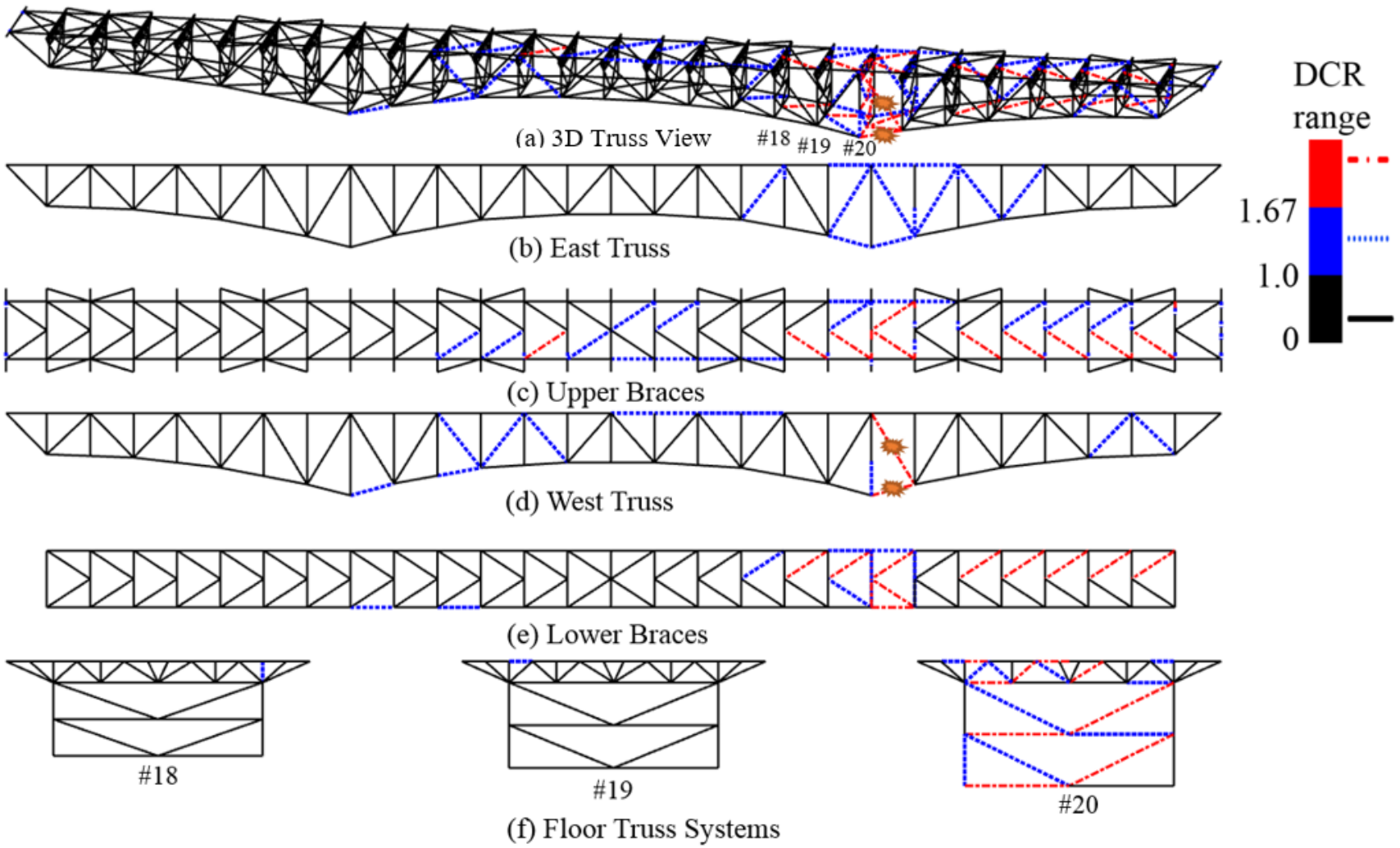

Source: FHWA.

Figure 64. Illustration. *DCR* spectra for the Design Bridge for DMR cases 3, 5, and 8.

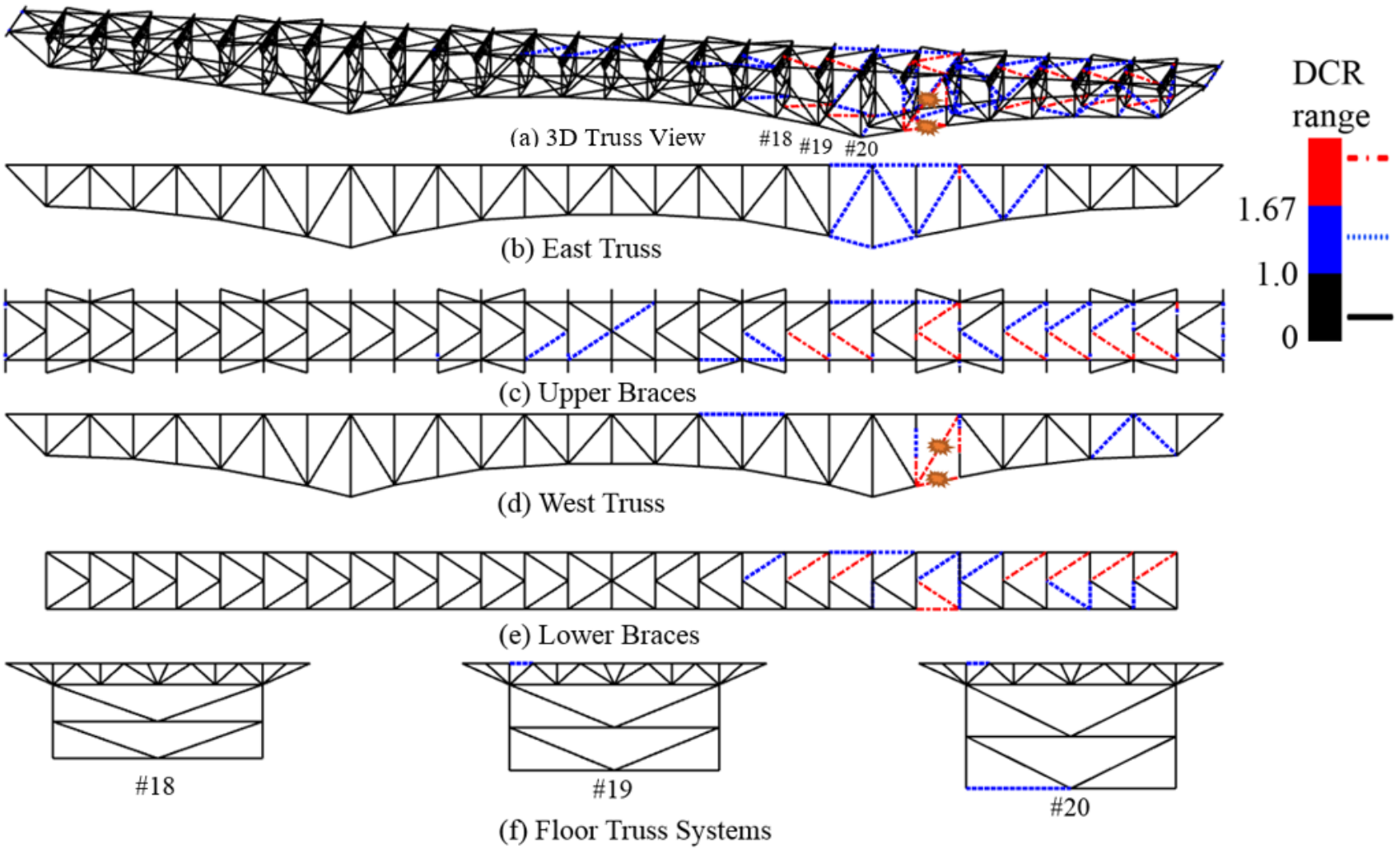

Source: FHWA.

Figure 65. Illustration. *DCR* spectra for the Design Bridge for DMR case 4.

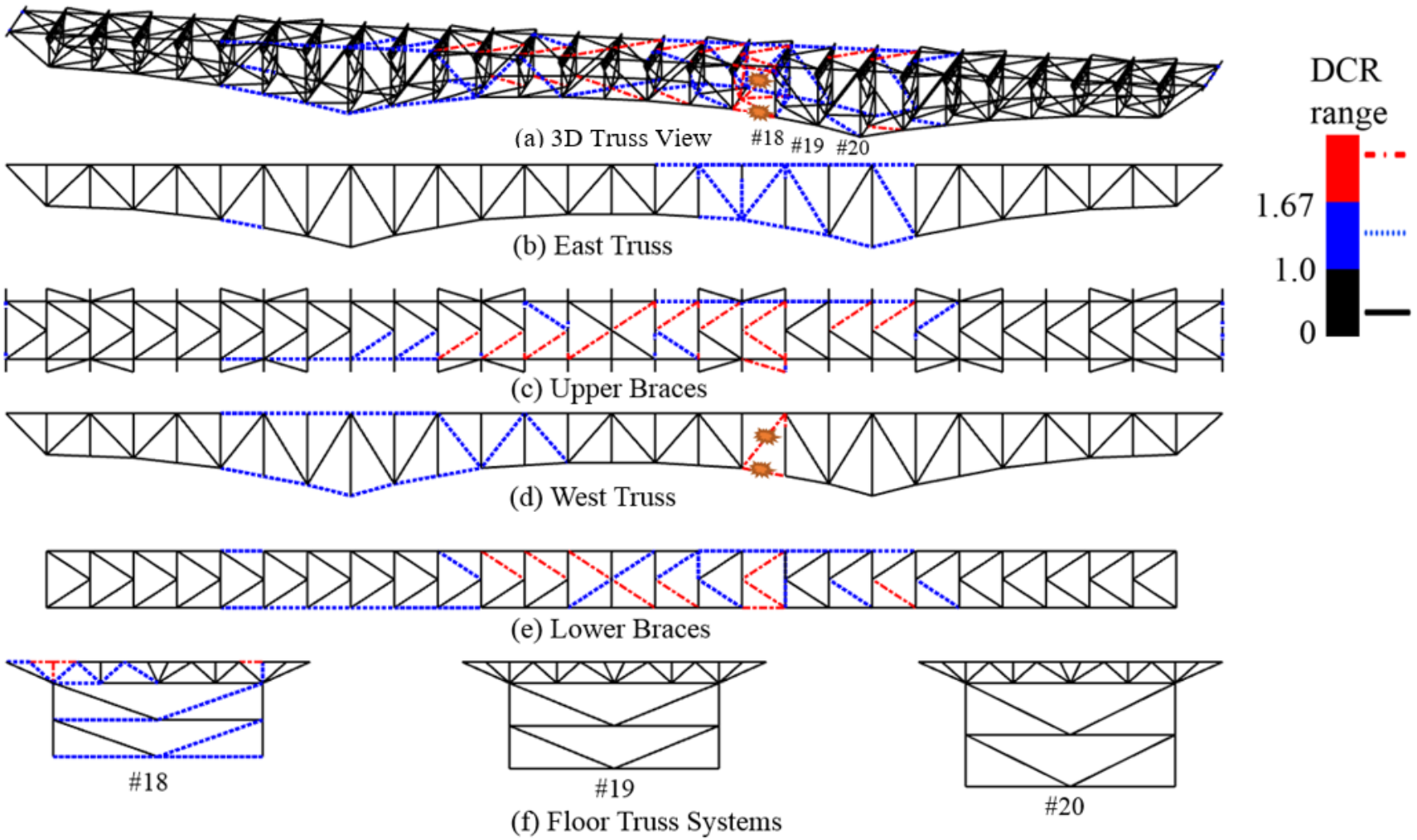

Source: FHWA.

Figure 66. Illustration. *DCR* spectra for the Design Bridge for DMR case 9.

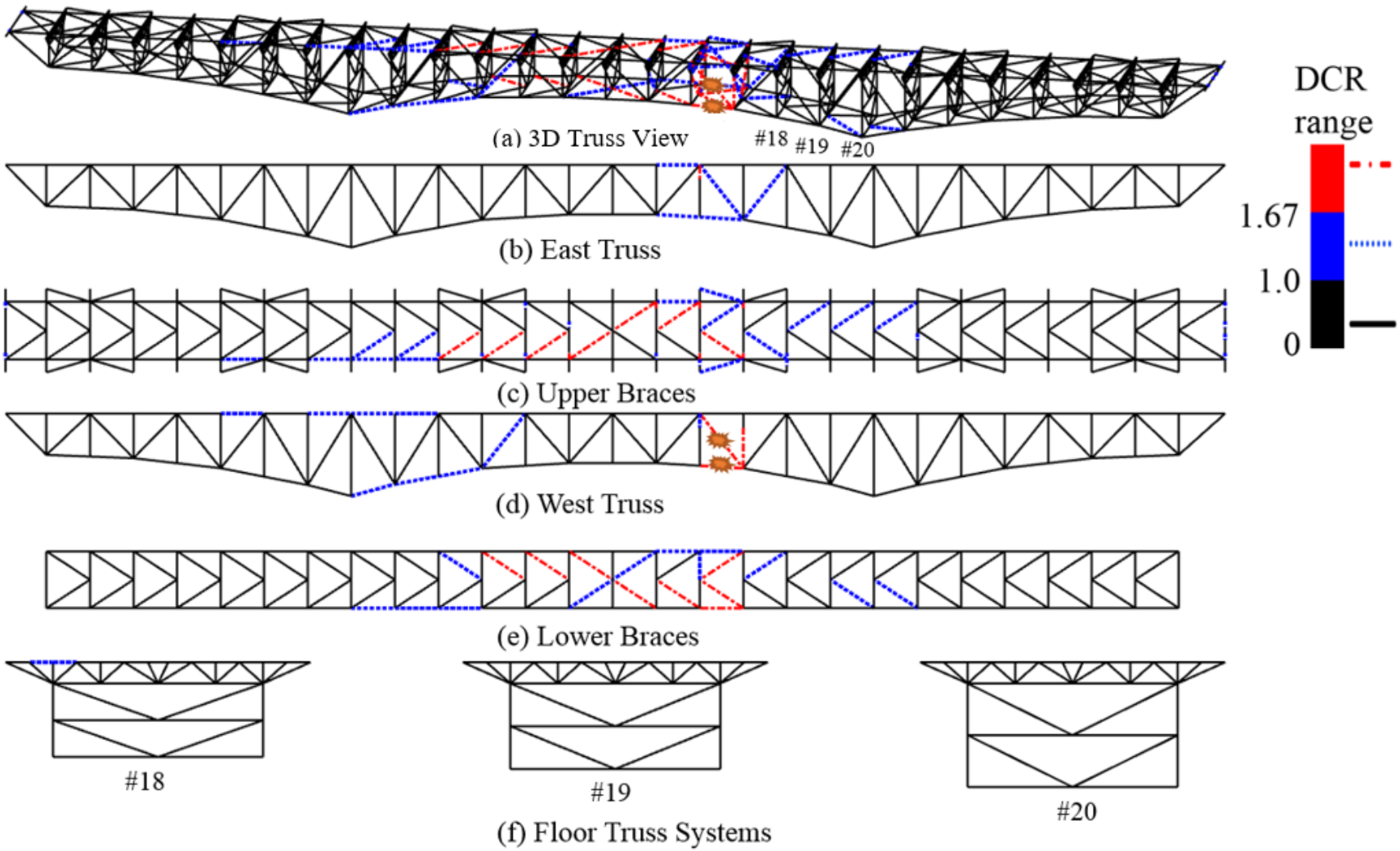

Source: FHWA.

Figure 67. Illustration. *DCR* spectra for the Design Bridge for DMR case 10.

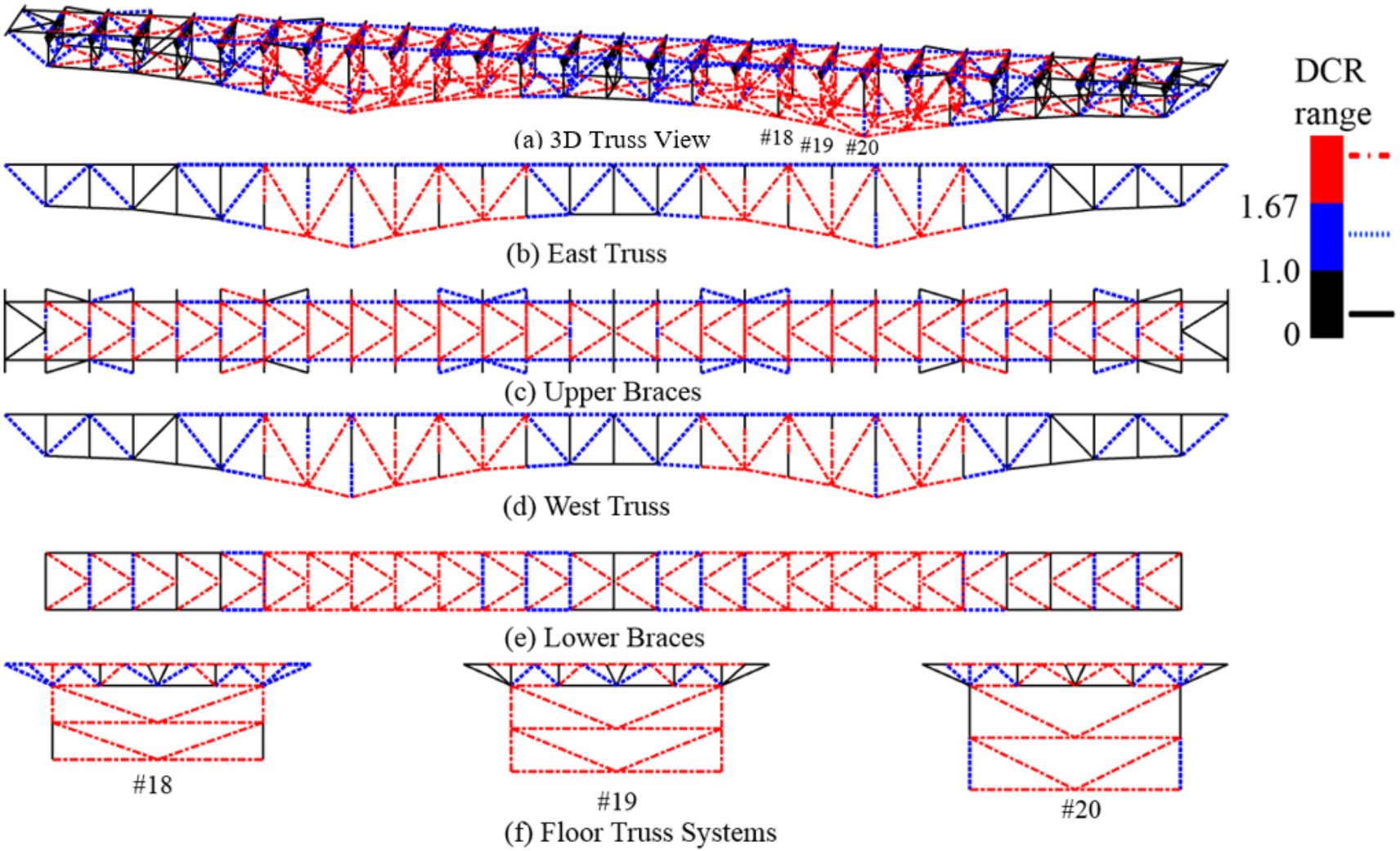

Source: FHWA.

Figure 68. Illustration. Complete envelope of *DCR* for the Design Bridge representing 40 DMR cases (10 DMR cases in each quarter of the bridge).

Table 21. Percentage change in the reaction force for corresponding MR cases.

Support Number	Direction	MR Case 1	MR Case 2	MR Case 3	MR Case 4	MR Case 9	MR Case 10
1	East	−0.3	−0.4	−0.1	−0.5	0.0	−0.2
1	West	−0.3	−0.5	−0.1	−0.5	0.0	−0.2
8	East	−1.1	−1.5	−0.7	−2.0	−0.2	−0.9
8	West	2.1	3.6	1.0	4.5	0.2	2.3
20	East	1.9	3.1	1.2	4.6	0.8	3.3
20	West	−2.5	−5.4	−1.2	−7.6	−0.9	−5.5
27	East	−0.4	−0.6	−0.4	−1.2	−0.6	−1.5
27	West	0.6	1.7	0.2	2.7	0.7	2.7

Table 22. Percentage change in the reaction force for corresponding DMR cases.

Support Number	Direction	DMR Case 1	DMR Case 2	DMR Case 3	DMR Case 4	DMR Case 9	DMR Case 10
1	East	0.0	−0.1	−0.3	−0.3	−0.2	−0.3
1	West	0.0	−0.1	−0.3	−0.4	−0.3	−0.3
8	East	−0.1	−0.3	−0.9	−1.1	−0.7	−0.8
8	West	0.4	1.4	1.9	2.7	1.8	1.9
20	East	1.3	2.3	1.2	1.7	1.1	1.1
20	West	−1.7	−4.0	−1.8	−3.2	−2.0	−1.7
27	East	−1.1	−1.4	−0.2	−0.2	0.0	−0.1
27	West	1.3	2.3	0.3	0.8	0.4	0.2

Table 23. Number of elements in each range of ALP analysis: *DCR* metric.

Loading Condition	$DCR \leq 1.0$	$1.0 < DCR \leq 1.67$	$DCR > 1.67$
MR	1,766	214	118
DMR	1,689	207	202

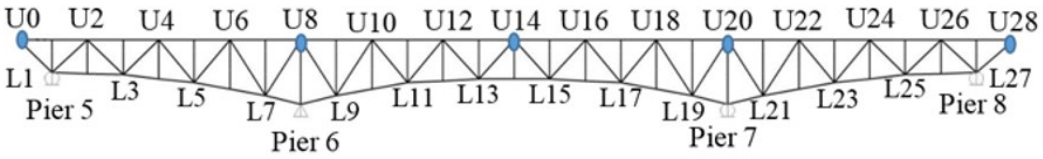

Source: FHWA.

A. West side truss.

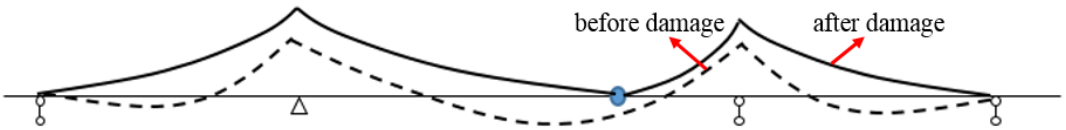

Source: FHWA.

B. Moment diagram of the west side truss.

Figure 69. Illustrations. Moment diagram of the west side truss (assuming the truss as a continuous beam) before any damage and after blast damage at a certain panel.

ALP (DMR) Analysis for Design Bridge: SR Metric

Figure 70 through figure 75 show ALP spectra in terms of the *SR* metric corresponding to six DMR cases. The results in terms of *SR* are consistent with those in terms of *DCR*. Figure 76 shows the envelope of the *SR* metric for the full bridge based on *SR* in figure 70 through figure 75 for one-quarter of the bridge. This envelope is similar to that for *DCR* in figure 68.

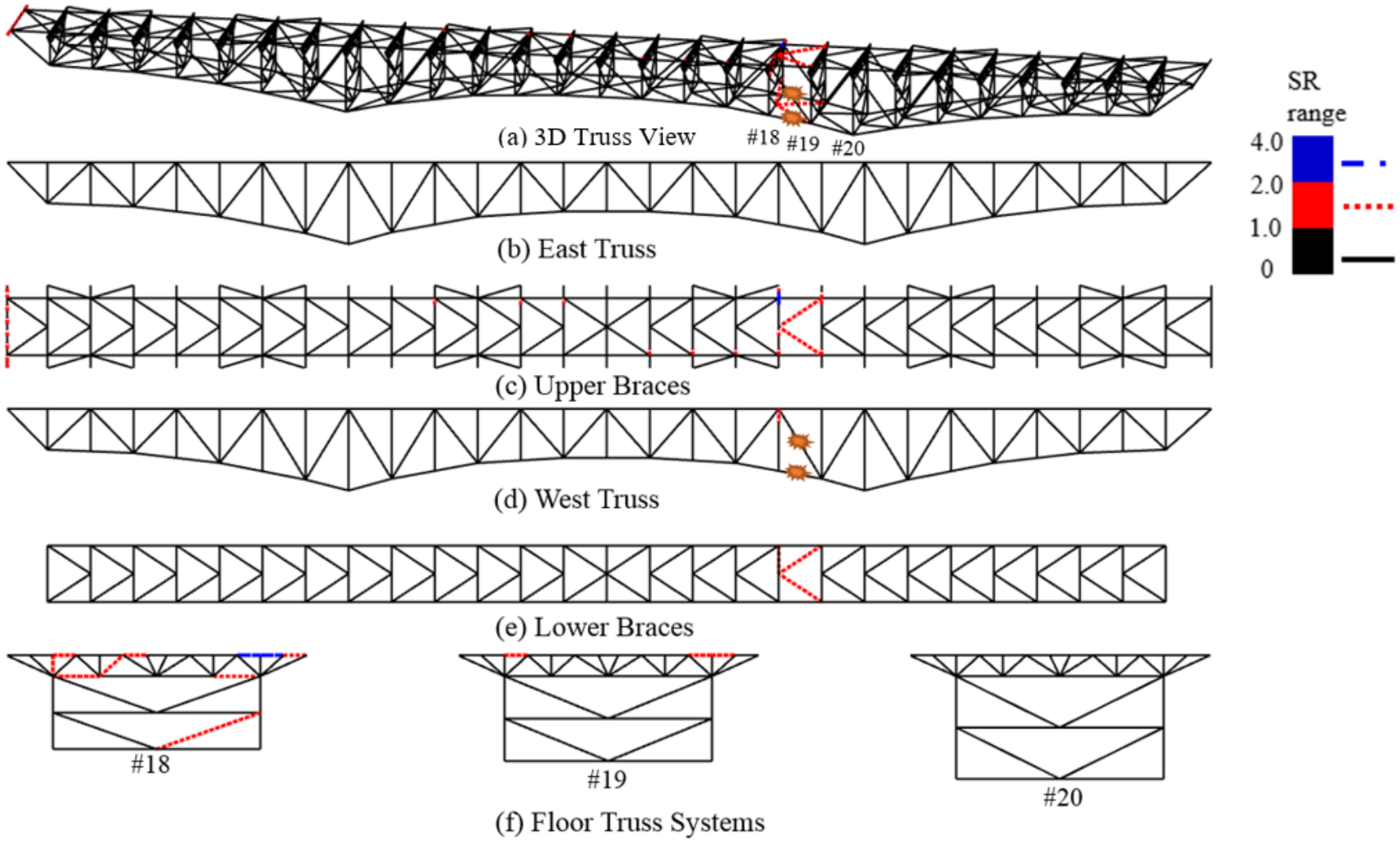

Source: FHWA.

Figure 70. Illustration. *SR* spectra for the Design Bridge for DMR case 1.

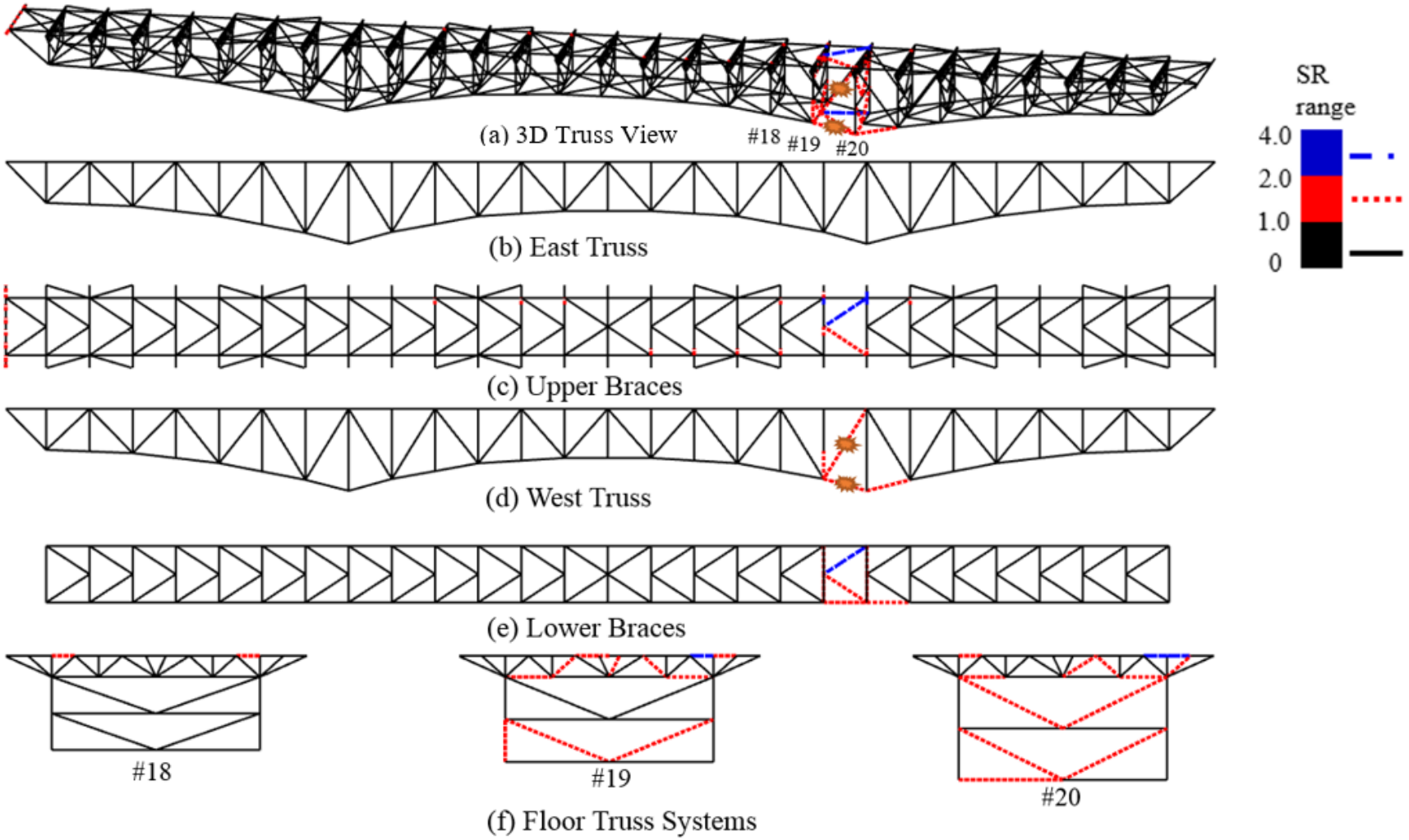

Source: FHWA.

Figure 71. Illustration. *SR* spectra for the Design Bridge for DMR cases 2, 6, and 7.

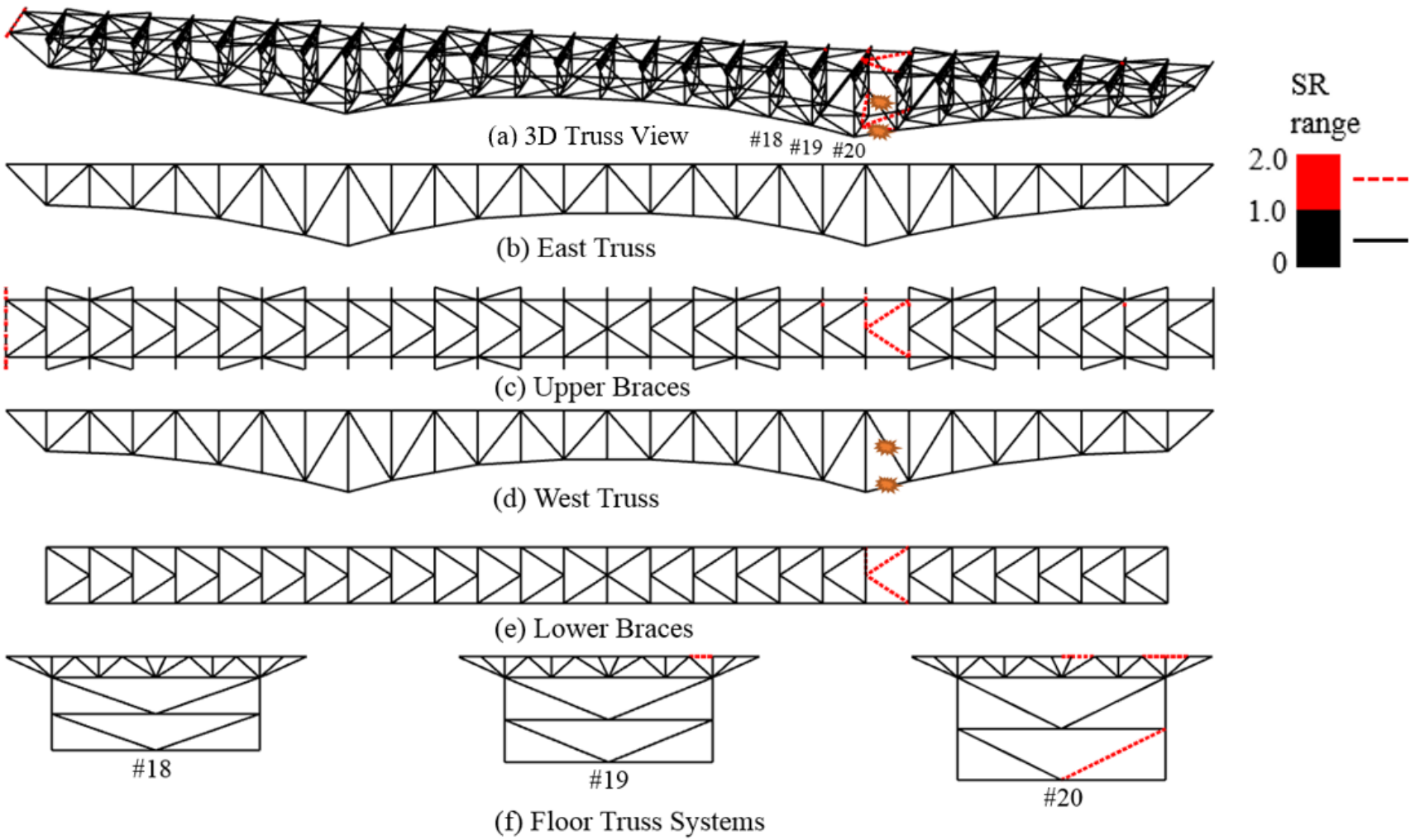

Source: FHWA.

Figure 72. Illustration. *SR* spectra for the Design Bridge for DMR cases 3, 5, and 8.

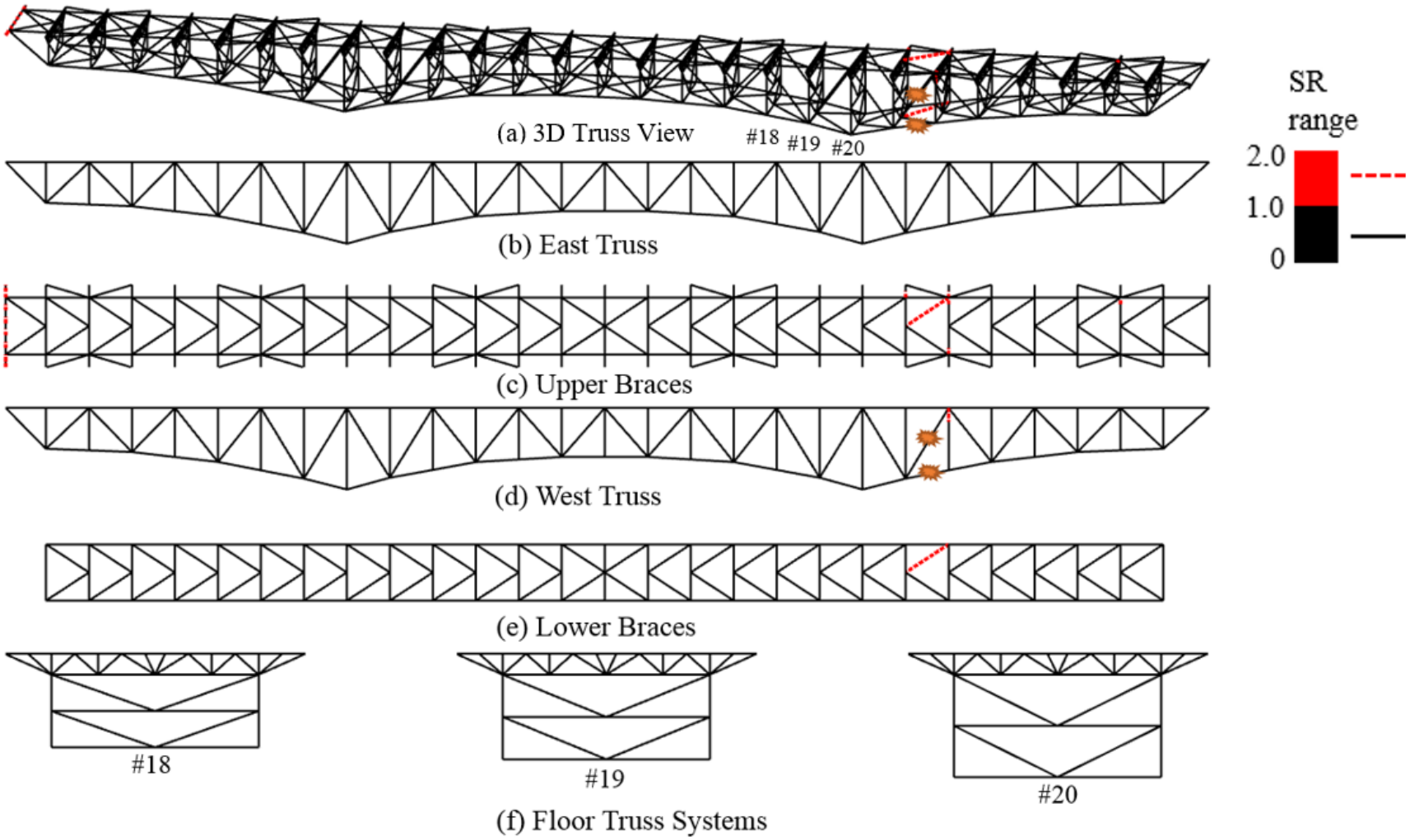

Source: FHWA.

Figure 73. Illustration. *SR* spectra for the Design Bridge for DMR case 4.

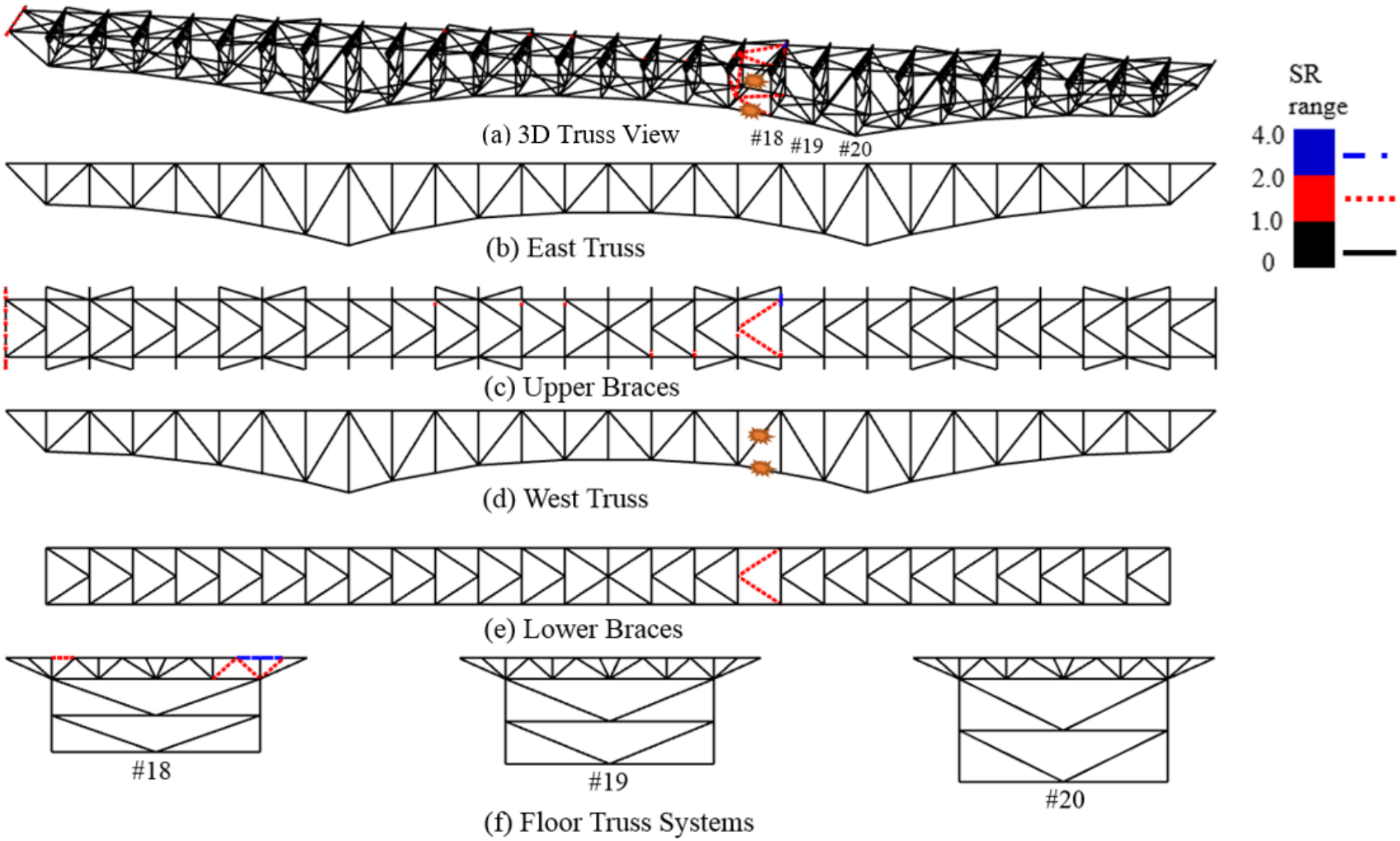

Source: FHWA.

Figure 74. Illustration. *SR* spectra for the Design Bridge for DMR case 9.

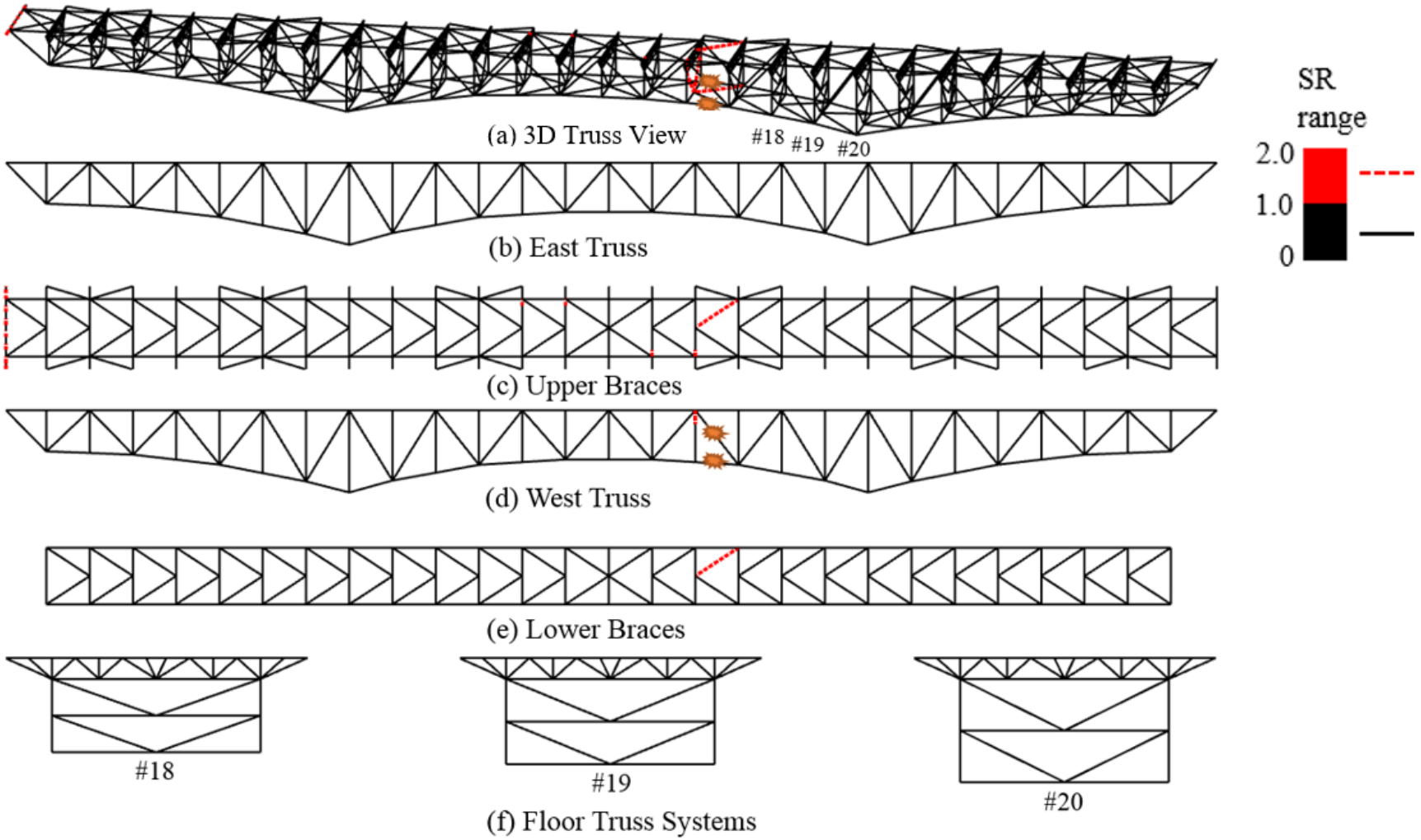

Source: FHWA.

Figure 75. Illustration. *SR* spectra for the Design Bridge for DMR case 10.

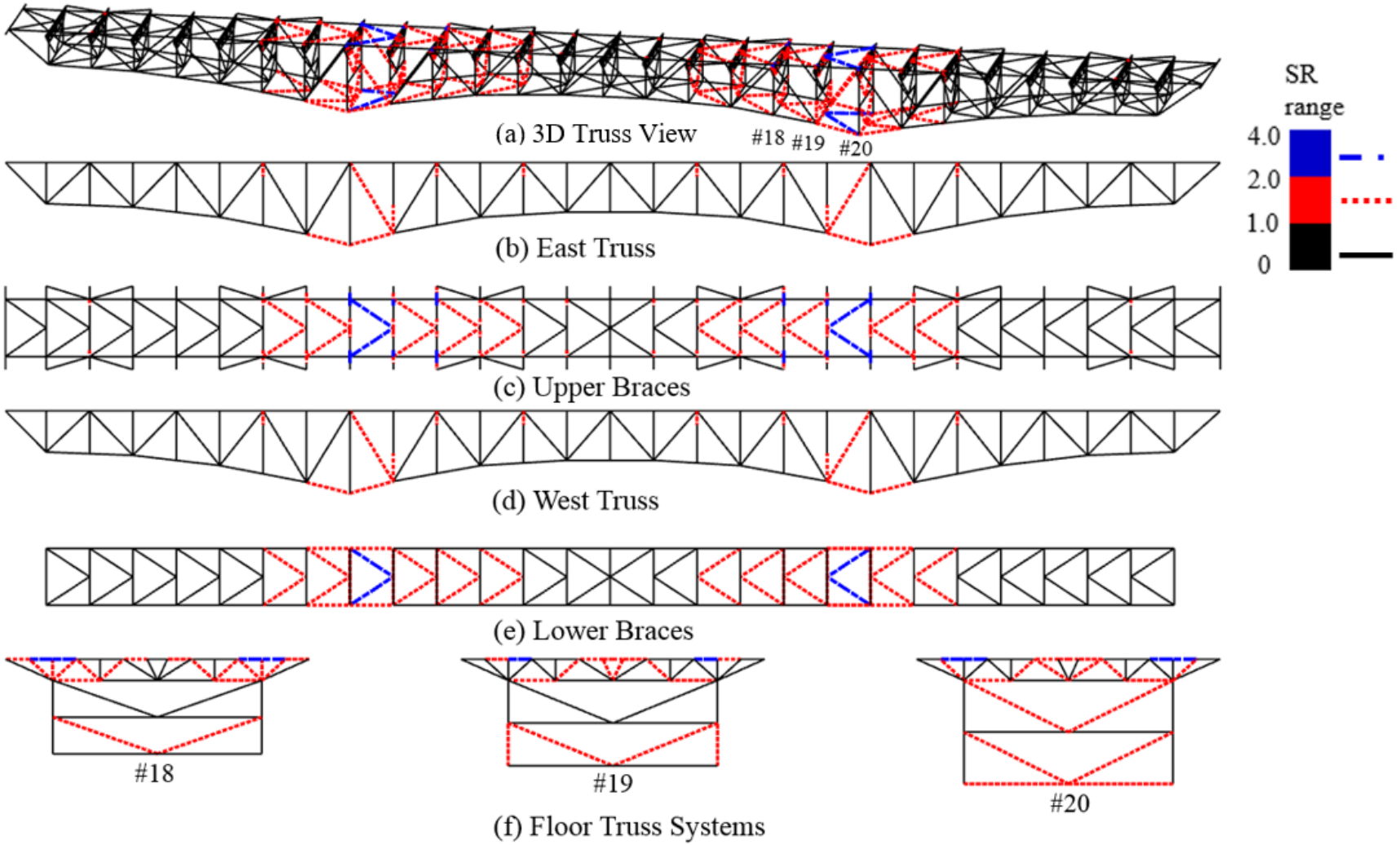

Source: FHWA.

Figure 76. Illustration. Complete envelope of *SR* for the Design Bridge representing 40 DMR cases (10 DMR cases in each quarter of the bridge).

CHAPTER 5. RETROFITS FOR ENHANCING ALP

SEISMIC RETROFITS

Most existing long-span truss bridges undergo seismic retrofits during major rehabilitation to address deterioration and other vulnerabilities because they were not designed according to current design standards and may be vulnerable to damage during earthquakes. Currently, ALP vulnerability is not addressed as part of this major rehabilitation process. Hence, a detailed investigation was performed on the retrofit methods that could be effective during both seismic and sudden member loss scenarios.

When the seismic resistance of a bridge is found to be insufficient, a retrofit may be needed to reduce the demand experienced by bridge components. Such retrofits include seismic isolation and energy dissipation systems (Pan et al. 2010a, b; Kandemir et al. 2011; Agrawal et al. 2012; Agrawal and Amjadian 2016), member strengthening (Imbsen and Liu 1993; Matson and Buckland 1995; Liu et al. 1997; Imbsen and Schamber 1999), buckling-restrained braces (BRBs) (Usami et al. 2005; Chen et al. 2011; Uang and Bruneau 2018), and replaceable fuses (El-Bahey and Bruneau 2011; Saravanan et al. 2018). During an earthquake, seismic demand is transferred from the substructure to the superstructure. Hence, most seismic retrofits focus on the substructure for effective control and dissipation of input seismic energy. For member loss hazards that initiate at the superstructure level, load is transferred from the superstructure to the substructure because of load redistribution. Moreover, the loading during these hazards is of very short duration and must be countered within the superstructure through effective redistribution among members such that the safety of the bridge system is guaranteed. An even higher standard (no damage or minimal damage to the bridge system and its components) may be required, depending on the importance of the bridge. Because of significant differences between seismic and MR demands, common seismic retrofit measures for substructure elements such as bearings, seats, columns, piers, cap beams, column-to-cap joints, abutments, and foundations are not applicable to sustain demand during sudden member loss. Only the member strengthening approach that is generally used for seismic retrofit of truss bridges (Imbsen and Liu 1993; Matson and Buckland 1995; Liu et al. 1997; Imbsen and Schamber 1999) may also be useful in enhancing the resistance against sudden loss demands.

Conventional Seismic Retrofit Schemes

Commonly used seismic retrofits, such as isolation bearings and supplemental damping systems, are designed to dissipate input energy without affecting the ALPs. However, retrofits such as member strengthening (e.g., adding cover plates to increase the effective area), lateral bracing enhancement, and stiffening of bracing systems may be effective in resisting both seismic and MR or blast load demands.

For major truss members, the capacity to sustain member loss can be improved by increasing the cross-sectional area, changing the sectional shape, or both. An optimized sectional shape, such as a box shape rather than an I shape, may improve the radius of gyration, which in turn could increase the capacity of compressive members. BRBs consist of a hollow box section filled with core material and can provide stable energy dissipation capacity under dynamic excitations with

similar behaviors in both tension and compression because global buckling of the core member of BRBs is restrained (Usami et al. 2005). Both these retrofits (increasing the cross-sectional area and BRBs) are effective in increasing the buckling capacity of compression members. In long-span truss bridges, horizontal or lateral bracing systems are significant secondary members. Horizontal or lateral bracings are installed between girders to prevent lateral buckling of compression flange of girders. These bracings can also participate in load redistribution from one truss to another and need to be designed for extra loading induced by sudden MRs. Another potential retrofit approach is modification of the bridge system. For example, the Brooklyn Bridge was retrofitted nonseismically by adding six arches to reduce loading on the stiffening truss, as shown in figure 77.

Source: FHWA.

Figure 77. Photo. Retrofit of the Brooklyn Bridge with six arch systems.

Several examples of retrofit of bridges where retrofit involved measures other than member strengthening, such as addition of bracings and strengthening of FSs, have been observed from the literature. The seismic retrofit measures for the Golden Gate Bridge included replacement and addition of top and bottom lateral bracings and strengthening of vertical truss members and truss connections (Golden Gate Bridge Authority 2014). Other measures were also taken to minimize the effect of ground motions on structures, such as converting five simply supported truss spans into a continuous truss system, installing seismic expansion joints at the north and south ends of the viaduct truss, and installing isolator bearings atop the new steel support towers. Figure 78 shows the schematic of various seismic retrofits to this bridge.

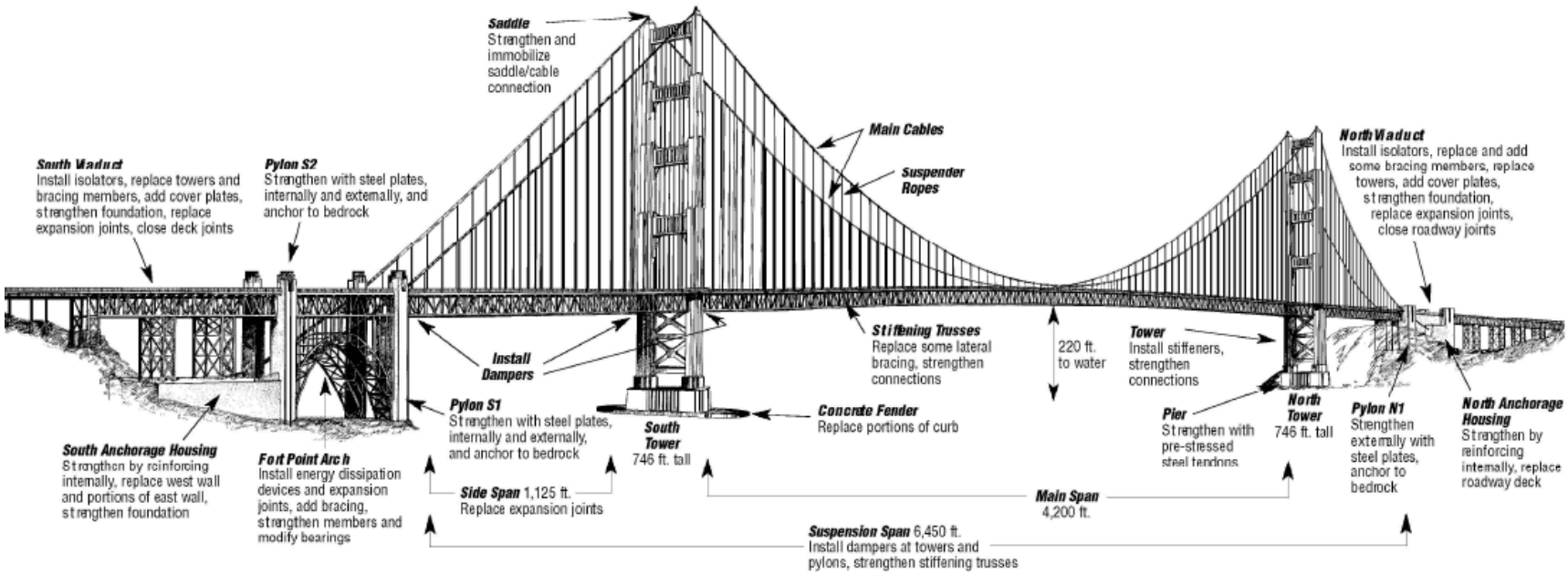

Figure 78. Illustration. Schematic of seismic retrofits to the Golden Gate Bridge.

During seismic retrofit of the Auburn-Foresthill Bridge (figure 79), which is California's tallest bridge, analysis revealed that the bracing members near the abutments carried much of the seismic load (Reno and Pohll 2010). Large BRBs, capable of handling up to 450 kN (2,003 kips), were installed at these locations to absorb some of the input seismic energy and reduce deformations. Replacement of bolted connections and gusset plates was also performed for increased strength.

Figure 79. Photo. Auburn-Foresthill Bridge, California's tallest bridge.

The Tennessee Department of Transportation performed seismic retrofit of the I-40 Mississippi River Bridge, which is a steel tied-arch bridge (figure 80). Retrofits in this bridge included diaphragm or cross frame replacement, bottom lateral retrofit, bearing replacement, and expansion joints replacement.

Figure 80. Photo. I-40 Mississippi River Bridge (steel tied-arch bridge).

Based on the case studies of seismic retrofits discussed in this section, effective retrofits that could also enhance the three-dimensionality of a truss system for greater distribution of member force and robust ALP (in addition to seismic resistance) can be summarized as follows:

1. Vertical cross bracing, diaphragm or cross frame replacement.
2. Longitudinal truss enhancement.
3. Top or bottom lateral bracing enhancement.

These retrofit strategies are investigated in detail in the following section.

Seismic Retrofit of the I-35W Bridge

To investigate the effectiveness of seismic retrofits on ALP, it is important to ensure that the Design Bridge analyzed in the previous chapter has sufficient capability to withstand seismic loads. The I-35W Bridge was located in Minnesota, which is a low seismic hazard region. Hence, seismic demands on the bridge were investigated for a high seismic region (San Diego, CA). Seismic analysis of the bridge was performed for a 2,500-year earthquake (SD2500) with short-period (S_s) and 1-second-period (S_1) ground accelerations of 0.979 and 0.377 *g*, respectively, using the response spectrum approach in AASHTO LRFD (AASHTO 2014). Figure 81 shows the seismic response spectra for SD2500. Because the fundamental period of the I-35W Bridge was about 2.23 s, the spectral acceleration during this period was about 0.2 *g*. A vertical seismic component was not included because the foundation and the soil interaction were not considered in evaluating seismic demand on the bridge. Seismic load effect was combined with *DL*s and *LL*s using equation 10.

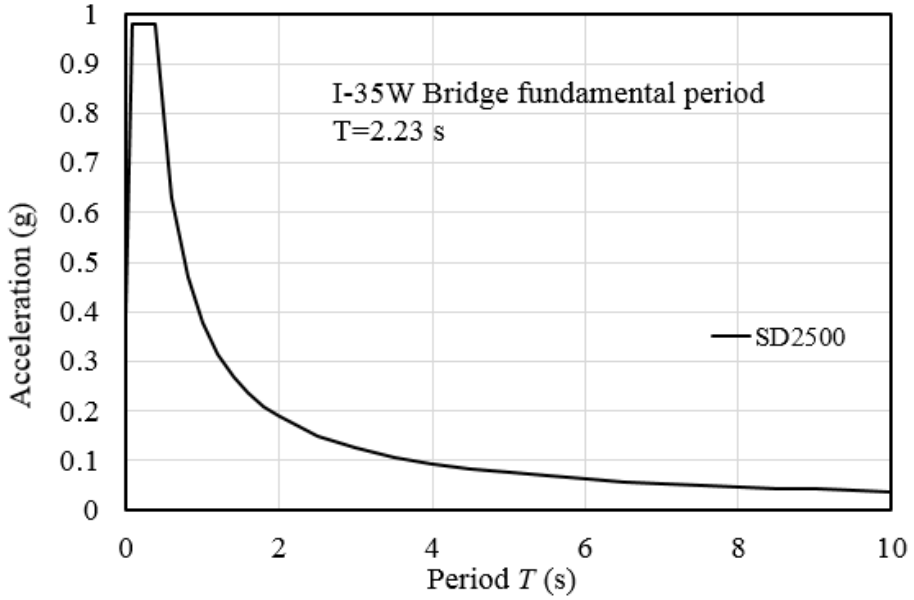

Source: FHWA.

Figure 81. Graph. Seismic response spectra for 2500-year earthquake in San Diego, CA.

Analysis results indicated that the *DCR* of all members of the bridge for *DL*, *LL*, and seismic load combinations was between 0.9 and 1.0. Hence, the bridge was in elastic range when subjected to SD2500 and did not require seismic retrofit. However, similar to the investigation of the Design Bridge in the previous chapter, some members of this bridge were strengthened so that the *DCR* of all members for *DL*, *LL*, and seismic load combinations was about 0.9. Although this *DCR* value may be conservative during the actual seismic design of bridges, the *DCR* of all members was limited to 0.9 so that the change in *DCR* due to MR could be easily evaluated to identify ALPs.

The increase in the weight of steel in the bridge because of this retrofit was approximately 3.42 percent. This increase in steel weight was approximately 0.98 percent for low seismic regions such as Minnesota and New York City. The seismically retrofitted bridge for SD2500 was termed "Base Bridge" for further MR and retrofit analysis. Figure 82 shows detailed views of the bridge and its components after retrofit. Retrofitted members of the bridge in this figure are shown as red dotted lines. The figure demonstrates that some members of the trusses, the upper and lower braces, and the FS were retrofitted to limit the *DCR* to 0.9.

Sudden member loss analysis was conducted for the *DL* and *LL* combination in equation 11 to check the effectiveness of seismic retrofit for load redistribution after the removal of a member. Results were compared with those for the Design Bridge (the bridge without seismic retrofit) by counting truss members falling into different *DCR* limit states, as shown in table 24 and table 25. These two tables show that the number of truss members with $DCR > 1.67$ (i.e., member possibly undergoing inelastic deformation) decreased from 118 for the Design Bridge to 75 for the Base Bridge for MR scenarios. Likewise, the number of truss members with $DCR > 1.67$ decreased from 202 for the Design Bridge to 117 for the Base Bridge for DMR scenarios. These results demonstrate the limited effectiveness of seismic retrofit (through member strengthening only) during sudden member loss because of the lack of new load paths created. The Base Bridge was used to investigate the effectiveness of other retrofit measures that involved changing the three-dimensionality of the bridge.

Table 24. Number of members in each range for different *DCR* limit states under MR scenarios for the Design Bridge and Base Bridge.

Bridge	$DCR \leq 1.0$	$1.0 < DCR \leq 1.67$	$DCR > 1.67$	$DCR > 1.0$
Design Bridge	1,766	214	118	332
Base Bridge	1,845	178	75	253

Table 25. Number of members in each range for different *DCR* limit states under DMR scenarios for the Design Bridge and Base Bridge.

Bridge	$DCR \leq 1.0$	$1.0 < DCR \leq 1.67$	$DCR > 1.67$	$DCR > 1.0$
Design Bridge	1,689	207	202	409
Base Bridge	1,768	213	117	330

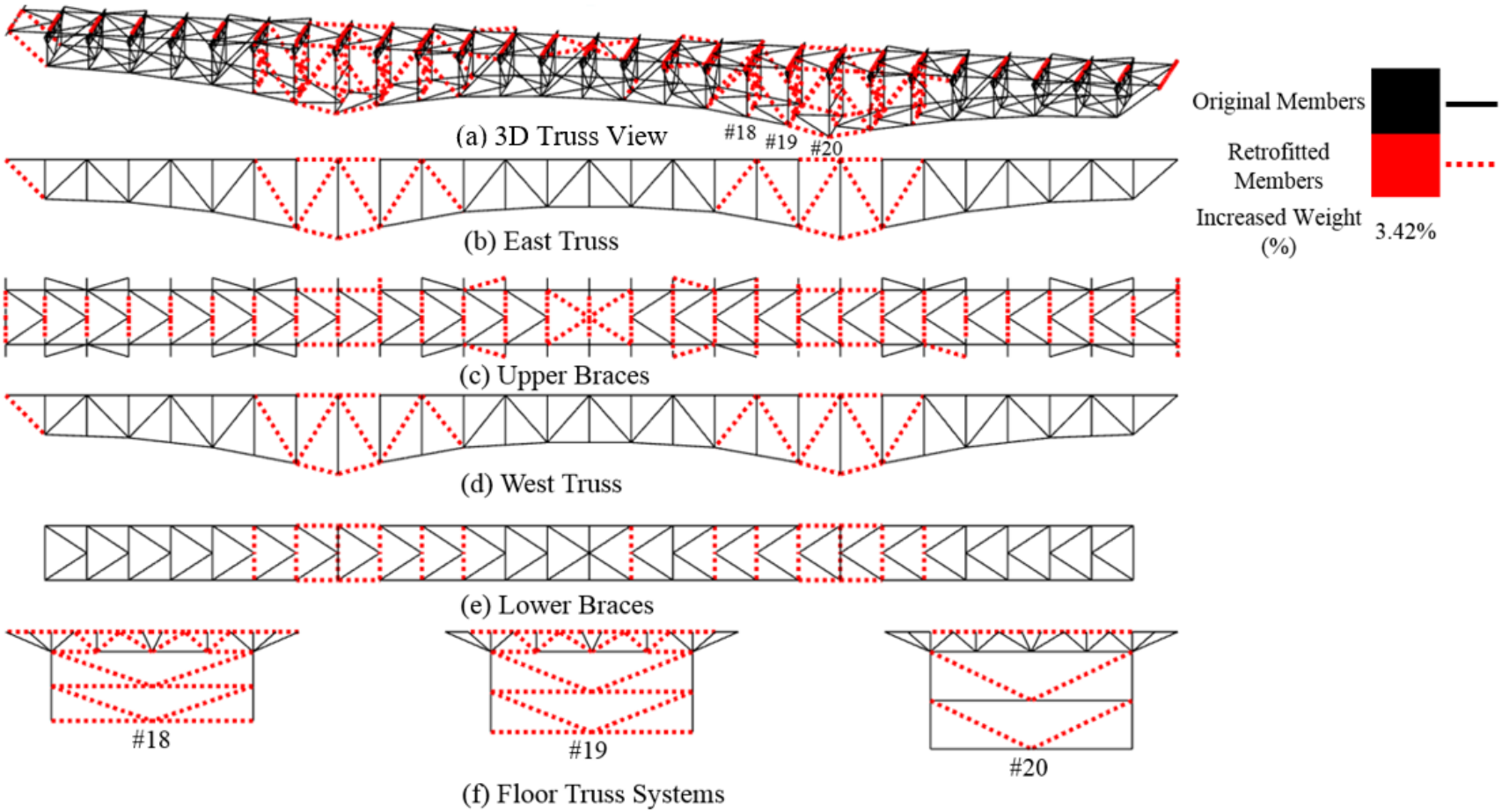

Source: FHWA.

Figure 82. Illustration. Members of the Design Bridge retrofitted for SD2500 by member strengthening to obtain the Base Bridge for the ALP analysis.

PBD AND RETROFIT FOR SUDDEN MEMBER LOSS

PBD is a rational approach to designing a new structure or evaluating an existing structure. By identifying specific structural performance objectives, an engineer can use PBD to design a structure that satisfies desired serviceability or strength-level targets. By accounting for the significance of inelastic structural response, the overall performance of the structure is controlled during the PBD process.

There are a variety of performance-based criteria and design parameters based on the type of structure, the materials, the hazards to which the structure is exposed, and the analysis approach adopted. The criteria can be either qualitative or quantitative for different performance levels. PBD framework was first adopted in earthquake engineering for seismic design and retrofit of structures. Seismic retrofit philosophy is based on the concept of minimizing loss of life and serious injury to the public through acceptable bridge performance. A similar PBD approach has been considered for retrofitting truss bridges to enhance their ALP.

The PBD approach in this research considered two types of design criteria for long-span steel truss bridges: *DCR* through elastic analysis and *SR* through inelastic analysis using an LS-DYNA model that includes both geometrical and material nonlinearities. For each design criterion, various limit states that correspond to different damage levels are presented in table 26 and table 27.

Table 26. Allowable indicators for various performance levels using *DCR* metric.

***DCR* Limit State (SAP2000)**	**Performance Level**
$DCR \leq 1.0$	No damage: allowable stress level (elastic behavior), no impact on traffic mobility.
$1.0 < DCR \leq 1.67$	Minor damage: intermediate state between allowable (elastic) and plastic, controlled traffic mobility, minor damage at yield point.
$DCR > 1.67$	Major damage: some members of the bridge system may experience yielding. Collapse prevention.

Table 27. Allowable indicators for various performance levels using *SR* metric.

***SR* Limit State (LS-DYNA)**	**Performance Level**
$SR \leq 1.0$	No damage: elastic range.
$1.0 < SR \leq 2.0$	Minor damage: low ductility.
$2.0 < SR \leq 4.0$	Moderate damage: moderate ductility, repairable damage.
$SR > 4.0$	Significant damage: minimum risk of collapse.

Significant differences exist between seismic and MR or DMR demands. Perhaps the most obvious difference is the broadness of the affected zone or region. Seismic demands are global (i.e., they affect the whole bridge and excite lower modes of the bridge). MR or DMR demands involve localized damage initiation events and very short time durations (compared to earthquake excitations) and so affect higher modes. Based on these characteristics of MR or DMR scenarios, it is expected that seismic retrofits may not be comprehensive enough to resist

MR or DMR demands and that the three-dimensionality characteristics of the structure may be more effective at resisting MR or DMR demand than seismic demand, even for bridges with perfectly symmetric geometry (Ettouney et al. 2006; Ettouney and Alampalli 2014, 2016).

Because of these differences between seismic and MR or DMR demands, it is expected that the analysis performed for the seismic retrofit may not be sufficient to withstand member loss demands. A detailed investigation is needed to identify the shortfalls of the seismic retrofits in MR or DMR scenarios. These limitations could be identified by observing the shortcomings of total bridge performance (displacements) and the shortcomings of member-based performance metrics (strain). Hence, further retrofits of the Base Bridge for MR or DMR scenarios were performed based on the demands of the corresponding acceptance limits.

A typical long-span truss bridge consists of side trusses and horizontal and vertical load-supporting systems, such as horizontal top and bottom bracing systems and FSs. When these subsystems function together as a whole, they contribute to the three-dimensionality of the bridge in load redistribution after MR or DMR events. When designing a bridge for *DL*s, *LL*s, and seismic loads, the relative contribution of seismic load to the total stress in a member is negligible compared to those from *DL* and *LL* (i.e., major loading on the bridge is in the vertical direction only). Adding a few extra members in the horizontal system could improve the horizontal stiffness of the bridge and thus the seismic resistance. However, results show that horizontal (top or bottom) bracing enhancement is less efficient than enhancements in the vertical system, such as FSs or DM systems, for improving vertical resistance against deformation induced during MR or DMR events. Nevertheless, enhancing horizontal (top or bottom) bracings does contribute to the three-dimensionality of the bridge, which is important for resisting the torsion that the bridge may undergo about its longitudinal axis after MR or DMR events. Although the bracing system is a secondary subsystem in the main truss structure, it is essential because it provides stability to the main girders during construction. It also contributes to the distribution of load effect as well as provides restraint to compression flanges or chords where they would otherwise be free to buckle laterally.

In addition to the performance levels presented in table 26 and table 27, the cost of retrofits and the practical issues concerning increase in truss weight and complexity of the joint should also be considered in evaluating the effectiveness of retrofits. Because effective retrofits to enhance ALP may depend on the characteristics of a bridge, retrofits presented in this chapter are based on a trial and error approach. For the I-35W truss bridge, the following four strategies for retrofit against MR or DMR demands were investigated:

1. Member strengthening only.
2. Adding bracings in the FS plus member strengthening.
3. Adding DMs plus member strengthening.
4. Adding DMs plus adding bracings in the FS plus member strengthening.

Table 28 shows the cases of MR retrofit strategies to be investigated for different *DCR* limits.

Table 28. Retrofit strategies for MRs.

DCR Range	Retrofit Type Case	MR Retrofit Strategy Description
$1.0 < DCR \leq 1.67$	1-1	Member strengthening only
$1.0 < DCR \leq 1.67$	2-1	Adding bracings in the FS + member strengthening
$1.0 < DCR \leq 1.67$	3-1	Adding DMs + member strengthening
$1.0 < DCR \leq 1.67$	4-1	Adding DMs + adding bracings in the FS + member strengthening
$0 < DCR \leq 1.0$	1-2	Member strengthening only
$0 < DCR \leq 1.0$	2-2	Adding bracings in the FS + member strengthening
$0 < DCR \leq 1.0$	3-2	Adding DMs + member strengthening
$0 < DCR \leq 1.0$	4-2	Adding DMs + adding bracings in the FS + member strengthening

HAZARD EVENTS

The hazard events used in this chapter for the Base Bridge follow the same types (MR or DMR) used in chapter 4 for the Design Bridge.

DCR-BASED RETROFIT SCHEMES

The *DCR*-based retrofit implies that the bridge was retrofitted following the retrofit strategies in table 28 to achieve *DCR* limits of 1.0, 1.67, and 5.0. A *DCR* limit of 1.67 implies initiation of yielding in some members (which can be considered essentially elastic behavior), and a *DCR* limit of 5.0 implies significant damage to the truss members without causing collapse. The rationale for the 1.67 limit is that the bridge member should be able to use the maximum capacity up to the yield limit for the extreme event scenarios of MR or DMR. However, depending on the importance of the bridge, a bridge owner can also select a *DCR* limit of 5.0 to economize the design.

Retrofits for MR

Similar to the MR analysis in chapter 4 on the Design Bridge, MR analysis was performed by considering 10 cases of MR to obtain the complete envelope shown in figure 83. Figure 84 through figure 87 show the distribution of retrofitted members for retrofit types 1-1, 2-1, 3-1, and 4-1 in table 28, respectively, for a desired performance level of $1.0 \leq DCR \leq 1.67$. Increase in the weight of steel in the bridge for these retrofit types was 26, 24, 15, and 11 percent, respectively, as shown in table 29. Likewise, increase in the weight of steel for retrofit types 1-2, 2-2, 3-2, and 4-2 in table 28 for $DCR \leq 1.0$ was 70, 65, 27, and 24 percent, respectively.

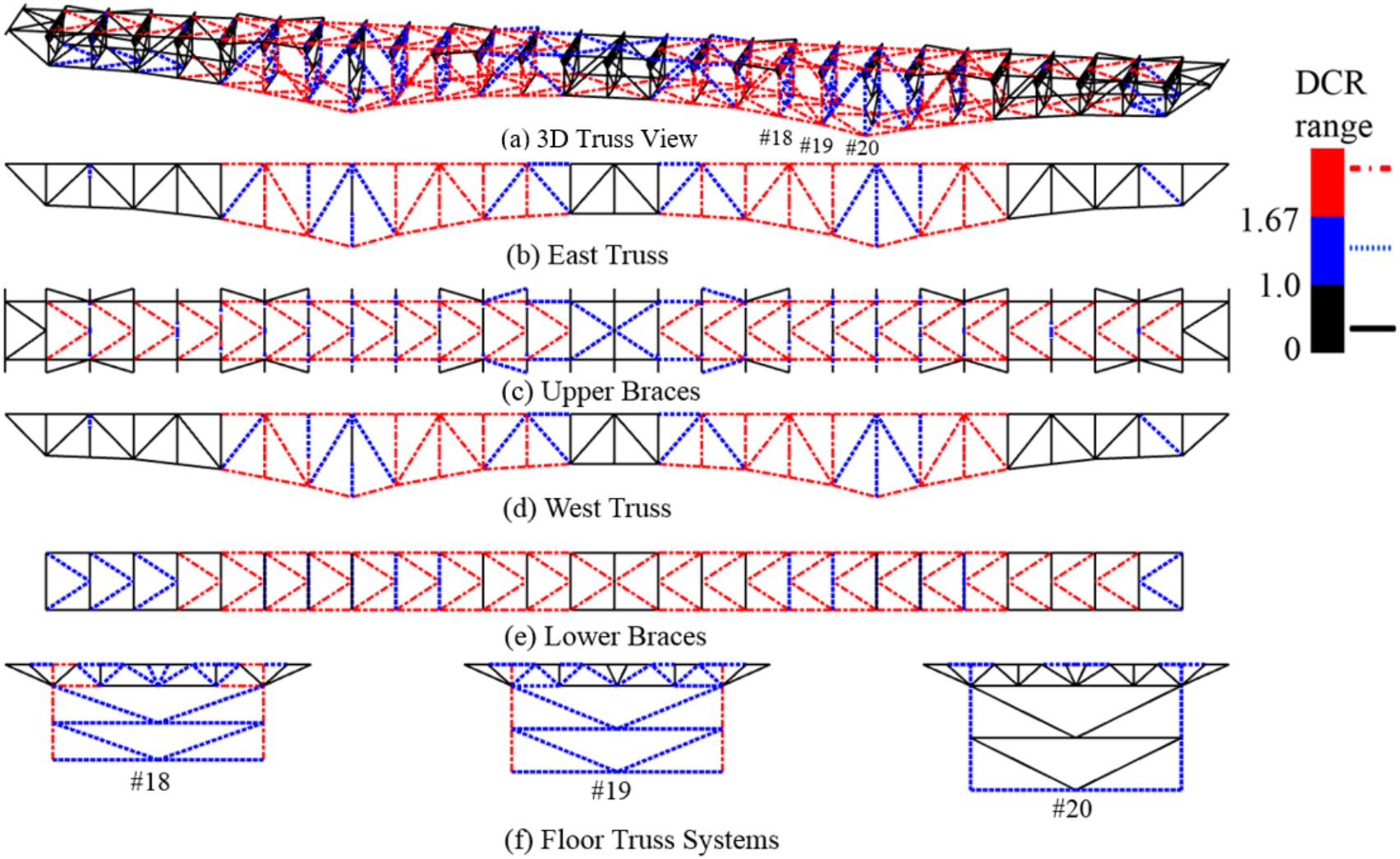

Source: FHWA.

Figure 83. Illustration. Complete envelope of *DCR* for the Base Bridge representing 40 MR cases (10 removal cases in each quarter of the bridge).

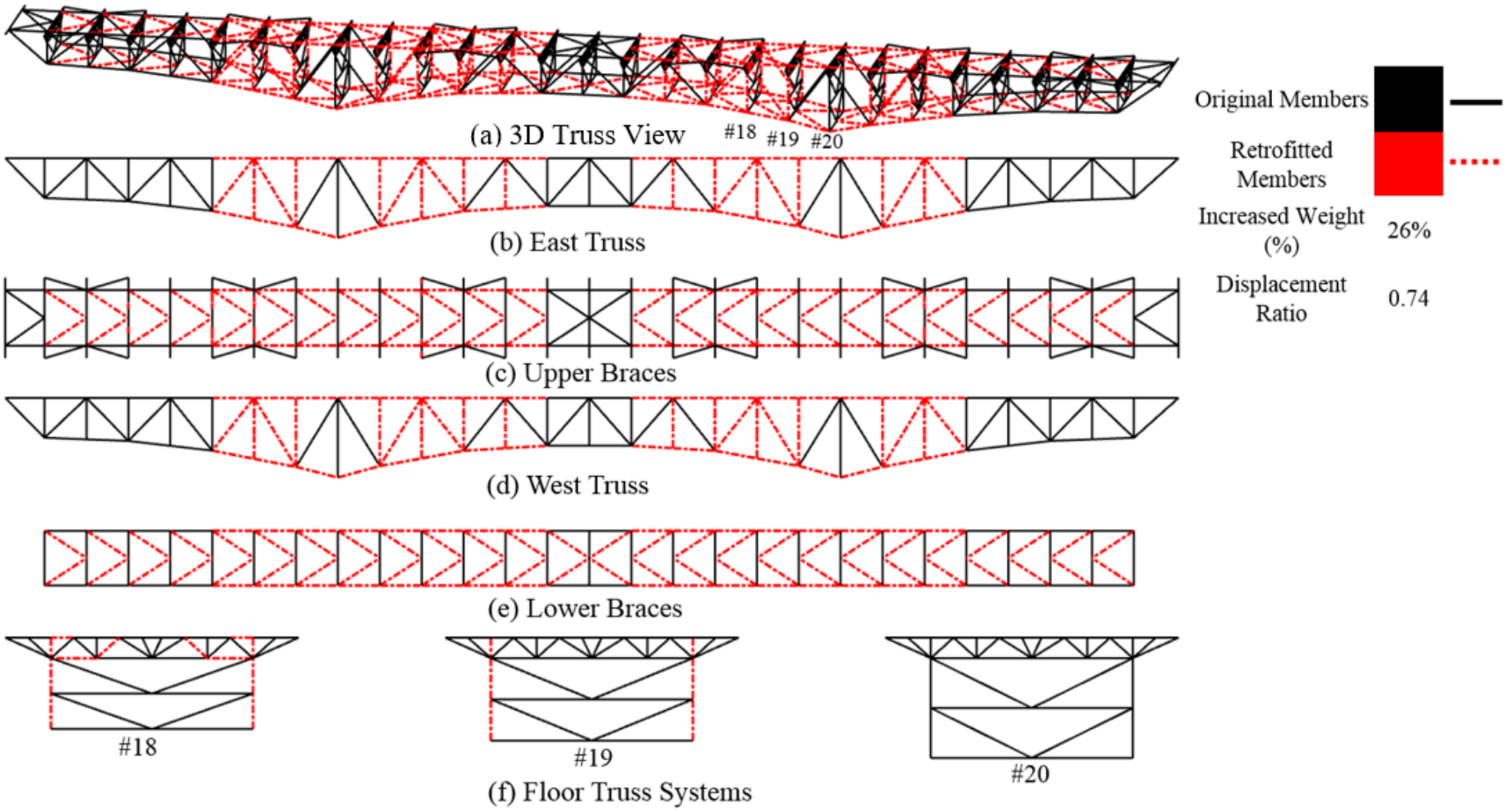

Source: FHWA.

Figure 84. Illustration. Member strengthening retrofit of the Base Bridge for MR based on *DCR* ≤ 1.67 limit state.

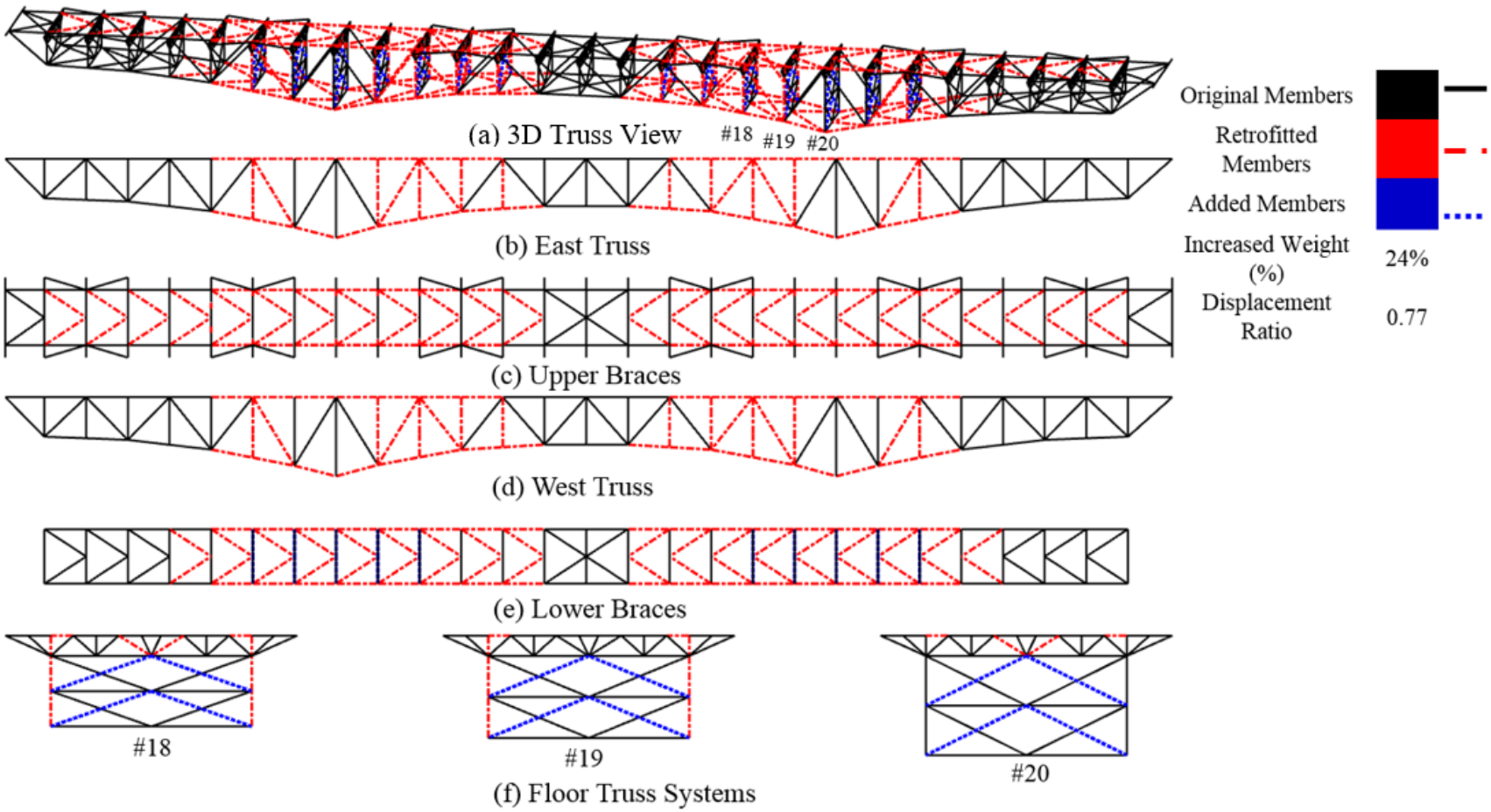

Source: FHWA.

Figure 85. Illustration. Addition of bracings in the floor truss systems and member strengthening retrofit of the Base Bridge for MR based on *DCR* ≤ 1.67 limit state.

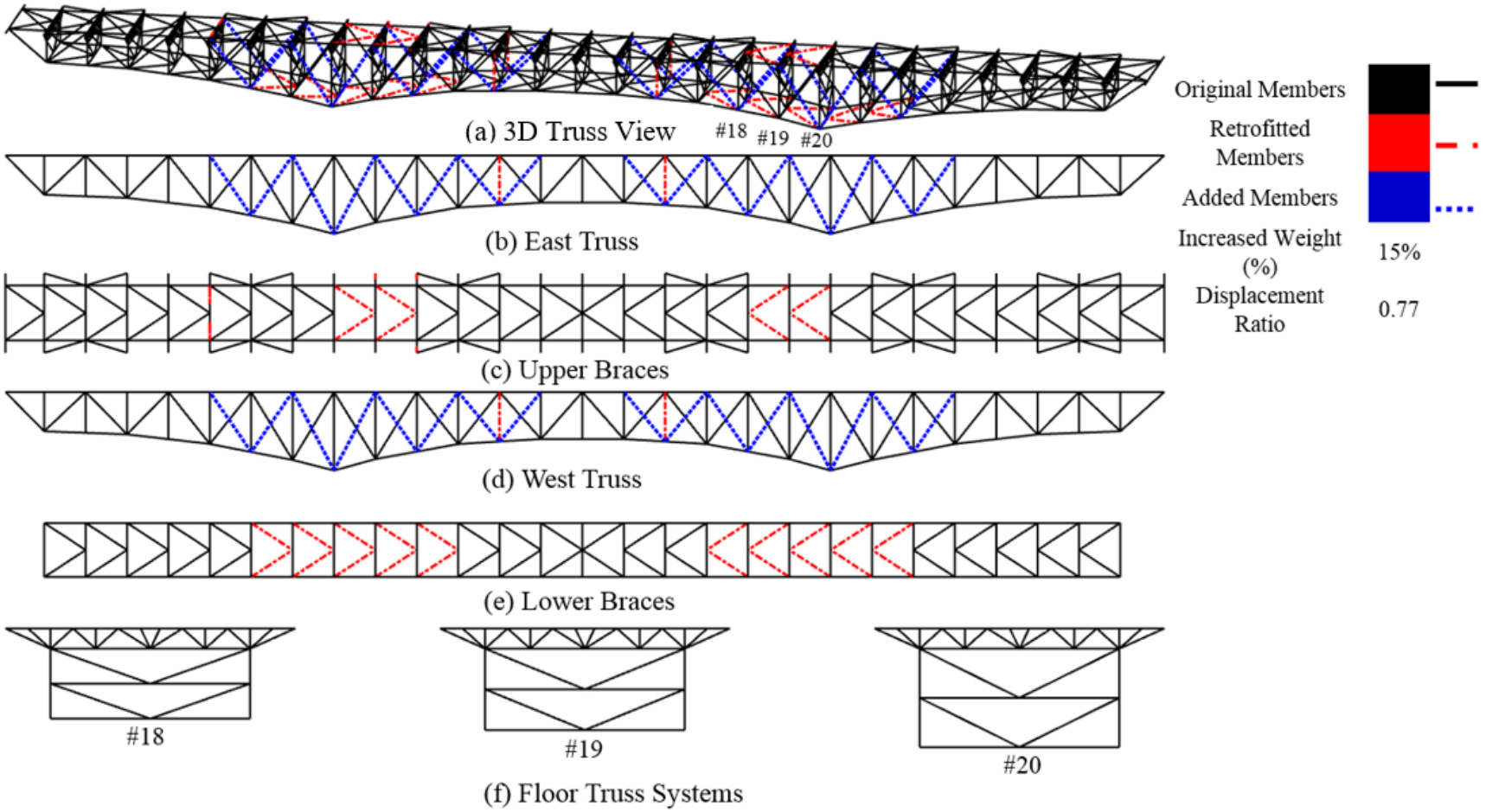

Source: FHWA.

Figure 86. Illustration. Addition of DMs and member strengthening retrofit of the Base Bridge for MR based on *DCR* ≤ 1.67 limit state.

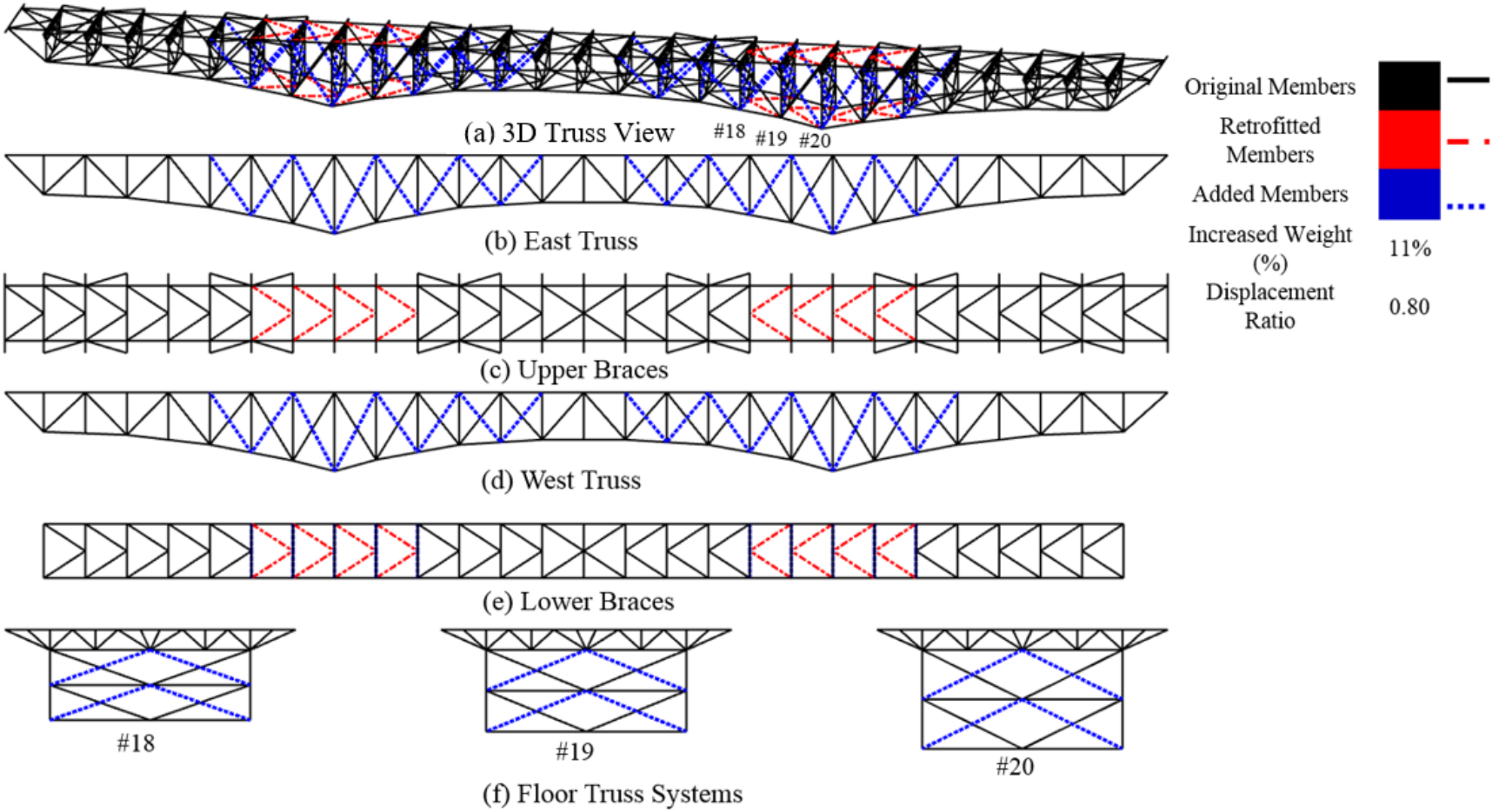

Source: FHWA.

Figure 87. Illustration. Addition of bracings in the floor truss systems, addition of DMs, and member strengthening retrofit of the Base Bridge for MR based on *DCR* ≤ 1.67 limit state.

Table 29. Increase in the weight of steel and DispRs for different MR retrofit strategies.

DCR Value	MR Retrofit Strategy	Additional Increased Weight (kN)	Increased Weight (%)	DispR
≤1.67	1-1	7,924	26	0.74
≤1.67	2-1	7,232	24	0.76
≤1.67	3-1	4,408	15	0.77
≤1.67	4-1	3,493	11	0.80
≤1.0	1-2	21,351	70	0.63
≤1.0	2-2	19,517	64	0.64
≤1.0	3-2	8,251	27	0.66
≤1.0	4-2	7,255	24	0.68

1 kN = 0.225 kips.
Note: The total steel weight of the Base Bridge was 30,378 kN.

To compare the effectiveness of different retrofit strategies in terms of displacement reduction, maximum vertical displacements corresponding to MR cases were normalized with respect to a reference maximum allowable displacement limit. According to section 2.5.2.6.2 of AASHTO (2014), the deflection limits for steel vehicular bridges can be considered as span length/800 for general conditions and span length/300 for the vehicular load on cantilever arms. For the abnormal loading conditions (MR or DMR) in this study, a higher level of deflection could be considered because of the rare probability of occurrence of MR or DMR events. In this research, the deflection limit used for the elastic analysis was span length/800 and for the nonlinear analysis in LS-DYNA was span length/300. It should be noted that these deflection limits are empirical and are based on very old criteria for short-span bridges. Generally, long-span bridges, including long-span truss bridges, can tolerate much higher levels of displacement without inelastic stress in any of the members. For example, the displacement limit where any member of the Base Bridge (without retrofit) will reach the yield stress is 507 mm (19.96 inches), whereas the displacement limits by span length/800 and span length/300 are 406 mm (15.98 inches) and 1,082 mm (42.6 inches), respectively.

Table 29 shows the magnitude of percentage weight increase and displacement ratio (DispR) for the four groups of retrofit strategies for two performance levels (i.e., $1.0 \leq DCR \leq 1.67$ and $DCR \leq 1.0$). Figure 88 shows plots of weight increase and DispRs for the four groups of retrofit strategies. DispR was selected as the indicator of the PBD and was defined as the peak of the maximum vertical displacement of the retrofitted bridge among 10 MR cases in table 20 for each retrofit strategy divided by the allowable deflection limit discussed in the previous paragraph.

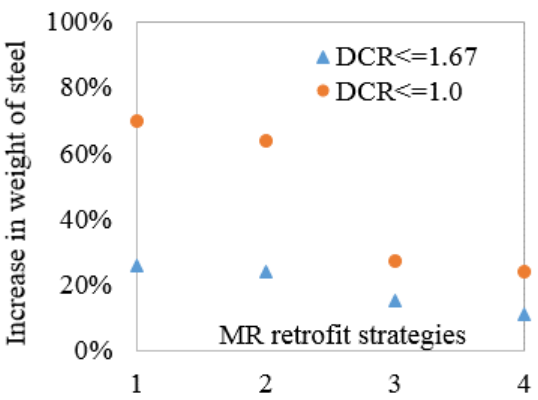

Source: FHWA.

A. Increase in weight of steel.

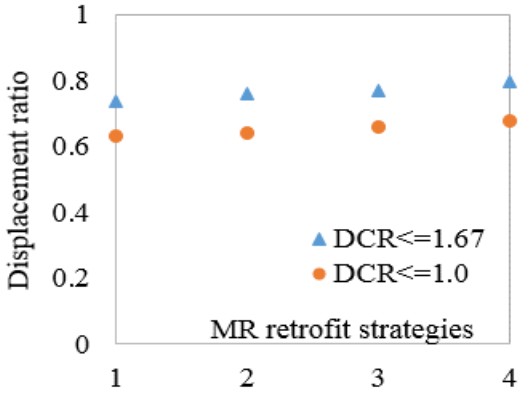

Source: FHWA.

B. Displacement ratio.

Figure 88. Graphs. Increase in weight of steel and DispRs for different MR retrofit strategies.

Table 29 and figure 88 demonstrate that the percentage increase in steel weight decreased from 26 to 11 percent for $1.0 \leq DCR \leq 1.67$ and from 70 to 24 percent $DCR \leq 1.0$ for retrofit strategies 1 to 4, whereas DispRs were similar for all retrofit strategies. This shows that all retrofit strategies had approximately similar performance. However, the member strengthening only retrofit was the least efficient, and the member strengthening combined with adding DMs and FS members retrofit was the most efficient from both cost (or weight of steel) and performance (displacement) points of view. This is important because an increase in the weight of the bridge would result in added seismic demand on the bridge member, thereby increasing seismic vulnerability while addressing vulnerability due to MR or DMR loads.

It should be noted that the addition of members (e.g., diagonal, FS, bracings) to improve ALP of the bridge can be formulated as an optimization problem with performance criteria in terms of *DCR* and DispR. Such optimization could yield much more efficient retrofit strategies than 4-1 and 4-2 that could enhance the ALP of the bridge much more with less corresponding increase in the weight of steel. However, such optimization for a complex long-span bridge would be very computationally expensive but could be investigated in future research. In this context, retrofit strategies 4-1 and 4-2 may not be the most optimized but can be considered to illustrate the potential of the three-dimensionality of the entire bridge system in improving ALP of long-span truss bridges. Retrofit strategies 4-1 or 4-2 also show that improvement in ALP of long-span truss bridges requires 3D interaction of added members with different vertical systems rather than a single vertical system of the bridge.

Retrofits for DMR

Similar to the DMR analysis in chapter 4 on the Design Bridge, DMR analysis was performed by considering six cases of DMR to obtain the complete envelope shown in figure 89. The bridge was retrofitted by four different retrofit strategies for performance levels $1.0 \leq DCR \leq 1.67$ and $DCR \leq 1.0$ in table 28. Table 30 shows the percentage increase in the weight of steel and the DispRs for eight cases of retrofits. Similar to the MR case, retrofit strategy 4 (i.e., 4-1 and 4-2) was the most efficient in terms of increase in the weight of steel, and the displacement

performance was similar among all four retrofit strategies. Figure 90 shows plots of the increase in the weight of steel and the DispRs for the four types of retrofits. The trend in this figure is similar to that for the MR retrofit cases in figure 88. The increase in weight of the steel was higher for DMR than for MR.

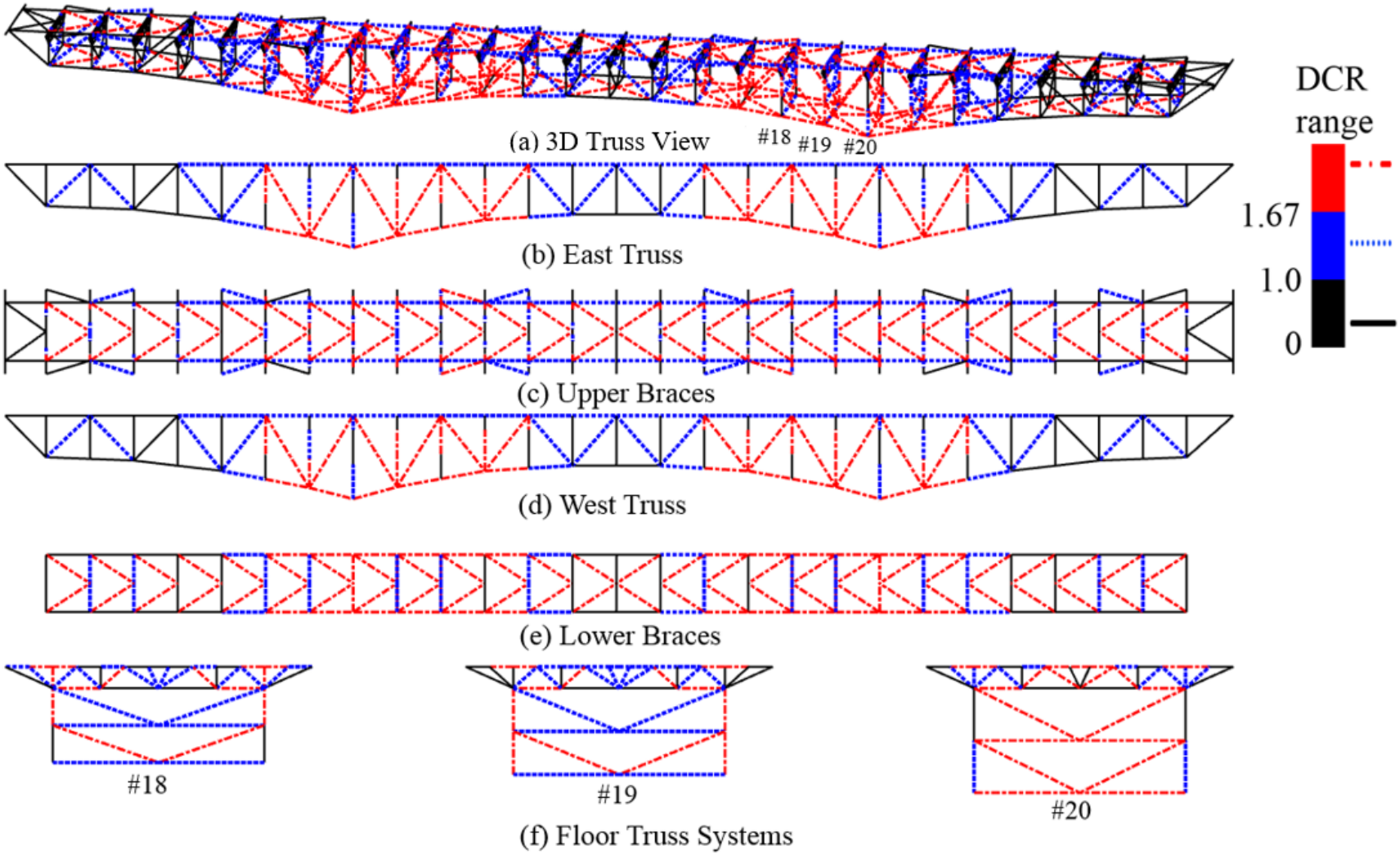

Source: FHWA.

Figure 89. Illustration. Complete envelope of *DCR* for the Base Bridge representing 40 DMR load cases (10 DMR cases in each quarter of the bridge).

Table 30. Increase in the weight of steel and DispRs for different DMR retrofit strategies.

DCR Value	DMR Retrofit Strategy	Additional Increased Weight (kN)	Increased Weight (%)	DispR
≤1.67	1-1	10,014	33	0.77
≤1.67	2-1	8,734	31	0.78
≤1.67	3-1	36,796	21	0.81
≤1.67	4-1	35,738	18	0.83
≤1.0	1-2	55,988	84	0.61
≤1.0	2-2	13,463	77	0.62
≤1.0	3-2	2,422	39	0.64
≤1.0	4-2	4,079	35	0.67

1 kN = 0.225 kips.
Note: The total steel weight of the Base Bridge was 30,378 kN.

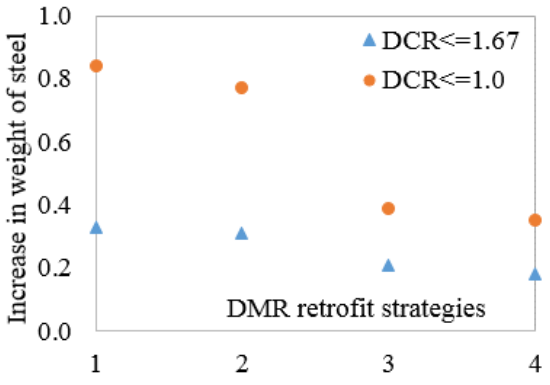

Source: FHWA.

A. Increase in weight of steel.

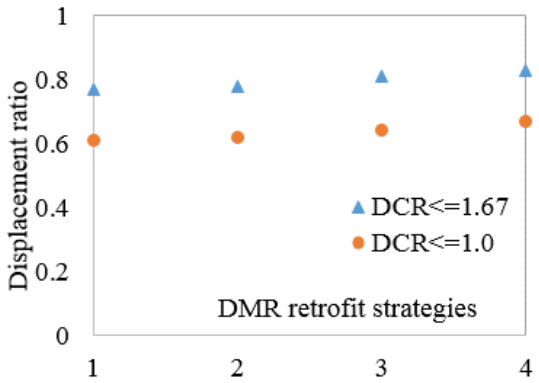

Source: FHWA.

B. Displacement ratio.

Figure 90. Graphs. Increase in weight of steel and DispRs for different DMR retrofit strategies.

SR-BASED RETROFIT SCHEMES

For *SR*-based retrofit, three levels of performance in terms of *SR* (which are correlated to levels of ductility) are defined in table 31. When the *SR* is equal to or less than 1.0, the bridge system is in the elastic range. When $SR \leq 2.0$ (low ductility), some members are allowed to have strain beyond the yield limit because of the ductility of steel. For this level of performance, no retrofit is needed for an assumed MR or DMR loading scenario. When bridge members are allowed a ductility of medium level, *SR* is assumed to be less than or equal to 4.0. Allowable bridge deflection for the three levels of *SR* and ductility are shown in table 31. Figure 91 illustrates the subjective relationship between *DCR* and *SR* metrics.

Table 31. *SR*-based retrofit levels for an assumed blast intensity.

Performance Level	*SR*	Displacement Ratio (≤1.0)	Comment
Elastic range	$SR \leq 1.0$	$L/800$	Linear elastic range
Low ductility	$SR \leq 2.0$	$L/300$	No retrofit needed
Medium ductility	$SR \leq 4.0$	$L/300$	Not observed

L = bridge span length.

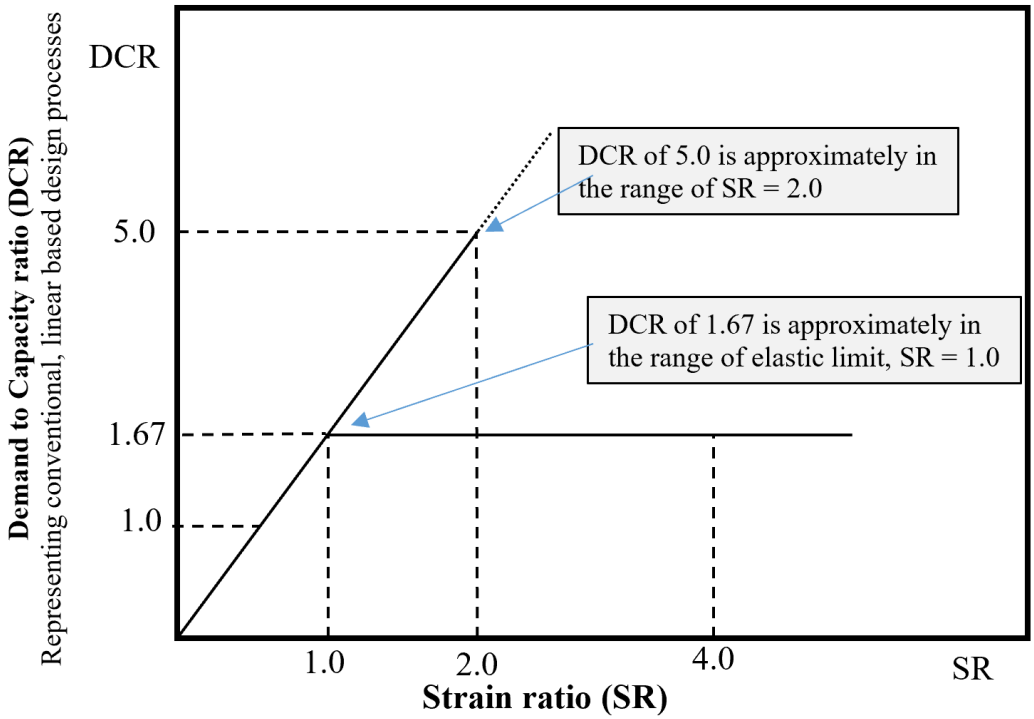

Source: FHWA.

Figure 91. Graph. Subjective relationships between *DCR* and *SR* metrics.

During inelastic analysis in LS-DYNA, both peak dynamic and steady-state results were used for comparison. The four types of retrofit strategies in table 28 were investigated for both MR and DMR loading scenarios.

Retrofits for MR

Figure 92 shows the complete envelope of truss members of the bridge for MR scenarios in terms of the three levels of *SR*. This figure demonstrates that, although many truss members had *SR*s in the range of $1.0 < SR \leq 2.0$, none of the truss members had an $SR > 2.0$. Hence, the only level of retrofit required was for the performance level $SR \leq 1.0$, when a retrofit strategy will reduce the *SR* of members shown in red dotted lines to *SR* less than or equal to 1.0. Hence, there are only four retrofit strategies for the first performance level and no retrofit requirements for performance levels 2 and 3. Table 32 shows the increase in the weight of steel for the $SR \leq 1.0$ limit state for the four retrofit strategies.

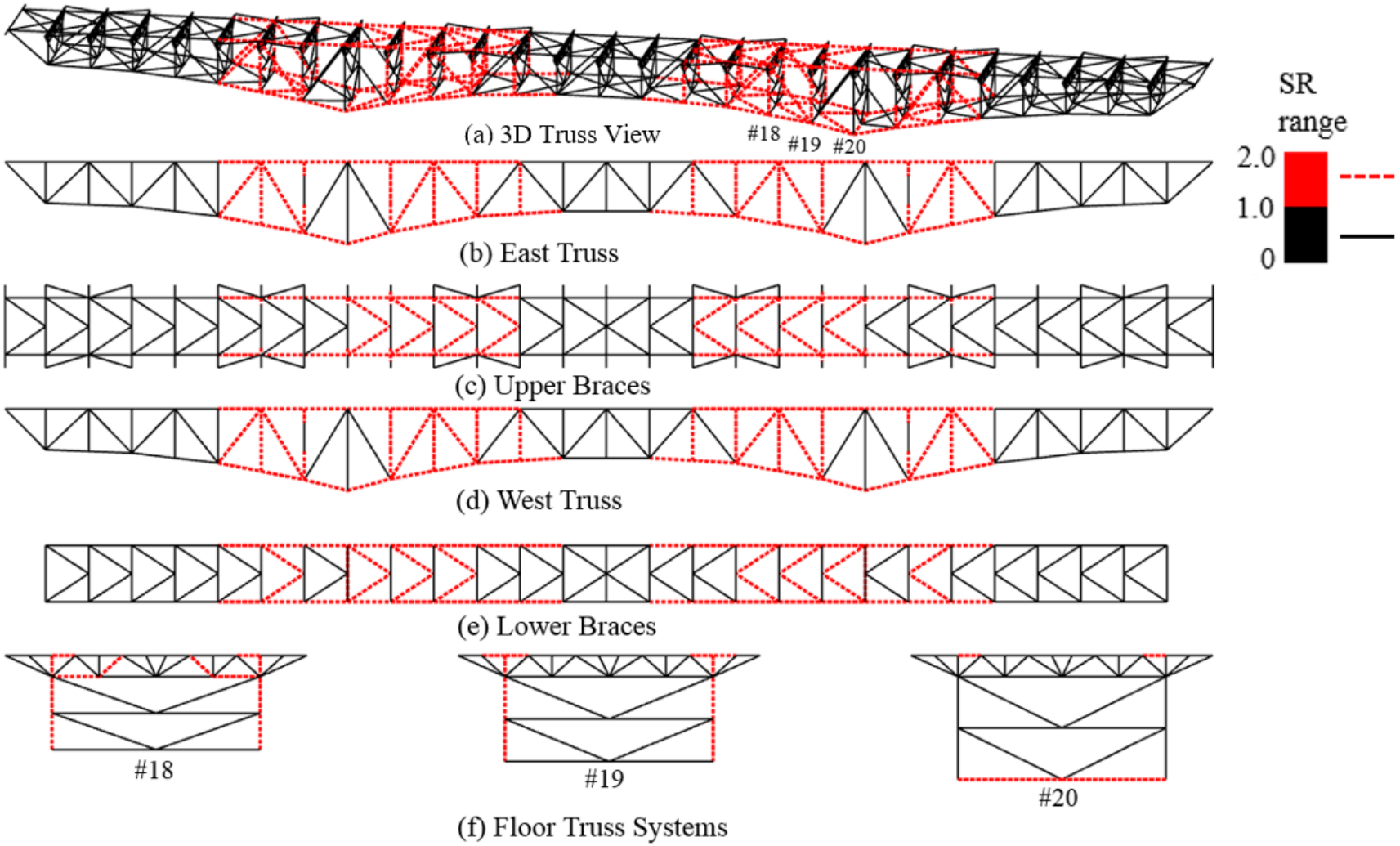

Source: FHWA.

Figure 92. Illustration. Complete envelope of *SR* for the Base Bridge representing 40 MR cases (10 removal cases in each quarter of the bridge).

Table 32. Percentage increase in the weight of steel for different MR retrofit strategies based on *DCR* and *SR* limit states.

Performance Level	Limit State	1: Member Strengthening Only	2: Adding Bracings in FS + Member Strengthening	3: Adding DMs + Member Strengthening	4: Adding DMs + Adding Bracings in FS + Member Strengthening
Factor of safety (>1.0)	$DCR \leq 1.0$	70	64	27	24
Elastic limit state	$1.0 < DCR \leq 1.67$	26	24	15	11
Elastic limit state (peak strain)	$SR \leq 1.0$[a]	23	20	13	9
Elastic limit state (steady-state strain)	$SR \leq 1.0$[b]	18	16	9	7
Low ductility	$DCR \leq 5.0$	NA	NA	NA	NA
Low ductility	$SR \leq 2.0$	0	0	0	0
Medium ductility	$SR \leq 4.0$	NO	NO	NO	NO

[a]MR demands using the peak of NLD strain.
[b]MR demands using the peak of steady-state strain.
NA = not applicable; NO = not observed.

After removal of a member, bridge members undergo peak dynamic strain (or displacement) before damping out to steady-state strain (or displacement), as shown in the time history response in figure 45. Hence, the performance level $SR \leq 1.0$ could be imposed on either the peak dynamic strain or the steady-state strain. The percentage increase in steel weight for these two types of strain is presented in separate rows of table 32 corresponding to the elastic limit state for peak strain and the elastic limit state for steady-state strain. Because $SR \leq 1.0$ is an elastic limit state, the percentage increase in weight corresponding to $DCR \leq 1.0$ and $1.0 \leq DCR \leq 1.67$, which are also elastic limit states, are shown in table 32 for comparison. Table 32 demonstrates that the percentage increase in the weight of steel considering inelastic behavior of the bridge during MR was much smaller than that based on *DCR* (which considers elastic behavior of the bridge). Furthermore, the percentage increase in weight considering $SR \leq 1.0$ for peak dynamic strain was slightly higher than that considering $SR \leq 1.0$ for steady-state strain. For example, for retrofit strategy 4, which was found to be the most cost-effective based on *DCR*, the percentage increase in weight for $1.0 \leq DCR \leq 1.67$ was 11 percent, whereas it was 9 and 7 percent for $SR \leq 1.0$ for peak dynamic and steady-state strains, respectively. These results are illustrated in a bar chart in figure 93.

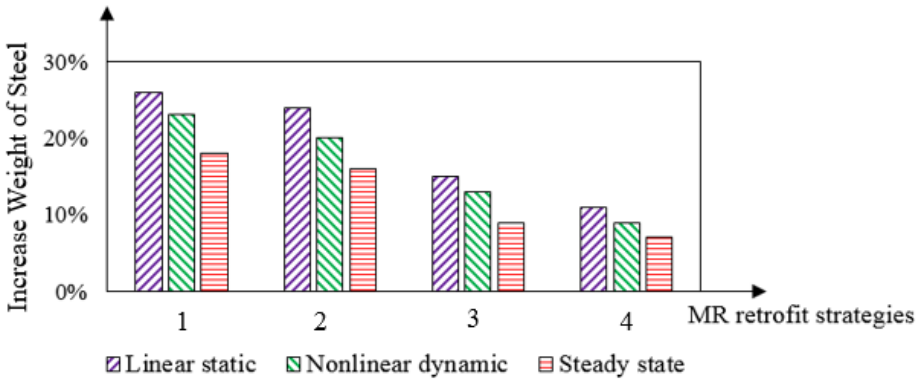

Source: FHWA.

Figure 93. Chart. Percentage increase in the weight of steel for different MR retrofits based on *SR* limit states.

The results illustrated in figure 93 can have significant implications on the design of retrofit strategies. For a given retrofit strategy, for example retrofit strategy 3, performing inelastic analysis in LS-DYNA instead of elastic analysis in SAP2000 could result in cost savings of 6 percent of the weight of steel if $SR \leq 1.0$ is based on steady-state strain. However, if it is important to consider $SR \leq 1.0$ based on peak dynamic strain, this cost savings in the weight of steel could be just 2 percent. This cost savings of 2 percent could be significantly more than the savings in analysis costs for performing elastic analysis. Generally, factors for labor and other costs are significantly more than material cost factors. Analysis models that consider material and geometric nonlinearities also give more reliable retrofit performance results and are able to provide a more realistic picture of actual damage in the event of sudden member loss.

Retrofits for DMR

Figure 94 shows the complete envelope of truss members of the bridge for DMR scenarios in terms of the three levels of *SR*. Figure 94 demonstrates that many truss members had *SR*s in the range of $1.0 < SR \leq 2.0$ and a few bracings had $SR > 2.0$. Hence, two levels of retrofit were required: (1) reducing members with $1.0 < SR \leq 2.0$ to $SR \leq 1.0$, and (2) reducing members with $2.0 < SR \leq 4.0$ to $SR \leq 2.0$. For performance level 1 ($SR \leq 1.0$), four retrofit scenarios were investigated for DMR cases. For performance level 2 ($SR \leq 2.0$), because only eight secondary bracings and a few members in the FSs needed retrofits, the member strengthening retrofit strategy (strategy 1) was efficient in reducing *SR* to ≤ 2.0. The weight increase in this case was 3 percent. Table 33 shows increase in weight of steel for $SR \leq 1.0$ for the four retrofit strategies.

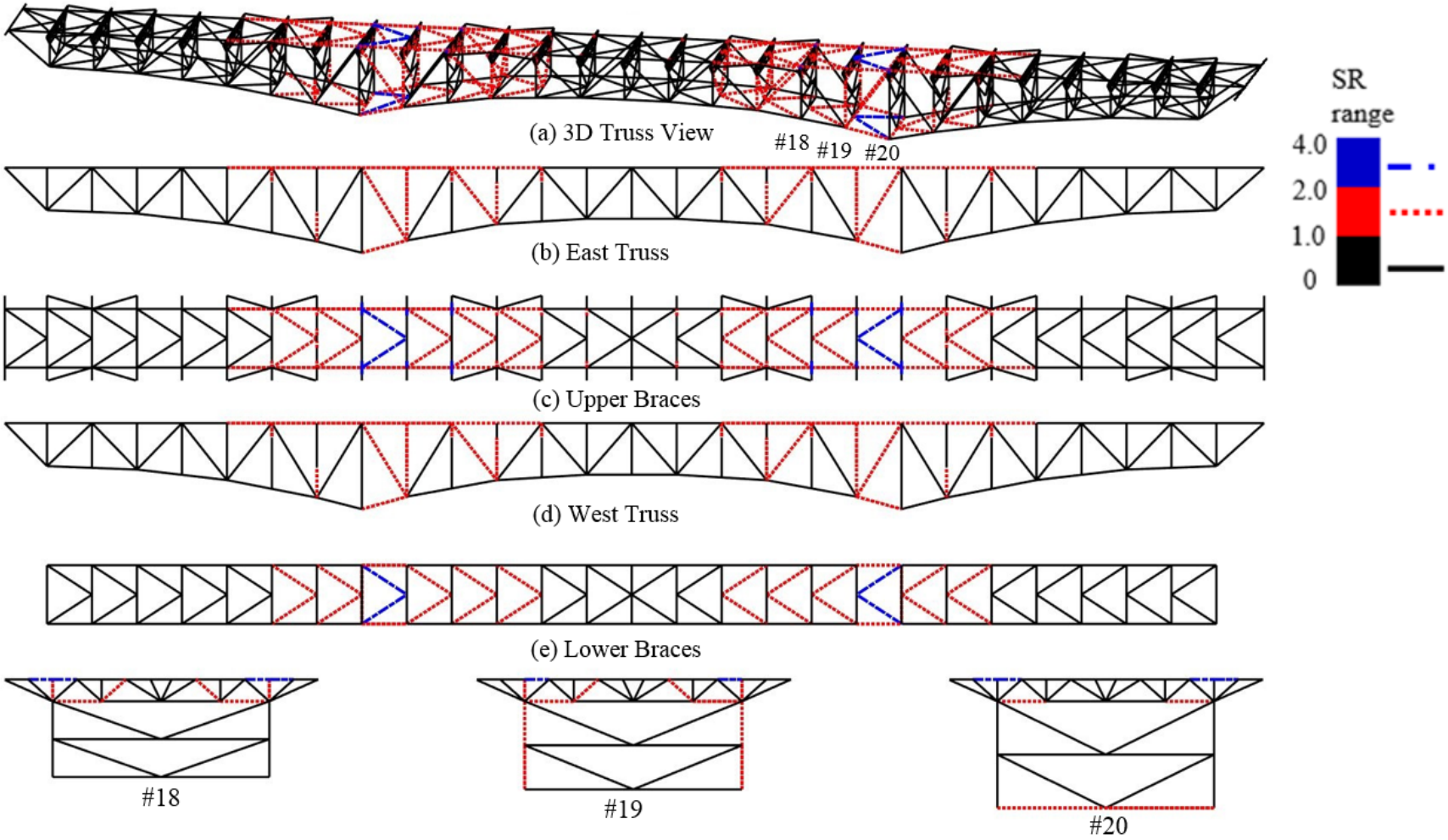

Source: FHWA.

Figure 94. Illustration. Complete envelope of *SR* for the Base Bridge representing 40 DMR cases (10 DMR cases in each quarter of the bridge).

Table 33. Percentage increase in the weight of steel for different DMR retrofit strategies.

Performance Level	Limit State	1: Member Strengthening Only	2: Adding Bracings in FS + Member Strengthening	3: Adding DMs + Member Strengthening	4: Adding DMs + Adding Bracings in FS + Member Strengthening
Factor of safety (>1.0)	$DCR \leq 1.0$	84	77	40	35
Elastic limit state	$1.0 < DCR \leq 1.67$	33	31	23	18
Elastic limit state (peak strain)	$SR \leq 1.0$[a]	33	31	19	15
Elastic limit state (steady-state strain)	$SR \leq 1.0$[b]	25	22	16	13
Low ductility	$DCR \leq 5.0$	NA	NA	NA	NA
Low ductility	$SR \leq 2.0$	3	NA	NA	NA
Medium ductility	$SR \leq 4.0$	NO	NO	NO	NO

[a]DMR demands using the peak of NLD strain.
[b]DMR demands using the peak of steady-state strain.
NA = not applicable; NO = not observed.

The percentage increase in the weight of steel for $SR \leq 1.0$, where SR is calculated by peak dynamic and steady-state strains, is presented in separate rows of table 33 corresponding to elastic limit state for peak strain and elastic limit state for steady-state strain). The percentage increase in the weight of steel corresponding to $DCR \leq 1.0$ and $1.0 \leq DCR \leq 1.67$, which are also elastic limit states, are shown in table 33 for comparison. Table 33 demonstrates that the percentage increase in the weight of steel by considering inelastic behavior of the bridge during DMR was much smaller than that based on DCR for retrofits 3 and 4, which are effective in improving ALP.

Furthermore, the percentage increase in weight considering $SR \leq 1.0$ for peak dynamic strain was slightly higher than that considering $SR \leq 1.0$ for steady-state strain, particularly for retrofit strategy 4. For example, for retrofit strategy 4, which was found to be the most cost-effective based on DCR, percentage increase in the weight of steel for $1.0 \leq DCR \leq 1.67$ was 18 percent, whereas it was 15 and 13 percent for $SR \leq 1.0$ for peak dynamic and steady-state strains, respectively. These two increases in weight of steel were 9 percent and 7 percent, respectively, for the MR scenario (table 32). These results are illustrated in a bar chart in figure 95. The trend of results for DMR scenarios was the same as that for MR scenarios, although the increase in the weight of steel was more in DMR cases because they represent more extreme loading scenarios.

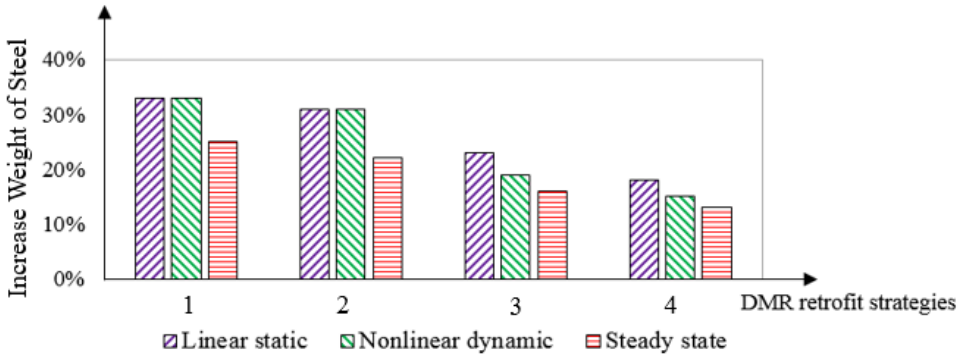

Source: FHWA.

Figure 95. Chart. Percentage increase in the weight of steel for different DMR retrofits based on *SR* limit states.

DYNAMIC LOAD AMPLIFICATION

Three types of displacements can be obtained for each of the four retrofit strategies. Analysis of MR and DMR cases in SAP2000 gives linear static displacement, whereas NLD analysis in LS-DYNA gives both peak dynamic and steady-state displacements. For example, as shown in the time history plot of vertical displacement at node 18 on the west side truss in figure 45 in chapter 3, the magnitude of the peak dynamic displacement was 613 mm (24.13 inches), whereas the steady-state displacement was 504 mm (19.84 inches) after the vibration damped out and the bridge gradually reached steady-state equilibrium. From the results of simulations, three displacements for the lower nodes of trusses of the bridge were recorded to calculate nonlinear static (NLS) and NLD factors. The NLS factor is calculated as the steady-state displacement from LS-DYNA divided by the linear static displacement from SAP2000. Likewise, the NLD factor is calculated as the peak dynamic displacement from LS-DYNA divided by the linear static displacement from SAP2000. Table 34 and table 35 show the maximum NLS and NLD factors for 10 MR and 10 DMR cases, respectively. These tables also show the dynamic load amplification (DLA) factor, which is NLD divided by NLS. The NLS factors for both MR and DMR cases were about 1, which was expected. The steady-state displacement from LS-DYNA was expected to be slightly higher than the linear static value from SAP2000 because of modeling of geometrical and material nonlinearities and finite-element formulation (B-S beam element in LS-DYNA versus frame element in SAP2000). The NLD factor varied from 1.06 to 1.75 for MR cases and from 1.18 to 2.02 for DMR cases, depending on the severity of the MR or DMR loading. The DLA factor, which could be considered the amplification in response because of dynamic loading, varied from 1.05 to 1.60 for MR cases and from 1.14 to 1.71 for DMR cases. For a mass attached to an undamped spring, the DLA is 2 (Chopra 2000).

Table 34. DLA for different MR analysis cases and scenarios.

MR Case	NLS Factor	NLD Factor	DLA
1	1.10	1.75	1.60
2	1.09	1.30	1.19
3	1.09	1.29	1.18
4	1.01	1.06	1.05
5	1.03	1.19	1.16
6	1.02	1.13	1.11
7	1.02	1.31	1.28
8	1.01	1.12	1.11
9	1.09	1.66	1.51
10	1.01	1.30	1.29
Range	1.01–1.10	1.06–1.75	1.05–1.60

Table 35. DLA for different DMR analysis cases and scenarios.

DMR Case	NLS Factor	NLD Factor	DLA
1	1.11	1.79	1.62
2	1.19	2.02	1.71
3	1.08	1.28	1.18
4	1.04	1.18	1.14
5	1.08	1.28	1.18
6	1.19	2.02	1.71
7	1.19	2.02	1.71
8	1.08	1.28	1.18
9	1.12	1.78	1.59
10	1.03	1.43	1.39
Range	1.03–1.19	1.18–2.02	1.14–1.71

The recent AASHTO *Guide Specifications for Analysis and Identification of Fracture Critical Members and System Redundant Members* recommended a DLA of 1.4 for long-span truss bridges (AASHTO 2018a). Table 34 shows that a DLA factor of 1.4 is conservative for eight cases of MR and slightly less conservative for MR cases 1 and 9. Hence, considering some conservatism in the design practice (i.e., *DCR* may be slightly less than 1 instead of being just 1), the DLA factor of 1.4 recommended in AASHTO (2018a) seems to be sufficient when using simplified design using commercial software such as SAP2000. It should be noted that the DLA factor for DMR for some cases was slightly higher than that for MR, which was expected because the dynamic effect of sudden DMR was expected to be higher than that for MR.

Table 36 and table 37 show linear static displacement from SAP2000 and peak dynamic and steady-state displacements from LS-DYNA for MR and DMR cases, respectively, normalized by the elastic deflection limit of span length/800 in AASHTO (2014). These ratios were calculated for MR and DMR loads for the four retrofit strategies investigated to achieve performance levels in terms of *SR* and *DCR*. Only results for performance levels representing elastic behavior of the retrofitted bridge in the event of MR or DMR (i.e., $SR \leq 1.0$ and $1.0 \leq DCR \leq 1.67$) are presented in table 36 and table 37. All displacements stayed below the allowable displacement limit. In

addition, the steady-state, peak, and linear static displacements all stayed below or around the displacement limit of span length/800, which was 406 mm (15.98 inches) for the I-35W Bridge. Although the added percentage weight of steel because of retrofit decreased from retrofit strategies 1 to 4, the maximum DispRs for MR and DMR loads were similar for retrofit strategies 1 to 4. This shows that the increased displacement because of added steel to the bridge was counterbalanced by the increased stiffness because of the retrofit.

Table 36. DispRs for MR cases of ALP-retrofitted bridge with the elastic deflection limit $L/800$ for the four retrofit strategies.

MR Case	NLD, Steady State ($SR \leq 1.0$)				NLD, Peak Response ($SR \leq 1.0$)				Linear Static ($1.0 \leq DCR \leq 1.67$)			
	1	2	3	4	1	2	3	4	1	2	3	4
Case 1	0.98	0.77	0.8	0.83	0.82	0.91	0.62	0.68	0.69	0.68	0.60	0.60
Case 2	0.89	0.98	0.92	0.94	0.96	1.00	0.76	0.83	0.74	0.72	0.66	0.67
Case 3	0.84	0.94	0.94	0.96	0.92	0.94	0.78	0.87	0.7	0.68	0.68	0.68
Case 4	0.66	0.71	0.78	0.81	0.62	0.71	0.6	0.65	0.58	0.58	0.59	0.59
Case 5	0.74	0.85	0.93	0.95	0.8	0.85	0.81	0.88	0.66	0.65	0.68	0.68
Case 6	0.69	0.79	0.89	0.93	0.71	0.76	0.76	0.82	0.62	0.61	0.66	0.66
Case 7	0.78	0.73	0.79	0.82	0.71	0.85	0.61	0.66	0.62	0.63	0.59	0.59
Case 8	0.64	0.70	0.77	0.81	0.6	0.70	0.59	0.65	0.56	0.56	0.58	0.58
Case 9	0.97	0.78	0.8	0.83	0.77	0.88	0.62	0.68	0.69	0.68	0.6	0.6
Case 10	0.91	0.78	0.8	0.83	0.88	0.99	0.61	0.67	0.72	0.72	0.6	0.6
Maximum	0.98	0.98	0.94	0.96	0.96	1.00	0.81	0.88	0.74	0.72	0.68	0.79
Weight increase percentage	18	16	9	7	23	20	13	9	26	24	15	11

Table 37. DispRs for DMR cases of ALP-retrofitted bridge with the elastic deflection limit $L/800$ for the four retrofit strategies.

DMR Case	NLD, Steady State ($SR \leq 1.0$)				NLD, Peak Response ($SR \leq 1.0$)				Linear Static ($1.0 \leq DCR \leq 1.67$)			
	1	2	3	4	1	2	3	4	1	2	3	4
Case 1	0.83	0.84	0.93	0.96	0.93	0.83	0.94	0.91	0.79	0.70	0.71	0.70
Case 2	0.96	0.97	0.89	0.92	1.05	0.95	0.88	0.85	0.84	0.75	0.68	0.67
Case 3	0.61	0.66	0.96	0.99	0.88	0.79	0.99	0.97	0.73	0.65	0.70	0.70
Case 4	0.56	0.6	0.93	0.96	0.82	0.72	0.96	0.93	0.70	0.62	0.7	0.69
Case 9	0.77	0.72	0.77	0.81	0.85	0.74	0.75	0.74	0.75	0.66	0.61	0.60
Case 10	0.74	0.75	0.77	0.81	0.92	0.82	0.74	0.74	0.80	0.70	0.61	0.60
Maximum	0.96	0.97	0.96	0.99	1.05	0.95	0.99	0.97	0.84	0.75	0.71	0.70
Weight increase percentage	25	22	16	13	33	31	19	15	33	31	23	18

CRITICAL EVALUATION OF RETROFIT PERFORMANCE

Results of this detailed investigation showed that the member strengthening only or the section strengthening was the least cost-effective approach for improving the resistance of the bridge against MR or DMR events. Rather, strengthening in combination with improvement in the bridge truss system by adding new members was significantly more efficient at enhancing ALP of the bridge. Among the four retrofit strategies investigated, the fourth retrofit strategy was the

most sophisticated because it involved three major subcomponents of the bridge. Results presented in this chapter show that the design of retrofits for ALPs is an optimization problem that, when solved through complex and time-consuming finite-element simulations, can result in a retrofit strategy that can potentially improve the ALP of long-span truss bridges without any significant increase in the cost of the retrofit.

CHAPTER 6. IKITSUKI BRIDGE MODELING, ALP ANALYSIS, AND PERFORMANCE-BASED RETROFITS

INTRODUCTION

In previous chapters, the ALP of the I-35W Bridge, which was a deck-truss bridge, was investigated. Through-truss bridges, such as the Ed Koch (Queensboro) Bridge in New York City and the Commodore Barry Bridge over the Delaware River between Pennsylvania and New Jersey, are another prevalent type of long-span truss bridges. In this chapter, the ALP of a long-span through-truss bridge was investigated following the approach developed for the I-35W Bridge. The Ikitsuki Bridge, shown in figure 96, connecting Ikitsuki to Hirado Island in Japan, is the longest continuous truss bridge in the world, with a main span of 400 m (1,311.48 ft) and two side spans of 200 m (655.74 ft) each. Construction of the bridge was completed in July 1991. Previous research on this bridge focused on the nonlinear seismic response properties of the bridge (Kubota et al. 2004). In an inspection in December 2009, a critical crack was found in a DM near an intermediate support (Nakamura et al. 2016; Wang et al. 2017). This crack began and propagated as a fatigue crack due to wind-induced vibration. Because fatigue cracks are localized structural damage, progressive, and often lead to loss of a critical member, this bridge is a good candidate for investigation of ALP in long-span through-truss bridges. This bridge was selected for study in this research because of the availability of bridge plans, section details, and monitoring data. Results of this investigation demonstrate that the approach in this research is applicable to similar types of long-span bridges in the United States.

Figure 96. Photo. Ikitsuki Bridge connecting Ikitsuki and Hirado Island in Japan.

FINITE-ELEMENT MODELING OF THE BRIDGE

The finite-element modeling approach for the Ikitsuki Bridge was similar to that for the I-35W Bridge using LS-DYNA and SAP2000. The FEM of the bridge in LS-DYNA included main side trusses, floor trusses, floor stringers, and secondary bracing members. All truss members, bracings, and stringers were modeled by B-S beam elements using the Mat 98 material model in LS-DYNA to account for both geometric and material nonlinearity and strain hardening in steel. Each element of the truss was modeled by a single beam element. In addition, the deck system was modeled by shell elements with elastic material for imposing *DL* of the concrete deck on the truss system. Overall, the LS-DYNA model had 3,230 beam elements and 128 shell elements.

The model in SAP2000 was similar to that in LS-DYNA except the equivalent nodal mass was assigned at deck stringers instead of shell elements. The deck in LS-DYNA was assigned a low Young's modulus of elasticity so that the stiffness of the deck did not add to the stiffness of the truss (i.e., the deck was modeled just to transfer *DL* and *LL* from the deck to the truss). All beam elements in SAP2000 were assigned elastic material properties. The two trusses of the bridge are on the north and south sides, and traffic on the bridge is in east and west directions. Figure 97 shows the elevation, plan, and side views of the bridge. Piers P4, P5, and P7 of the bridge have roller supports, and pier P6 has fixed support.

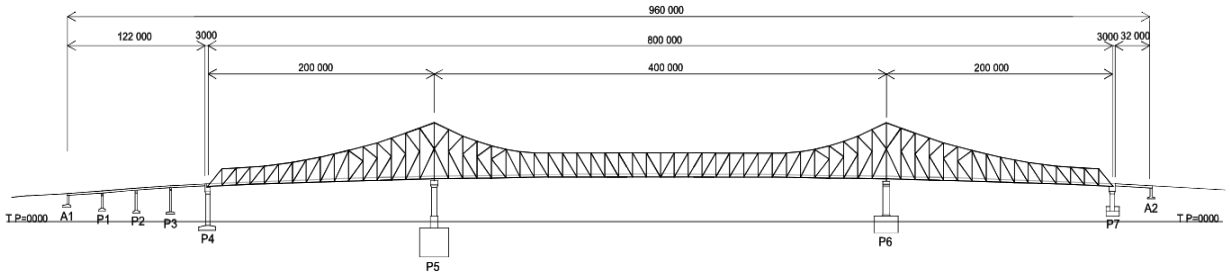

© 2018 Shozo Nakamura, Nagasaki University, Japan.
1 mm = 0.0394 inches.

A. Elevation view.

© 2018 Shozo Nakamura, Nagasaki University, Japan.
1 mm = 0.0394 inches.

B. Plan view.

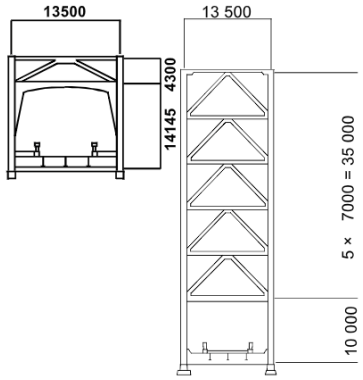

© 2018 Shozo Nakamura, Nagasaki University, Japan.
1 mm = 0.0394 inches.

C. Side view.

Figure 97. Illustrations. Overall layout drawing of Ikitsuki Bridge (unit: mm).

Loads and Load Combinations

Analysis of the two FEMs (SAP2000 and LS-DYNA) was performed for *DL* and *LL*. The seismic load scenario has not been investigated because the bridge was built in 1991 when seismic design criteria were well established. *DL* and *LL* were applied per load combinations in equations 8 and 9 in chapter 2. Although the bridge was designed according to Japanese code, the *LL* applied in the study follows the AASHTO LRFD specifications (2014).

The deck system of the bridge is composed of a concrete-filled I-beam grid floor 0.16 m (0.63 inches) in thickness. The design compressive strength of the concrete was 24 MPa (3.48 ksi). The weight of steel in the entire bridge is approximately 64,200 kN (14,432.73 kips), which consists of the main structure (43,700 kN (9,824.15 kips)), floor system (8,780 kN (1973.82 kips)), and lateral bracings and cross frames (11,720 kN (2,634.76 kips)). Unit weights of steel and reinforced concrete are 77 kN/m^3 (494.58 lb/ft^3) and 24.5 kN/m^3 (157.37 lb/ft^3), respectively. According to Kubota et al. (2004), the main truss members, accessories, and concrete deck weigh 64,200 kN (14,432.73 kips), 3,100 kN (696.91 kips), and 48,800 kN (10,970.68 kips), respectively. The sum of these is 113,000 kN (25,403.41 kips). In the FEM, the total weight of steel members was 88,948 kN (19,996.31 kips), and the weight of the concrete deck was 23,224 kN (5,220.96 kips). The sum of these is 112,172 kN (25,217.27 kips), which is approximately 0.7-percent different from the total weight calculated by Kubota et al. (2004). This comparison is shown in table 38. Table 39 shows the eight support reactions for different load combinations on both sides of the bridge. The *LL* is approximately 13.5 percent of the *DL*. The two supports in the central span carry approximately 96.2 percent of the *DL*.

Table 38. *DL*s on the Ikitsuki Bridge.

Component	Kubota et al. (2004) (kN)	FEM (kN)
Steel members	64,200	88,948
Accessories	3,100	Not applicable
Concrete deck	48,800	23,224
Sum	113,000	112,172

1 kN = 0.225 kips.

Table 39. Support reactions for the Ikituski Bridge under different load combinations.

Truss	Support	Boundary Condition	Steel System Only (kN)	*DL* (kN)	*DL* + *LL* (kN)
North side	P4	Roller	848	1,340	1,658
	P5	Roller	21,393	26,783	30,261
	P6	Pin	21,386	26,777	30,254
	P7	Roller	847	1,339	1,656
South side	P4	Roller	848	1,340	1,658
	P5	Roller	21,393	26,783	30,261
	P6	Pin	21,386	26,777	30,254
	P7	Roller	847	1,339	1,656

1 kN = 0.225 kips.

Verification of the As-Built Bridge Model

Kubota et al. (2004) obtained the natural frequencies of the first 10 modes of the bridge using a finite-element formulation. Table 40 and table 41 show comparisons between the natural frequencies presented by Kubota et al. (2004) and those obtained from the SAP2000 and LS-DYNA models in this research, respectively. Figure 98 shows comparisons between mode shapes from Kubota et al. (2004) and those from the LS-DYNA model. The maximum difference between the natural frequencies from Kubota et al. (2004) and those from the SAP2000 and LS-DYNA models was approximately 1.67 and 2.16 percent, respectively. Mode shapes from the LS-DYNA model also matched very well to those from Kubota et al. (2004). Because the FEM by Kubota et al. (2004) was based on as-built drawings and the models in this research are based on information received from Nagasaki University in developing the model in Kubota et al. (2004), the FEMs in SAP2000 and LS-DYNA represent the structural behavior of the Ikitsuki Bridge well. It should be noted that Kawabata et al. (2011) measured the natural frequencies of the first 10 modes of the bridge through ambient vibration. Measured frequencies are generally 10-percent higher than those from FEMs because of the nonidealized condition of actual bridge connections and components. If bridge-specific results are desired, a calibrated FEM based on monitoring data may be more suitable for ALP analysis. However, updating the FEM using monitoring data for such a long-span bridge is a complex optimization task and is beyond the scope of this research.

Table 40. Comparison between natural frequencies of the Ikitsuki Bridge from the FEM by Kubota et al. (2004) and the SAP2000 model.

Mode Number	Natural Frequency From FEM by Kubota et al. (2004)	Natural Frequency From SAP2000 Model	Difference (%)
1	0.237	0.239	0.75
2	0.352	0.356	1.04
3	0.496	0.491	−1.05
4	0.584	0.576	−1.39
5	0.614	0.614	0.05
6	0.630	0.621	−1.49
7	0.820	0.828	0.24
8	0.882	0.867	−1.67
9	0.932	0.940	0.88
10	1.036	1.034	−0.16

Table 41. Comparison between natural frequencies of the Ikitsuki Bridge from the FEM by Kubota et al. (2004) and the LS-DYNA model.

Mode Number	Natural Frequency From FEM by Kubota et al. (2004)	Natural Frequency From LS-DYNA Model	Difference (%)
1	0.237	0.241	1.77
2	0.352	0.359	2.07
3	0.496	0.507	2.16
4	0.584	0.592	1.38
5	0.614	0.622	1.35
6	0.630	0.635	0.72
7	0.820	0.834	0.93
8	0.882	0.877	−0.61
9	0.932	0.947	1.59
10	1.036	1.048	1.18

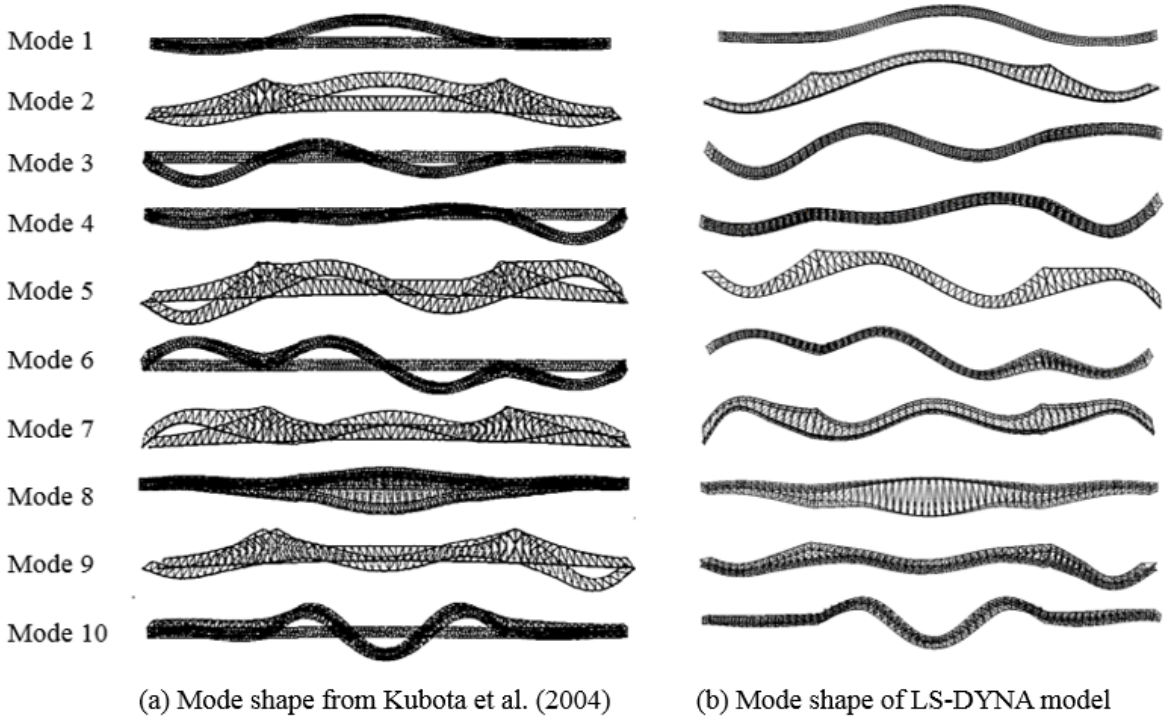

Source: FHWA.

Figure 98. Illustration. Comparison between mode shapes of the Ikitsuki Bridge based on Kubota et al. (2004) and the LS-DYNA model.

BEHAVIOR OF THE AS-BUILT BRIDGE

Figure 99 shows *DCR* for the as-built bridge with a service load condition of $DL + 1.0LL$. In this figure, truss members with *DCR* less than 1.0 are shown in solid black lines and those with *DCR* greater than 1.0 but less than 1.67 are shown in blue dotted lines. Stress in members shown in blue dotted lines is more than allowable stress under the service load condition $DL + 1.0LL$, probably because of differences in *LL* standards in the AASHTO LRFD specifications (2014) and Japanese design specifications. However, none of the members of the truss had *DCR* exceeding 1.67.

For a bridge that has been designed for service loads, *DCR* for all members must be less than 1.0. To study ALP in a well-designed bridge, retrofit of members with *DCR* greater than 1.0 was performed by member strengthening so that *DCR* of all members became less than 0.9. This model of the bridge was designated as the "Design Bridge." The member strengthening to modify the as-built bridge into the Design Bridge resulted in an increase in the weight of the steel by 16.03 percent. Figure 100 shows the distribution of members in the bridge with retrofitted members indicated in red dotted lines. Although target *DCR* during member strengthening for this bridge was 0.9, *DCR* spectra for ALP analysis in the next section were plotted for limit states of allowable (1.0) and yield (1.67) stress limits.

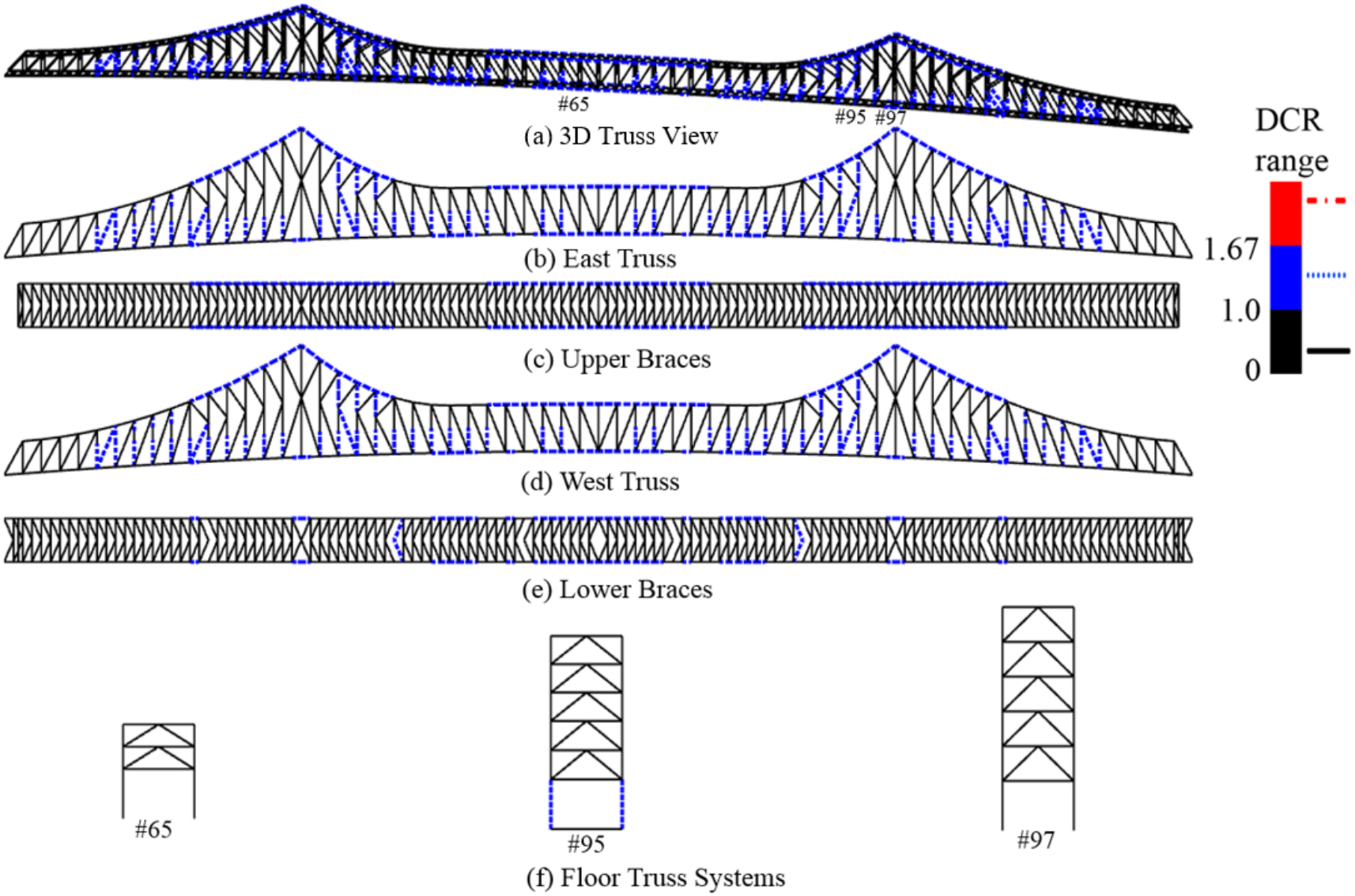

Source: FHWA.

Figure 99. Illustration. *DCR* spectra for the as-built bridge subjected to service loads.

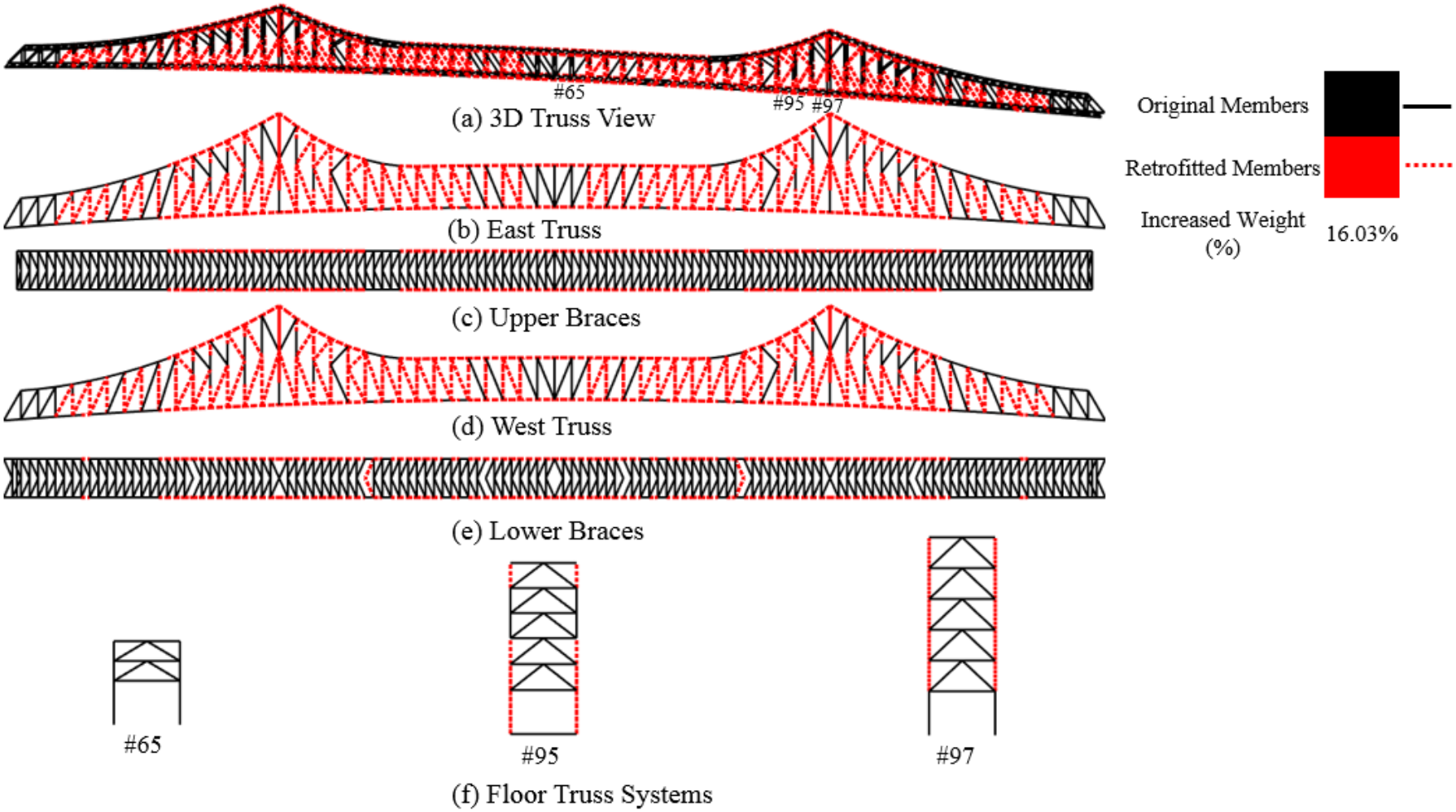

Source: FHWA.

Figure 100. Illustration. Members of the as-built bridge retrofitted by member strengthening to obtain Design Bridge for the ALP analysis.

ALP ANALYSIS OF THE DESIGN BRIDGE

For the Ikitsuki Bridge, ALP was investigated for only two cases of MR. After a series of trial and error studies, the most critical members in the Ikitsuki Bridge were found to be the upper chord members. Hence, two upper chord members on the east side were selected for removal: one near P6 (case 1 of MR) and the other in the central span (case 2 of MR). The MR analysis was performed in SAP2000 for *DCR* and in LS-DYNA for *SR* metrics. The MR analysis in SAP2000 was elastic static analysis and was performed by executing the SAP2000 model of the bridge after removing a target member from the model. *DCR* for all truss members was calculated from the results of this analysis. The MR analysis in LS-DYNA was dynamic and considered geometrical and material nonlinearities and stress hardening in steel.

ALP (MR) Analysis for Design Bridge: *DCR* Metric

Figure 101 and figure 102 show ALP in terms of *DCR* for MR cases 1 and 2, respectively. For MR case 1 in figure 101, the upper chord U98-U99 in the side span on the east side truss was removed. This led to load redistribution in the damaged system and increase in demand in truss members on the east side near the damaged zone; the increase in demand was much less significant in truss members on the opposite (west) side. As observed in the I-35W Bridge, damage (or increase in demand because of load redistribution) was concentrated around the damaged member. The increased demand in the upper brace system around the damaged panel indicates the three-dimensionality effect in load redistribution from one side truss to the other. If one imagines the lower chord and upper chord members acting as a force couple, the height of the FS can be considered the moment arm. Near central supports, tension in upper chord members and compression in lower chord members of the same panel create a resisting moment to balance the external moment produced by the *DL* and *LL*. Because of the long span of this continuous bridge, there were significant negative moments near central supports P5 and P6. Increasing the height of the FSs near these central supports means increasing the moment arm to control the force increase in the truss members. As shown in figure 101, there are five levels of braces with a total height of 45 m (147.64 ft) in the FS near the central supports. The height of the FSs is 19 m (62.34 ft) in the middle of the central span. Multiple levels of transverse braces provide lateral support to the vertical members to reduce the risks of buckling. In addition, the transverse braces can provide more torsional stiffness to the virtual hollow closed box section created by the two side trusses, the deck system, and the upper brace system. The enhanced torsional stiffness can ensure structural stability when some damage exists. For MR case 1, 13 members had *DCR* greater than 1.67.

Figure 102 shows the results for MR case 2, in which upper chord member U65-U66 near the center of the main span in the east side truss was removed. Figure 102 demonstrates that the loss of an upper chord member far from the supports has less impact than loss of a member near the supports (as in MR case 1 in figure 101). The number of members with *DCR* of more than 1.0 decreased from 209 in MR case 1 to 145 in MR case 2. The impacted region was concentrated near the damaged panel. Both upper and lower braces nearby participated in the load redistribution.

Figure 103 shows the complete envelope for the entire bridge considering the symmetry of the bridge in the west and east sides. This envelope was created by applying *DCR* results for the two

MR cases to other locations of the bridge (i.e., applying MR case 1 results to symmetric upper chord members near pier P5 on the east side truss and piers P5 and P6 on the west side truss, and applying MR 2 case results to a symmetric upper chord member near the central span in the west side truss). The boundary conditions of roller support and fixed support at P5 and P6, respectively, had a negligible effect on creating this envelope based on symmetric geometry of the truss. A total of 575 members exceeded the allowable stress. Among these members, 68 members had *DCR* greater than 1.67 (i.e., these members yielded).

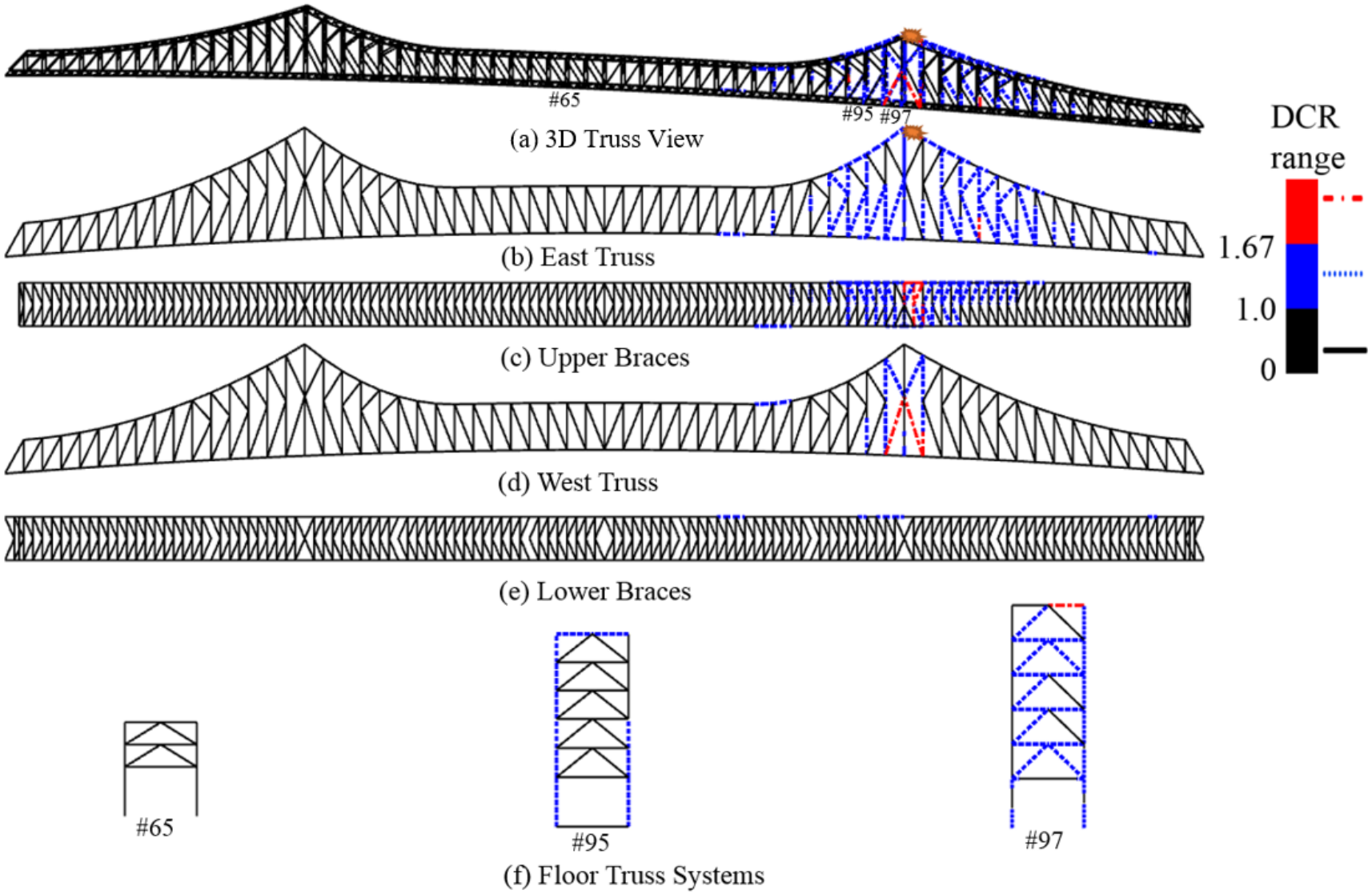

Source: FHWA.

Figure 101. Illustration. *DCR* spectra for the Design Bridge for upper chord MR (MR case 1).

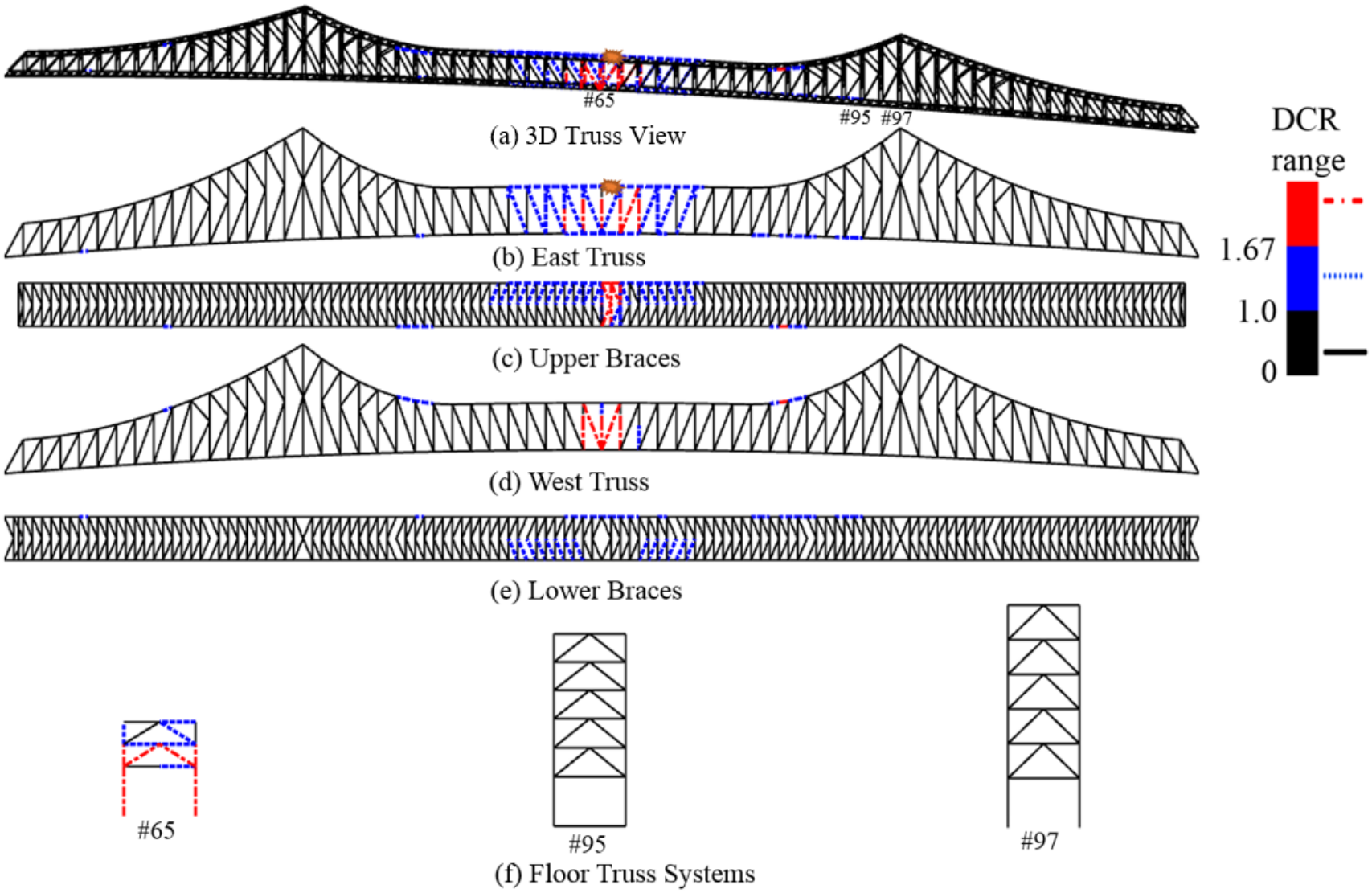

Source: FHWA.

Figure 102. Illustration. *DCR* spectra for the Design Bridge for upper chord MR (MR case 2).

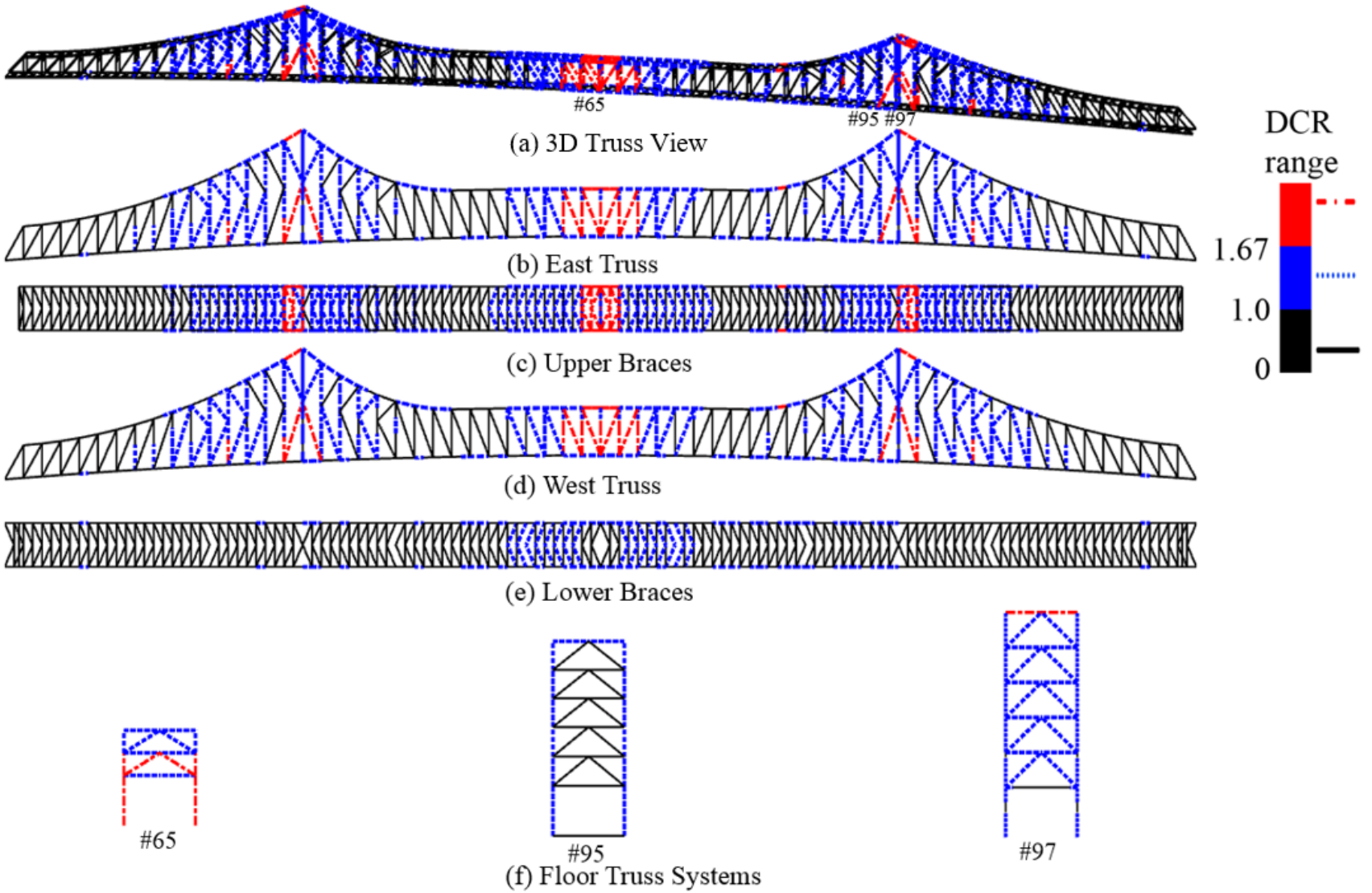

Source: FHWA.

Figure 103. Illustration. Complete envelope of *DCR* for the Design Bridge representing eight MR cases (two removal cases in each quarter of the bridge).

ALP (MR) Analysis for Design Bridge: *SR* Metric

Figure 104 and figure 105 present the *SR* metric for two MR cases. Several members had *SR*s between 1.0 and 2.0 and between 2.0 and 4.0 limit states. These two limit states correspond to minor and moderate damage in the bridge, respectively. Similar to figure 103, figure 106 shows the envelope of *SR* metric for the entire bridge. Among all members of the bridge, 86 members had *SR* between 1.0 and 2.0, and 10 members had *SR* greater than 2.0 (i.e., these members yielded and had repairable damage).

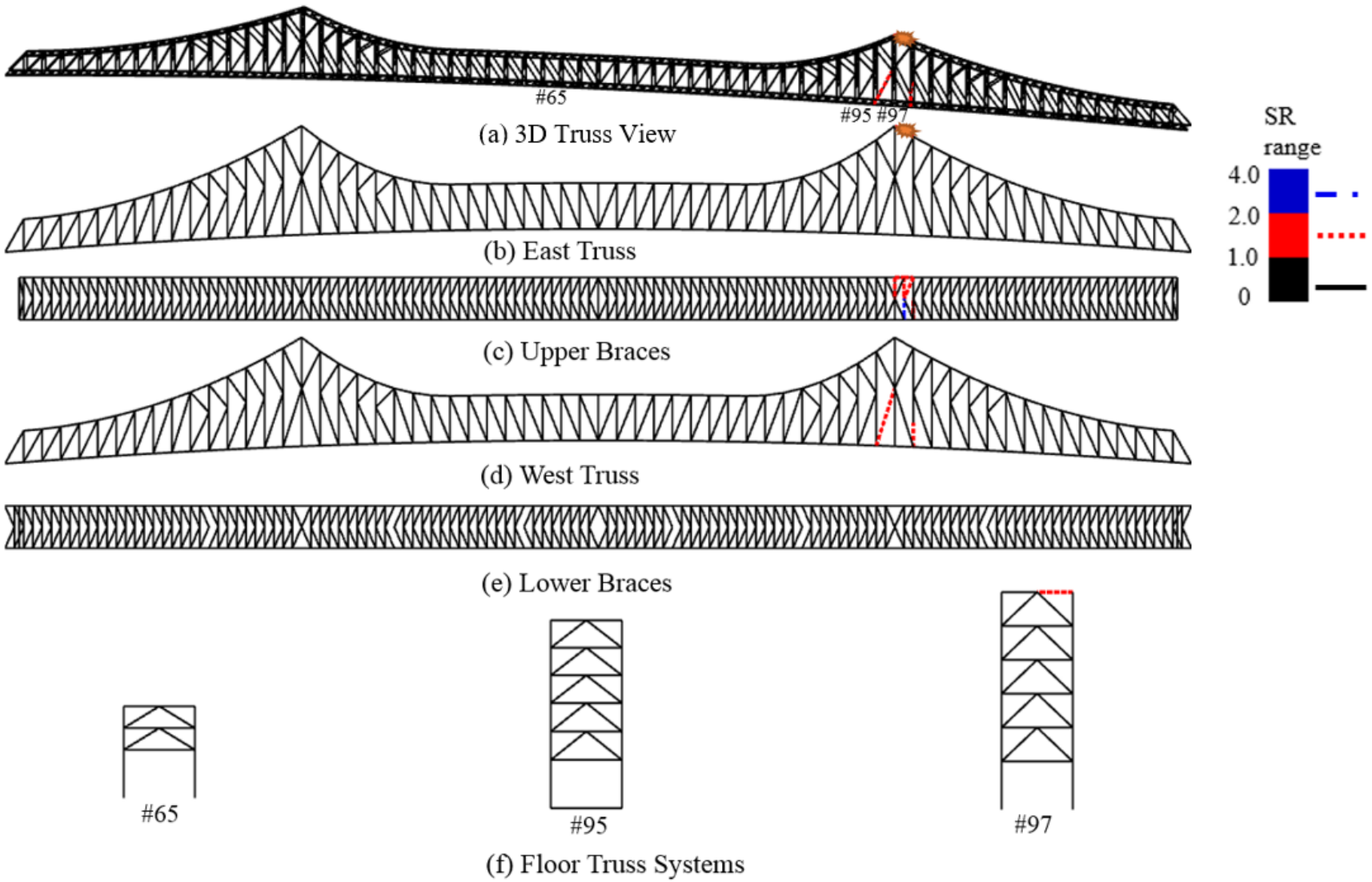

Source: FHWA.

Figure 104. Illustration. *SR* spectra for the Design Bridge for upper chord MR (MR case 1).

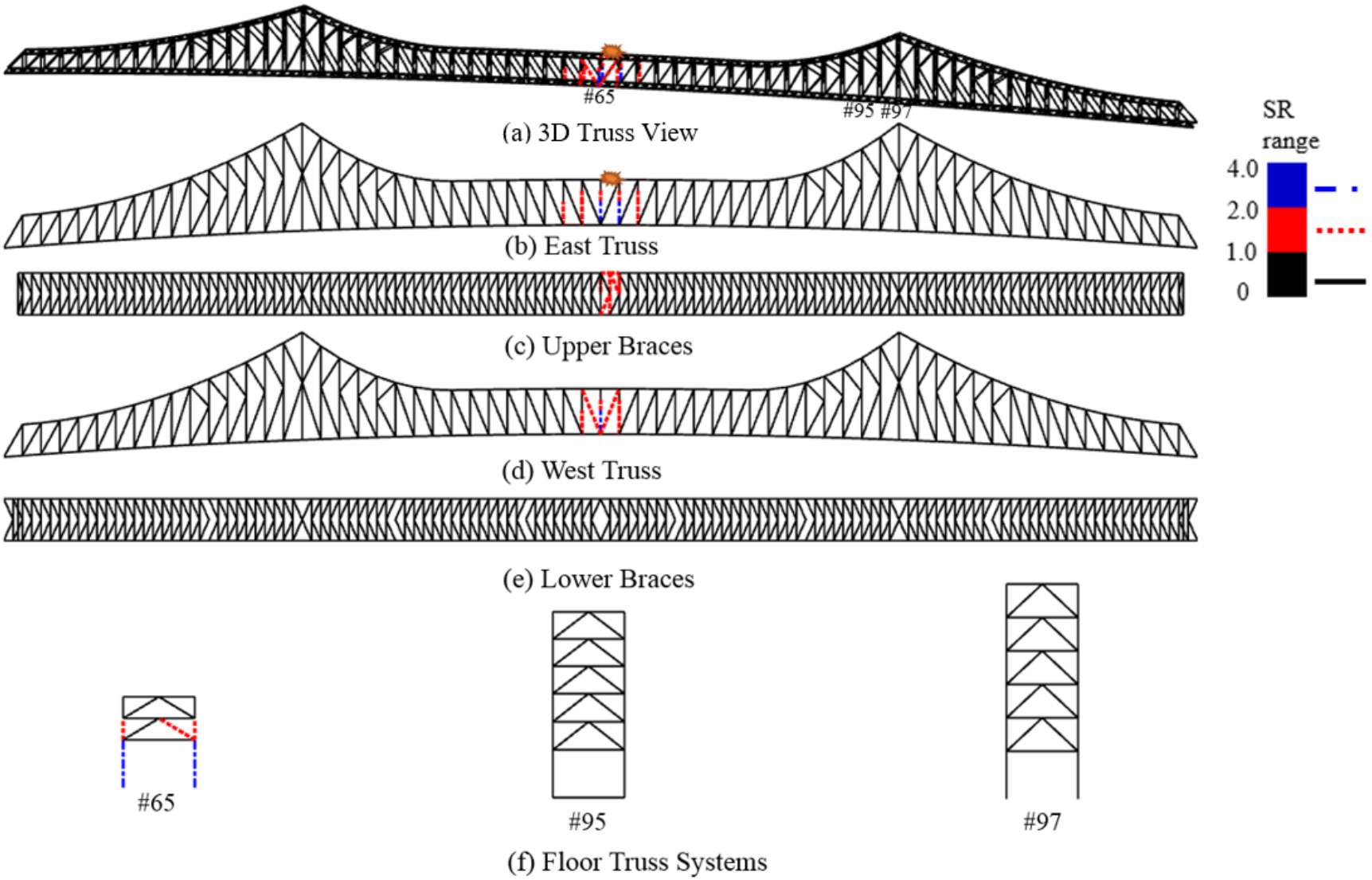

Source: FHWA.

Figure 105. Illustration. *SR* spectra for the Design Bridge for upper chord MR (MR case 2).

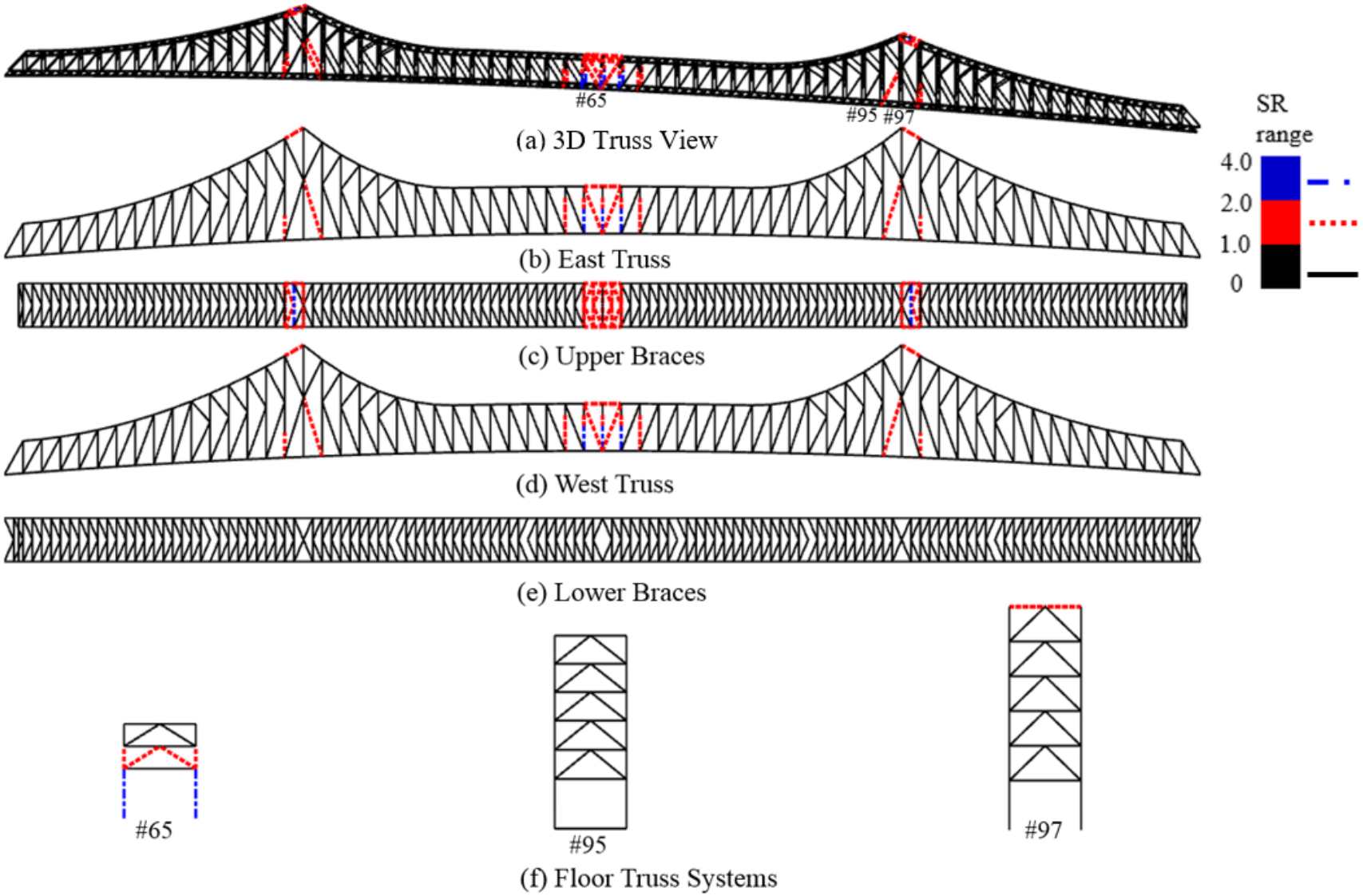

Source: FHWA.

Figure 106. Illustration. Complete envelope of *SR* for the Design Bridge representing eight MR cases (two removal cases in each quarter of the bridge).

PERFORMANCE-BASED RETROFITS

Performance of Retrofits in Terms of *DCR*

Similar to the investigation of retrofit of the I-35W Bridge in chapter 5, the four retrofit strategies in table 28 were investigated for the two performance levels of $DCR \leq 1.0$ and $1.0 \leq DCR \leq 1.67$ for the Ikitsuki Bridge. These four retrofit strategies are as follows: (1) member strengthening only, (2) member strengthening plus adding transverse braces for the FS at the supports, (3) member strengthening plus adding DMs at two panels near the supports, and (4) member strengthening plus adding members to the FS and DMs as described in strategies 2 and 3. Distribution of retrofitted members for these four retrofit strategies for performance level $1.0 \leq DCR \leq 1.67$ is shown in figure 107 to figure 110. Because of the long span of the Ikitsuki Bridge, it is not cost-effective to add members along the entire length of the bridge. In this case, the weight of the bridge may increase significantly when extra diagonals and braces are added in the central span even though the ALP of the bridge may not improve significantly. On the other hand, adding members around the supports is effective in improving the ALP. Member strengthening is the most effective for members in the central span.

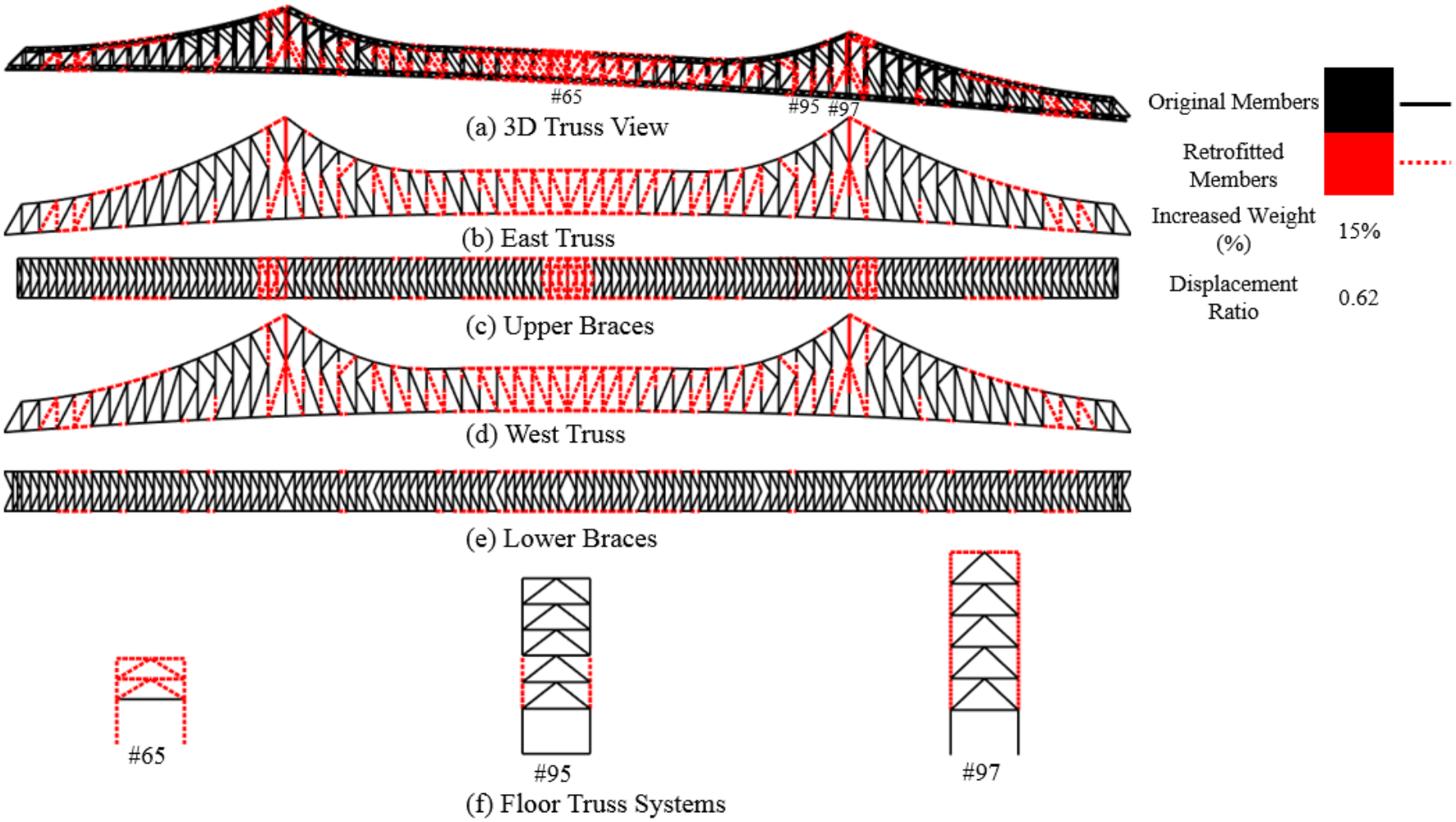

Source: FHWA.

Figure 107. Illustration. Member strengthening retrofit of the Design Bridge for MR based on $1.0 \leq DCR \leq 1.67$ limit state.

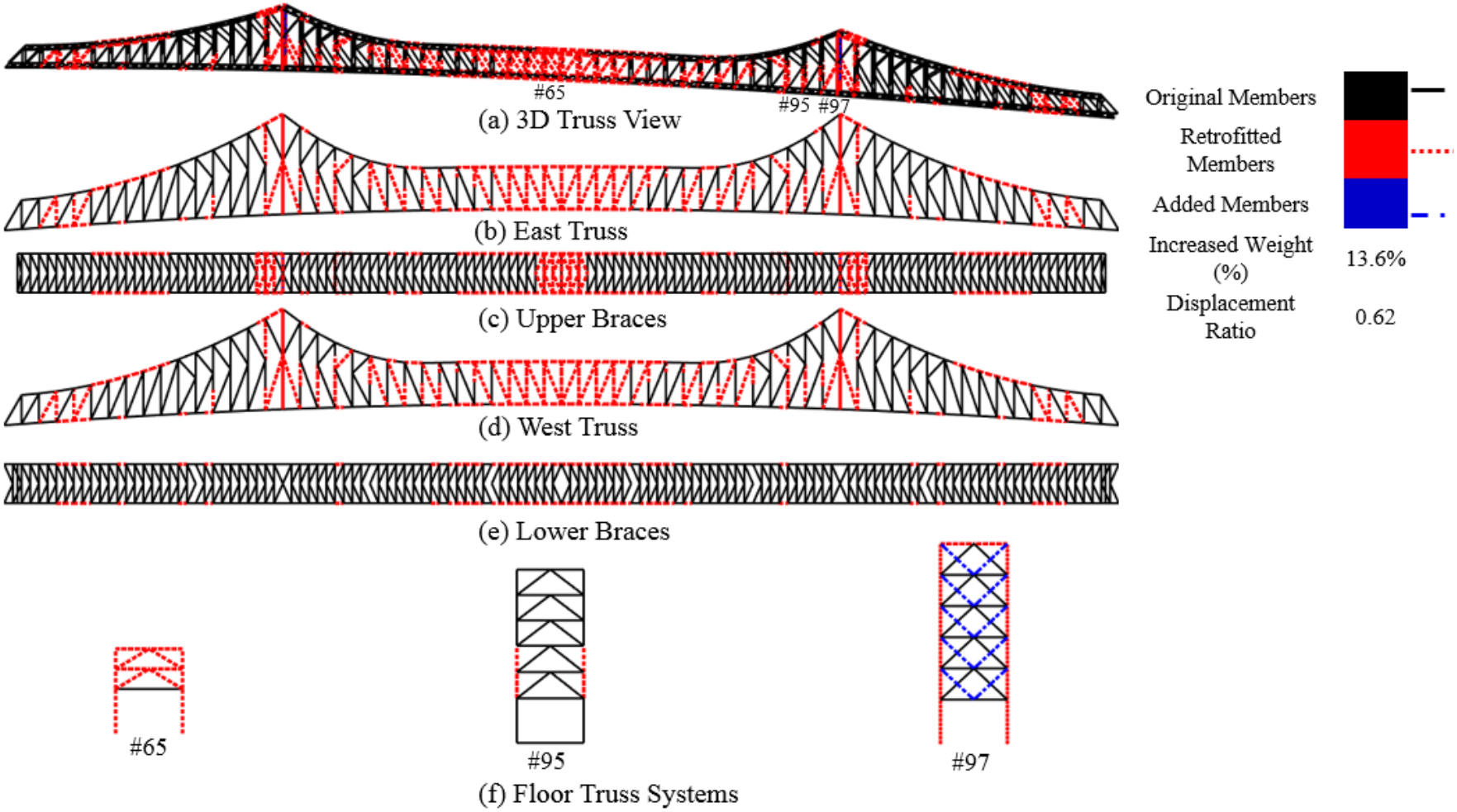

Source: FHWA.

Figure 108. Illustration. Addition of floor truss members and member strengthening retrofit of the Design Bridge for MR based on $1.0 \leq DCR \leq 1.67$ limit state.

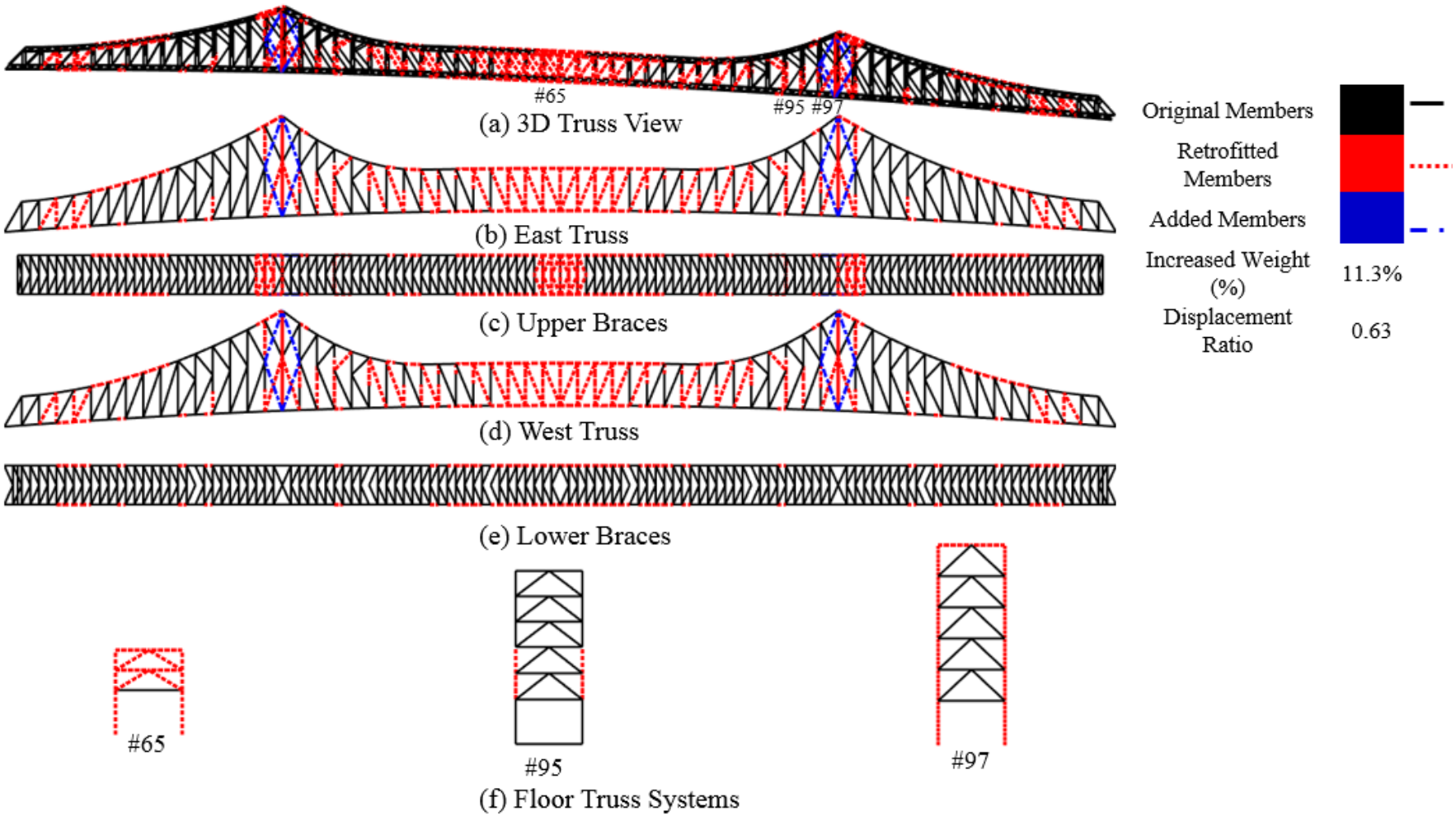

Source: FHWA.

Figure 109. Illustration. Addition of DMs and member strengthening retrofit of the Design Bridge for MR based on $1.0 \leq DCR \leq 1.67$ limit state.

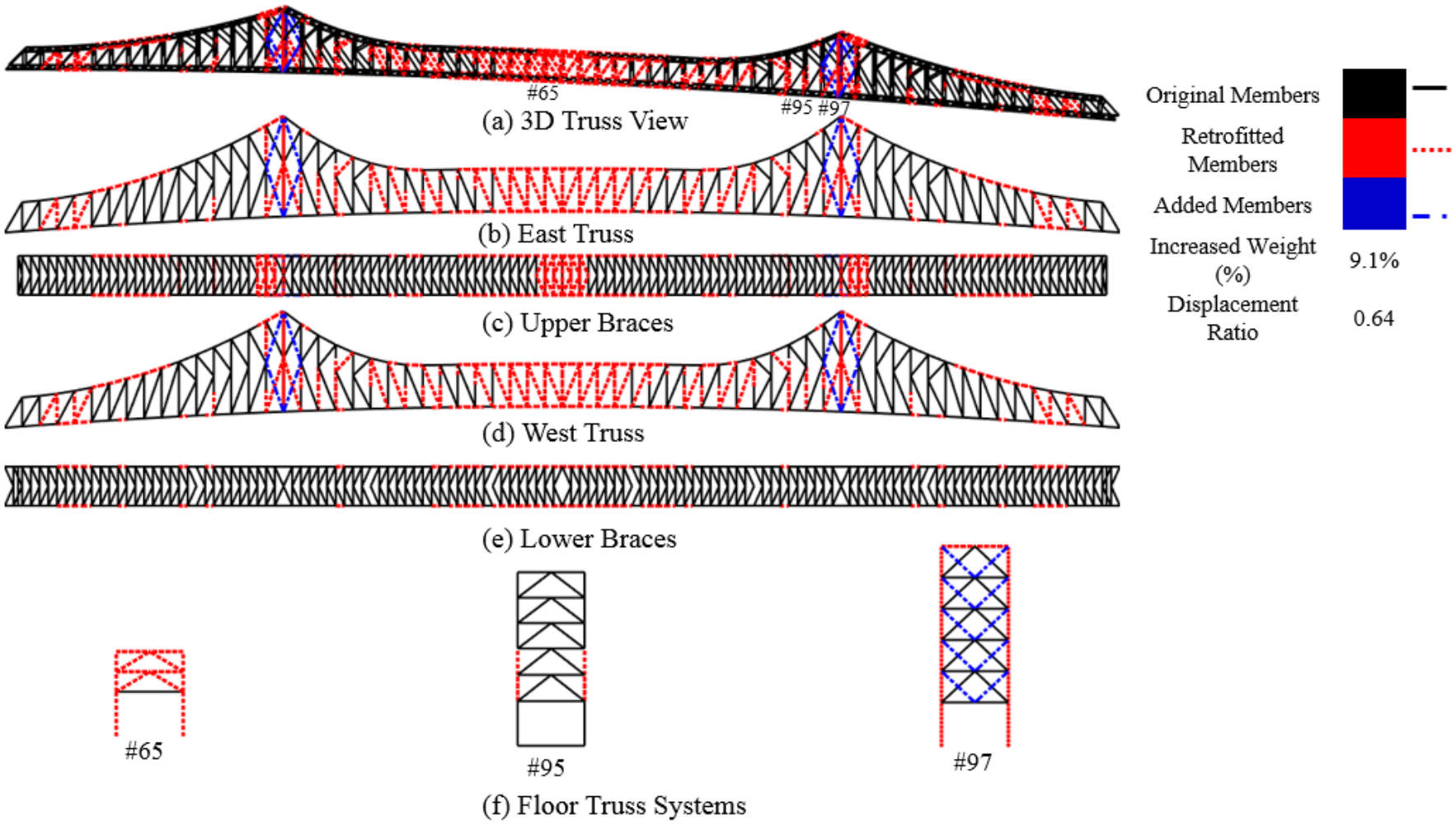

Source: FHWA.

Figure 110. Illustration. Addition of floor truss members and DMs and member strengthening retrofit of the Design Bridge for MR based on $1.0 \leq DCR \leq 1.67$ limit state.

The DispR is calculated as the maximum of the maximum vertical displacements of the retrofitted bridge divided by the allowable deflection limit, as shown in table 42, for each retrofit strategy. For the Ikitsuki Bridge, the deflection limit is taken as span length⁄300 because the bridge can tolerate a much higher level of displacement than span length⁄800 without causing inelastic stress in any of the members.

Table 42 shows the percentage increase in steel weight and DispR for eight retrofit cases (MR case 1 and case 2 for each of the four retrofit strategies). Members added in retrofit strategies 2, 3, and 4 are shown in blue dotted lines in figure 108 to figure 110, respectively. Retrofit strategy 4 was again the most efficient in terms of additional weight increase, whereas the displacement performance was similar for all retrofit cases. The percentage increase in steel weight decreased from 15 to 9.1 percent for $1.0 \leq DCR \leq 1.67$ and from 36.7 to 21.4 percent for $DCR \leq 1.0$ for retrofit strategies 1 to 4, whereas DispRs were similar for all retrofit strategies. These results demonstrate that all retrofit strategies have approximately similar performance but retrofit strategy 4 is the most cost-effective because of the more significant three-dimensionality effect created by the addition of braces and DMs.

Table 42. Increase in the weight of steel and DispRs for different MR retrofit strategies based on *DCR* limit state.

DCR Value	MR Retrofit Strategy	Additional Increased Weight (kN)	Increased Weight (%)	DispR
≤1.67	1-1	15,595	15.0	0.62
≤1.67	2-1	14,065	13.6	0.62
≤1.67	3-1	11,735	11.3	0.63
≤1.67	4-1	9,419	9.1	0.64
≤1.0	1-2	38,061	36.7	0.61
≤1.0	2-2	33,613	32.4	0.61
≤1.0	3-2	28,196	27.2	0.63
≤1.0	4-2	22,233	21.4	0.64

1 kN = 0.225 kips.
Note: The total steel weight of the Base Bridge was 103,708 kN.

Performance of Retrofits in Terms of *SR*

The complete envelope of the *SR* metric for the entire bridge in figure 106 indicates that 10 members have $SR \geq 2.0$. The increase in the weight of steel to change these members to $SR \leq 2$ is approximately 2 percent. Table 43 shows results for the four retrofit strategies when performance requirements are set in the elastic zone (corresponding to $SR \leq 1.0$). Distribution of retrofitted members for these four cases of retrofits is similar to that for $1.0 \leq DCR \leq 1.67$. Similar to observations from the I-35W Bridge and the *DCR*-based retrofit in table 43, the percentage of added steel weight decreases from 13 to 7 percent for retrofits 1 to 4. Retrofit strategy 4 is the most effective and the most economical because of the increased three-dimensionality from added members. This strategy also shows that both member strengthening in the central span and member additions near supports are effective in improving ALP of the bridge.

Table 43. Increase in the percentage weight of steel for different MR retrofit strategies based on *DCR* and *SR* limit states.

Performance Level	Limit State	1: Member Strengthening Only	2: FS + Member Strengthening	3: DM + Member Strengthening	4: FS + DM + Member Strengthening
Elastic limit state	$DCR \leq 1.0$	37	32	27	21
Elastic limit state	$1.0 < DCR \leq 1.67$	15	14	11	9
Elastic limit state	$SR \leq 1.0$	13	12	8	7
Low ductility	$DCR \leq 5.0$	NA	NA	NA	NA
Low ductility	$SR \leq 2.0$	2	NA	NA	NA
Medium ductility	$SR \leq 4.0$	0	0	0	0

NA = not applicable.

CHAPTER 7. LABORATORY AND FIELD TESTING RECOMMENDATIONS

To investigate ALP and effective retrofit strategies of long-span truss bridges, several important assumptions were made. These assumptions were based on experience and the best judgment of the research team members. This chapter reviews some of those assumptions and makes recommendations for improving them via experimental and analytical verifications. All future experimental verifications should focus on three targets: system (full bridge) performance, component behavior, and joint performance (by considering connected components at a typical joint).

SYSTEM BEHAVIOR

Modeling Methods

In chapter 3, the FEM used in this research was compared with well-known accurate baselines, and their similarity was verified and demonstrated. However, numerous factors might affect the overall system behavior during and after an MR event. The effects of those factors on the overall system need to be tested. Numerous truss bridges were built decades ago, and now they are suffering from aging and deterioration. Field tests could be performed before the demolition of one such bridge. For example, Azizinamini (2002) performed ultimate load tests on a steel truss bridge (the Rock Creek Bridge). Before demolition, the Rock Creek Bridge was disassembled by disconnecting the floor cross beams and moved to the laboratory of the University of Nebraska–Lincoln. To understand the behavior of an old steel truss bridge with forging tension members, tests were performed before and after the retrofit of the forged tension components.

However, as mentioned in chapter 3, not many laboratory or field studies on the removal or fracture of members have been performed to investigate the ALP. Field testing of ALPs through destructive testing of decommissioned bridges can be an attractive solution to challenges involving progressive collapse testing in laboratories. For the full bridge test, testing scales should be carefully checked to balance the cost and accuracy.

Similar to the work done by Azizinamini (2002), full-scale bridge testing with appropriate validation by numerical processes for MR is recommended. This full-scale test can use a decommissioned bridge. A single member of such a bridge can be removed using mechanical means. Proper instrumentations for measuring resulting strains and displacements need to be part of the experiment. The loading on the bridge can be increased carefully while monitoring the bridge's responses. Validation of different analytical modeling methods, including but not limited to the methods presented in this research, can be performed during this large-scale field test. This type of experiment will help to find optimal modeling processes and to identify any source of errors in such modeling techniques.

After completion of the field study, a typical joint of the bridge should be carefully taken out and tested in the laboratory to understand the behavior and modeling of the joints of truss bridges. This exercise should be performed for as many typical truss joints as possible. If joints from decommissioned bridges are not available, typical joints in critical truss bridges should be fabricated in the laboratory based on original design details of the bridge to develop empirical models for these joints that can be used in FEMs.

ALP Quantification

The full-scale test can also be used to validate the ALP methodology presented in this research. This validation will require extensive sensor arrays throughout the bridge to keep track of the changes in load paths before and after MR. Component testing might be necessary to obtain properties of a single component, but it is not always sufficient to address the adequacy of ALPs. Because an ALP is a load path from the location of damage to the bridge supports, such a load path may need to be simulated in full. This would require modeling of a whole system, or most of the system, rather than a single component.

COMPONENT BEHAVIOR

Joint Simulation

In the physical bridge model, joint performance is not clearly understood because of the complex stresses involved around the joint region. In a typical truss bridge, a joint in a truss may connect compression and tension members in the longitudinal direction through gusset plates. Any damage to a truss member may cause significant bending stresses at the joint connecting the member with the gusset plate (Hao 2010). Numerous tests on gusset plates after the collapse of the I-35W Bridge have shown that the behavior of stresses in the gusset plates is very complex. This behavior could be even more complex at joints connecting transverse floor trusses with the main longitudinal truss.

During finite-element modeling of the bridges in this research, it was assumed that joints of truss bridges are totally rigid and infinitesimal in size (i.e., their physical size was ignored in the FEM) and remain intact during the bridge's response to hazards (e.g., MR). Even though these assumptions are consistent with the current state of practice, their accuracies and effects on the retrofit results are not well documented. Therefore, a robust set of experimental and analytical tests are recommended to investigate all or some of these assumptions. Figure 111 illustrates finite-element representation of a physical joint.

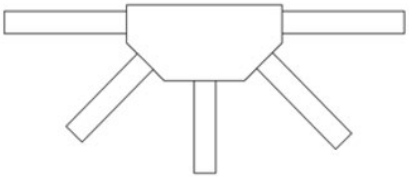

Source: FHWA.

A. Physical joint.

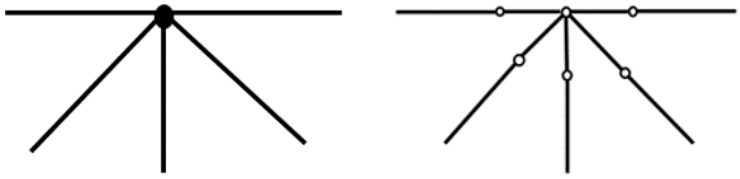

Source: FHWA.

B. Analytical representation.

Figure 111. Illustrations. Representations of joints.

In two example bridges investigated in LS-DYNA, truss members were modeled by B-S beam elements connected through rigid joints. During the investigation of the collapse of the I-35W Bridge, Schultheisz et al. (2008) studied the global model of the bridge (consisting of beam and shell elements) by building a very detailed model of two affected joints (U10 and L11) to examine the fine details of stress distribution of these joints. The FHWA global model modeled truss members and gusset plates by shell elements, whereas the fine detailed model used

solid-element representations, which was partly motivated by a goal of considering stress concentrations associated with the riveted connections. This detailed model had approximately 2.7 million DOFs, as illustrated in figure 112. For investigating alternate path in truss bridges, a similar study can be performed by developing a model of the bridge where truss elements can be modeled by B-S beam elements and truss joints in the region affected by sudden loss of a member can be modeled by either shell or solid elements. However, the level of model complexity and simulation time will be drastically higher in this case, although results are likely to be a better representation of the behavior of joints after sudden loss of members.

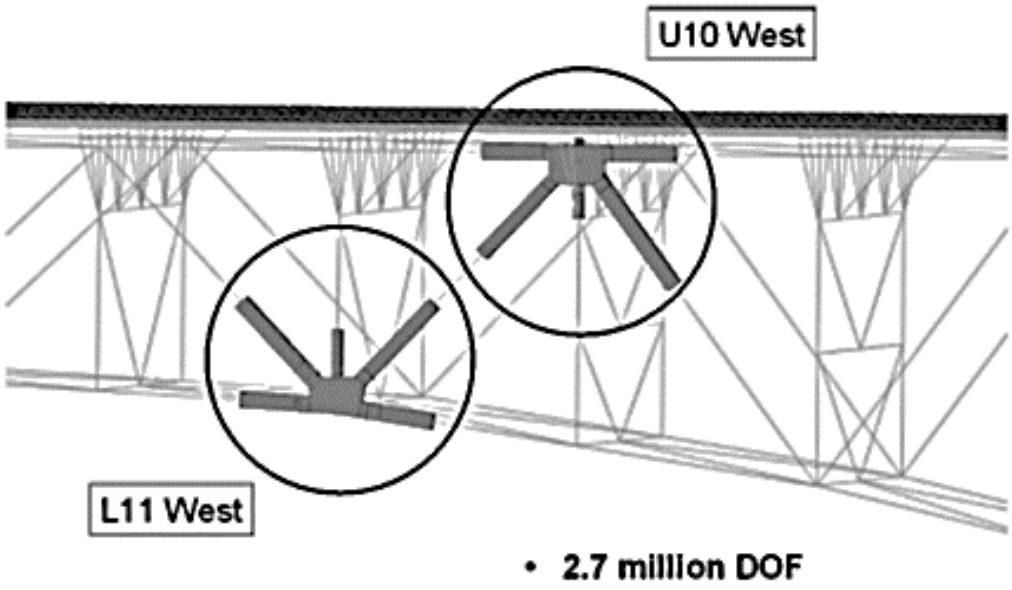

Source: NTSB.

Figure 112. Illustration. Detailed FHWA global model of the I-35W Bridge with fine detailed model of U10W and L11W joints (Schulthesiz et al. 2008).

HAZARD SIMULATION

Single MR

This research provides a simple process for retrofitting bridges that are subject to single MR. The choice of the single member to be removed, as argued in previous chapters, should be based on the objective judgment of the bridge engineer. Currently, no objective process is available to aid bridge engineers in selecting the members to be removed. An obvious process would be to remove all members one by one. Such a process could be resource-intensive. In this research, both *DCR* and *SR* were used as objective criteria for MR. However, an optimal process for MR that considers the risk exposure of different members in addition to quantities such as *DCR* or *SR* is needed. Such an approach may be more practical and may aid bridge engineers in making efficient selections.

Blast Simulation: ALP Modeling

An assumed blast's effects on components of the bridge under certain conditions (i.e., simultaneous failure of two members) was simulated. For simplicity, such an assumption ignored the following:

1. An exact location of the blast source.
2. An exact weight of the blast event.
3. The dynamic blast wave propagation that might affect nearby bridge components.

The simplifying assumptions used in this research were justified by the limited resources of this project. However, the relationships between the blast source location, the blast weight, and the dynamic effects on bridge members and the resulting degradations of those members need detailed analytical investigation and experimental testing. The results of those tests can be documented in a monograph that can be used by bridge engineers to accurately predict damage in bridge members due to blast loading without having to model the blast event dynamically. Figure 113 shows a general illustration of such a monograph. The availability of such a monograph will not only improve the accuracy of the process described in this report but also save immense computational resources. Because of their sensitive nature, such monographs can be made available on a need-to-know basis.

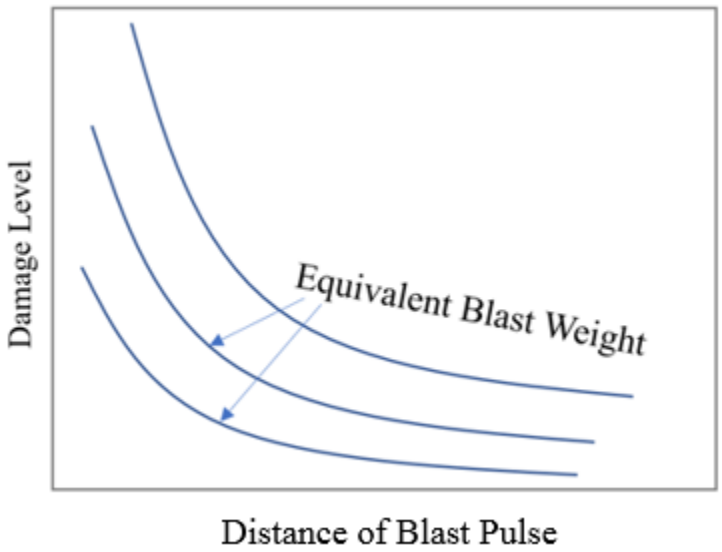

Source: FHWA.

Figure 113. Graph. Typical blast damage monograph.

Blast Simulation: Member Strengthening Modeling

Blast loading on bridges is frequently modeled based on simplifying assumptions. For example, the role of bridge decks on blast pressure distribution on structural members of the bridge systems is ignored, or the blast source is assumed to be on top of the bridge deck (I-35W Bridge) or within the bridge portal (Ikitsuki Bridge).

The first assumption is a conservative assumption because it ignores the energy dissipated by the damage to the bridge deck. It also ignores the role of the bridge deck in redistributing the blast pressure, as shown in figure 114-A. The second assumption ignores many other possible locations of the blast pressure, such as near a bridge support or directly under the bridge deck, as shown in figure 114-B.

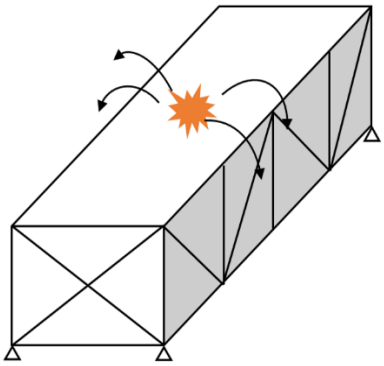

Source: FHWA.

A. Blast source near the deck.

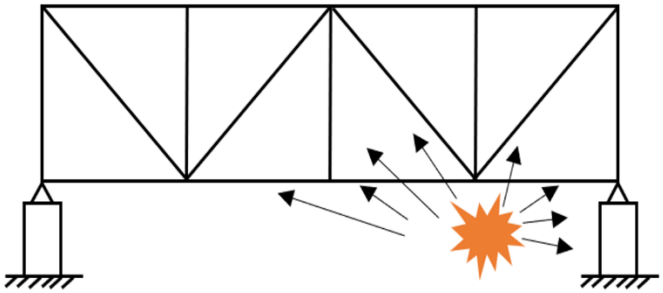

Source: FHWA.

B. Blast source near the supports.

Figure 114. Illustrations. Illustration of blast load on a bridge.

If bridge engineers find these simplifying assumptions to be either too conservative or too permissible, one possible solution would be to use a coupled direct blast-bridge analysis and design process. Such a process would be resource-intensive and difficult to perform. Another approach would be to perform physical tests supported by analytical experiments. These tests should be designed to address these assumptions and make it possible to use and modify the ALP process from this research to produce results that are more accurate.

PERFORMANCE-BASED DESIGN

Two alternate methodologies for the design or retrofit of bridges based on MR or DMR were presented in chapters 5 and 6. For these abnormal demands, both linear static analysis and NLD analysis processes were investigated. For the linear static process, *DCR* was used as the metric for acceptance limits, whereas for the NLD process, *SR* was used as the metric for acceptance limits. Different performance levels for each analysis process and metric, as shown in figure 91 (in chapter 5), have been provided.

The acceptance limits used in figure 91 are based on the personal judgment and experience of the authors of this report. It has been shown that acceptance limits are related to acceptable risk by the stakeholders (Ettouney and Alampalli 2010a, b). Therefore, it is recommended to investigate the relationship between acceptable risk levels during MR and blast hazards and the different acceptance limits proposed in this research. Bridge engineers can then adjust those acceptance limits depending on desired acceptable risk levels for different bridges.

RETROFIT METHODS AND TECHNOLOGIES

During the retrofit processes described in chapters 5 and 6, manual adjustments of member size or shape were performed to reach the required acceptance limits. Retrofit options did not involve the use of advanced materials or technologies. Examples of advanced materials or technologies for retrofitting bridges include but are not limited to the use of fiberglass reinforced plastic (FRP) wrapping, FRP sections, and so forth (Ettouney and Alampalli 2010b). It is believed that using advanced materials and technologies in retrofits in addition to the ALP-based strategies illustrated in chapters 5 and 6 might result in even more cost-benefit results. The use of such a combined strategy is beyond the scope of this project. However, it is recommended as a future research and development effort.

CHAPTER 8. CONCLUSIONS, LIMITATIONS, AND FUTURE WORK

SUMMARY AND CONCLUSIONS

An extensive investigation on ALP of long-span bridges in the event of loss of a member or members was performed for two example long-span truss bridges: the I-35W Bridge in Minneapolis, MN, which collapsed in 2007, and the Ikituski Bridge in Japan, which is the longest continuous steel truss bridge in the world. Although ALP has been defined qualitatively in the literature, a quantitative interpretation of ALP was developed in this research. Bridge designers commonly use *DCR* to design truss bridge members within the allowable stress limit, whereas they use *SR* as a limit between elastic and inelastic behaviors. Using these two design metrics, ALP is defined as the spectrum of the surrounding member undergoing load redistribution to prevent collapse after sudden damage to a member or members of a bridge because of abnormal events such as member loss or blast loading. Comparison of such spectra of bridge members before and after retrofit can also provide information on the effectiveness of a retrofit scheme.

The work performed in this research included calibration of long-span bridge models using available data in the literature, validation of the material model based on available analytical results, simulation of sudden MRs, and development of a performance-based methodology to retrofit the bridge against abnormal events, such as sudden loss of members. Key highlights and conclusions of this research are as follows:

- Generally, investigation of sudden MR or progressive collapse is conducted by using either an elastic model or a very fine model of a truss bridge in software such as LS-DYNA, where elements are meshed using shell elements. The former approach limits the work to elastic behavior, whereas the latter approach is computationally intensive and not feasible for long-span bridges. In this research, the suitability of modeling a truss element using a B-S beam element in LS-DYNA was validated through several known examples. These validation examples as well as comparisons between models of bridges in SAP2000 and LS-DYNA demonstrated that the B-S element with material model Mat 98 can be used to investigate progressive collapse of long-span bridges even when the bridge's behavior becomes nonlinear. However, the B-S element with the Mat 98 material model cannot simulate strength deterioration in the event of buckling. For long-span bridges, buckling of members can be evaluated separately by local or global buckling analysis before and after MR scenarios. A FEM in LS-DYNA using a B-S beam element and the Mat 98 material model can provide information on nonlinear behavior of the bridge in the event of MR and is computationally more efficient than models using shell elements to model the bridge elements.

- Simulation of blast loading on long-span bridges is very complicated, requires finer meshing of elements, and may require the use of software such as ConWep, which is labeled distribution statement C and may not be available to all bridge engineers freely. Hence, the effects of blast loading were simulated by the loss of two members simultaneously. More research is needed on quantifying the effects of blast loads on truss bridge members.

- Single and dual member removal analysis demonstrated that the bridge members that were not designed to carry structural loads, such as the lower and upper braces, actually participated in the redistribution of loads among members of trusses on two sides of the bridge and the transverse FS. However, the zone of affected members in the event of damage to a critical member was limited to the vicinity of the damaged member. After damage to a critical member, geometrical asymmetry in the bridge tended to cause global torsional motion of the bridge about its longitudinal axis. This motion was resisted by (1) a virtual 3D geometrical box section (hollow closed boxed section) created by trusses on two sides together with the deck, stringers, and upper and lower braces, and (2) the FSs that act as diaphragms to supply rigidity to this hollow closed box section. These observations imply that the three-dimensionality of long-span truss bridges has a significant effect on their ability to survive after the loss of a critical member or members.

- In both the SAP2000 and LS-DYNA models, joints in truss bridges were modeled as rigid. Stresses in truss members connected through these joints were primarily axial because of *DL*s and *LL*s. However, in the event of sudden loss of a member or members, contributions of axial stress to *DCR* decreased significantly, whereas contributions of stresses due to in-plane and out-of-plane bending moments to *DCR* increased significantly. Hence, truss bridge analysis that considers truss members as primarily axial load-carrying members is not valid in situations of sudden member loss. In addition, simulations of the I-35W Bridge, which is a deck-truss bridge, showed that lower chord members were more dominant and effective in transferring loads to supports than upper chord members. On the other hand, upper chord members were more dominant in through-truss bridges, such as the Ikitsuki Bridge.

- Generally, seismic retrofit of truss bridges is done either by isolating or dissipating input seismic energy through seismic isolation and energy dissipation devices or by strengthening deficient members (i.e., increasing the cross-sectional areas of members by adding an angle or cover plate or changing the sectional shape). Simulation results have shown that these seismic retrofits have a limited effect on the ALP of truss bridges after sudden loss of a member because of the way demands are transmitted during seismic and member loss events. During a seismic event, loads are transmitted from supports to the superstructure, where mitigation measures such as isolation, energy dissipation, and member strengthening are effective. However, during sudden member loss events, loads are transmitted from the superstructure to supports. In this case, load redistributions must occur in the superstructure before support components can participate in transmitting loads to the ground. The three-dimensionality of the bridge cross section plays a significant role in this load redistribution within the superstructure.

- Another significant difference between demands because of seismic and sudden member loss events is the broadness of the affected zone or region. Demands during sudden member loss are limited to near the damaged member (because of the local initiation of the event and the short time duration (compared to earthquake excitations)) and affect much higher modes than those during seismic loads. Effects of seismic loads are global and affect the entire bridge system.

- The effectiveness of retrofit measures, such as member strengthening and addition of extra members as diagonal or FSs and bracings, was investigated through simulation of both linear and nonlinear FEMs. Results showed that using member strengthening had only limited effectiveness in improving the ALP of the bridge, whereas retrofit measures that improved the three-dimensionality of the bridge (i.e., adding DMs, floor truss members, and upper or lower bracing members) were significantly more cost-effective in improving the ALP of the bridge while minimizing the increase in the weight of added steel (because of retrofit). These results indicated that retrofitting to improve ALP is an optimization problem where bridge truss members can be added in a certain orientation to improve performance during member loss while minimizing any increase in the weight of steel (i.e., cost). This type of retrofitting will also be effective in addressing seismic demands on the bridge.

- A PBD approach, similar to the seismic design and retrofit of structures, was considered for retrofitting truss bridges to enhance their ALP. By accounting for the significance of the inelastic structural response, the overall performance of the structure is controlled in the PBD process. Two types of design criteria were considered for long-span steel truss bridges: *DCR* through elastic analysis and *SR* through inelastic analysis using an LS-DYNA model that modeled both geometrical and material nonlinearities. The increase in the weight of retrofit for the same level of performance (i.e., when $DCR \leq 1.67$ and $SR \leq 1.0$, which are both elastic limits) was less when analysis was performed using the inelastic model in LS-DYNA. This savings in costs was equivalent to approximately 2 percent less weight of added steel needed for the most effective retrofit strategy. However, overall savings in dollars will be much higher after factoring in labor and other costs (such as transportation) associated with 2-percent savings in steel weight. The savings in the weight of steel could be more if an optimization process is implemented when designing retrofits. Hence, performing inelastic analysis when designing retrofit strategies for ALP is recommended over linear elastic analysis.

- Compared with the single MR scenario, DMR (to represent blast loading) is significantly more severe. However, a real blast scenario may cause more damage to the bridge system. Further detailed investigation is needed on this issue.

LIMITATIONS AND FUTURE WORK

The following represent some limitations of this research and possible suggestions for future work:

- The joints simulated in the analytical models were assumed to be rigid and of infinitesimal size. In addition, joints were assumed to be intact during the bridge response to hazards. However, because the physical joints have more complicated stress behavior, the simulation of joints and the interaction of beam elements with the joint region should be investigated in detail. A dominating joint failure rather than a member failure may lead to collapse of the bridge. A possible compromise to detailed joint simulation may be to model selected critical truss joints and elements in the affected zone by finer shell elements to examine stress distribution while still modeling other joints and elements by

B-S elements. This approach could significantly optimize computational effort while significantly improving the reliability of the modeling.

- When modeling the two example bridges, the deck system was modeled in LS-DYNA by shell elements with elastic material only for imposing *DL* of the concrete deck on the truss system. In SAP2000, the effect of the concrete deck was included as weight at truss joints (without explicit modeling of the deck). The Young's modulus of the deck in LS-DYNA was reduced such that the displacement profile of the truss in LS-DYNA matched that in SAP2000. Hence, elastic behavior of the concrete deck itself did not affect the behavior of members affected by sudden loss of a critical member. However, a more realistic modeling of the deck by considering nonlinear concrete material (without reducing its Young's modulus) should be considered in future studies to investigate the effect of the deck on load redistribution during sudden member loss.

- The blast hazard simulated by a DMR scenario was only a crude approximation of the effect of member loss due to blast loads. More research, including laboratory testing (mentioned in chapter 7), is recommended to investigate the correlation between the blast load parameters (location, amount of TNT) and the number of members and number of bays that may be affected.

- Only four types of retrofit strategies were explored in the study, including member strengthening and addition of extra members (e.g., diagonal, FS, bracings), to improve ALP of the bridge. Among these four strategies, member strengthening only was found to be the least efficient approach. However, advanced materials or technologies can be used to design more efficient strategies than those investigated in this research. Other retrofit strategies that enhance the three-dimensionality of the bridge, such as several levels of transverse bracings near a central support or adding bracings for the DMs in the main truss girders, should also be investigated.

- For long-span bridges, such as the Ikitsuki Bridge, retrofit of panels around supports was found to be more effective than retrofit of members in the central span. Because of retrofit, stiffness around the supports was increased, which eventually helped to control the maximum displacement in the central span. However, further research is needed for other types of long-span bridges to develop prescriptive recommendations that can be used by bridge engineers.

APPENDIX A. *SR* CALCULATION

3D BEAM ELEMENT TRANSFORMATION MATRIX

A 3D beam has two nodes (N1 (beginning node, X_1, Y_1, and Z_1) and N2 (ending node, X_2, Y_2, and Z_2)), with six DOFs, three translation displacements, and three rotation displacements in each node. Normally, a beam could be oriented either by its angles of roll or by means of the global coordinates of an arbitrarily chosen reference point that lies in one of the principal planes of the member but not on its centroid axis. In LS-DYNA, a reference node N3 (X_3, Y_3, and Z_3) is defined.

Displacement Vector of 3D Beam in Global Coordinates

3D beam displacements and rotations of the *i*th beam are defined as the vector in equation 17:

$$\{U\}_i = \begin{Bmatrix} \{U\}_{i1} \\ \{U\}_{i2} \end{Bmatrix} \tag{17}$$

Where the six displacement and rotational measures of the first and second nodes are $\{U\}_{i1}$ and $\{U\}_{i2}$. They can be defined as in equations 18 and 19:

$$\{U\}_{i1} = \begin{Bmatrix} u_{1X} \\ u_{1Y} \\ u_{1Z} \\ \theta_{1X} \\ \theta_{1Y} \\ \theta_{1Z} \end{Bmatrix} \tag{18}$$

$$\{U\}_{i2} = \begin{Bmatrix} u_{2X} \\ u_{2Y} \\ u_{2Z} \\ \theta_{2X} \\ \theta_{2Y} \\ \theta_{2Z} \end{Bmatrix} \tag{19}$$

Note that u_{jk} and θ_{jk} represent the displacement (in mm) and rotation (in rad) in the global axis for the *j*th node and *k*th global DOF, respectively. Note that for a two-node beam $j = 1, 2$ and for a 3D geometry $k = X, Y, Z$. The order of the vector $\{U\}_{i1}$ and $\{U\}_{i2}$ is 6×1, whereas the order of the vector $\{U\}_i$ is 12×1.

Rotation Matrix From Global to Local

Global displacements in the *XYZ* coordinate system (as shown in figure 115), as an output file of nonlinear finite-element calculation from LS-DYNA, are transformed into local *rst* (*xyz*) system by the member rotation matrix ***r*** determined in the following steps.

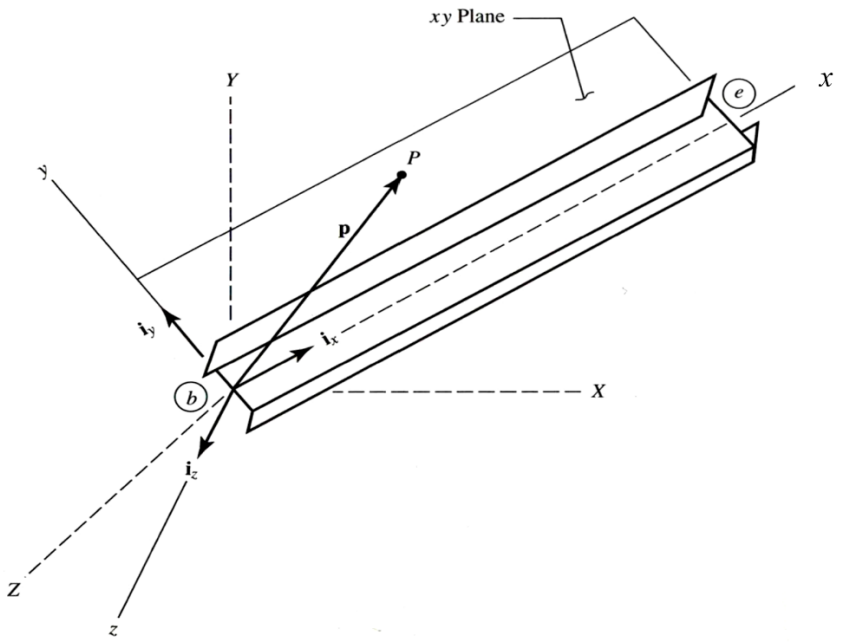

Source: FHWA.

Figure 115. Illustration. 3D beam global and local coordinate specification.

The position vector ***p***, directed from member begin N1 to the reference node N3, lies in the local *st* (*xy*) plane and can be written as in equation 20:

$$\boldsymbol{p} = (X_3 - X_1)\boldsymbol{I_X} + (Y_3 - Y_1)\boldsymbol{I_Y} + (Z_3 - Z_1)\boldsymbol{I_Z} \quad (20)$$

Here, $\boldsymbol{I_X}$, $\boldsymbol{I_Y}$, and $\boldsymbol{I_Z}$ are the unit vectors in the *X*, *Y*, and *Z* directions, respectively. Because the direction cosines of the local *r*(*x*) axis are already known from the global coordinates of the member ends, the direction cosines of the local *t*(*z*) axis ($\boldsymbol{i_t}$) can be conveniently established using the following relationship: cross product of $\boldsymbol{i_r}$ (the direction cosines of the local *r* (*x*) axis) and ***p*** divided by the magnitude of the vector that results from the cross product, as shown in equation 21:

$$\boldsymbol{i_t} = \frac{\boldsymbol{i_r} \times \boldsymbol{p}}{|\boldsymbol{i_r} \times \boldsymbol{p}|} \quad (21)$$

With both now known, the direction cosines of the local *s*(*y*) ($\boldsymbol{i_s}$) can be obtained via equation 22:

$$\boldsymbol{i_s} = \boldsymbol{i_t} \times \boldsymbol{i_r} \quad (22)$$

Here, $\boldsymbol{i_r}$, $\boldsymbol{i_s}$, and $\boldsymbol{i_t}$ are unit vectors in local *x*, *y*, and *z* directions. The member 3 × 3 rotation matrix ***r*** can now be obtained by arranging the components using the formula in equation 23:

$$\begin{bmatrix} i_r \\ i_s \\ i_t \end{bmatrix} = r_{3\times3} \begin{bmatrix} I_X \\ I_Y \\ I_Z \end{bmatrix} \tag{23}$$

The total beam transformation 12 × 12 matrix $[T]_i$ is formed as in equation 24:

$$[T]_i = \begin{bmatrix} r & o & o & o \\ o & r & o & o \\ o & o & r & o \\ o & o & o & r \end{bmatrix} \tag{24}$$

In which ***o*** represents a 3 × 3 null matrix.

Displacement Vector of 3D Beam in Local Coordinates

Thus, the nodal displacement or rotational vector in local coordinates is as in equation 25:

$$\{U_L\}_{i_{12\times1}} = [T]_{i_{12\times12}} \{U\}_{i_{12\times1}} \tag{25}$$

In which 3D beam local displacements and rotations of the *i*th beam are defined as the vector in equation 26:

$$\{U_L\}_i = \begin{Bmatrix} \{U_L\}_{i1} \\ \{U_L\}_{i2} \end{Bmatrix} \tag{26}$$

Where the six displacement and rotational measures of the first and second nodes are $\{U\}_{i1}$ and $\{U\}_{i2}$, and they can be defined as in equations 27 and 28:

$$\{U_L\}_{i1} = \begin{Bmatrix} u_{1r} \\ u_{1s} \\ u_{1t} \\ \theta_{1r} \\ \theta_{1s} \\ \theta_{1t} \end{Bmatrix} \tag{27}$$

$$\{U_L\}_{i2} = \begin{Bmatrix} u_{2r} \\ u_{2s} \\ u_{2t} \\ \theta_{2r} \\ \theta_{2s} \\ \theta_{2t} \end{Bmatrix} \tag{28}$$

Strain-Displacement Relations

For Euler beam, strain due to bending about the local *t-t* axis can be expressed as in equation 29:

$$\varepsilon_t(r,s) = -s\frac{d^2u_s}{dr^2} \tag{29}$$

Similarly, strain due to bending about the local *s-s* axis can be expressed as in equation 30:

$$\varepsilon_s(r,t) = -t\frac{d^2u_t}{dr^2} \tag{30}$$

Equations 29 and 30 assume that the *t-t* and *s-s* axes are the principal axes of inertia of the beam. The total bending strain along the beam is as in equation 31:

$$\varepsilon_{ts}(r,t,s) = \varepsilon_s(r,t) + \varepsilon_t(r,s) = -t\frac{d^2u_t}{dr^2} - s\frac{d^2u_s}{dr^2} \tag{31}$$

The axial strain due to the axial deformation is as in equation 32:

$$\varepsilon_r = \frac{u_{2r} - u_{1r}}{L} \tag{32}$$

Note that L is the total length of the beam.

Combining the axial strain resulting from bending moments and axial force, the strain distribution in a general 3D beam is obtained from equation 33:

$$\varepsilon(r,t,s) = \varepsilon_r + \varepsilon_s(r,t) + \varepsilon_t(r,s) = \frac{u_{2r} - u_{1r}}{L} - t\frac{d^2u_t}{dr^2} - s\frac{d^2u_s}{dr^2} \tag{33}$$

Bending in the Local *s-r*, *t-r* Plane

The beam displacement is assumed as the cubic displacement function in equation 34:

$$u_s(r) = \alpha_1 + \alpha_2 r + \alpha_3 r^2 + \alpha_4 r^3 = [\alpha_1 \quad \alpha_2 \quad \alpha_3 \quad \alpha_4]\begin{Bmatrix} 1 \\ r \\ r^2 \\ r^3 \end{Bmatrix} \tag{34}$$

The constant α_i in matrix $[\alpha] = [\alpha_1\ \alpha_2\ \alpha_3\ \alpha_4]$ can be evaluated by applying displacement and rotation boundary conditions at the nodal ends of the beam as in equation 35:

$$\{\alpha\} = \begin{bmatrix} 1 & 0 & 0 & 0 \\ 0 & 1 & 0 & 0 \\ -\frac{3}{L^2} & -\frac{2}{L} & \frac{3}{L^2} & -\frac{1}{L} \\ \frac{2}{L^3} & \frac{1}{L^2} & -\frac{2}{L^3} & \frac{1}{L^2} \end{bmatrix} \begin{Bmatrix} u_{1s} \\ \theta_{1t} \\ u_{2s} \\ \theta_{2t} \end{Bmatrix} \tag{35}$$

The strains in the *s*-*r* plane are expressed as in equation 36:

$$\varepsilon_t(r,s) = -s[0 \quad 0 \quad 2 \quad 6r]\{\alpha\} \tag{36}$$

To express the strains in the *s*-*r* plane as a function of nodal displacements as in equation 37:

$$\varepsilon_t(r,s) = -s[\beta] \begin{Bmatrix} u_{1s} \\ \theta_{1t} \\ u_{2s} \\ \theta_{2t} \end{Bmatrix} \tag{37}$$

Where $[\beta]$ is calculated using equation 38:

$$[\beta] = [0 \quad 0 \quad 2 \quad 6r] \begin{bmatrix} 1 & 0 & 0 & 0 \\ 0 & 1 & 0 & 0 \\ -\frac{3}{L^2} & -\frac{2}{L} & \frac{3}{L^2} & -\frac{1}{L} \\ \frac{2}{L^3} & \frac{1}{L^2} & -\frac{2}{L^3} & \frac{1}{L^2} \end{bmatrix} \tag{38}$$

For bending in the *t*-*r* plane and using a similar process as before, strains can be evaluated as in equation 39:

$$\varepsilon_s(r,t) = -t[\beta] \begin{Bmatrix} u_{1s} \\ \theta_{1t} \\ u_{2s} \\ \theta_{2t} \end{Bmatrix} \tag{39}$$

In general, the maximum strains occur at either end of the beam (i.e., $r = 0$ or $r = L$). Based on the methodology developed in the previous equations, strains are produced at four corner points for both ends of each beam element, as shown in figure 116.

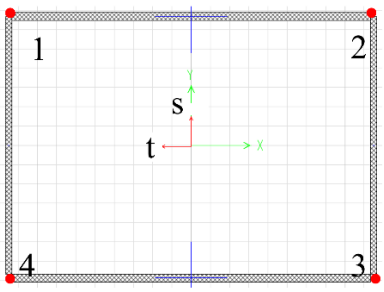

Source: FHWA.

Figure 116. Illustration. Output locations for strain for a beam section.

STRAINS FROM 3D BEAM ELEMENT INTERNAL FORCES CALCULATION

The other possible approach to verify the strain is a force-based method. For the type 2 resultant beam in LS-DYNA, the element forces and moments are output at the first node of the beam connectivity. Based on the beam equilibrium, the second nodal forces are yielded. The B-S beam uses the classical Timoshenko beam formulation. Thus, for the internal forces of B-S beam element formulation, the functional forms relating the overall response of the beam are adopted (e.g., moment–curvature relations).

Axial Force

The internal axial force (F_{1r}) can be calculated from the elongation (δ) of the beam and the axial stiffness (K^a), as in equation 40:

$$F_{1r} = K^a \delta \tag{40}$$

K^a can be calculated by equation 41:

$$K^a = \frac{EA_c}{L} \tag{41}$$

Where L is the original length of the beam.

Bending Moments

Based on the deformation rotations, the bending moments are obtained by equations 42 and 43:

$$\begin{Bmatrix} M_{1s} \\ M_{2s} \end{Bmatrix} = \frac{K_s^b}{1+\varphi_s} \begin{bmatrix} 4+\varphi_s & 2-\varphi_s \\ 2-\varphi_s & 4+\varphi_s \end{bmatrix} \begin{Bmatrix} \theta_{1s} \\ \theta_{2s} \end{Bmatrix} \tag{42}$$

$$\begin{Bmatrix} M_{1t} \\ M_{2t} \end{Bmatrix} = \frac{K_t^b}{1+\varphi_t} \begin{bmatrix} 4+\varphi_t & 2-\varphi_t \\ 2-\varphi_t & 4+\varphi_t \end{bmatrix} \begin{Bmatrix} \theta_{1t} \\ \theta_{2t} \end{Bmatrix} \tag{43}$$

Equation 42 is for bending moments M_{1s} and M_{2s} in the local *r*-*t* plane, and equation 43 is for bending moments M_{1t} and M_{2t} in the *r*-*s* plane. The bending constants K_s^b and K_t^b and shape factors φ_s and φ_t can be determined by equations 44, 45, 46, and 47, respectively:

$$K_s^b = \frac{EI_s}{L} \tag{44}$$

$$K_t^b = \frac{EI_t}{L} \tag{45}$$

$$\varphi_s = \frac{12EI_s}{GA_sL^2} \tag{46}$$

$$\varphi_t = \frac{12EI_t}{GA_tL^2} \tag{47}$$

Where:

K_s^b = flexural stiffness in the *s* direction.
K_t^b = flexural stiffness in the *t* direction.
φ_s = shear factor in the *s* direction.
φ_t = shear factor in the *t* direction.
A_s = effective area in shear in the *s* direction.
A_t = effective area in shear in the *t* direction.
I_s = moment of inertia about the *s*-axis.
I_t = moment of inertia about the *t*-axis.

Torsional Moment

The torsional moment is produced based on the torsional deformation rotation (θ_{1r}) and the torsional stiffness (K^t) as in equation 48:

$$M_{1r} = K^t\theta_{1r} \tag{48}$$

K^t can be calculated by equation 49:

$$K^t = \frac{GJ_t}{L} \tag{49}$$

Where J_t is the torsion constant for the section.

The remaining internal force components can be found from beam equilibrium.

APPENDIX B. CROSS-SECTIONAL AREA OF TRUSS MEMBERS FOR THE I-35W BRIDGE

Table 44 through table 47 detail the cross-sectional areas of truss members for the I-35W Bridge.

Table 44. Cross-sectional area of upper chord members for I-35W Bridge model.

Upper Chord Member	Cross-Sectional Area (m^2)
U0-U1	3.55×10^{-2}
U1-U2	3.55×10^{-2}
U2-U3	4.90×10^{-2}
U3-U4	4.90×10^{-2}
U4-U5	3.55×10^{-2}
U5-U6	3.55×10^{-2}
U6-U7	7.16×10^{-2}
U7-U8	7.16×10^{-2}
U8-U9	6.48×10^{-2}
U9-U10	6.48×10^{-2}
U10-U11	4.90×10^{-2}
U11-U12	4.90×10^{-2}
U12-U13	9.13×10^{-2}
U13-U14	9.13×10^{-2}
U14-U15	9.13×10^{-2}
U15-U16	9.13×10^{-2}
U16-U17	4.90×10^{-2}
U17-U18	4.90×10^{-2}
U18-U19	6.48×10^{-2}
U19-U20	6.48×10^{-2}
U20-U21	7.16×10^{-2}
U21-U22	7.16×10^{-2}
U22-U23	3.55×10^{-2}
U23-U24	3.55×10^{-2}
U24-U25	4.90×10^{-2}
U25-U26	4.90×10^{-2}
U26-U27	4.68×10^{-2}
U27-U28	4.68×10^{-2}

1 m^2 = 10.764 ft^2.

Table 45. Cross-sectional area of lower chord members for I-35W Bridge model.

Lower Chord Member	Cross-Sectional Area (m^2)
L1-L2	4.29×10^{-2}
L2-L3	4.29×10^{-2}
L3-L4	4.68×10^{-2}
L4-L5	4.68×10^{-2}
L5-L6	6.03×10^{-2}
L6-L7	6.03×10^{-2}
L7-L8	1.16×10^{-1}
L8-L9	1.16×10^{-1}
L9-L10	4.68×10^{-2}
L10-L11	4.68×10^{-2}
L11-L12	6.48×10^{-2}
L12-L13	6.48×10^{-2}
L13-L14	8.97×10^{-2}
L14-L15	8.97×10^{-2}
L15-L16	6.48×10^{-2}
L16-L17	6.48×10^{-2}
L17-L18	4.68×10^{-2}
L18-L19	4.68×10^{-2}
L19-L20	1.16×10^{-1}
L20-L21	1.16×10^{-1}
L21-L22	6.03×10^{-2}
L22-L23	6.03×10^{-2}
L23-L24	4.68×10^{-2}
L24-L25	4.68×10^{-2}
L25-L26	4.29×10^{-2}
L26-L27	4.29×10^{-2}

1 m^2 = 10.764 ft^2.

Table 46. Cross-sectional area of vertical members for I-35W Bridge model.

Vertical Member	Cross-Sectional Area (m^2)
U1-L1	2.74×10^{-2}
U2-L2	1.45×10^{-2}
U3-L3	2.74×10^{-2}
U4-L4	1.45×10^{-2}
U5-L5	2.90×10^{-2}
U6-L6	1.45×10^{-2}
U7-L7	3.26×10^{-2}
U8-L8	1.25×10^{-1}
U9-L9	3.26×10^{-2}
U10-L10	1.45×10^{-2}
U11-L11	2.74×10^{-2}
U12-L12	1.45×10^{-2}
U13-L13	2.74×10^{-2}
U14-L14	1.45×10^{-2}
U15-L15	2.74×10^{-2}
U16-L16	1.45×10^{-2}
U17-L17	2.74×10^{-2}
U18-L18	1.45×10^{-2}
U19-L19	3.26×10^{-2}
U20-L20	1.25×10^{-1}
U21-L21	3.26×10^{-2}
U22-L22	1.45×10^{-2}
U23-L23	2.90×10^{-2}
U24-L24	1.45×10^{-2}
U25-L25	2.74×10^{-2}
U26-L26	1.45×10^{-2}
U27-L27	2.74×10^{-2}

1 m^2 = 10.764 ft^2.

Table 47. Cross-sectional area of DMs for I-35W Bridge model.

Diagonal Member	Cross-Sectional Area (m^2)
U0-L1	3.95×10^{-2}
L1-U2	5.16×10^{-2}
U2-L3	1.79×10^{-2}
L3-U4	2.29×10^{-2}
U4-L5	4.19×10^{-2}
L5-U6	3.72×10^{-2}
U6-L7	6.65×10^{-2}
L7-U8	4.77×10^{-2}
U8-L9	5.98×10^{-2}
L9-U10	9.00×10^{-2}
U10-L11	5.68×10^{-2}
L11-U12	6.65×10^{-2}
U12-L13	3.72×10^{-2}
L13-U14	3.18×10^{-2}
U14-L15	3.18×10^{-2}
L15-U16	3.72×10^{-2}
U16-L17	6.65×10^{-2}
L17-U18	5.68×10^{-2}
U18-L19	9.00×10^{-2}
L19-U20	5.98×10^{-2}
U20-L21	4.77×10^{-2}
L21-U22	6.65×10^{-2}
U22-L23	3.72×10^{-2}
L23-U24	4.19×10^{-2}
U24-L25	2.29×10^{-2}
L25-U26	1.93×10^{-2}
U26-L27	5.16×10^{-2}
L27-U28	5.74×10^{-2}

$1\ m^2 = 10.764\ ft^2$.

APPENDIX C. THE CALCULATION OF *DCR* FOR COMPRESSION AND TENSION MEMBERS

COMPRESSION MEMBER

To illustrate the calculation of *DCR*, a typical compression member (member L8-L9 of the I-35W Bridge) is used as an example. This member has a box section, and the corresponding cross-sectional properties and demand are shown in table 48 and table 49, respectively. The detailed calculation of *DCR* for this member can be expressed as follows in equation 50 through equation 56:

$$F_e = \frac{\pi^2 E}{\left(\frac{KL}{r_g}\right)^2} = 7.095 \times 10^8 \text{ Pa} \tag{50}$$

$$\frac{\sigma_y}{F_e} = \frac{3.447 \times 10^8}{7.095 \times 10^8} = 0.486 < 2.25 \tag{51}$$

$$F_{cr} = \left[0.658^{\frac{\sigma_y}{F_e}}\right] \times \sigma_y = 2.813 \times 10^8 \text{ Pa} \tag{52}$$

$$P_c = \frac{P_n}{\Omega} = \frac{3.266 \times 10^7}{1.67} = 1.956 \times 10^7 \text{ N} \tag{53}$$

$$M_{cx} = \frac{\sigma_y \times S_{xx}}{\Omega} = \frac{3.447 \times 10^8 \times 0.0206}{1.67} = 4.252 \times 10^6 \text{ N} \cdot \text{m} \tag{54}$$

$$M_{cy} = \frac{\sigma_y \times S_{yy}}{\Omega} = \frac{3.447 \times 10^8 \times 0.0160}{1.67} = 3.303 \times 10^6 \text{ N} \cdot \text{m} \tag{55}$$

$$DCR = \frac{P_r}{P_c} + \frac{8}{9}\left(\frac{M_{rx}}{M_{cx}} + \frac{M_{ry}}{M_{cy}}\right) = \frac{1.495 \times 10^7}{1.956 \times 10^7} + \frac{8}{9}\left(\frac{10521.41}{4.525 \times 10^6} + \frac{1.057 \times 10^6}{3.303 \times 10^6}\right) = 1.051 > 1.00 \tag{56}$$

Where:

F_e = Euler stress.
r_g = radius of gyration.
F_{cr} = critical stress.
P_n = nominal axial force using ASD.

Table 48. Cross-sectional properties of the compression member.

Parameter	Value
Section area (A_c)	0.1161 m^2
Sectional moment of inertia about x-axis (S_{xx})	0.0206 m^3
Sectional moment of inertia about y-axis (S_{yy})	0.0160 m^3
Member length (L)	11.880 m

1 m = 3.281 ft; 1 m^2 = 10.764 ft^2; 1 m^3 = 35.315 ft^3.

Table 49. Demand of the compression member.

Parameter	Value
Axial force (P_r)	1.539×10^6 N
Moment about x-axis (M_{rx})	285.5 N·m
Moment about y-axis (M_{ry})	1.075×10^6 N·m

1 N = 0.225 lb; 1 N·m = 0.738 lb·ft.

TENSION MEMBER

Likewise, the calculation of *DCR* for a typical tension member (member L11-L12 of the I-35W Bridge) is detailed in this section. This member has a box section, and its cross-sectional properties and demand are shown in table 50 and table 51, respectively. The detailed calculation of *DCR* for this member can be expressed as follows in equation 57 through equation 60:

$$P_c = \frac{P_n}{\Omega} = \frac{2.235 \times 10^7}{1.6} = 1.339 \times 10^7 \text{ N} \tag{57}$$

$$M_{cx} = \frac{\sigma_y \times S_{xx}}{\Omega} = \frac{4.585 \times 10^6}{1.67} = 2.746 \times 10^6 \text{ N} \cdot \text{m} \tag{58}$$

$$M_{cy} = \frac{\sigma_y \times S_{yy}}{\Omega} = \frac{3.620 \times 10^6}{1.67} = 2.168 \times 10^6 \text{ N} \cdot \text{m} \tag{59}$$

$$DCR = \frac{P_r}{P_c} + \frac{8}{9}\left(\frac{M_{rx}}{M_{cx}} + \frac{M_{ry}}{M_{cy}}\right) = \frac{7.564 \times 10^6}{1.339 \times 10^7} + \frac{8}{9}\left(\frac{1.262 \times 10^4}{2.746 \times 10^6} + \frac{1.131 \times 10^5}{2.168 \times 10^6}\right) = 0.615 < 1.00 \tag{60}$$

Table 50. Cross-sectional properties of the tension member.

Parameter	Value
Section area (A_c)	0.06484 m^2
Sectional moment of inertia about x-axis (S_{xx})	0.0133 m^3
Sectional moment of inertia about y-axis (S_{yy})	0.0105 m^3
Member length (L)	11.597 m

1 m = 3.281 ft; 1 m^2 = 10.764 ft^2; 1 m^3 = 35.315 ft^3.

Table 51. Demand of the tension member.

Parameter	Value
Axial force (P_r)	7.564×10^6 N
Moment about x-axis (M_{rx})	1.262×10^4 N·m
Moment about y-axis (M_{ry})	1.131×10^5 N·m

1 N = 0.225 lb; 1 N·m = 0.738 lb·ft.

ACKNOWLEDGMENTS

The authors sincerely acknowledge the help of Professor Shozo Nakamura from Nagasaki University (Japan) with the FEM of the Ikitsuki Bridge.

REFERENCES

AASHTO. (2010). *AASHTO LRFD Bridge Design Specifications*, 5th Ed., American Association of State Highway and Transportation Officials, Washington, DC.

AASHTO. (2012). *AASHTO LRFD Bridge Design Specifications*, 6th Ed., American Association of State Highway and Transportation Officials, Washington, DC.

AASHTO. (2014). *AASHTO LRFD Bridge Design Specifications*, 7th Ed. American Association of State Highway and Transportation Officials, Washington, DC.

AASHTO. (2017). *AASHTO LRFD Bridge Design Specifications*, 8th Ed. American Association of State Highway and Transportation Officials, Washington, DC.

AASHTO. (2018a). *Analysis and Identification of Fracture Critical Members and System Redundant Members*, American Association of State Highway and Transportation Officials, Washington, DC.

AASHTO. (2018b). *Guide Specifications for Internal Redundancy of Mechanically-Fastened Built-up Steel Members*. American Association of State Highway and Transportation Officials, Washington, DC.

Agrawal, A.K., Ghosn, M., Alampalli, S., and Pan, Y. (2012). "Seismic Fragility of Retrofitted Multispan Continuous Steel Bridges in New York." *Journal of Bridge Engineering, 17*(4), pp. 562–575, American Society of Civil Engineers, Reston, VA.

Agrawal, A.K. and Amjadian, M. (2016). "Seismic Component Devices," in *Innovative Bridge Design Handbook: Construction, Rehabilitation and Maintenance*, edited by Alessio Pipinato, pp. 531–553, Butterworth-Heinemann, Boston, MA.

AISC. (2010). *Specifications for Structural Steel Buildings*, American Institute of Steel Construction, Chicago, IL.

Arasaratnam, P., Sivakumaran, K.S., and Tait, M.J. (2011). "True Stress-True Strain Models for Structural Steel Elements." *ISRN Civil Engineering*, pp. 1–11, Hindawi Publishing Corporation, London, UK.

ASCE/SEI 7-10. (2010). *Minimum Design Loads for Buildings and Other Structures*. American Society of Civil Engineers, Reston, VA.

Astaneh-Asl, A. (2008). *Progressive Collapse of Steel Truss Bridges, the Case of I-35W Collapse.* In Proceedings of the 7th International Conference on Steel Bridges, Guimarães, Portugal.

Azizinamini, A. (2002). "Full Scale Testing of Old Steel Truss Bridge." *Journal of Constructional Steel Research, 58*(5–8), pp. 843–858, Elsevier, Amsterdam, Netherlands.

Barth, K., Michaelson, G., and Gonano, D. (2014). "Assessment of Redundancy Protocols for Short-Span Steel Truss Bridges." *Bridge Structures, 10*(2–3), pp. 105–114, IOS Press, Amsterdam, Netherlands.

Beauchamp, J.C., Chan, M.Y.T., and Pion, R.H. (1984). "Repair and Evaluation of a Damaged Truss Bridge-Lewes, Yukon River." *Canadian Journal of Civil Engineering, 11*(3), pp. 494–504, Canadian Science Publishing, Ottawa, Canada.

Belytschko, T., Schwer, L., and Klein, M.J. (1977). "Large Displacement, Transient Analysis of Space Frames." *International Journal for Numerical Methods in Engineering, 11*(1), pp. 65–84, John Wiley & Sons, Hoboken, NJ.

Blandford, G.E. (1996). "Large Deformation Analysis of Inelastic Space Truss Structures." *Journal of Structural Engineering, 122*(4), pp. 407–415, American Society of Civil Engineers, Reston, VA.

Blandford, G.E. (1997). "Review of Progressive Failure Analyses for Truss Structures." *Journal of Structural Engineering, 123*(2), pp. 122–129, American Society of Civil Engineers, Reston, VA.

Blanksvärd, T., Häggström, J., Nilimaa, J., Sabourova, N., Grip, N., Täljsten, B., Elfgren, L., Carolin, A., Paulsson, B., and Tu, Y. (2014). "Test to Failure of a Steel Truss Bridge: Calibration of Assessment Methods," in *Bridge Maintenance, Safety, and Life Extension*, edited by Arong Chen, Dan Frangopol, and Xin Ruan, pp. 1076–1081, CRC Press, Taylor & Francis Group, London, UK.

Casciati, F., Cimellaro, G.P., and Domaneschi, M. (2008). "Seismic Reliability of a Cable-Stayed Bridge Retrofitted with Hysteretic Devices." *Computers & Structures, 86*(17–18), pp. 1769–1781, Elsevier, Amsterdam, Netherlands.

Cha, H., Lyrenmann, L., Connor, R.J., and Varma, A.H. (2014). "Experimental and Numerical Evaluation of the Post-Fracture Redundancy of a Simple Span Truss Bridge." *Journal of Bridge Engineering, 19*(11), American Society of Civil Engineers, Reston, VA.

Chen, X., Ge, H., and Usami, T. (2011). "Seismic Demand of Buckling-Restrained Braces Installed in Steel Arch Bridges under Repeated Earthquakes." *Journal of Earthquake and Tsunami, 05*(02), pp. 119–150, World Scientific, Singapore.

Cho, H.N., Lim, J.K., and Choi, H.H. (2001). "Reliability-Based Fatigue Failure Analysis for Causes Assessment of a Collapsed Steel Truss Bridge." *Engineering Failure Analysis, 8*(4), pp. 311–324, Elsevier, Amsterdam, Netherlands.

Chopra, A.K. (2000). *Dynamics of Structures: Theory and Applications,* Pearson, Hoboken, NJ.

Computers and Structures, Inc. (2014). *SAP2000*, Version 17.0, Berkeley, CA.

CSA. (2006). *Canadian Highway Bridge Design Code CAN/CSA-S6-06*, Canadian Standards Association, Toronto, Ontario, Canada.

Csagoly, P.F. and Jaeger., L.G. (1979). "Multi-Load-Path Structures for Highway Bridges." *Transportation Research Record 711*, pp. 34–39, National Academy of Sciences, Washington, DC.

Dassault, S. (2013a). *ABAQUS 6.13 Abaqus/CAE User's Guide*, Dassault Systemes Simulia, Providence, RI.

Dassault, S. (2013b). *ABAQUS 6.13 Theoretical Manual*, Dassault Systemes Simulia, Providence, RI.

DataHub. (n.d.). "Steel Bridge Database." (website). Available online: http://datacenterhub.org/dv_dibbs/view/1024:dibbs/experiments_dv, last accessed May 15, 2020.

Davalos, J. F. (1989). *Geometrically Nonlinear Finite Element Analysis of a Glulam Timber Dome*, PhD thesis, Virginia Polytechnic Institute and State University, Blacksburg, VA.

DelGrego, M., Culmo, M., and DeWolf, J. (2008). "Performance Evaluation Through Field Testing of Century-Old Railroad Truss Bridge." *Journal of Bridge Engineering, 13*(2), pp. 132–138, American Society of Civil Engineers, Reston, VA.

DOD. (2009). *Unified Facilities Criteria: Design of Buildings to Resist Progressive Collapse*, Report No. UFC4-023-03, United States Department of Defense, Washington, DC.

Diggelmann, L.M., Connor, R.J., and Sherman, R.J. (2013). *Evaluation of Member and Load-Path Redundancy on the US-421 Bridge over the Ohio River*, Federal Highway Administration, Washington, DC.

Dyke, S.J., Caicedo, J.M., Turan, G., Bergman, L.A., and Hague, S. (2003). "Phase I Benchmark Control Problem for Seismic Response of Cable-Stayed bridges." *Journal of Structural Engineering, 129*(7), pp. 857–872, American Society of Civil Engineers, Reston, VA.

El-Bahey, S. and Bruneau, M. (2011). "Buckling Restrained Braces as Structural Fuses for the Seismic Retrofit of Reinforced Concrete Bridge Bents." *Engineering Structures, 33*(3), pp. 1052–1061, Elsevier, Amsterdam, Netherlands.

El-Tawil, S., Khandelwal, K., Kunnath, S., and Lew, H. S. (2007). *Macro Models for Progressive Collapse Analysis of Steel Moment Frame Buildings.* Presented at Structures Congress 2007, American Society of Civil Engineers, Long Beach, CA.

Ellingwood, B.R. (2006). "Mitigating Risk from Abnormal Loads and Progressive Collapse." *Journal of Performance of Constructed Facilities, 20*(4), pp. 315–323, American Society of Civil Engineers, Reston, VA.

Ellingwood, B.R. and Dusenberry, D.O. (2005). "Building Design for Abnormal Loads and Progressive Collapse." *Computer-Aided Civil and Infrastructure Engineering, 20*(3), pp. 194–205, Wiley, Hoboken, NJ.

Ellingwood, B.R., Smilowitz, R., Dusenberry, D.O., Duthinh, D., Lew, H.S., and Carino, N.J. (2007). *Best Practices for Reducing the Potential for Progressive Collapse in Buildings*, Report No. NISTIR 7396, National Institute of Standards and Technology, Gaithersburg, MD.

Ettouney, M., Smilowitz, R., Tang, M., and Hapij, A. (2006). "Global System Considerations for Progressive Collapse with Extensions to Other Natural and Man-Made Hazards." *Journal of Performance of Constructed Facilities, 4*(20), American Society of Civil Engineers, Reston, VA.

Ettouney, M. and Alampalli, S. (2010a). *Infrastructure Health in Civil Engineering, Volume I: Theory and Components*, CRC Press, Boca Raton, FL.

Ettouney, M. and Alampalli, S. (2010b). *Infrastructure Health in Civil Engineering, Volume II: Applications and Management*, CRC Press, Boca Raton, FL.

Ettouney, M. and Alampalli, S. (2014). *Progressive Collapse Principles of Bridge Structures.* Presented at the 10th International Conference on Shock and Impact Loads on Structures, Singapore.

Ettouney, M. and Alampalli, S. (2016). *Risk Management in Civil Infrastructures*, CRC Press, Boca Raton, FL.

FHWA. (n.d.). "National Bridge Inventory." (website). Available online: https://www.fhwa.dot.gov/bridge/nbi.cfm, last accessed May 14, 2020.

FHWA. (2013). *TechBrief: Evaluation of Member and Load Path Redundancy on the US-421 Bridge over the Ohio River*, Report No. FHWA-HRT-13-105, Federal Highway Administration, Washington, DC.

FHWA. (2015). *Load and Resistance Factor Design (LRFD) for Highway Bridge Superstructures*, NHI Course Nos. 130081, 130081A, and 130081B, Federal Highway Administration, Washington, DC.

Fiorillo, G., Miao, F., and Ghosn, M. (2015). "Direct Redundancy Evaluation of Bridges Designated as Fracture-Critical." *Journal of Performance of Constructed Facilities, 30*(3), American Society of Civil Engineers, Reston, VA.

Fisher, J.W., Pense, A.W., and Roberts, R. (1977). "Evaluation of Fracture of Lafayette Street Bridge." *Journal of the Structural Division, 103*(ST7), pp. 1339–1357, American Society of Civil Engineers, Reston, VA.

Frangopol, D.M. and Curley, J.P. (1987). "Effect of Damage and Redundancy on Structural Reliability." *Journal of Structural Engineering, 113*(7), pp. 1533–1549, American Society of Civil Engineers, Reston, VA.

Frangopol, D.M. and Imai, K. (2004). "Reliability of Long Span Bridges Based on Design Experience with the Honshu-Shikoku Bridges." *Journal of Constructional Steel Research, 60*(3–5), pp. 373–392, Elsevier, Amsterdam, Netherlands.

Golden Gate Bridge Authority. (2014). "Golden Gate Bridge Seismic Retrofit Project." Available online: https://www.goldengate.org/assets/1/6/bridge-projects-seismic-retrofit-schematic.pdf, last accessed April 9, 2020.

Grub, M.A., Wilson, K.E., White, C.D., and Nickas, W.N. (2015). *Load and Resistance Factor Design (LRFD) for Highway Bridge Superstructures–Reference Manual*, Report No. FHWA-NHI-15-047, Federal Highway Administration, Washington, DC.

GSA. (2003). *Progressive Collapse Analysis and Design Guidelines for New Federal Office Buildings and Major Modernization Projects*, General Services Administration, Washington, DC.

GSA. (2016). *Progressive Collapse Analysis and Design Guidelines for Progressive Collapse Resistance*, General Services Administration, Washington, DC.

Hallquist, J.O. (2014). *LS-DYNA Keyword User's Manual,* Version 971, Livermore Software Technology Corporation, Livermore, CA.

Hao, S. (2010). "I-35W Bridge Collapse." *Journal of Bridge Engineering, 15*(5), pp. 608–614, American Society of Civil Engineers, Reston, VA.

Higgins, C., Dusicka, P., and Scott, M. (2012). *Experimental Tests and Numerical Analyses of Steel Truss Bridge Gusset Connections*, Report No. OTREC-RR-12-03, Oregon Transportation Research and Education Consortium (OTREC), Portland, OR.

Hill, C.D., Blandford, G.E., and Wang, S.T. (1989). "Post-Buckling Analysis of Steel Space Trusses." *Journal of Structural Engineering, 115*(4), pp. 900–919, American Society of Civil Engineers, Reston, VA.

Imbsen, R. and Liu. W. (1993). *Seismic Evaluation of Benicia-Martinez Bridge*. Presented at the First US Seminar on Seismic Evaluation and Retrofit of Steel Bridges, University of California at Berkeley.

Imbsen, R. and Schamber, R. (1999). "Seismic Retrofit of the North Approach Viaduct of the Golden Gate Bridge." *Transportation Research Record 1688*, pp. 154–162, National Academy of Sciences, Washington, DC.

Izzuddin, B.A., Vlassis, A.G., Elghazouli, A.Y., and Nethercot, D.A. (2008). "Progressive Collapse of Multi-Storey Buildings Due to Sudden Column Loss - Part I: Simplified Assessment Framework." *Engineering Structures, 30*(5), pp. 1308–1318, Elsevier, Amsterdam, Netherlands.

Jelinek, J.J. and Bartlett, F. M. (2002). "Material Properties of Historical Bridge Steel," in *Proceedings of the 30th Annual Conference of the Canadian Society of Civil Engineering*, pp. 1313–1322, Canadian Society for Civil Engineering, Montreal, Canada.

Kanaji, H., Kitazawa, M., and Suzuki, N. (2003). *Seismic Retrofit Strategy Using Damage Control Design Concept and the Response Reduction Effect for a Long-Span Truss Bridge.* Presented at the 19th US–Japan Bridge Engineering Workshop Panel on Wind and Seismic Effects, US–Japan Cooperative Program in Natural Resources, Tsukuba Science City, Japan.

Kandemir, E.C., Mazda, T., Nurui, H., and Miyamoto, H. (2011). "Seismic Retrofit of an Existing Steel Arch Bridge Using Viscous Damper." *Procedia Engineering, 14*, pp. 2301–2306, Elsevier, Amsterdam, Netherlands.

Kawabata, S., Koga, T., Takahashi, K., Nakamura, S., and Wu, Q. (2011). "Verification of Analytical Model of the Ikitsuki Bridge by Ambient Vibration Measurement." *Proceedings of Constructional Steel, 19*(11), pp. 1–6, Japanese Society of Steel Construction, Tokyo.

Kingery, C.N. and Bulmash, G. (1984). *Airblast Parameters from TNT Spherical Air Burst and Hemispherical Surface Burst*, Report ARBRL-TR-02555, Army Ballistic Research Laboratory, Aberdeen Proving Ground, MD.

Kubota, K., Inuzuka, H., Wu, Q., Takahashi, K., and Nakamura, S. (2004). "Natural Vibration and Nonlinear Seismic Response Properties of Continuous Truss Bridge." *Journal of Constructional Steel Research, 12*(11), pp. 1–8.

Lee, G.C., Mohan, S., Huang, C., and Fard, B.N. (2013). *A Study of US Bridge Failures (1980–2012),* Technical Report 13-0008, Multidisciplinary Center for Earthquake Engineering Research (MCEER), Buffalo, NY.

Liao, M., Okazaki, T., Ballarini, R., Schultz, A.E., and Galambos, T.V. (2009). *Analysis of Critical Gusset Plates in the Collapsed I-35W Bridge,* Structures Congress 2009, American Society of Civil Engineers, Reston, VA.

Liao, M., Okazaki, T., Ballarini, R., Schultz, A.E., and Galambos, T.V. (2011). "Nonlinear Finite-Element Analysis of Critical Gusset Plates in the I-35W Bridge in Minnesota." *Journal of Structural Engineering, 137*(1), pp. 59–68, American Society of Civil Engineers, Reston, VA.

Lichtenstein, A.G. (1993). "The Silver Bridge Collapse Recounted." *Journal of Performance of Constructed Facilities, 7*(4), pp. 249–261, American Society of Civil Engineers, Reston, VA.

Liu, S., Bartlett, F.M., and Zhou, W. (2013). "Alternative Load Paths in Steel Through-Truss Bridges: A Case Study." *Journal of Bridge Engineering, 18*(9), pp. 920−928, American Society of Civil Engineers, Reston, VA.

Liu, W. D., Nobari, F.S., Schamber, R.A., and Imbsen, R.A. (1997). "Performance Based Seismic Retrofit of Benicia-Martinez Bridge," in *Proceedings of the 2nd National Seismic Conference on Bridges and Highways*, pp. 509–523, Sacramento, CA.

Lwin, M. (2012). *Clarification of Requirements for Fracture Critical Members,* FHWA Memorandum HIBT 10, Federal Highway Administration, Washington, DC.

Matson, D.D. and Buckland, P.G. (1995). "Experience with Seismic Retrofit of Major Bridges," in *Proceedings of the 1st National Seismic Conference on Bridges and Highways*, San Diego, CA.

Mueller, W.H. and Wagner, A.L. (1984). *Plastic Behavior of Steel Angle Columns*, Research Report, Civil/ Structural Engineering, Portland State University, Portland, OR.

Murtha-Smith, E. (1988). "Alternate Path Analysis of Space Trusses for Progressive Collapse." *Journal of Structural Engineering, 114*(9), pp. 1978–1999, American Society of Civil Engineers, Reston, VA.

Mustafa, S., Matsumoto, Y., and Yamaguchi, H. (2018). "Vibration-Based Health Monitoring of an Existing Truss Bridge Using Energy-Based Damping Evaluation." *Journal of Bridge Engineering, 23*(1), American Society of Civil Engineers, Reston, VA.

Nagavi, R.S. and Aktan, A. E. (2003). "Nonlinear Behavior of Heavy Class Steel Truss Bridges." *Journal of Structural Engineering, 129*(8), pp. 1113–1121, American Society of Civil Engineers, Reston, VA.

Nakamura, S., Okumatsu, T., Nishikawa, T., and Okabayashi, T. (2016). "Fatigue Damage of a Diagonal Member in a Steel Truss Bridge Due to Wind-Induced Vibration," in *Developments in International Bridge Engineering*, edited by Alp Caner, Polat Gülkan, and Khaled Mahmoud, pp. 211–220, Springer, Cham, Switzerland.

NTSB. (1968). *Collapse of US 35 Highway Bridge, Point Pleasant, West Virginia, December 15, 1967*, Highway Accident Report HAR-71-01, National Transportation Safety Board, Washington, DC.

NTSB. (2008a). *Safety Recommendation (H08-1)*, National Transportation Safety Board, Washington, DC.

NTSB. (2008b). *Structural Investigation Group Chairman Factual Report*, NTSB Report No. 08-015, National Transportation Safety Board, Washington, DC.

NTSB. (2008c). *Data Report: State-by-State Bridge Counts*, NTSB Data Report, Case Number HWY07MH024, National Transportation Safety Board, Washington, DC.

NTSB. (2008d). *Highway Accident Report Interstate 35W Collapse over the Mississippi River Minneapolis, Minnesota, August 1, 2007*, NTSB/HAR-08/03, National Transportation Safety Board, Washington, DC.

Ocel, J.M. and Wright, W.J. (2008). *Finite Element Modeling of I-35W Bridge Collapse - Final Report*, Federal Highway Administration, Turner-Fairbank Highway Research Center, McLean, VA.

Pan, Y., Agrawal, A.K., Ghosn, M., and Alampalli, S. (2010a). "Seismic Fragility of Multispan Simply Supported Steel Highway Bridges in New York State. I: Bridge Modeling, Parametric Analysis, and Retrofit Design." *Journal of Bridge Engineering, 15*(5), pp. 448–461, American Society of Civil Engineers, Reston, VA.

Pan, Y., Agrawal, A.K., Ghosn, M., and Alampalli, S. (2010b). "Seismic Fragility of Multispan Simply Supported Steel Highway Bridges in New York State. II: Fragility Analysis, Fragility Curves, and Fragility Surfaces." *Journal of Bridge Engineering, 15*(5), pp. 462–472, American Society of Civil Engineers, Reston, VA.

Papadrakakis, M. (1983). "Inelastic Post-Buckling Analysis of Trusses." *Journal of Structural Engineering, 109*(9), pp. 2129–2147, American Society of Civil Engineers, Reston, VA.

Prendergast, J. (1995). "Oklahoma City Aftermath." *Civil Engineering, 65*(10), p. 42, American Society of Civil Engineers, Reston, VA.

Randers-Pehrson, G. and Bannister, K. (1997). *Airblast Loading Model for DYNA2D and DYNA3D*, Report ARL-TR-1310, Army Ballistic Research Laboratory, Aberdeen Proving Ground, MD.

Reno, M.L. and Pohll, M.N. (2010). "Seismic Retrofit of California's Auburn-Foresthill Bridge." *Transportation Research Record, 2201*, pp. 83–94, National Academy of Sciences, Washington, DC.

Sanders Jr., W., Elleby, H.A., Klaiber, F.W., and Reeves, M.D. (1975). *Ultimate Load Behavior of Full-Scale Highway Truss Bridges*, Summary Report ISU-ERI-Ames-76035, Iowa Department of Transportation, Ames, IA.

Saravanan, M., Goswami, R., and Palani, G.S. (2018). "Replaceable Fuses in Earthquake Resistant Steel Structures: A Review." *International Journal of Steel Structures, 18*(3), pp. 868–879, Springer, New York.

Sarraf, M. and Bruneau, M. (1998). "Ductile Seismic Retrofit of Steel Deck-Truss Bridges. II: Design Applications." *Journal of Structural Engineering, 124*(11), pp. 1263–1271, American Society of Civil Engineers, Reston, VA.

Schmidt, L.C. and Gregg, B.M. (1980). "A Method for Space Truss Analysis in the Post-Buckling Range." *International Journal for Numerical Methods in Engineering, 15*(2), pp. 237–247, Wiley, Hoboken, NJ.

Schultheisz, C.R., Kushner, A.S., Nakamura, T., Ocel, J., Wright, W., and Li, M. (2008). "Minneapolis I-35W Bridge Collapse–Engineering Evaluations and Finite Element Analyses." Available online: http://www.simulia.com/download/pdf 2010/Schultheisz_SCC2010.pdf, last accessed April 9, 2020.

Sirisak, S. (1996). *Structural Integrity Evaluation of Truss Bridges*, PhD thesis, Vanderbilt University, Nashville, TN.

Uang, C.M. and Bruneau, M. (2018). "State-of-the-Art Review on Seismic Design of steel Structures." *Journal of Structural Engineering, 144*(4), American Society of Civil Engineers, Reston, VA.

Usami, T., Lu, Z., and Ge, H. (2005). "A Seismic Upgrading Method for Steel Arch Bridges Using Buckling-Restrained Braces." *Earthquake Engineering and Structural Dynamics*, *34*(4–5), pp. 471–496, International Association for Earthquake Engineering, Tokyo, Japan.

Wang, Q., Nakamura, S., Okumatsu, T., and Nishikawa, T. (2017). "Comprehensive Investigation on the Cause of a Critical Crack Found in a Diagonal Member of a Steel Truss Bridge." *Engineering Structures, 132*, pp. 659–670, Elsevier, Amsterdam, Netherlands.

Warren Jr., J.E. (1998). *Nonlinear Stability Analysis of Frame-Type Structures with Random Geometric Imperfections Using a Total-Lagrangian Finite Element Formulation*, PhD thesis, Virginia Polytechnic Institute and State University, Blacksburg, VA.

Williams, F.W. (1964). "An Approach to the Non-Linear Behavior of the Members of a Rigid Jointed Plane Framework with Finite Deflections." *The Quarterly Journal of Mechanics and Applied Mathematics, 17*(4), pp. 451–469, Oxford University Press, London, UK.

Williamson, E.B., Bayrak, O., Williams, G.D., Davis, C.E., Marchand, K.A., McKay, A.E., Kulicki, J., and Wassef, W. (2010). *Blast-Resistant Highway Bridges: Design and Detailing Guidelines,* NCHRP Report 645, National Cooperative Highway Research Program, Transportation Research Board, Washington, DC.

Zoli, T. and Woodward, R. (2005). "Design of Long Span Bridges for Cable Loss," in *IABSE Symposium Report 90*, pp. 17–25, International Association for Bridge and Structural Engineering, Zurich, Switzerland.

Recycled
Recyclable

HRDI-20/11-20(WEB)E